



Provided by the author(s) and University of Galway in accordance with publisher policies. Please cite the published version when available.

Title	Experimental and computational analysis of the mechanical behavior of poly(lactic-co-glycolic acid) during degradation for medical implant applications
Author(s)	Neghabat Shirazi, Reyhaneh
Publication Date	2016-01-25
Item record	http://hdl.handle.net/10379/5707

Downloaded 2024-05-14T00:59:21Z

Some rights reserved. For more information, please see the item record link above.



Experimental and Computational Analysis of the Mechanical Behaviour of Poly(lactic-co-glycolic acid) During Degradation for Medical Implant Applications

By

Reyhaneh Neghabat Shirazi MSc (2009)

A thesis submitted to the National University of Ireland as fulfilment
of the requirements for the Degree of Doctor of Philosophy.



Discipline of Biomedical Engineering,
College of Engineering and Informatics,
National University of Ireland, Galway.

Supervisors: **Prof. Peter McHugh** and **Dr. Yury Rochev**

January 2016

Table of Contents

Abstract.....	i
Acknowledgements	iii
List of Publications.....	iv
Abbreviations and Nomenclature	v
1 Introduction.....	1
1.1 Background	1
1.2 Thesis Objectives.....	5
1.3 Thesis Overview	6
2 Background.....	10
2.1 Introduction	10
2.2 Biodegradable Polymers	10
2.2.1 Biomedical Applications.....	11
2.2.2 Degradation Mechanism.....	13
2.2.3 Bulk vs. Surface Degradation	14
2.2.4 Factors Affecting the Degradation Rate.....	14
2.2.5 Mechanical Properties of Biodegradable Polymers.....	15
2.3 Nanoindentation	18
2.3.1 Indenter Tip.....	19
2.3.2 Load-Displacement Curve	19

2.3.3	Hardness and Elastic Modulus Determination	20
2.3.4	Factors Affecting Nanoindentation Test Data	22
2.4	Computational Modelling for Degradation of Biodegradable Polymers ...	29
2.4.1	Hydrolytic Reaction Rate.....	29
2.4.2	Diffusion	30
2.4.3	Reaction-Diffusion Models.....	31
2.4.4	Mechanical Property Prediction	32
2.5	Conclusion	33
2.6	Figures	35
2.7	Tables	41
3	Theoretical and Numerical Methods.....	43
3.1	Introduction	43
3.2	Theoretical Methods.....	44
3.2.1	Continuum Mechanics	44
3.2.2	Entropy Spring Theory.....	50
3.2.3	Polymer Degradation Model (Molecular Weight Model)	54
3.2.4	Nanoindentation Analysis	56
3.3	Numerical Methods.....	59
3.3.1	Numerical Solution for Structural Problems.....	59
3.3.2	Semi-analytical and Numerical Solutions for Polymer Degradation Problems (Molecular Weight Model)	63
3.3.3	The Mechanical Properties Model.....	66
3.3.4	Coupling Molecular Weight and Mechanical Properties Models	67
3.4	Conclusion	68

3.5	Figures	70
4	Experimental Methods	76
4.1	Introduction	76
4.2	Materials and Sample Preparations.....	76
4.3	<i>In-vitro</i> Degradation	77
4.4	Surface Morphology.....	78
4.5	Molecular Weight Determination	78
4.6	Crystallinity.....	79
4.7	Surface Roughness and Pile-up.....	79
4.8	Mechanical Properties	79
4.8.1	Indenter-Microscope Distance Calibration	80
4.8.2	Area Function Calibration	80
4.8.3	Indentation of PLGA Material	81
4.9	Conclusion	82
4.10	Figures	83
4.11	Table.....	86
5	Nanomechanical Properties of Solvent-cast PLGA Films During Degradation.....	87
5.1	Overview	87
5.2	Introduction	87
5.3	Material and Methods	89
5.4	Results	91
5.4.1	Mass Loss and Water Content	91
5.4.2	Surface Morphology.....	91

5.4.3	Molecular Weight.....	92
5.4.4	Crystallinity.....	93
5.4.5	Mechanical Properties	93
5.5	Discussion.....	94
5.6	Conclusion	100
5.7	Figures	102
6	Modelling the Degradation and Elastic Properties of PLGA Films and Regular Open-cell Tissue Engineering Scaffolds.....	109
6.1	Overview	109
6.2	Introduction	110
6.3	Methods	113
6.3.1	Model Implementation	113
6.3.2	PLGA Film	114
6.3.3	PLGA Scaffold	114
6.4	Results	116
6.4.1	Model Calibration.....	116
6.4.2	Comparison of the Semi-analytical and Numerical Solutions of the Molecular Weight Model for PLGA films	117
6.4.3	Effect of Thickness on the Young's Modulus of PLGA Films	117
6.4.4	Degradation Behaviour and Effective Elastic Modulus for PLGA Scaffolds	118
6.5	Discussion.....	120
6.6	Conclusion	125
6.7	Figures	126
6.8	Table.....	139

7	Nanoindentation of Undegraded Solvent-cast and Compression-moulded PLGA	140
7.1	Overview	140
7.2	Introduction	140
7.3	Materials and Methods	143
7.4	Results	144
7.4.1	Elastic Modulus and Hardness	144
7.4.2	Influence of Unloading Rate	145
7.4.3	Influence of Pile-Up due to Plastic Deformation	145
7.5	Discussion	146
7.6	Conclusion	152
7.7	Figures	153
7.8	Table	159
8	Nanoindentation of Degraded Solvent-cast and Compression-moulded PLGA	160
8.1	Overview	160
8.2	Introduction	161
8.3	Methods	163
8.3.1	Materials and Experimental Methods	163
8.3.2	Computational Modelling	164
8.4	Results	165
8.4.1	Mass Loss and Water Uptake	165
8.4.2	Molecular Weight	165
8.4.3	Mechanical Properties	166
8.4.4	Model Calibration	167

8.5	Discussion.....	168
8.6	Conclusion.....	172
8.7	Figures.....	173
9	Discussion and Conclusions	179
9.1	Introduction	179
9.2	Overview and Novelty.....	179
9.3	Summary and Discussion	180
9.4	Conclusions	186
9.5	Future Research	188
	Appendices.....	190
	References	199

Abstract

Biodegradable polymers such as PLGA have been used in a wide range of biomedical applications due to their hydrolytic degradation and biocompatibility. The mechanical performance of biodegradable polymers during degradation is strongly influenced by the degradation rate. The size dependent degradation mechanisms in these polymers lead to different degradation rates which make significant differences in the mechanical properties of different sized medical device components. Therefore, a clear understanding of the degradation behaviour and the mechanical performance of PLGA material during degradation is required.

In this thesis, the mechanical properties of PLGA materials prepared by solvent casting and compression moulding are evaluated using the nanoindentation technique. The measured elastic modulus and hardness are strongly depth dependent for both forms of the material, for indentations less than 3000 nm. The mechanical properties of PLGA material are significantly influenced by the material processing method. The solvent-cast material is more elastically compliant and plastically softer than the compression-moulded material and it also shows lower work hardening characteristics.

Changes in the mechanical properties of PLGA material under simulated physiological degradation conditions are evaluated. The relationship between the changes in the molecular weight and the Young's modulus of PLGA material is established. It is shown that the PLGA mechanical properties during degradation do not decrease until the number average molecular weight of the polymer chains reaches a critical molecular weight of 1500 g mol^{-1} . The experimental observations demonstrate that there is no significant difference in the degradation rate and the

changes in the mechanical properties of PLGA thicker than 120 μm . It is shown that the material processing methods considered here do not have a significant effect on the degradation rate and the mechanical performance of PLGA material.

A computational modelling framework is developed to predict the degradation behaviour and the changes in the mechanical properties of PLGA material during degradation. The degradation behaviour is predicted using both analytical and numerical solutions. When applied to PLGA films, semi-analytical solution cannot capture the differences in degradation rates for films of thickness above 25 μm . When applied to PLGA scaffolds, architecture of the scaffold does not have a significant influence on the degradation rate, but it determines the initial stiffness of the scaffold. The size of the scaffold strut controls the degradation rate and the mechanical collapse. A critical length scale due to competition between diffusion of degradation products and autocatalytic degradation is determined to be in the range 2-100 μm . Below this range, slower homogenous degradation occurs; however, for larger samples faster autocatalytic degradation occurs. The experimental observations for the degradation rate and the mechanical performance of PLGA materials support the computational modelling predictions.

In conclusion, the use of experimental testing methods and computational modelling in this thesis has led to an improved understanding of the mechanical performance of solvent-cast and compression-moulded PLGA materials with different thicknesses during degradation.

Acknowledgements

First, I would like to express my sincere gratitude to my supervisors Prof. Peter McHugh and Dr. Yury Rochev for their support, knowledge, and guidance over the years that it took to prepare this thesis.

I would like to acknowledge my funding support provided by the Structured PhD Programme in Biomedical Engineering and Regenerative Medicine (BMERM), funded under the Programme for Research in Third-Level Institutions (PRTL) Cycle 5 and co-funded under the European Regional Development Fund (ERDF).

I would like to thank Dr. Fawaz Aldabbagh and Dr. Andrea Erxleben for providing the GPC and XRD equipment in the school of Chemistry, NUI Galway. I would also like to thank Proxy Biomedical Ltd for sample preparation. Thanks to Christopher Magee, Gerard Hawkins, and Benjamin Chalmers for help with GPC measurements. Thanks also to the NUI Galway technical staff: Mr. Patrick Kelly, Mr. David Connolly, Mr. William Kelly, Mr. Liam Brennan, and Dr. Eadaoin Timmins for technical assistance and to Ms. Jane Bowman, Ms. Catherine Feeney, and Ms. Sharon Gilmartin for all the help throughout the years.

I would like to thank my best friend, William, for all his knowledge, patience, help, and support over the years. Also, thanks to all my friends and postgraduate students, particularly those on the third floor for the lunch time entertainment.

Finally, and most importantly, I would like to thank my dearest, my parents, Afsaneh and Saied, and my brother, Damoon, for their emotional and financial supports. To Afsaneh, thank you for your patience and never-ending love over the years.

List of Publications

The work presented in this thesis has appeared in the following publications:

Chapter 5: Shirazi RN, Aldabbagh F, Erxleben A, Rochev Y, McHugh P. Nanomechanical properties of poly(lactic-co-glycolic acid) film during degradation. *Acta Biomaterialia* 2014; 10: 4695-4703.

Chapter 6: Shirazi RN, Ronan W, Rochev Y, McHugh P. Modelling the degradation and elastic properties of poly(lactic-co-glycolic acid) films and regular open-cell tissue engineering scaffolds. *Journal of the Mechanical Behavior of Biomedical Materials* 2016; 54:48-59.

Chapter 7: Shirazi RN, Rochev Y, McHugh P. Nanoindentation of solvent-cast and compression-moulded poly(lactic-co-glycolic acid) to determine elastic modulus and hardness. *Polymer Testing* 2016; 50:111-118.

The following publications, arising from work in this thesis, are in preparation:

Chapter 6: Shine R, Shirazi RN, Sweeney CA, Kelly N, Rochev Y, McHugh P. Computational modelling techniques for the degradation of biodegradable polyesters for applications in medical device design.

Chapter 8: Shirazi RN, Aldabbagh F, Rochev Y, McHugh P. Effect of material thickness and processing method on poly(lactic-co-glycolic acid) degradation and mechanical performance.

Abbreviations and Nomenclature

Abbreviations

AFM	Atomic force microscopy
BDF	Backward differentiation formulas
CM1000	1mm compression-moulded plate
DMF	Dimethylformamide
DMT	Derjaguin-Muller-Toporov model
GND	Geometrically necessary dislocations
GPC	Gel permeation chromatography
JKR	Johnson-Kendall-Robert model
MWD	Molecular weight distributions
PBS	Phosphate-buffered saline solution
PC	Polycarbonate
PCL	Poly(ϵ -caprolactone acid)
PDE	Partial differential equation
PDI	Polydispersity index
PDLLA	Poly(D,L-lactide acid)
PDMS	Polydimethylsiloxane
PGA	Poly(glycolic acid)
PLA	Poly(lactic acid)
PLGA	Poly(lactic-co-glycolic acid)
PLLA	Poly(L-lactide acid)
PMMA	Poly(methyl methacrylate)
PS	Polystyrene

PTFE	Polytetrafluoroethylene
RVE	Representative volume element
SC120	0.12 mm solvent-cast film
SC250	0.25 mm solvent-cast film
SEM	Scanning electron microscopy
UHMWPE	Ultra-high molecular weight polyethylene
XRD	X-ray diffraction

Nomenclature

h	Indenter displacement
h_c	Contact depth
h_m	Maximum indentation depth
h_p	Permanent depth
h_s	Sink-in depth
\dot{h}_h	Creep rate at the end of holding time
F	Indentation load
F_{max}	Maximum indentation load
\dot{F}_h	Load decay rate during the holding time
\dot{F}_u	Initial unloading rate
E_i	Elastic modulus of the indenter
E_r	Reduced elastic modulus
E_s	Elastic modulus of the specimen
H_{IT}	Indentation hardness
S	Contact stiffness
S_c	Corrected contact stiffness
S_e	Entropy of a polymer network

S_l	Slope of the loading curve
W_e	Elastic indentation work
W_p	Plastic indentation work
W_t	Total indentation work
ν_i	Poisson's ratio of the indenter
ν_s	Poisson's ratio of the specimen
A	Indentation contact area
b	Indenter geometry constant
c	Material properties constant
C_1, C_2, C_3	Tip rounding constants
k	Strength coefficient
m	Power law exponent of the unloading curve
m_l	Power law exponent of the loading curve
n	Work hardening exponent
γ	Pile-up correction constant
η	Plasticity index
κ	Correction factor
ϵ	Indenter geometry constant
A_s	Surface area of the Petri dish
V_s	Volume of the polymer solution
m_{ini}	Initial mass of the polymer
m_d	Polymer mass in the dry condition
m_w	Polymer mass in the wet condition
ρ_p	Polymer density
ρ_s	Mass concentration of the solution
A_0	Initial total cross sectional area
A_{free}	Free surface area
C	Concentration
C_{COOH}	Concentration of carboxylic end groups

C_e	Concentration of ester bonds of polymer chains
C_{e0}	Initial concentration of ester bonds of polymer chains
\hat{C}_e	Non-dimensional form of the ester bond concentration
\bar{C}_e	Volume-averaged of the non-dimensional form of the ester bond
C_m	Concentration of monomers
\hat{C}_m	Non-dimensional form of the monomer concentration
C_w	Concentration of water
D	Diffusion coefficient
D_0	Intrinsic diffusion coefficient
\hat{D}	Non-dimensional form of diffusion coefficient
D_{eff}	Effective diffusion coefficient
R	Acid reaction product
E	Young's modulus
E_0	Initial Young's modulus
$E_{effective}$	Effective modulus
E^*	Normalised effective modulus
M_0	Average molar mass
M_n	Number average molecular weight of polymer
M_{n0}	Initial number average molecular weight of polymer
\bar{M}_n	Volume-averaged of number average molecular weight
M_n^{crit}	Critical number average molecular weight of polymer
M_w	Weight average molecular weight
N	Number of polymer chains per unit volume
N_0	Initial number of polymer chains
N_{chains}	Total number of polymer chains
N_{total}	Sum of polymer units in a group of chains
n_{total}	Total number of chains in a group of chains
$R_{scissions}$	Ratio of random scissions to end scissions
k'	Acid dissociation constant

k_1	Non-catalytic reaction rate constant
k_2	Autocatalytic reaction rate constant
l	Film thickness
l_{char}	Characteristic diffusion length
l_{diff}	Diffusion length
x	Distance through the film thickness
\hat{x}	Normalised distance through the film thickness
t	Time
\hat{t}	Normalised time
α	Diffusion porosity constant
β	Dissociation power of the acid end group
a_c	Absorption coefficient
c_c	Convective coefficient
d_c	Damping coefficient
f_c	Conservative flux convection coefficient
f_s	Conservative flux source
k_c	Mass coefficient
s_c	Source term
L_0	Initial length of elastic solid
k_B	Boltzmann's constant
l_l	Length of each link in a single polymer chain
n_l	Number of links in a single polymer chain
s_e	Entropy of a single polymer chain
F	Applied load
H	Helmholtz free energy
I	Internal energy
P	Probability distribution of the end-to-end length of a polymer chain
T	Absolute temperature
U	Strain energy potential

I_1	First deviatoric strain invariant
a	Probability distribution constant
c_1, c_2	Arbitrary constants
f	Uniaxial tensile force
F_R	Reaction force
r	End-to-end length of a single polymer chain
$\overline{r^2}$	Mean square chain length
\mathbf{B}	Element shape function gradient matrix
$\widehat{\mathbf{B}}$	Global shape function gradient matrix
\mathbf{D}	Fourth order tensor of elastic modulus
\mathbf{E}	Green-Lagrangian strain tensor
\mathbf{F}	Deformation gradient
\mathbf{B}_{left}	Left Cauchy-Green deformation tensor
\mathbf{C}_{right}	Right Cauchy-Green deformation tensor
\mathbf{F}_{ext}	External force vector
\mathbf{G}	Residual forces vector
\mathbf{I}	Identity tensor
J	Jacobian
\mathbf{K}	Global stiffness matrix
\mathbf{N}	Element shape function matrix
$\widehat{\mathbf{N}}$	Global shape function matrix
\mathbf{P}	First Piola-Kirchhoff stress
\mathbf{R}	Orthogonal rotation tensor
\mathbf{U}	Material stretch tensor
\mathbf{V}	Spatial stretch tensor
\mathbf{n}	Unit normal vector
\mathbf{t}	Traction vector
\mathbf{u}	Displacement vector
\mathbf{u}_e	Nodal displacement vector

S_V	Surface of the body
V_0	Undeformed reference volume
V	Deformed volume
ε	Strain
ε_A	Nominal strain
λ_i	Principal stretches
λ	Lamé constant
K	Bulk modulus
μ	Shear modulus
ν	Poisson's ratio
σ	Stress
Σ_0	Nominal stress
$\boldsymbol{\sigma}$	Cauchy stress
σ^{pr}	Principal stress
σ_y	Yield strength
α_d	Damping factor
δ_{ij}	Kronecker delta
P_m	Polymer chains with m degree of polymerisation
P_n	Polymer chains with n degree of polymerisation
P_{n-m}	Polymer chains with n-m degree of polymerisation
R_{RMS}	Root mean squared value of the surface roughness
R_a	Surface roughness average value
T_g	Glass transition temperature
T_m	Melting temperature

1 Introduction

1.1 Background

Biodegradable polymers such as PLGA have been used in a wide range of biomedical applications. Biodegradable coatings particularly, can protect the bare surface of the metal from corrosion attack caused by a biological environment (Gulati et al., 2012; Li et al., 2010a; Xi et al., 2010). Biodegradable coatings can be used for load bearing implants (Gulati et al., 2012) and drug-eluting stent systems for which the stent surfaces are coated with biodegradable polymers containing drugs (Engineer et al., 2011; Jackson et al., 2004; Pan et al., 2006; Shanshan et al., 2013; Westedt et al., 2006; Xi et al., 2010). Also, biodegradable polymers have been used as temporary scaffolds in tissue engineering which provide an appropriate three dimensional environment for cells to proliferate and differentiate and also support the mechanical properties until the regenerated tissue is structurally stabilised (Clark et al., 2014; Cui et al., 2009; Jung et al., 2012; Lee et al., 2007; Lichun et al., 1998; Lu et al., 2001; Pan and Ding, 2012; Perron et al., 2009; Ren et al., 2005; Saito et al., 2013; Waris et al., 2004; Yang et al., 2008). Polyesters are a class of biodegradable polymers which are widely used due to their biocompatibility (Anderson and Shive, 2012; Brożyna et al., 2015) and hydrolytic degradation of the ester bonds that produces low molecular weight water soluble fragments, which enter the Krebs cycle of the cell and are further broken down to carbon dioxide and water.

There have been several methods used to fabricate biodegradable materials, including solvent casting and compression moulding. The solvent casting method has been commonly used for the preparation of biodegradable films, which involves

using organic solvents in order to dissolve the polymer, casting, and drying steps (Houchin and Topp, 2009; Huang et al., 2007; Lichun et al., 1998; Lu et al., 1999; Lu et al., 2001; Pamula and Menaszek, 2008; Pan et al., 2007; Schliecker et al., 2003; Steele et al., 2011; Vey et al., 2008; Witt and Kissel, 2001; Xi et al., 2010). This method usually requires a long time for solvents to evaporate from the polymer during the drying steps (Manson and Dixon, 2012). Also, the residual solvent in the polymer may be harmful to cells or nearby tissues. The compression moulding method is useful because of its simplicity and capability for producing materials without using organic solvents (Grizzi et al., 1995; Witt et al., 2000); however, the heat treatment process may cause the degradation of polymer (Gogolewski and Mainil-Varlet, 1997). Therefore, the properties of biodegradable polymers are expected to be affected by different processing methods (Cui et al., 2008; Fouad et al., 2005; Miller et al., 2001; Rhim et al., 2006).

A way to evaluate the performance of such biodegradable polymers during degradation in the body is to replicate the *in-vivo* conditions by exposing materials to simulated physiological conditions by immersion in phosphate-buffered saline with pH 7.4 and at body temperature (37°C) (Houchin and Topp, 2009; Huang et al., 2007; Li et al., 2010a; Lu et al., 1999; Lu et al., 2000; Ma et al., 2011; Oh et al., 2006; Pamula and Menaszek, 2008; Vey et al., 2012; Vey et al., 2008; Wu and Ding, 2005). Degradation of biodegradable polyesters such as PLGA depends on the size of the polymer specimen due to the autocatalytic effect of the carboxylic acid degradation products, which accumulate inside the polymer matrix and accelerate the degradation rate (Chen et al., 1997; Dunne et al., 2000; Grayson et al., 2005; Grizzi et al., 1995; Lu et al., 1999; Park, 1995; Witt and Kissel, 2001).

The change in the mechanical properties of biodegradable polymers during degradation is a critical design factor. In order for an implant to function, it must have appropriate mechanical properties and an adequate degradation rate to maintain the mechanical integrity of the material during degradation. Previous studies have been focused on the mechanical performance of PLGA scaffolds

(Agrawal et al., 2000; Cao et al., 2006; Lu et al., 2000; Wu and Ding, 2004; Wu et al., 2006b; Yang et al., 2010) and PLGA blended with some other materials (Yang et al., 2008; Zhou et al., 2012) for load bearing applications; however, the number of studies on the mechanical performance of biodegradable coatings is limited. Mechanical performance of biodegradable coatings in stent applications (Engineer et al., 2011; Jackson et al., 2004; Pan et al., 2006; Shanshan et al., 2013; Westedt et al., 2006; Xi et al., 2010), for instance, is of significant importance when one considers coating deformation on stent expansion and mechanical loading on contact with the arterial tissue. Therefore, a clear understanding of degradation and the evolution of the mechanical properties of biodegradable coatings during degradation is required.

In general, a wide range of mechanical testing methods are used to measure the mechanical properties of biodegradable polymers (Daniels et al., 1990; Hayman et al., 2014; Li et al., 2010b; Steele et al., 2011; Törmälä et al., 1987). In particular, heterogeneity due to degradation may cause inaccuracy in mechanical test, e.g. localisation of strain in a tensile test. Additionally, the low stiffness and strength of some biodegradable polymers due to degradation can lead to inaccurate test results, e.g. in a flexural test the self-weight of the specimen may be significant or in a tensile test failure may occur during gripping. Given the difficulties in using traditional mechanical testing, nanoindentation testing provides possibilities for testing the mechanical properties of biodegradable polymers (Maxwell and Tomlins, 2011; Wright-Charlesworth et al., 2005). Nanoindentation is a technique that can be used to evaluate the nano- micro-mechanical properties of a small volume of material (Lucca et al., 2010), thin films (Bull, 2005; Geng et al., 2005; Lin and Kim, 2012; Xu et al., 2011; Zhou and Komvopoulos, 2006), and heterogeneous samples (Maxwell and Tomlins, 2011; Oyen, 2013), and particularly to measure the elastic modulus and hardness of materials (Oliver and Pharr, 1992; 2004). Additionally, indentation testing allows for local mapping of inhomogeneous samples as a result of degradation (Rettler et al., 2013).

Despite a wide range of indentation applications for determining the mechanical properties of materials, applying this measurement technique to compliant materials such as polymers is very challenging. Adhesion between the indenter and the polymer causes difficulties in determining the contact point, i.e. the point where the indenter comes into contact with the material surface (Carrillo et al., 2005; Deuschle et al., 2007; Kaufman and Klapperich, 2009), which may cause significant errors in calculating the mechanical properties of polymer (Deuschle et al., 2007; Kaufman and Klapperich, 2009). The time-dependent properties of polymers may cause inaccurate mechanical property measurements (Briscoe et al., 1998; Feng and Ngan, 2002; Tang and Ngan, 2003a). Additionally, when the contact involves plastic deformation, the formation of pile-up underneath the indenter may cause overestimation of the mechanical property measurements (Bolshakov and Pharr, 1998; Oliver and Pharr, 2004). The depth dependence of elastic deformation has been observed in various polymers which causes the larger elastic modulus for smaller indentation depths (Alisafaei et al., 2014; Alisafaei et al., 2013; Briscoe et al., 1998; Chandrashekar et al., 2015; Charitidis, 2010; Chong and Lam, 1999; Fang and Chang, 2004; Lam and Chong, 2000; Shen et al., 2005; Wrucke et al., 2013). Given these, it is very important to consider the factors which affect the mechanical property measurements when applying nanoindentation for polymers.

Despite extensive experimental studies, the degradation behaviour of biodegradable polymers is poorly understood due to the size dependent degradation of these materials. Computational modelling has led to an improved understating of the degradation behaviour of biodegradable polymers. One of the most important mechanisms to include when developing a model of polymer degradation behaviour is diffusion transport, as it plays a critical role in determining the type of degradation that will occur given that autocatalysis is the fundamental reason for the size dependence. The extent of autocatalysis is controlled by the material diffusion length. Reaction-diffusion models have been developed which have significant potential to assess the rate of degradation and to aid the design of

biodegradable devices (Chen et al., 2011; Ford Versypt et al., 2013; Wang et al., 2008). Additionally, a number of models have been presented to predict the mechanical properties of degradable polymers (Hayman et al., 2014; Soares et al., 2010; Vieira et al., 2014; Vieira et al., 2011; Wang et al., 2010). In particular a physically-based model motivated by the hydrolytic random scissions of the polymer chains linked with a formulation which describes the elastic modulus of biodegradable polymers during degradation has been proposed (Wang et al., 2010).

1.2 Thesis Objectives

The overall objective of this thesis is to evaluate the mechanical properties of biodegradable polymers during degradation and to develop a computational modelling framework to accurately predict the degradation behaviour and the mechanical performance during degradation. This research is specifically focused on PLGA material which is an important and widely used biodegradable polymer.

In this thesis, for the first time, the mechanical property degradation of solvent-cast and compression-moulded PLGA materials with different thicknesses is evaluated using the nanoindentation technique. The difficulties involved in performing nanoindentation on PLGA material are considered. A computational modelling framework is developed that couples a reaction-diffusion based molecular weight model and the molecular network based mechanical properties model in order to predict the degradation behaviour and the changes in the mechanical properties of PLGA during degradation.

The specific objectives of this thesis are as follows:

- To study *in-vitro* degradation of solvent-cast PLGA films and to evaluate the mechanical behaviour of the films during degradation using the nanoindentation technique.

- To develop a computational modelling framework to predict the molecular weight reduction and the relationship between the molecular weight and the Young's modulus of PLGA material.
- To predict the degradation rate and the changes in the Young's modulus of PLGA films of different thicknesses and of a range of regular open-cell tissue engineering PLGA scaffolds.
- To characterise the PLGA material response under variation in applied load and loading rate using the nanoindentation technique and to compare the effect of two different material processing methods on the material response.
- To make practical recommendations on appropriate test parameters for successful nanoindentation testing of the PLGA material.
- To evaluate experimentally the effects of material thickness and processing method on the *in-vitro* degradation, and the related changes in the mechanical properties, of the PLGA material.

1.3 Thesis Overview

Chapter 2 provides a background of biodegradable polymers and their biomedical applications. The degradation mechanism and the factors affecting the degradation rate are described. The mechanical properties of biodegradable polymer are reviewed. An overview of the nanoindentation technique and the factors which affect the indentation measurement are presented. The computational modelling for degradation and the mechanical properties of biodegradable polymers is discussed.

In **Chapter 3**, the theoretical and numerical methods for the computational analyses presented in this thesis are provided. A brief introduction to the relevant continuum mechanics theory is given. The finite element method and the numerical solution procedure that is employed in this thesis for structural problems are described. Entropy spring theory is presented, followed by an overview of the

elasticity of a molecular network for polymers. A computational model is developed based on this theory in order to predict the relationship between the elastic modulus and the molecular weight of PLGA material during degradation. A degradation kinetics model based on the reaction-diffusion phenomena is presented in order to predict the changes in the molecular weight distribution of PLGA material during degradation. Semi-analytical and numerical solution methods for this model are given. Then, the coupling of these two models is described. A description of the nanoindentation analysis which is used in this thesis to evaluate the mechanical properties of PLGA material is presented.

Chapter 4 presents the materials which are used in this thesis. The sample preparations are described. Then, the experimental methods which are used to characterise the materials during degradation are presented. These methods include optical microscopy and scanning electron microscopy (to consider the surface morphology), gel permeation chromatography (to determine the molecular weight), X-ray diffraction (to determine crystallinity), nanoindentation (to evaluate the mechanical properties), and atomic force microscopy (to analyse the surface roughness of the sample before indentation and to investigate the amount of pile-up after indentation). The calibration process and the testing protocol for nanoindentation of PLGA material are described.

In **Chapter 5**, *in-vitro* degradation and the changes in the mechanical properties of solvent-cast PLGA film are investigated. The changes in the molecular weight, surface morphology, and crystallinity of the material are evaluated during degradation. The changes in the mechanical properties of the material during degradation are evaluated using the nanoindentation technique. The relationship between the changes in the elastic modulus and the molecular weight of PLGA during degradation is demonstrated.

Chapter 6 provides a computational investigation of degradation and the changes in the mechanical properties of PLGA films with different thicknesses and of a range

of regular open-cell tissue engineering scaffolds. The coupling of the reaction-diffusion based molecular weight model and the molecular network based mechanical properties model, which was described in Chapter 3, is used in this chapter for the computational modelling. This framework is successfully applied to accurately capture the observed degradation behaviour and the changes in the elastic modulus of PLGA films presented in Chapter 5. The effect of architecture and the size of the scaffold strut on the degradation rate and the mechanical behaviour of PLGA scaffolds are considered.

Nano- and micro-mechanical properties of solvent-cast and compression-moulded PLGA materials are investigated in **Chapter 7**. The elastic modulus and hardness of these materials are evaluated for a wide range of applied loads and loading rates. The influence of the two different material processing methods (solvent casting and compression moulding), viscoelasticity, and indentation pile-up behaviour of the material are considered. The indentation data is analysed using an existing method to correct for pile-up in the calculations. The appropriate test parameters are presented for successful nanoindentation testing for PLGA material.

The effects of material thickness and processing method on the degradation rate and the changes in the mechanical properties of PLGA material during degradation are investigated in **Chapter 8**. The changes in the molecular weight, mass loss and water content, and the mechanical properties of solvent-cast and compression-moulded materials of different thicknesses are evaluated. The experimental results generated in this chapter are compared to the experimental results presented in Chapter 5. The computational model predictions on critical length scale presented in Chapter 6 are validated, and the model parameters are updated based on the experimentally observed results for the different materials.

Finally, in **Chapter 9**, a brief overview of the novelty of the work performed is given. The key findings of this thesis are summarised and the outcomes of each result

chapters are discussed, followed by overall conclusions in this thesis. Some indications for experimental and computational works are proposed for future.

2 Background

2.1 Introduction

This chapter provides an overview of the main topics of relevance to this thesis. A brief introduction to biodegradable polymers and their biomedical applications is presented in section 2.2. The degradation mechanism and the factors affecting the degradation rate are described, followed by a review on the mechanical properties of biodegradable polymers. An overview of the nanoindentation techniques and the factors which affect the indentation measurement is presented in section 2.3. Finally, the computational modelling of degradation and mechanical property prediction for biodegradable polymers is presented in section 2.4.

2.2 Biodegradable Polymers

Interest in biodegradable polymers has increased significantly during the recent decades because of their successful clinical applications in a wide range of biomedical areas. The main advantage of these biomaterials is that they are gradually absorbed by the human body. Also, these materials are able to facilitate tissue regeneration through the interaction of the material with immunologic cells such as macrophages (Anderson and Shive, 2012). Furthermore, biodegradable polymers can be used as a temporary scaffold for tissue regeneration either to grow cells (Li et al., 2010a; Lichun et al., 1998) or tissue *in-vitro* (Ren et al., 2005) or to generate tissue *in-vivo* (Jung et al., 2012).

The main classes of synthetic biodegradable polymers are: polyanhydrides, polyesters, and polyorthoesters. The three most common poly(α -hydroxy-esters) are poly(glycolic acid) (PGA), poly(lactic acid) (PLA), and poly(ϵ -caprolactone acid)

(PCL). PLA contains an asymmetric carbon atom, and therefore has two optical isomers, i.e. L (+) and D (-) which are called poly(L-lactide acid) (PLLA) and poly(D,L-lactide acid) PDLLA, respectively.

Poly(lactic-co-glycolic acid) (PLGA) is a copolymer of PGA and PLA. The chemical structure of PLGA is shown in Figure 2.1. The synthesis of PLGA polymers can be performed by direct polycondensation or by ring-opening polymerisation of PGA and PLA. Ring-opening polymerisation is the most efficient route to obtain high molecular weight copolymers (Dechy-Cabaret et al., 2004). Generally, the simple polycondensation is less expensive, but the resulting polymers have low and uncontrollable molecular weights (Naughton et al., 1997).

2.2.1 Biomedical Applications

Applications for biodegradable polymers depend on the degradation time, which can be tailored from days to years, and the mechanical properties. Polymers for tissue engineering applications may need to degrade within a time frame which is compatible to the tissue healing (weeks to years). However, for drug delivery applications, the degradation time decreases and the polymers need to degrade within days to weeks.

The degradation of PGA is between six and twelve months and it degrades faster than PLA due to its relatively hydrophilic nature. The extra methyl group (CH₃) in the PLA repeating unit makes it more hydrophobic compared with PGA. Hydrophobicity reduces the molecular affinity to water and leads to a slower rate of hydrolysis. Therefore, PLA maintains mechanical integrity for longer and its degradation takes more than twelve months. The morphology and crystallinity strongly influence the rate of degradation and mechanical properties of PLA (Renouf-Glauser et al., 2005).

In order to achieve intermediate degradation rates between PGA and PLA, various lactic and glycolic acid ratios (50:50, 65:35, 75:25, 85:15, 90:10) are used to synthesise PLGA. The degradation rates of amorphous PLGA are faster than either

semi-crystalline or crystalline PLA or PGA. However, PLGA polymers containing equal amounts of glycolic and lactic acids (50:50) are hydrolysed at a much faster rate than any of those containing a higher proportion of either PLA or PGA, because they have the lowest crystallinity. For other compositions, the degradation rate of PLGA decreases when the content of hydrophobic PLA copolymer increases (Vey et al., 2012). Table 2.1 provides the physical and mechanical properties and also the typical applications of PGA, PLA, and PLGA polymers. This information shows that the mechanical properties of PLA and PLGA (50:50) are similar; however, PLA degrades significantly slower than PLGA (50:50). Therefore, it is important to know the degradation time as well as mechanical properties for material selection and device design.

Biodegradable polymers were initially used in *in-vivo* applications with low magnitudes of mechanical loading such as wound closures and sutures. However, the use of biodegradable polymers has increased in structural applications and environments with high loads. PLGA copolymers, with different PLA/PGA ratios, are currently used for a variety of medical implant applications and they are among the few synthetic polymers approved by the FDA for human clinical applications, including surgical suturing (Xu et al., 2008), tissue engineering scaffolds (Clark et al., 2014; Cui et al., 2009; Lee et al., 2007), and orthopaedic fixation devices (screw, pins, rods, and tacks) (Waris et al., 2004). PLGA has been fabricated into scaffold by a number of different techniques, including gas foaming (Yoon and Park, 2001), sintering (Shi et al., 2010), porogen or salt leaching (Lin et al., 2002), compression moulding (Wu and Ding, 2004), electrospinning (Bashur et al., 2006), polymer printing (Ge et al., 2009), or a combinations of these techniques (Lee et al., 2005; Oh et al., 2006; Vozzi et al., 2003; Wu et al., 2006a).

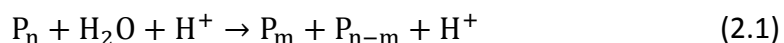
PLGA films have been shown to provide a suitable substrate for retinal pigment epithelium cell culture (Lu et al., 2001), and for formation of a bone matrix (Karp et al., 2003). PLGA is also used as a coating for load bearing implants (Gulati et al., 2012), and drug-eluting stent systems (with coating thickness of 10-200 μm) for

which the stent surfaces are coated with biodegradable polymers containing drugs (Engineer et al., 2011; Jackson et al., 2004; Pan et al., 2006; Shanshan et al., 2013; Westedt et al., 2006; Xi et al., 2010). PLGA has been used to deliver chemotherapeutic (Jie et al., 2010), protein (Andreas et al., 2011), and antibiotics (Jeong et al., 2008). For the drug delivery applications, PLGA is mostly fabricated into microspheres or microparticles (Arnold et al., 2007; Klose et al., 2006). The drug release profiles may vary depending on the environmental conditions and the properties of the drug delivery system (size, porosity, density, and shape) and the polymer (molecular weight, crystallinity, lactic and glycolic acid ratios) (Fredenberg et al., 2011; Klose et al., 2008). Table 2.2 shows a number of commercially available PLGA polymers.

2.2.2 Degradation Mechanism

The degradation process of biodegradable polyesters such as PLGA is based on a hydrolytic mechanism. Diffusion of water into the polymer causes a hydrolytic scission of the ester bonds of the polymer chains leading to a decrease in the molecular weight. At this stage, the degradation products are not small enough to become soluble, and no significant change in the material weight is detected. With time, the molecular weight of degradation products is reduced by further hydrolysis, leading to the formation of water soluble oligomers and monomers which diffuse from the bulk of the material to the surface and then to the surrounding solution, causing significant weight loss (Pamula and Menaszek, 2008; Vey et al., 2012). A schematic of the hydrolytic degradation of biodegradable polyesters is shown in Figure 2.2.

The hydrolytic degradation can be catalysed by the local acidic pH within PLGA, and acid-catalysed ester hydrolysis can be summarised as follows (Ford Versypt et al., 2013):



where P_n , P_m , and P_{n-m} are the polymer chains having degree of polymerisation n , m , and $n - m$, respectively, and H^+ is the acid catalyst. The acidic catalysis can be due to the strong acid in the medium (non-catalytic reaction) or the carboxylic acid end groups of the polymer chains (autocatalytic reaction).

2.2.3 Bulk vs. Surface Degradation

Polymer degradation is generally classified as either bulk degradation or surface degradation. For surface degradation, the rate of polymer degradation at the surface is faster than the rate of penetration of water into the bulk of the polymer and the degradation of polymer occurs from the surface inward. For bulk degradation, the penetration of water into the bulk of the polymer is faster than the polymer degradation and the degradation of polymer occurs throughout the polymer bulk. A schematic of surface and bulk degradation for biodegradable polymers is shown in Figure 2.3.

2.2.4 Factors Affecting the Degradation Rate

The degradation rate of biodegradable polymers has been shown to be dependent on many factors. A full understanding of the degradation behaviour of biodegradable polymers is required in order to consider the influences of different factors on the degradation rate of these materials. The degradation rate can be affected by the size of the polymer sample (Dunne et al., 2000; Grayson et al., 2005; Grizzi et al., 1995; Lu et al., 1999; Witt and Kissel, 2001), the initial molecular weight (Grayson et al., 2005; Lu et al., 1999), the copolymer composition (lactic to glycolic ratio for PLGA) (Lu et al., 1999; Vey et al., 2012), the crystallinity (Chye Joachim Loo et al., 2005), and the environmental conditions such as temperature (Grayson et al., 2005), pH (Zolnik and Burgess, 2007), fluid flow (Agrawal et al., 2000), and mechanical loading (Dreher et al., 2015; Li et al., 2010b; Smutz et al., 1991; Yang et al., 2010).

The size of the sample has a significant effect on the rate of degradation. It has been shown that large size samples degrade faster than the smaller ones due to the

autocatalytic effect of the acidic degradation products accumulated inside the polymer matrix which accelerates the degradation process (Dunne et al., 2000; Grayson et al., 2005; Grizzi et al., 1995; Lu et al., 1999; Witt and Kissel, 2001).

The initial molecular weight of the polymer has a major effect on the degradation rate; low molecular weight polymers degrade faster than high molecular weight polymers (Grayson et al., 2005; Lu et al., 1999). The degradation rate also can be influenced by the end group functionalisation. Polymers with blockage of acidic end group, such as the free carboxylic group, degrade faster because the presence of carboxylic acid groups accelerates the autocatalytic chain scission process from the very beginning of the degradation process, due to the increased hydrophilicity (Atala and Mooney, 2013).

The temperature of the environment also affects the degradation rate. Diffusion of water at temperatures above the glassy state is facilitated by the chain motions. Therefore, the degradation rate of the polymer is faster when the polymer is placed in an environment at a temperature higher than its glass transition temperature (T_g) (Grayson et al., 2005).

The mechanical loading affects the degradation behaviour of biodegradable polymers (Dreher et al., 2015; Li et al., 2010b; Smutz et al., 1991; Yang et al., 2010). It has been shown that applying tensile loads to electrospun PLGA scaffolds accelerates the loss of ultimate strength (Li et al., 2010b). In addition, the results of strain controlled bending of a moulded polyorthoester have shown an accelerated loss of flexural yield and modulus (Smutz et al., 1991).

2.2.5 Mechanical Properties of Biodegradable Polymers

In order for an implant to function, it must have appropriate mechanical properties and an adequate degradation rate to maintain the mechanical integrity of the material during degradation. The changes in the mechanical properties of biodegradable polymers during degradation have been widely studied as a critical

design factor (Ginjunpalli et al., 2014; Hayman et al., 2014; Kranz et al., 2000; Lam et al., 2002; Lin et al., 2003; Pan and Ding, 2012; Saito et al., 2013; Saito et al., 2012; Shum and Mak, 2003). It has been shown that the mechanical strength decreases after the molecular weight reduces (Saha and Tsuji, 2006; Tsuji, 2000, 2002; Tsuji and Ikada, 2000; Tsuji et al., 2000; Weir et al., 2004a; Weir et al., 2004c; Wu and Ding, 2004).

Different strategies have been employed to tailor the degradation rate and the mechanical properties of biodegradable polymers to suit different biomedical applications, such as blending with other materials (Ginjunpalli et al., 2014; Kranz et al., 2000; Steele et al., 2011; Yang et al., 2008; Zhou et al., 2012). It has been shown that incorporation of lower molar mass polyethylene glycol into PLGA film causes a reduction in the tensile strength compared with PLGA; however, it allows for a greater paclitaxel release rate in drug delivery applications (Steele et al., 2011).

The lactic and glycolic acid ratio can also be varied to alter the mechanical performance during degradation (Pan and Ding, 2012; Wu and Ding, 2004). The mechanical properties of PLGA porous scaffolds with different lactic and glycolic acid ratios of 85:15 and 75:25 were studied by Wu and Ding (2004) during *in-vitro* degradation in phosphate-buffered saline solution at 37°C. It was shown that the compression moduli of PLGA 85:15 and PLGA 75:15 scaffolds were found to decrease after 11 weeks and 6 weeks of degradation, respectively. In contrast, PDLLA scaffolds retained their mechanical stability over 28 weeks of degradation under the same conditions. Since the degradation rate has a major effect on the mechanical performance of biodegradable polymers, any factors including temperature, pH of the environment, and mechanical loading, that affect the rate of molecular weight degradation, may affect the mechanical properties (Dreher et al., 2015; Hayman et al., 2014; Li et al., 2010b; Perron et al., 2009).

The polymer fabrication method should also be considered for designing biomedical applications. There are several methods to fabricate biodegradable polymers,

including solvent casting and compression moulding. The solvent casting method has been commonly used for the preparation of biodegradable films which involves using organic solvents in order to dissolve the polymer, casting, and drying steps (Houchin and Topp, 2009; Huang et al., 2007; Lichun et al., 1998; Lu et al., 1999; Lu et al., 2001; Pamula and Menaszek, 2008; Pan et al., 2007; Schliecker et al., 2003; Steele et al., 2011; Vey et al., 2008; Witt and Kissel, 2001; Xi et al., 2010). This method requires a long time for solvents to evaporate from the polymer during the drying steps (Manson and Dixon, 2012). The residual solvents in the material may affect the mechanical properties of the film (Rhim et al., 2006) and may be harmful to cells or nearby tissues. Therefore, there are strict requirements regarding the presence of residual solvents in biomedical implants.

In the compression moulding process, the polymer is preheated and placed in a heated mould. Then pressure is applied in order to force the material to fill the mould. The compression moulding method is useful because of its simplicity and capability for producing materials without using organic solvents (Grizzi et al., 1995; Witt et al., 2000); however, the heat treatment process may cause degradation of polymer (Gogolewski and Mainil-Varlet, 1997). The heat treatment has a significant effect on the initial molecular weight and the mechanical behaviour of the material (Weir et al., 2004b). Additionally, the heat treatment may cause a change in the degree of crystallinity of the material (Chye Joachim Loo et al., 2005; Fouad et al., 2005). Crystallinity affects the mechanical properties of biodegradable polymers; alignment of the polymer chains in crystalline regions causes the polymer chains to strongly bond to each other which can cause an increase in the material strength (Takayama et al., 2011).

In general, a wide range of mechanical testing methods are used to measure the mechanical properties of biodegradable polymers. Uniaxial tensile testing and flexural testing are the most common methods (Daniels et al., 1990; Hayman et al., 2014; Li et al., 2010b; Steele et al., 2011; Törmälä et al., 1987). In these methods, the test specimen may be either the product to be implanted or it can be the

standard test geometry, e.g. a dog-bone for tensile testing. In particular, two aspects of common biodegradable polymers pose challenges for mechanical testing: (i) heterogeneity due to degradation may cause inaccuracy in mechanical test, e.g. localisation of strain in a tensile test (ii) the low stiffness and strength of some biodegradable polymers due to degradation can lead to inaccurate test results, e.g. in a flexural test the self-weight of the specimen may be significant or in a tensile test failure may occur during gripping. Non-destructive testing methods, such as nanoindentation overcome many of these limitations (Maxwell and Tomlins, 2011; Wright-Charlesworth et al., 2005).

2.3 Nanoindentation

Nanoindentation is a technique that has been widely used to characterise the mechanical properties of a small volume of material (Lucca et al., 2010), thin films (Bull, 2005; Geng et al., 2005; Lin and Kim, 2012; Xu et al., 2011; Zhou and Komvopoulos, 2006), and heterogeneous samples (Maxwell and Tomlins, 2011; Oyen, 2013) at micro- and nano-scales and particularly to measure the elastic modulus and hardness. In this technique, an indenter tip with a known geometry is driven into the material to be tested by applying an increasing load. The load used is typically in the mN range and the indents are typically to depths of nm. This instrument allows precise control of either load or displacement during a test. In the load controlled measurement, when the contact load reaches the preset maximum value F_{max} , the load is reduced to zero. In the displacement controlled measurement, when the penetration depth reaches the preset maximum depth h_m , the load is reduced to zero. As the procedure is performed, the load-displacement is continuously monitored during the loading and unloading processes. A typical load-displacement curve for an indentation is shown in Figure 2.4 (A).

2.3.1 Indenter Tip

Choosing diamond as a tip material provides an indenter with a high elastic modulus, no plastic deformation, low friction, and a perfect geometry to make a well-defined indentation impression. The Berkovich indenter is a three-sided pyramid and provides a sharply pointed tip compared with the Vickers or spherical indenters. This indenter is commonly used for measurements of nanomechanical properties, especially for extremely thin films requiring shallow indentation. However, pointed indenters produce a plastic strain impression and assessing the elastic modulus is a non-trivial task (Alisafaei et al., 2014).

2.3.2 Load-Displacement Curve

The solution of the elastic contact problem which is the basis of the indentation analysis procedure was proposed by Hertz (1881). In this theory, the problem of the elastic contact between two spherical surfaces with different radii and elastic constants is analysed. This basic theory was expanded by Sneddon (1965) to establish relationships between the load, displacement, and contact area for many simple punch geometries. He proposed that the loading portion of the load-displacement curve can be described by a power law expression as follows:

$$F = ch^{m_l} \quad (2.2)$$

where F is the indentation load, h is the displacement of the indenter, m_l is the power law exponent of the loading curve, and c is a constant which depends on the material properties. The value of the exponent m_l depends on the indenter geometry ($m_l = 2$ for cones or the Berkovich indenter, $m_l = 1.5$ for a sphere or paraboloid, and $m_l = 1$ for a flat-ended cylindrical punch).

For a conical indenter, the load is proportional to the displacement at very low penetration depths. At this stage the contact is mainly elastic. Then, it is followed by a transition region from elastic to plastic deformation in which the exponent of

the loading curve changes to 1.5 (Troyon et al., 2012; Zeng and Chiu, 2001). At higher load, the load is proportional to the displacement squared and a full elastic-plastic deformation is observed beneath the indenter.

For purely elastic materials, the unloading curve would retrace the loading curve. In contrast, for indentation of elastic-plastic materials, there is a permanent depth h_p due to the plastic deformation that remains in the material (Figure 2.4). With this, the unloading curve can be described as follows:

$$F = b(h - h_p)^m \quad (2.3)$$

where b is a geometric constant depending on the indenter tip and m is the power law exponent of the unloading curve, which is assumed to be equal to 2 for a perfect Berkovich indenter (Oliver and Pharr, 1992); however, empirical estimations have been shown to be in the range $1.2 \leq m \leq 1.6$ for a Berkovich indenter for a wide variety of metals and ceramics (Oliver and Pharr, 1992; Oliver and Pharr, 2004). This is due to the fact that the unloaded shape of indents is not perfectly conical or pyramidal but exhibits a subtle convex curvature (Oliver and Pharr, 2004); hence, the power law exponent depending on the material, is related to the shape of the deformed surface.

2.3.3 Hardness and Elastic Modulus Determination

The earliest experiments in which load-displacement sensing indentation methods were used to measure mechanical properties were performed by Tabor (1948). In this study, the indentation of a number of metals deformed by hardened spherical indenters was examined. Later, the load-displacement sensing indentation testing was used for measuring the elastic modulus and hardness of materials.

In such an analysis, evaluation of the contact area is crucial to assess accurately the mechanical properties of the material. The contact area can be measured directly by atomic force microscopy (AFM) (Jee and Lee, 2010) or scanning electron

microscopy (SEM) (Moeller, 2009). However, the size of the residual impression is often only few microns and this makes it very difficult to obtain a direct measurement using optical techniques. Alternatively, analytical techniques have been proposed to determine the contact area, and the two most commonly used were proposed by Doerner and Nix (1986) and Oliver and Pharr (1992).

In the Oliver and Pharr method, the contact area describes the projected (or cross sectional) area of the indenter and is a function of contact depth h_c , i.e. the vertical distance along which contact is made between the indenter and the material (Figure 2.4 (B)). The area function that quantifies the projected contact area is determined by a calibration of the indenter tip by indenting a material such as fused silica which is assumed to have a constant known Young's modulus. The calibration is made by indenting at varying penetration depths with the assumption that at those depths, the area function corresponds to the ideal contact area of a perfect pyramid indenter.

Indentations on many materials may result in both elastic and plastic deformations. A particularly meaningful quantity in indentation hardness is the mean contact pressure, and is determined by dividing the indenter load by the area function. The mean contact pressure, when determined under condition of a fully developed plastic zone, is usually defined as the indentation hardness of the specimen material (Fischer-Cripps, 2006).

In nanoindentation, the elastic modulus of the specimen can be estimated from the slope of the unloading of the load-displacement curve. Of particular concern is how the slope of the unloading curve, i.e. contact stiffness S (Figure 2.4 (A)), should be measured from the load-displacement curve. Fitting a straight line to the upper portion of the unloading curve is a simple way (Doerner and Nix, 1986); however, for some materials with a large amount of elastic recovery, the unloading curve is not linear. Hence, a linear fit to the upper part of the unloading data is not suitable for all materials. In most cases, a second degree polynomial is a reasonable fit but it

is not necessarily the best one. An alternative procedure is a least square fitting procedure which was proposed by Oliver and Pharr (1992) to determine the values of m and b in the power law expression for the unloading curve given in Eq. (2.3), and then S can be determined by differentiation of this equation.

2.3.4 Factors Affecting Nanoindentation Test Data

This section is mainly focused on the challenges for performing the indentation test and determining the hardness and the elastic modulus. The most significant phenomena which are considered in this section are the time-dependent properties, pile-up, initial contact point, adhesion, surface roughness, and indentation size effects.

2.3.4.1 Time-dependent Properties

Polymers are typically loading rate dependent, and one aspect of material rate dependence is viscoelasticity. In nanoindentation, viscoelasticity causes the indenter to continue penetrating the material during the initial part of unloading, which results in a forward-going *nose* in the unloading curve (Figure 2.5 (A)). This phenomenon occurs when the creep rate of the material, i.e. the rate of increase in the indentation depth, is initially higher than the imposed unloading rate. In this case, the slope of the initial part of the unloading curve is changed which causes a negative contact stiffness and therefore inaccurate mechanical property measurements (Briscoe et al., 1998; Feng and Ngan, 2002; Tang and Ngan, 2003a).

One way to eliminate this nose is to use a holding time between loading and unloading at the maximum load F_{max} (Figure 2.5 (B)), in order to allow the material to relax and therefore the creep rate to dissipate prior to unloading. The appropriate holding time should be selected based on the creep and the unloading rates used in the experiment for each material. The holding time should be long enough such that the rate of increase in the indentation depth, i.e. the creep rate, is less than 1% per minute (Chudoba and Richter, 2001). Additionally, due to the time-dependent properties, the unloading curve and therefore the contact stiffness

depend on the unloading rate. A sufficiently fast unloading rate is desirable to limit the relaxation phenomenon for viscoelastic materials (Fischer-Cripps, 2006; Jakes et al., 2012; Ngan and Tang, 2002). When the unloading rate is high enough relative to the creep rate, it might be unnecessary even to apply the holding period.

Procedures have been suggested to reduce the effect of the time-dependent behaviour of materials in nanoindentation by correcting the contact stiffness measurement (Feng and Ngan, 2002; Ngan et al., 2005; Tang and Ngan, 2003a). A procedure was proposed by Feng and Ngan (2002) to correct the contact stiffness using a simple formula. This method is based on a Maxwell model including a spring and a dashpot in series. It was shown that the effect of creep can be reduced by adding a correction term to the (apparent) contact stiffness S as follows:

$$\frac{1}{S} = \frac{1}{S_c} + \frac{\dot{h}_h}{|\dot{F}_u|} \quad (2.4)$$

where \dot{h}_h is the creep rate at the end of holding time, \dot{F}_u is the initial unloading rate, and S_c is the corrected contact stiffness. Based on this formula, the corrections will be minimal when the displacement rate is small enough relative to the unloading rate ($\dot{h}_h/|\dot{F}_u| \approx 0$). This will occur when either $\dot{h}_h \approx 0$ or \dot{F}_u is very large. This shows the importance of choosing a long holding time, which will allow the system to stabilise and thereby reduce \dot{h}_h , and a high unloading rate.

Tang and Ngan (2003a) used the method proposed by Feng and Ngan in order to fit the creep curve for very compliant materials. They implemented Eq. (2.4) for calculating the contact depth to eliminate the effect of creep on the modulus measurement for polymeric materials.

Following this, Ngan et al. (2005) extended Eq. (2.4) from a linear viscoelastic form to a power law viscoelastic form as follows:

$$\frac{1}{S_c} = \left(\frac{1}{S} - \frac{\dot{h}_h}{\dot{F}_u} \right) \frac{1}{1 - \frac{\dot{F}_h}{\dot{F}_u}} \quad (2.5)$$

where \dot{F}_h is the load decay rate during the holding time, which needs to be measured as well as the creep rate and the initial unloading rate.

The approaches presented here for correcting the contact stiffness need to accurately capture the slope at the beginning of unloading, and do so using a fit to the data; however, it has been shown that these methods are highly sensitive to the form of the function used to fit the slope (Jakes et al., 2012).

2.3.4.2 Pile-Up

In indentation into an elastic-plastic material, when the contact involves plastic deformation, the sides of the residual impression do not remain straight and the surface of the specimen may be drawn upwards (pile-up) or downwards (sink-in) underneath the indenter depending on the material properties. This is illustrated in Figure 2.6, where for pile-up the contact depth h_c is greater than the maximum indentation depth h_m ($h_c > h_m$), and the opposite is the case for sink-in ($h_m > h_c$). For pile-up, contact occurs outside the theoretical contact area of the indenter at the maximum indentation depth, and for sink-in contact occurs within this contact area.

For an isotropic, rate-independent elastic-plastic material, the mechanical behaviour depends on the Young's modulus E , yield strength σ_y , and work hardening exponent n , and can be described in one-dimension by conventional stress-strain relationships as follows:

$$\begin{aligned} \sigma &= E\varepsilon \quad \text{for } \varepsilon \leq \sigma_y/E \\ \sigma &= k\varepsilon^n \quad \text{for } \varepsilon \geq \sigma_y/E \end{aligned} \quad (2.6)$$

where σ is stress, ε is strain, and k is the strength coefficient.

In pile-up, the phenomenon occurs because there is substantial plastic flow, due to a large ratio of Young's modulus to yield strength (E/σ_y) (low σ_y) and low work hardening (McElhane et al., 1998). For materials with small E/σ_y (high σ_y) and high work hardening, the material is more elastically compliant in indentation and sink-in occurs.

When pile-up is very large, the true contact area is larger than the nominal contact area which is based on the cross-sectional area of the indenter tip; consequently, the elastic modulus and hardness are overestimated (Bolshakov and Pharr, 1998; Oliver and Pharr, 2004). The results of finite element analysis by Bolshakov and Pharr (1998) showed that pile-up is significant when the ratio of the permanent depth to the maximum depth (h_p/h_m) is larger than 0.7 and the degree of work hardening is small.

It has been shown that there is a linear relationship between h_p/h_m and the ratio of the slope of the unloading curve S to the slope of the loading curve S_l as follows (Hay et al., 1998):

$$\frac{S}{S_l} = \frac{m_l}{m} \left(1 - \frac{h_p}{h_m}\right) \quad (2.7)$$

where m_l is the power law exponent of the loading curve which is equal to 1.35 when $h_p/h_m > 0.4$. Through finite element analysis, it was shown that the true contact area depends on S/S_l due to pile-up (Hay et al., 1998). In this method S/S_l can be determined continuously at every depth of interest during indentation.

2.3.4.3 Initial Contact Point

In nanoindentation, the indenter must first make contact with the specimen before the displacement measurement can be taken. It is sometimes very difficult to decide at which point the indenter comes into contact with the surface. The initial

contact depth is usually made to be as small as possible; however, due to the lack of load resolution, typically not better than ± 100 nN, the smallest maximum loads which practically can be applied are tens of micronewtons. Therefore, producing indents of less than 1 nm is difficult (Fischer-Cripps, 2013; Lucca et al., 2010). This may cause a considerable penetration in compliant materials which leads to significant errors in estimating the contact area and therefore the hardness and elastic modulus (Carrillo et al., 2005; Deuschle et al., 2007; Kaufman and Klapperich, 2009). It has been shown that the error due to the surface detection can cause the calculated modulus to be five times larger than the actual value (Kaufman and Klapperich, 2009). To attempt to address such uncertainty, the initial contact point can be set as the first point at which the load starts to increase, which appears as a sharp rise in the load data (Cao et al., 2005).

2.3.4.4 Adhesion

For most polymeric and compliant materials, adhesion between the indenter and the surface of the specimen occurs as the indenter approaches the surface (pull-on adhesion) and during the indenter retraction (pull-off adhesion). This results in a region of negative load in the load-displacement curve (Cao et al., 2005; Carrillo et al., 2005; Ebenstein and Wahl, 2006) and complicates determination of the contact point which then results in overestimation of the elastic modulus (Deuschle et al., 2007; Kaufman and Klapperich, 2009). Extremely low elastic modulus and surface roughness of compliant polymers, which enables mutual approach of the sample surface and the indenter, play key roles in the adhesion effect (Tabor, 1977).

There are a number of models that have been developed to describe the effect of adhesion on contact mechanics behaviour. The Derjaguin-Muller-Toporov (DMT) model (Derjaguin et al., 1975) accounts for adhesion forces outside the contact area. This model is most applicable for materials with high modulus. The Johnson-Kendall-Robert (JKR) model (Johnson et al., 1971) describes the adhesion forces within the contact area. Therefore, this model is used for materials with low

modulus. For indents performed with the spherical tip, the JKR model has been shown to provide a more accurate measurement of the modulus of the material (Carrillo et al., 2005; Grunlan et al., 2001).

2.3.4.5 Surface Roughness

In the nanoindentation technique, the measured indentation depth is used to estimate the residual contact area and subsequently to calculate the hardness and elastic modulus of the material; therefore, the surface roughness can have a significant influence on the measurements. When the indenter comes into contact with a valley (Figure 2.7 (A)) the true contact area is underestimated and consequently the calculated hardness is overestimated. On the other hand, when the indenter comes into contact with a peak (Figure 2.7 (B)), the non-uniform contact increases the localised stress at the points of contact, deforming the material to a greater depth at relatively low loads. This may result in a greater penetration depth and lower calculated hardness. The International Standard ISO 14577-4 stipulates that the surface roughness average value (R_a) should be less than 5% of the maximum indentation depth h_m to avoid the effect of roughness on the indentation measurements.

2.3.4.6 Indentation Size Effects

In nanoindentation, experimental results often show an increase in hardness with decreasing indentation depth. Such indentation size effects have been observed in metals, where the plastic deformation may not only depend on the strain, but also on the gradient of plastic strain which is associated with geometrically necessary dislocations (GND) (Elmustafa and Stone, 2003). However, the indentation size effects in polymers are more complicated as this phenomenon has been also observed in elastic deformation. The depth dependence of the elastic modulus has been experimentally observed in various polymers such as epoxy (Alisafaei et al., 2014; Chong and Lam, 1999; Lam and Chong, 2000), polycarbonate (PC) (Briscoe et al., 1998; Chong and Lam, 1999; Fang and Chang, 2004), poly(methyl methacrylate)

(PMMA) (Briscoe et al., 1998), polydimethylsiloxane (PDMS) (Alisafaei et al., 2013; Charitidis, 2010; Wrucke et al., 2013), silicon rubber (Chandrashekar et al., 2015), nylon (PA66) (Shen et al., 2005), and polystyrene (PS) (Briscoe et al., 1998). The length scale at which indentation size effects occur in polymers can vary widely in different polymers. For example, for nylon (PA66) (Chandrashekar et al., 2015), the depth dependence of hardness was only observed for indentation depths smaller than 200 nm; however, for PC, PMMA, and PS, the depth dependence of hardness was observed for indentation depths smaller than 1000 nm (Briscoe et al., 1998; Chong and Lam, 1999; Fang and Chang, 2004). For epoxy, this phenomenon was observed for indentation depths smaller than 3000 nm (Alisafaei et al., 2014; Chong and Lam, 1999; Lam and Chong, 2000). It has been shown that ultra-high molecular weight polyethylene (UHMWPE) (Briscoe et al., 1998) and polytetrafluoroethylene, known as Teflon (PTFE), (Li and Bhushan, 2000) do not show any indentation size effects in the range of 20 nm up to several microns.

The factors described above can affect the nanoindentation measurements and may cause overestimation of the elastic modulus. The depth dependence of the indentation modulus may be related to a variety of reasons, including the formation of a specific interfacial region between the indenter and the polymer surface during indentation (Tweedie et al., 2007), lower entanglement interactions at the surface due to the surface dynamics of polymers (Zhou and Komvopoulos, 2006), changes in the material properties through thickness (Briscoe et al., 1998; Charitidis, 2010), tip imperfection (Flores and Calleja, 1998), material rate dependence (Briscoe et al., 1998; Tang and Ngan, 2003a; Zhou and Komvopoulos, 2006), pile-up (Bolshakov and Pharr, 1998; Oliver and Pharr, 2004), adhesion (Dokukin and Sokolov, 2012; Gupta et al., 2007; Liao et al., 2010), surface roughness (Zhang et al., 2004), and higher order displacement gradients (Alisafaei et al., 2014; Alisafaei et al., 2013; Briscoe et al., 1998; Charitidis, 2010; Chong and Lam, 1999; Flores and Calleja, 1998; Han, 2010; Lam and Chong, 2000; Tranchida et al., 2007; Tweedie et al., 2007; Voyiadjis et al., 2014; Zhang et al., 2004).

2.4 Computational Modelling for Degradation of Biodegradable Polymers

A number of models have been proposed to describe the degradation of biodegradable polymers (Sackett and Narasimhan, 2011) including PLGA (Ford Versypt et al., 2013). Reaction-diffusion models have been applied to a range of aliphatic polyesters (Antheunis et al., 2010; Antheunis et al., 2009; Chen et al., 2011; Han and Pan, 2009; Lyu et al., 2005; Prabhu and Hossainy, 2007; Soares and Zunino, 2010; Wang et al., 2008). Among these models, the ones which account for the autocatalytic effect are the most comprehensive, as autocatalysis plays a strong role in the degradation mechanism (Chen et al., 2011; Ford Versypt et al., 2013; Wang et al., 2008).

2.4.1 Hydrolytic Reaction Rate

In general, polymer degradation is assumed to follow pseudo first-order kinetics where degradation is a function of the concentration of only one of the three following species: polymer or ester bonds, water, or an acid catalyst (refer to Eq. (2.1)). This approach is appropriate for general non-catalytic hydrolytic reactions. However, the carboxylic end groups have a high degree of dissociation and may act as a catalyst to accelerate the hydrolysis. Where autocatalysis plays a strong role in the degradation trend, then pseudo first-order kinetics is insufficient (Siparsky et al., 1998b). Therefore, pseudo first-order should only be used in the early stages of degradation when the concentration of ester bonds has not decreased significantly.

In second-order kinetics, the concentrations of two species are allowed to vary. This approach has been used to model the degradation behaviour where autocatalytic hydrolysis kinetics is important. However, second-order kinetics is not able to capture the effects of partial dissociation of the carboxylic acid end groups (Siparsky et al., 1998a).

The rate of hydrolysis is measured by the increase in the concentration of carboxylic end groups C_{COOH} and can be described by a 1.5th-order kinetic expression which accounts for the partial dissociation effects of the carboxylic end groups as follows (Siparsky et al., 1998a):

$$\frac{dC_{COOH}}{dt} = k' C_w C_e C_{COOH}^{0.5} \quad (2.8)$$

where k' is the acid dissociation constant, C_w is the concentration of water, and C_e is the concentration of ester bonds.

The concentration of water can be assumed to be constant in polyesters as the rate of hydrolysis of degradable polyester is independent of the total water content of the polymers (Schmitt et al., 1994).

2.4.2 Diffusion

Diffusion is a mass transfer phenomenon that causes the distribution of a chemical species to become more uniform in space as time passes. Degradation refers to the loss of mass due to diffusion of water, small monomers, and soluble oligomers out of the polymer matrix. The simplest description of diffusion is given by Fick's law (Mehrer, 2007).

The rate of change of concentration at a point in space is proportional to the second derivative of concentration with space and is given by a differential equation as follows:

$$\frac{\partial C_i}{\partial t} = \nabla \cdot (D_i \nabla C_i) \quad (2.9)$$

where for species i , D_i is the diffusion coefficient ($m^2 s^{-1}$), and C_i is the concentration ($mol m^{-3}$).

The diffusion coefficient depends on the type of species (Griffiths et al., 1998) and the polymer states such as glassy or rubbery states (Karlsson et al., 2001). Diffusion coefficient of water in polymers is not very sensitive to polymer states. The diffusion coefficient of water in a crystalline PLA and amorphous glassy PLA samples at 37°C, which is less than the glass transition temperature of PLA, is $10^{-12} \text{ m}^2 \text{ s}^{-1}$. However, the diffusion coefficient of polymer chains may be 10^{-14} to $10^{-22} \text{ m}^2 \text{ s}^{-1}$ in melt states and it is lower than $10^{-22} \text{ m}^2 \text{ s}^{-1}$ in crystalline or glassy states (Lyu and Untereker, 2009).

2.4.3 Reaction-Diffusion Models

An early model based on the reaction-diffusion phenomena was proposed by Joshi and Himmelstein (1991) for polyorthoester disks. This model was used to compute the fractional amount of different species, i.e. anhydride, acid, and the drug substitute in the polymeric matrix. In this model, the molecular weight reduction of the polymer matrix is predicted with time. The model includes the acid reaction products as the only acid source to contribute to the autocatalytic effect. The following reaction-diffusion equation was proposed in this model:

$$\frac{\partial C_i}{\partial t} = \nabla \cdot (D_i \nabla C_i) + R_i \quad (2.10)$$

where R_i is the sum of synthesis and degradation rate of species. In this model, the diffusion coefficient was dependent on the concentration of species. The effective diffusivity of each species increases exponentially as a function of the local extent of polymer hydrolysis.

Prabhu and Hossainy (2007) modified the model proposed by Joshi and Himmelstein to predict degradation of PLA stent coatings and drug release kinetics. This model includes non-catalytic hydrolysis, which is dependent on the concentrations of water and polymer and also autocatalytic hydrolysis, which is dependent on the acidic monomer concentration. The effective diffusivity of each

water-soluble species increases exponentially as a function of the extent of polymer degradation in the same manner as in Thombre and Himmelstein (1984).

Wang et al. (2008) proposed a model based on the concentration of monomers and ester bonds. In this model, the concentration of ester bonds is governed by degradation and the concentration of monomers is governed by degradation and diffusion. The diffusivity of monomers is modelled as a linear function of porosity in this model. The hydrolytic degradation is modelled using individual rate constants for non-catalytic and autocatalytic reactions to allow for respective representation of the autocatalytic effects of the carboxylic acid end groups on the degradation. The model accurately predicted the experimentally observed degradation profiles of PLLA films.

2.4.4 Mechanical Property Prediction

A number of models have been developed to predict the mechanical performance of biodegradable polymers during degradation (Hayman et al., 2014; Soares et al., 2010; Vieira et al., 2014; Vieira et al., 2011; Wang et al., 2010). A model was developed by Vieira et al. (2014) based on the relationship between fracture strength and molecular weight for thermoplastic polymers to predict the mechanical properties of PLA-PCL fibres during degradation. Since this model is based on an empirical equation, the model parameters must be determined experimentally for each material and during degradation. Also, in this model, the hydrolytic degradation rate is assumed constant, which is a significant simplification for highly heterogeneous degradation as autocatalysis has a significant effect on degradation.

The model of Soares et al. (2010) relates the degradation rate to mechanical deformation in order to determine the mechanical properties of PLLA fibres loaded under uniaxial extension. The degradation behaviour is determined from a thermodynamic analysis of the degradation process and as degradation proceeds the material loses its ability to store energy.

Wang et al. (2010) proposed a model for amorphous biodegradable polymers, based on the relationship between the Young's modulus and the number of polymer chains. This model is physically motivated by the hydrolytic random scission of the polymer chains. The model assumes that the number of polymer chains above a critical molecular weight determines the Young's modulus as chain scissions occur. This model successfully predicted the experimentally observed degradation of PLLA films.

2.5 Conclusion

This chapter provides an overview of biodegradable polymers and their biomedical applications. PLGA material is used for a variety of medical implant applications including tissue engineering scaffolds and also it can be used as a coating for load bearing implants and drug-eluting stent systems. In order for an implant to function, it must have sufficient mechanical stability. Mechanical performance of biodegradable coatings in stent applications, for instance, is of significant importance when one considers coating deformation on stent expansion and mechanical loading on contact with the arterial tissue. Given this, the mechanical properties of PLGA films are investigated in Chapter 5 of this thesis for understanding the performance of biodegradable coatings during degradation. Additionally, consideration of PLGA in this context presents a *model system* allowing for the study of film degradation and the effect on mechanical properties in a relatively rapid testing time frame.

Given the importance of the size dependent degradation of biodegradable polymers in literature, the effect of the size of the sample on the degradation behaviour and the changes in the mechanical properties of PLGA material is considered computationally and experimentally in Chapters 6 and 8 of this thesis, respectively. In order to predict the degradation behaviour and the mechanical performance of PLGA structures, a computational modelling framework, described

in Chapter 3, is used which couples a reaction-diffusion based molecular weight model to a molecular network based mechanical properties model.

The depth dependence of the elastic modulus and hardness of PLGA material are investigated in Chapters 5 and 7 of this thesis and a number of factors which affect the nanoindentation measurements are addressed.

2.6 Figures

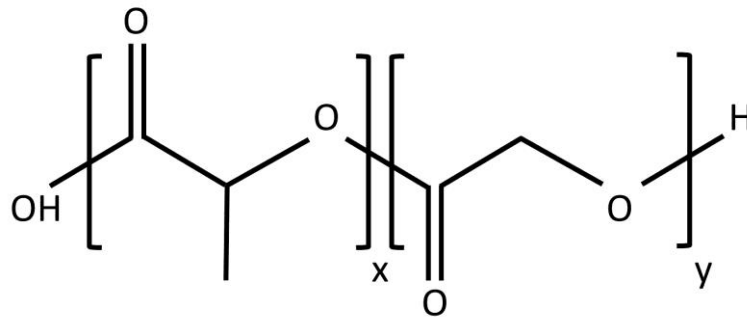


Figure 2.1: Chemical structure of PLGA, x is the number of lactic acid units and y is the number of glycolic acid units.

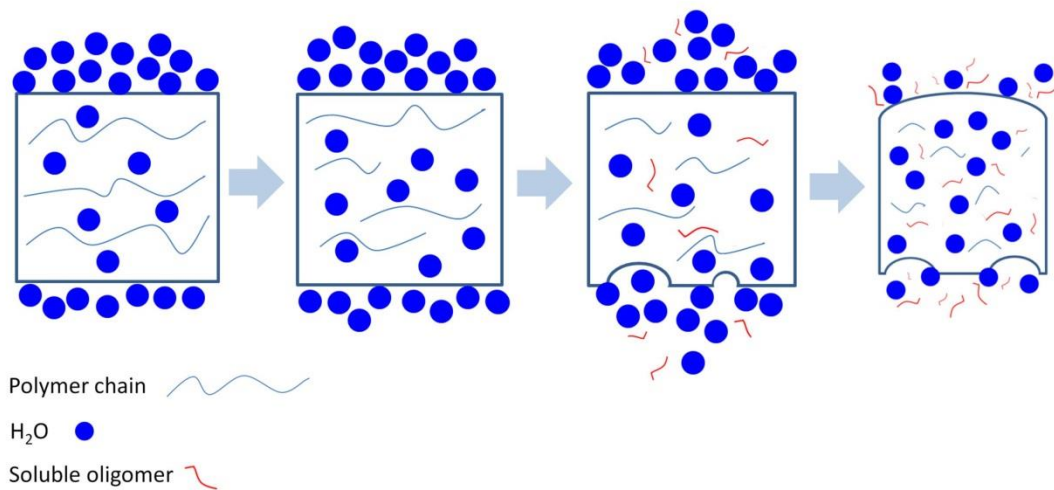


Figure 2.2: A schematic representation of the hydrolytic degradation of biodegradable polymers.

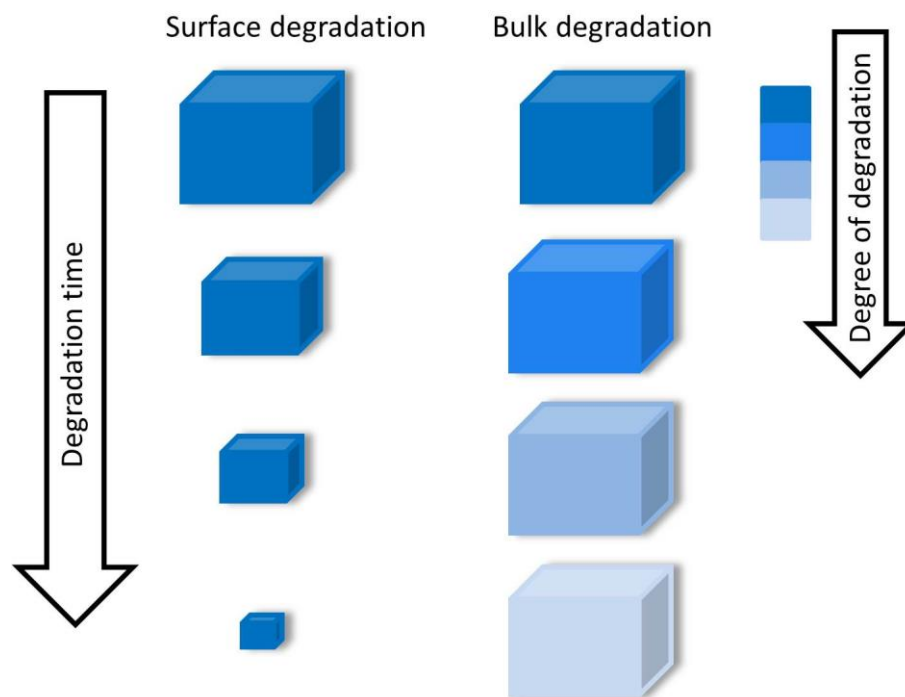


Figure 2.3: A schematic representation of surface and bulk degradation of biodegradable polymers.

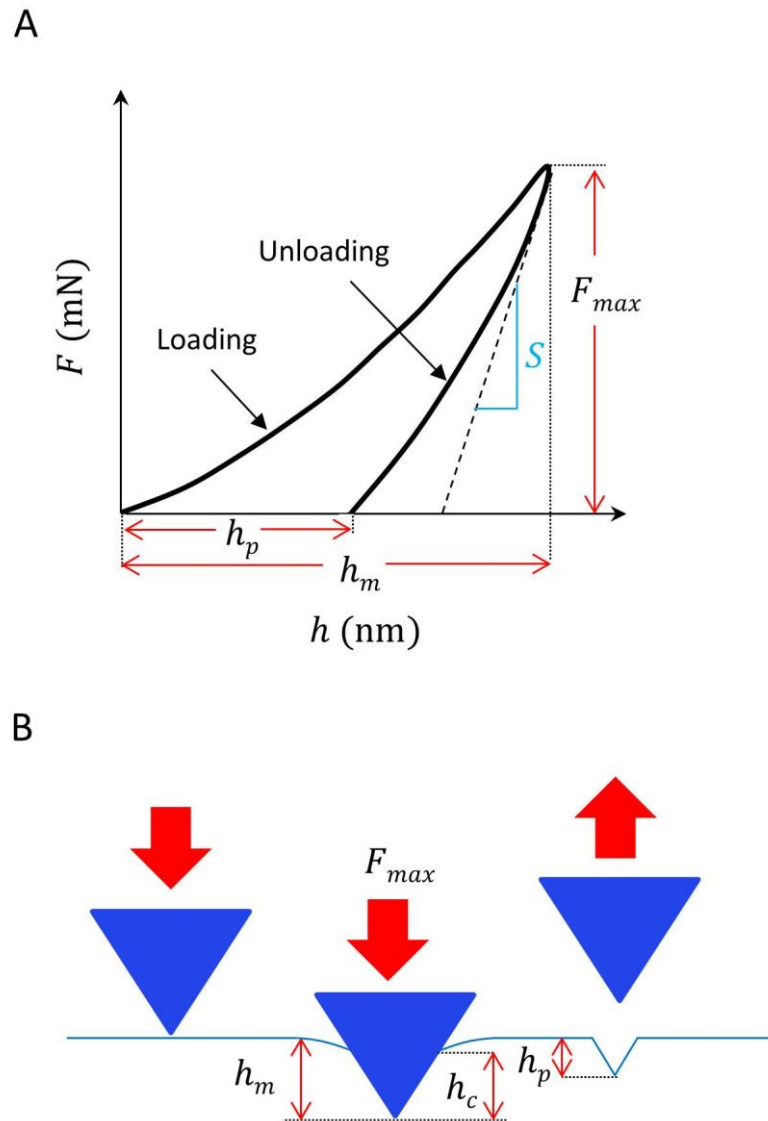


Figure 2.4: A schematic of a typical (A) load-displacement (F - h) curve and (B) an indentation process including loading and unloading. F =indentation load, h =displacement of the indenter, F_{max} =maximum load, S =contact stiffness, h_m =maximum indentation depth, h_p =permanent indentation depth, h_c =contact depth of the indenter with the sample at the maximum load.

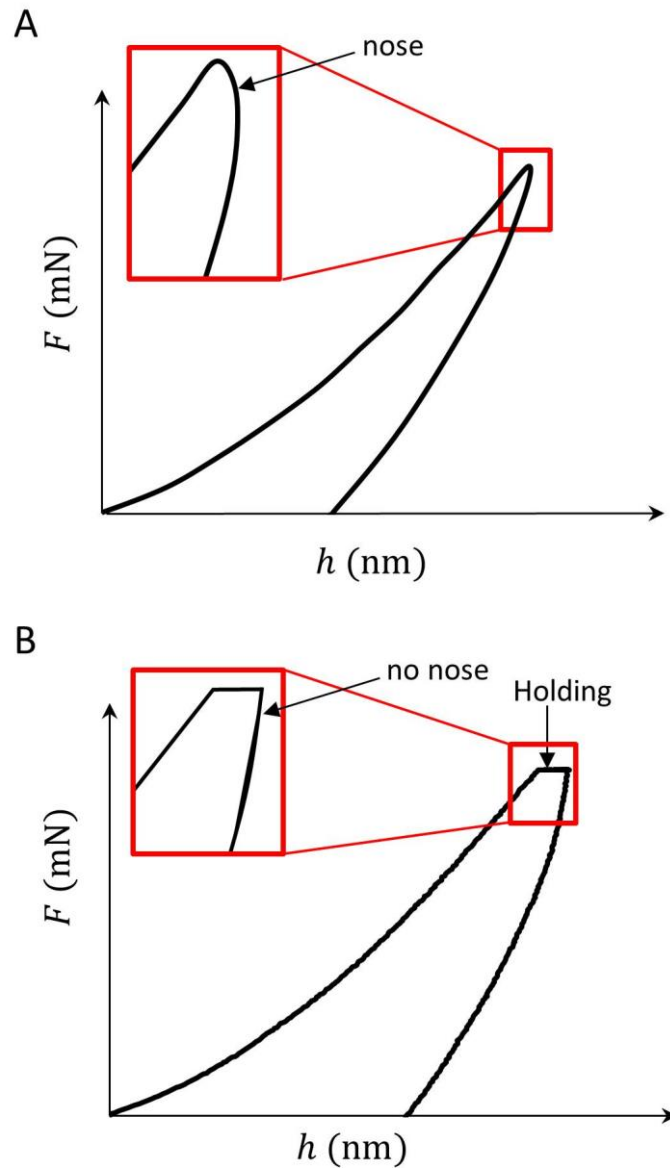


Figure 2.5: A schematic of the load-displacement (F - h) curve (A) with a forward-going nose due to viscoelasticity (B) with a holding time between loading and unloading at the maximum load F_{max} to eliminate the nose.

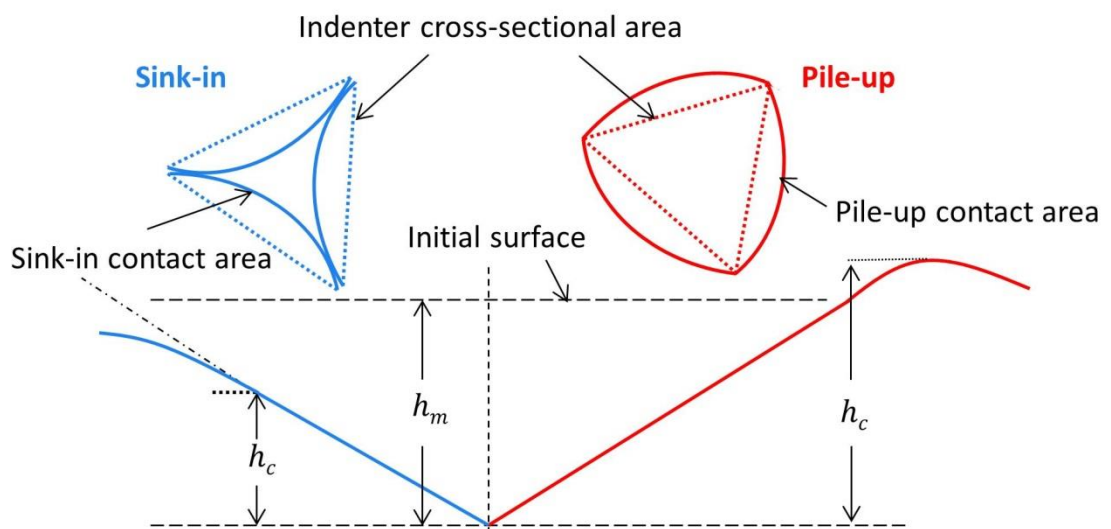


Figure 2.6: A schematic representation of pile-up and sink-in effects in indentation.

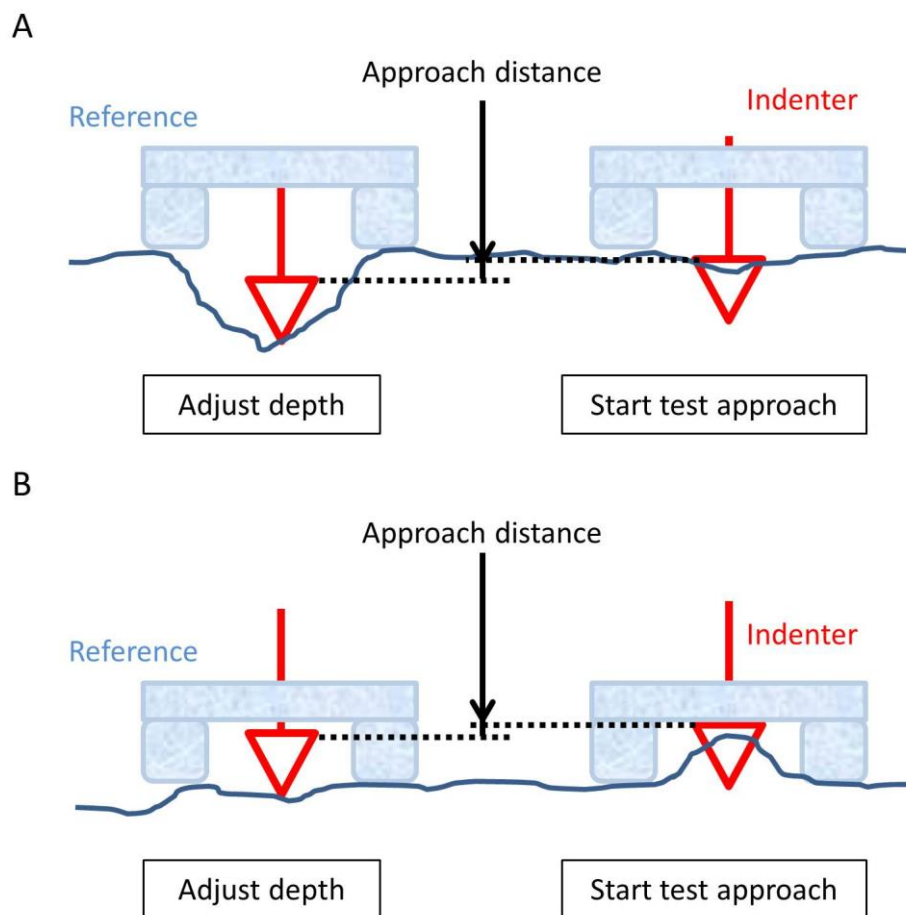


Figure 2.7: A schematic of indenters performed (A) in a hole showing the long approach distance (B) on a bump which causes the indenter starts the test already in the sample.

2.7 Tables

Table 2.1: Properties and applications of selected biodegradable polyesters (Atala and Mooney, 2013; Middleton and Tipton, 2000).

Polymer type	Crystallinity	T_m	T_g	Elongation Degradation			Typical applications
				Tensile modulus* (GPa)	Tensile strength* (MPa)	rate* (%) (months)	
PLLA	Semi-crystalline	185	57	3.1-3.7	60-70	2-6	Fracture fixation, ligament augmentation
PDLLA	Amorphous	none	n/a**	3.1-3.7	45-55	2-6	Drug delivery system
PGA	High crystallinity	225	36	6.5-7	90-110	1-2	Sutures
PLGA (50:50)	Amorphous	none	45-50	3.4-3.8	40-50	2-6	Sutures, fracture fixation, oral implant, drug delivery
PLGA (85:15)	Amorphous	none	50-55	3.3-3.5	60-70	2-6	Sutures, fracture fixation

T_m : melting temperature, T_g : glass transition temperature.

*Information is provided for PURASORB polymers by the suppliers.

**Not Available.

Table 2.2: List of commercially available PLGA polymers (Manavitehrani et al., 2016; Middleton and Tipton, 2000).

Composition	Trade name	Application	Manufacturer
PLGA (50:50)	Zoladex	Drug delivery	AstraZeneca
	Nutropin Depot	Drug delivery	Genetech
	Trelstar Depot	Drug delivery	Watson Pharma
	Sandostatin LAR	Drug delivery	Novartis
PLGA (85:15)	Biologically Quiet Biosphere	Suture anchors	Instrument Makar
	Biologically Quiet Mini-Screw	Suture anchors	Instrument Makar
	Biologically Quiet Staple	ACL reconstruction	Instrument Makar
PLGA (82:18)	SD Sorb 3mm	Suture anchors	Surgical Dynamics
	SD Sorb E-Z TAC	Suture anchors	Surgical Dynamics
	SD Sorb Meniscal Staple	Meniscus repair	Surgical Dynamics
	LactoSorb Screws and Plates	Craniomaxillofacial fixation	Biomet

3 Theoretical and Numerical Methods

3.1 Introduction

This chapter summarises the theoretical and numerical methods that are of specific relevance to this thesis. Section 3.2 covers theoretical methods and opens with an overview of the relevant aspects of continuum mechanics theory in section 3.2.1. Entropy spring theory is described in section 3.2.2, including an overview of the elasticity of a molecular network for polymers. An overview of the reaction-diffusion based molecular weight model of Wang et al. (2008), which predicts the changes in the molecular weight distribution during degradation, is presented in section 3.2.3. Finally, the nanoindentation analysis which is used in this thesis to evaluate the mechanical properties, particularly the elastic modulus and hardness, of the PLGA materials is described in section 3.2.4.

The numerical problem solving methods used in this thesis are overviewed in section 3.3. The numerical solution for the structural problems is presented in section 3.3.1. The semi-analytical and numerical solutions of the reaction-diffusion based molecular weight model are described in section 3.3.2. The molecular network based mechanical properties model is presented in section 3.3.3. Finally, the coupled modelling framework is described in section 3.3.4.

3.2 Theoretical Methods

3.2.1 Continuum Mechanics

3.2.1.1 Introduction

The following section presents an overview of the relevant aspect of continuum mechanics. For more detailed descriptions on continuum mechanics, the reader is referred to Malvern (1969). Standard notation is used throughout the following. A Cartesian coordinate system is used, with the three coordinate directions x_i , ($i = 1, 2, 3$). A dot product between two vectors, \mathbf{u} and \mathbf{v} , is described as follows:

$$\mathbf{u} \cdot \mathbf{v} = u_1 v_1 + u_2 v_2 + u_3 v_3 = \sum_i^3 u_i v_i = u_i v_i \quad (3.1)$$

A second order tensor \mathbf{A} has the components A_{ij} , ($i, j = 1, 2, 3$).

3.2.1.2 Deformation and Strain

A particle P_0 in the original unreformed reference volume V_0 has a position vector \mathbf{x} relative to an origin O , as shown in Figure 3.1. The position of particle P in the deformed volume V at time t is described by a position vector \mathbf{y} . The line vector $d\mathbf{x}$ describes the infinitesimal line element between the points P_0 and Q_0 in the original body. This vector is transformed to $d\mathbf{y}$ in the deformed body. Then the displacement \mathbf{u} can be defined as follows:

$$\mathbf{u} = \mathbf{y} - \mathbf{x} \quad (3.2)$$

$$u_i(\mathbf{x}, t) = y_i(\mathbf{x}, t) - x_i$$

The change in position of a body from its original configuration is described by the deformation gradient \mathbf{F} which is given as:

$$\mathbf{F} = \frac{\partial \mathbf{y}}{\partial \mathbf{x}} \quad (3.3)$$

$$F_{ij} = \frac{\partial y_i}{\partial x_j}$$

The determinant of the deformation gradient is known as Jacobian J which gives the volume change in the body as follows:

$$J = \det \mathbf{F} = \frac{V}{V_0} \quad (3.4)$$

The Green-Lagrangian strain tensor \mathbf{E} is defined as a function of deformation gradient as follows:

$$\mathbf{E} = \frac{1}{2} (\mathbf{F}^T \cdot \mathbf{F} - \mathbf{I}) \quad (3.5)$$

$$E_{ij} = \frac{1}{2} \left(\frac{\partial u_i}{\partial x_j} + \frac{\partial u_j}{\partial x_i} + \frac{\partial u_k}{\partial x_i} \frac{\partial u_k}{\partial x_j} \right)$$

where \mathbf{F}^T is the transpose of \mathbf{F} and \mathbf{I} is the identity tensor. For small deformations, the product of the infinitesimals is negligible, and the Green-Lagrangian strain tensor reduces to the infinitesimal strain tensor $\boldsymbol{\varepsilon}$:

$$\boldsymbol{\varepsilon} = \frac{1}{2} (\nabla \mathbf{u} + \nabla^T \mathbf{u}) \quad (3.6)$$

$$\varepsilon_{ij} = \frac{1}{2} \left(\frac{\partial u_i}{\partial x_j} + \frac{\partial u_j}{\partial x_i} \right)$$

The left and right Cauchy-Green deformation tensors \mathbf{B}_{left} and \mathbf{C}_{right} , respectively, can be defined as:

$$\begin{aligned} \mathbf{B}_{left} &= \mathbf{F} \cdot \mathbf{F}^T \\ \mathbf{C}_{right} &= \mathbf{F}^T \cdot \mathbf{F} \end{aligned} \quad (3.7)$$

The deformation gradient can be decomposed into orthogonal rotation tensor \mathbf{R} and symmetric spatial and material stretch tensors \mathbf{V} and \mathbf{U} , respectively, through:

$$\mathbf{F} = \mathbf{V} \cdot \mathbf{R} = \mathbf{R} \cdot \mathbf{U} \quad (3.8)$$

The eigenvalues of \mathbf{U} are known as principal stretches λ_i , ($i = 1, 2, 3$).

3.2.1.3 Tractions and Stresses

The Cauchy or true stress $\boldsymbol{\sigma}$ is defined as the force per unit area on the current configuration or the deformed body and it is related to the traction vector \mathbf{t} on a surface and the unit normal vector \mathbf{n} to the surface, as shown by:

$$\begin{aligned} \mathbf{t} &= \boldsymbol{\sigma} \cdot \mathbf{n} \\ t_i &= \sigma_{ij} n_j \end{aligned} \quad (3.9)$$

The principal stresses σ^{pr} can be determined from the solution to the eigenvalue equation:

$$(\boldsymbol{\sigma} - \sigma^{pr} \mathbf{I}) \cdot \mathbf{n} = 0 \quad (3.10)$$

where \mathbf{I} is the second order identity tensor. The principal stress is independent of the orientation of the coordinate system.

Two other commonly used stress tensors are the first and second Piola-Kirchhoff stress tensors. The first Piola-Kirchhoff stress \mathbf{P} , which is not symmetric, represents the force per unit area on the original configuration or the reference body and is defined as:

$$\mathbf{P} = J\boldsymbol{\sigma} \cdot \mathbf{F}^{-T} \quad (3.11)$$

The transpose of the first Piola-Kirchhoff stress is known as the nominal stress.

The total force applied by a traction acting on a free surface of the body can be computed by integrating the Cauchy stress over the deformed boundary or by integrating the first Piola-Kirchhoff stress over the same boundary in the undeformed configuration. Under the assumptions of infinitesimal deformation kinematics, all the above stress definitions become equal and can be represented by the stress tensor $\boldsymbol{\sigma}$.

3.2.1.4 Isotropic Linear Elasticity

Linear elasticity theory is based on the assumption of infinitesimal deformation kinematics. Linear elastic constitutive relations model the reversible behaviour of a material and for an isotropic linear elastic material, can be described by Hooke's law. In this case, the stress $\boldsymbol{\sigma}$ is a linear function of the infinitesimal strain $\boldsymbol{\varepsilon}$:

$$\sigma_{ij} = \lambda \varepsilon_{kk} \delta_{ij} + 2\mu \varepsilon_{ij} \quad (3.12)$$

where λ and μ are the Lamé constants and δ_{ij} is the Kronecker delta with the following property:

$$\delta_{ij} = \begin{cases} 1 & i = j \\ 0 & i \neq j \end{cases} \quad (3.13)$$

Using Voigt notation for the stress and strain quantities, where the stress and strain tensors are represented as vectors, Eq. (3.12) can be written in matrix form as follows:

$$\begin{bmatrix} \sigma_{11} \\ \sigma_{22} \\ \sigma_{33} \\ \sigma_{12} \\ \sigma_{13} \\ \sigma_{23} \end{bmatrix} = \begin{bmatrix} 2\mu + \lambda & \lambda & \lambda & 0 & 0 & 0 \\ \lambda & 2\mu + \lambda & \lambda & 0 & 0 & 0 \\ \lambda & \lambda & 2\mu + \lambda & 0 & 0 & 0 \\ 0 & 0 & 0 & \mu & 0 & 0 \\ 0 & 0 & 0 & 0 & \mu & 0 \\ 0 & 0 & 0 & 0 & 0 & \mu \end{bmatrix} \begin{bmatrix} \varepsilon_{11} \\ \varepsilon_{22} \\ \varepsilon_{33} \\ \varepsilon_{12} \\ \varepsilon_{13} \\ \varepsilon_{23} \end{bmatrix} \quad (3.14)$$

The Lamé constants can be related to the Young's modulus E and the Poisson's ratio ν through:

$$\mu = \frac{E}{2(1 + \nu)} \quad (3.15)$$

$$\lambda = \frac{\nu E}{(1 + \nu)(1 - 2\nu)}$$

The bulk modulus K is related to the Lamé constants as follows:

$$K = \frac{3\lambda + 2\mu}{3} \quad (3.16)$$

3.2.1.5 Hyperelasticity

Hyperelastic constitutive laws are used to model materials that respond elastically when subjected to larger strains. Hyperelastic materials are normally described in terms of a strain energy potential U which defines the strain energy stored in the material per unit of deformed volume. The neo-Hookean model is a common hyperelastic model (Athanasίου and Natoli, 2008). In this case, the strain energy is given as:

$$U = \frac{\mu}{2}(I_1 - 3) + \frac{K}{2}(J - 1)^2 \quad (3.17)$$

where I_1 is the first deviatoric strain invariant defined as:

$$I_1 = \lambda_1^2 + \lambda_2^2 + \lambda_3^2 \quad (3.18)$$

where λ_i are the principal stretches defined in section 3.2.1.2.

The strain energy relates the principal stretches and principal stresses as follows:

$$\sigma_i = \frac{\lambda_i}{\lambda_1 \lambda_2 \lambda_3} \frac{\partial U}{\partial \lambda_i}, i = 1, 2, 3 \quad (3.19)$$

Consider simple uniaxial extension of an incompressible material (for which the volume change is zero, i.e. $J = 1$), and the three principal stretches are not independent, but are constrained by $\lambda_1 \lambda_2 \lambda_3 = 1$. Hence, by symmetry, $\lambda_1 = \lambda$, and $\lambda_2 = \lambda_3 = \lambda^{-1/2}$. Therefore Eq. (3.17) can be written as:

$$U = \frac{\mu}{2} \left(\lambda^2 + \frac{2}{\lambda} - 3 \right) \quad (3.20)$$

From Eq. (3.19):

$$\sigma_1^{pr} = \mu \left(\lambda^2 - \frac{1}{\lambda} \right) \quad (3.21)$$

For infinitesimal strain $\lambda = 1 + \varepsilon$ and it follows from Eq. (3.21) that:

$$\sigma_1^{pr} = 3\mu\varepsilon = E\varepsilon \quad (3.22)$$

where E is the Young's modulus.

Thus, the equivalent Young's modulus of an incompressible neo-Hookean solid in uniaxial extension is 3μ , which is consistent with an incompressible linear elastic material (Eq. (3.15) when $\nu = 0.5$).

3.2.2 Entropy Spring Theory

The entropy spring model uses equilibrium thermodynamics to determine how stress is related to changes in both internal energy and entropy of a polymer network, and thus to determine a constitutive law. The polymer is considered as a three-dimensional network of long chains that are connected at a few points and form a continuous molecular framework. An overview of this theory is briefly presented below. Further detail on the elasticity of the molecular network theory can be found in Ward and Sweeney (2012).

3.2.2.1 The Thermodynamics of Deformation

In order to obtain the strain energy for the polymer network, it is necessary to determine the free energy of the polymer in the undeformed and deformed states. For an elastic solid of initial length L_0 which is extended under a uniaxial tensile force f , the change in internal energy dI during deformation is given by:

$$dI = f dL + T dS_e \quad (3.23)$$

where dS_e is the change in entropy S_e at absolute temperature T and dL is the change in the length after deformation. As the deformation is assumed to be incompressible, it is useful to consider the change in the Helmholtz free energy dH :

$$dH = dI - T dS_e - S_e dT = f dL - S_e dT \quad (3.24)$$

The elementary molecular theory of networks is based on the assumption that the internal energy of the ideal polymer chains can be ignored and the elasticity arises entirely from changes in entropy (entropic elasticity). The polymer chain will seek the lowest free energy and thus the maximum entropy. The entropy of a polymer chain is at its lowest when it is fully extended. For a chain that is not fully extended, the application of an external force will reduce the entropy and increase the free energy. In the following, the entropy of an undeformed and a deformed polymer

chain is considered in order to determine the strain energy of the polymer network and thus a constitutive relationship.

3.2.2.2 The Entropy of a Single Chain

First, the entropy of a polymer chain in the reference state is determined. It is convenient to consider a freely joined chain in which the molecules are joined by n_l links with equal length l_l . The chain is arranged with end P_0 at the origin and the other end is at point $Q_0(x_1, x_2, x_3)$ as shown in Figure 3.2 (A). The end-to-end length r is the length of the vector from P_0 to Q_0 . The probability distribution of the end-to-end length $P(r)$ has the form of a Gaussian error function (Figure 3.2 (B)) and is given as follows:

$$P(r)dr = \left(\frac{4a^3}{\sqrt{\pi}} \right) r^2 \exp(-a^2 r^2) dr \quad (3.25)$$

where $a^2 = 3/(2n_l l_l^2)$. Thus, the most probable length of a chain is not zero.

The entropy of a freely joined chain s_e is proportional to the logarithm of the number of possible configurations Ω so that:

$$s_e = k_B \ln \Omega \quad (3.26)$$

where k_B is Boltzmann's constant.

The number of configurations available to the chain is proportional to the probability that the chain end lies within an infinitesimal volume. The entropy of the chain is then given by:

$$s_e = c_1 - k_B a^2 r^2 = c_1 - k_B a^2 (x_1^2 + x_2^2 + x_3^2) \quad (3.27)$$

where c_1 is an arbitrary constant, and one will recall that the end of the chain is at the point $Q_0(x_1, x_2, x_3)$.

The mean square chain length $\overline{r^2}$ for the above expression for $P(r)$ is given through:

$$\overline{r^2} = \int_0^{\infty} r^2 P(r) dr = \frac{3}{2a^2} = n_l l_l^2 \quad (3.28)$$

Therefore, the root mean square chain length is proportional to the square root of the number of links in the chain $((\overline{r^2})^{1/2} = l_l \sqrt{n_l})$.

3.2.2.3 The Elasticity of a Molecular Network

The strain energy function for a molecular network can be calculated by assuming that it is given by the change in the entropy of a network of chains as a function of strain, i.e. the internal energy of the chains does not vary with strain. It is assumed here that the principal stretches λ_1 , λ_2 , and λ_3 are parallel to the three principal coordinate axes x_1 , x_2 , and x_3 . The deformation is also assumed to be affine, i.e. the macroscopic deformation is the same as the deformation of a line element on a polymer chain. The deformation of the polymer chain, when the chain end $Q_0(x_1, x_2, x_3)$ is displaced to point $Q(x'_1, x'_2, x'_3)$ (Figure 3.2 (C)) is described by:

$$\begin{aligned} x'_1 &= \lambda_1 x_1 \\ x'_2 &= \lambda_2 x_2 \\ x'_3 &= \lambda_3 x_3 \end{aligned} \quad (3.29)$$

The entropy of the chain after deformation is given by:

$$s'_e = c_2 - k_B a^2 (\lambda_1^2 x_1^2 + \lambda_2^2 x_2^2 + \lambda_3^2 x_3^2) \quad (3.30)$$

Therefore, the changes in the entropy of deformation of the polymer chain Δs_e can be described as follows:

$$\Delta s_e = s'_e - s_e = -k_B a^2 \{(\lambda_1^2 - 1)x_1^2 + (\lambda_2^2 - 1)x_2^2 + (\lambda_3^2 - 1)x_3^2\} \quad (3.31)$$

The total entropy change of the polymer network ΔS_e is given by:

$$\Delta S_e = \sum_1^N \Delta s_e = -k_B a^2 \left\{ (\lambda_1^2 - 1) \sum_1^N x_1^2 + (\lambda_2^2 - 1) \sum_1^N x_2^2 + (\lambda_3^2 - 1) \sum_1^N x_3^2 \right\} \quad (3.32)$$

where N is the chain density, i.e. the number of chains per unit volume in a polymer network. As there is no preferred directions for the x_1 , x_2 , or x_3 directions in the isotropic state, then:

$$\sum_1^N x_1^2 = \sum_1^N x_2^2 = \sum_1^N x_3^2 = \frac{1}{3} \sum_1^N r^2 = \frac{1}{3} N r^2 = \frac{1}{3} N \frac{3}{2a^2} = \frac{N}{2a^2} \quad (3.33)$$

Therefore the entropy change of the polymer network can be defined as:

$$\Delta S_e = \sum_1^N \Delta s_e = \frac{-1}{2} N k_B (\lambda_1^2 + \lambda_2^2 + \lambda_3^2 - 3) \quad (3.34)$$

Assuming no change in the internal energy of the polymer network on deformation ($\Delta I = 0$), the change in the Helmholtz free energy is obtained from Eq. (3.24) as:

$$\Delta H = -T \Delta S_e = \frac{1}{2} N k_B (\lambda_1^2 + \lambda_2^2 + \lambda_3^2 - 3) \quad (3.35)$$

If the strain energy function U is zero in the undeformed condition, then:

$$U = \Delta H = \frac{1}{2} N k_B T (\lambda_1^2 + \lambda_2^2 + \lambda_3^2 - 3) \quad (3.36)$$

The strain energy can be defined for a simple elongation in the x_1 direction for an incompressible material ($\lambda_1 \lambda_2 \lambda_3 = 1$, $\lambda_1 = \lambda$, and $\lambda_2 = \lambda_3 = \lambda^{-1/2}$) as follows:

$$U = \frac{1}{2} N k_B T \left(\lambda^2 + \frac{2}{\lambda} - 3 \right) \quad (3.37)$$

This equation is similar to the neo-Hookean strain energy function in Eq. (3.20). The constitutive parameter μ in Eq. (3.22), which is equivalent to the shear modulus of the material, can be determined as follows:

$$\mu = N k_B T \quad (3.38)$$

Therefore, substituting Eq. (3.38) into Eq. (3.22) the Young's modulus E of a molecular network can be related to the number of polymer chains per unit volume N through:

$$E = 3 N k_B T \quad (3.39)$$

This theory was modified by Wang et al. (2010) and is used in this thesis, through implementation in a MATLAB programme, in order to predict the changes in the Young's modulus of PLGA material during degradation based on the relationship between the Young's modulus and the number of polymer chains. This model is described in detail in a later section of this chapter as a mechanical properties model, which is used in Chapter 6 to simulate the mechanical behaviour of PLGA structures during degradation.

3.2.3 Polymer Degradation Model (Molecular Weight Model)

In this thesis, a phenomenological continuum model developed by Wang et al. (2008) is used to predict the reduction in the molecular weight of PLGA material. In

this model, the molecular weight distribution of the polymer is described by the mole concentration of polymer ester bonds C_e , which remain inside the polymer matrix, and the mole concentration of monomers C_m . Monomers are produced during the hydrolytic reaction and they can diffuse throughout the polymer and also into the surrounding aqueous medium. The rate of change of C_e is determined by the hydrolytic reactions (including non-catalytic and autocatalytic reactions) of the polymer chains.

The degradation behaviour of biodegradable polymers is captured by the following reaction-diffusion equations (Wang et al., 2008):

$$\frac{\partial C_m}{\partial t} = k_1 C_e + k_2 C_e C_m^\beta + \nabla \cdot (D_{eff} \nabla C_m) \quad (3.40)$$

$$\frac{\partial C_e}{\partial t} = -(k_1 C_e + k_2 C_e C_m^\beta) \quad (3.41)$$

where k_1 and k_2 are the reaction rate constants for the non-catalytic and autocatalytic reactions, respectively; the final term in Eq. (3.40) is the divergence of the gradient of C_m which accounts for the diffusion of monomers, and D_{eff} is the effective diffusion coefficient. The exponent β captures the non-linearity of the autocatalytic reaction, and accounts for dissociation of the acid end group. The effective diffusion coefficient D_{eff} is defined as:

$$D_{eff} = D_0 \left[1 + \alpha \left(1 - \frac{C_m + C_e}{C_{e0}} \right) \right] \quad (3.42)$$

where D_0 is an intrinsic diffusion coefficient, C_{e0} is the initial value of C_e , and α is a constant equal to 4.5 (Wang et al., 2008).

The average molecular weight of the polymer is calculated based on the concentration of ester bonds. It is assumed that the monomers are too small to

detect. Therefore, the number average molecular weight M_n , can be related to C_e as follows:

$$\frac{M_n}{M_{n0}} = \frac{C_e}{C_{e0}} \quad (3.43)$$

where M_{n0} is the initial number average molecular weight.

The monomer concentration and the ester bond concentration are obtained by solving Eqs. (3.40) - (3.42). The degradation of the polymer is then determined by the number average molecular weight of the polymer according to Eq. (3.43). This model is used in a one-dimensional model for films and in a three-dimensional model for scaffolds in Chapter 6 to predict the changes in the molecular weight of PLGA material during degradation.

3.2.4 Nanoindentation Analysis

In this thesis, the method proposed by Oliver and Pharr (1992), introduced in section 2.3, is used for the nanoindentation analysis in order to determine the elastic modulus and hardness of PLGA material from indentation load-displacement data. Figure 3.3 shows a typical indentation load-displacement curve and a schematic representation of a section through an indentation. This figure is based on the information presented in Figure 2.4, updated here to illustrate details of the Oliver and Pharr method.

The maximum penetration depth h_m is given by the sum of the contact depth of the indenter in the specimen at the maximum load h_c and the amount of sink-in h_s as follows:

$$h_m = h_c + h_s \quad (3.44)$$

Assuming that pile-up is negligible, the amount of sink-in is given by:

$$h_s = \epsilon \frac{F_{max}}{S} \quad (3.45)$$

where S is the contact stiffness, F_{max} is the maximum load, and ϵ is a constant which depends on the indenter geometry ($\epsilon = 0.72$ for the Berkovich indenter, $\epsilon = 0.75$ for a sphere or paraboloid, and $\epsilon = 1$ for a flat-ended cylindrical punch).

The contact stiffness S is evaluated by fitting Eq. (2.3) to the unloading data and then finding the derivative at the maximum load, as follows:

$$S = \left(\frac{dF}{dh} \right)_{max} = m F_{max} (h_m - h_p)^{-1} \quad (3.46)$$

where m is the power law exponent of the unloading curve and h_p is the permanent indentation depth. The constants m and h_p are determined by a least squares fitting procedure.

The contact area A describes the projected (or cross sectional) area of the indenter and is determined as a function of contact depth $A(h_c)$ as follows:

$$A(h_c) = C_1 h_c^2 + C_2 h_c + C_3 h_c^{0.5} + \dots \quad (3.47)$$

where C_1 is typically 24.5 for a perfect Berkovich indenter. The remaining constants (C_2, C_3, \dots) account for the tip rounding and other departures from the ideal shape (Oliver and Pharr, 2004).

The reduced elastic modulus E_r is determined from the contact stiffness and the area function as follows:

$$E_r = \frac{\sqrt{\pi} S}{2\kappa \sqrt{A(h_c)}} \quad (3.48)$$

where κ is a correction factor which equals 1 for an asymmetric tip when the half-included angle of the indenter is 90° , and varies slightly for other indenter geometries. A wide range of values has been reported for κ in different studies and there is no consensus on what value should be taken; however, Oliver and Pharr (2004) suggested a value of 1.034 for the Berkovich tip as used here.

The elastic modulus of the specimen E_s is given as follows:

$$\frac{1}{E_r} = \frac{1 - \nu_s^2}{E_s} + \frac{1 - \nu_i^2}{E_i} \quad (3.49)$$

where ν_i and E_i are the Poisson's ratio and the modulus of the indenter, which are equal to 0.07 and 1141 GPa for a diamond indenter, respectively and ν_s is the Poisson's ratio of the specimen.

The indentation hardness H_{IT} is defined using the maximum value of the applied load divided by the area function:

$$H_{IT} = \frac{F_{max}}{A(h_c)} \quad (3.50)$$

Plasticity index η is calculated as follows:

$$\eta = \frac{W_p}{W_p + W_e} = \frac{W_p}{W_t} \quad (3.51)$$

where W_p is the plastic work (which is the area between the loading and unloading curves), W_e is the elastic work (which is the area under the unloading curve), and W_t is the total work (which is the area under the loading curve). When the deformation is likely to be entirely elastic, $\eta = 0$. For fully plastic deformation, $\eta = 1$, and for elastic-plastic deformation, $0 < \eta < 1$. The Oliver and Pharr method described in this section is used in Chapters 5, 7, and 8 of this thesis to determine the mechanical properties of PLGA material.

3.3 Numerical Methods

3.3.1 Numerical Solution for Structural Problems

3.3.1.1 Principle of Virtual Work

The principle of virtual work states that the sum of the virtual work from internal strains is equal to the work from internal loads. Considering a body of volume V bounded by a surface S_V the internal and external virtual work can be represented in Voigt notation as follows:

$$\int_V \delta \boldsymbol{\varepsilon}^T \boldsymbol{\sigma} dV = \int_{S_V} \delta \mathbf{u}^T \mathbf{t} dS_V \quad (3.52)$$

where $\boldsymbol{\sigma}$ and \mathbf{t} are the stress and surface traction vectors, respectively, while, $\delta \boldsymbol{\varepsilon}$ is the virtual strain vector in the solid at time t , associated with the virtual displacement vector, $\delta \mathbf{u}$.

3.3.1.2 The Finite Element Method

The finite element method is a means of obtaining approximate numerical solutions to field problems. The body of volume V can be discretised into a finite number of small elements joined at nodes, which approximates the initial geometry of the body. The full collection of elements and nodes that represent the body is known as the finite element mesh. For structural problems, the finite element solution method is based on the principle virtual work.

The displacement and the strain within the particular finite element can be written in term of the nodal displacement \mathbf{u}_e as follows:

$$\begin{aligned} \delta \mathbf{u} &= \mathbf{N} \delta \mathbf{u}_e \\ \delta \boldsymbol{\varepsilon} &= \mathbf{B} \delta \mathbf{u}_e \end{aligned} \quad (3.53)$$

where \mathbf{N} is the element shape function matrix and \mathbf{B} is the element shape function gradient matrix. Substituting Eq. (3.53) in Eq. (3.52), the finite element approximation can be summed over all the elements in the mesh ($el: 1 \rightarrow nelm$) as follows:

$$\sum_{el=1}^{nelm} \int_V \mathbf{B}^T \delta \mathbf{u}_e^T \boldsymbol{\sigma} dV = \sum_{el=1}^{nelm} \int_{S_V} \mathbf{N}^T \delta \mathbf{u}_e^T \mathbf{t} dS_V \quad (3.54)$$

The following global expression can be obtained by performing the summation and assembling element quantities into global quantities:

$$\int_V \hat{\mathbf{B}}^T \boldsymbol{\sigma} dV = \int_{S_V} \hat{\mathbf{N}}^T \mathbf{t} dS_V \quad (3.55)$$

where $\hat{\mathbf{N}}$ is the global shape function matrix and $\hat{\mathbf{B}}$ is the global shape function gradient matrix.

The term on the right side of the equality is the global external force vector \mathbf{F}_{ext} :

$$\mathbf{F}_{ext} = \int_{S_V} \hat{\mathbf{N}}^T \mathbf{t} dS_V \quad (3.56)$$

For a linear elastic material (Hook's law presented in Eq. (3.12)) it can be seen that:

$$\boldsymbol{\sigma} = \mathbf{D}\boldsymbol{\varepsilon} = \mathbf{D}\hat{\mathbf{B}}\mathbf{u}_e \quad (3.57)$$

where \mathbf{D} is a 6 x 6 matrix of elastic constants for three-dimensional problems and \mathbf{u}_e is now the global nodal displacement vector for the whole mesh. By substituting Eq. (3.57) into Eq. (3.55), the equation can be rearranged as follows:

$$\left(\int_V (\widehat{\mathbf{B}}^T \mathbf{D} \widehat{\mathbf{B}}) dV \right) \mathbf{u}_e = \mathbf{F}_{ext} \quad (3.58)$$

$$\mathbf{K} \mathbf{u}_e = \mathbf{F}_{ext}$$

where \mathbf{K} is the global stiffness matrix. This is the global finite element stiffness equation. The solution to Eq. (3.58) is obtained by any appropriate numerical algorithm which involves the inversion of the stiffness matrix:

$$\mathbf{u}_e = \mathbf{K}^{-1} \mathbf{F}_{ext} \quad (3.59)$$

Substituting Eq. (3.56) into Eq. (3.55) and rearranging this in a more general non-linear form, which includes geometrical and material non-linearity, yields the following expression:

$$\int_V \widehat{\mathbf{B}}(\mathbf{u}_e)^T \boldsymbol{\sigma}(\mathbf{u}_e) dV - \mathbf{F}_{ext} = \mathbf{G}(\mathbf{u}_e) = \mathbf{0} \quad (3.60)$$

where \mathbf{G} is the out of balance/residual forces vector, and $\mathbf{G} = \mathbf{0}$ is a set of non-linear equations in \mathbf{u}_e , to be solved using an appropriate numerical algorithm.

3.3.1.3 Implicit Solutions

The above finite element equations for structural problems, most generally Eq. (3.60), can be solved using an implicit solution scheme. In this type of solution scheme, the state of the model is updated incrementally from time t to $t + \Delta t$.

The commercially available finite element solver COMSOL Multiphysics (v4.3b, COMSOL Inc., MA, USA) is used for finite element structural problem solution in this thesis. A modified implicit Newton-Raphson method, called the damped Newton method, is used in COMSOL. When applied in one-dimension, the damped Newton method can be used to find an approximate solution to an equation $f(x) = 0$

involving either a linear or a non-linear function $f(x)$ by taking a tangent to the function $f'(x)$ as follows:

$$x_{i+1} = x_i - \alpha_d \frac{f(x_i)}{f'(x_i)} \quad (3.61)$$

where x_i is the i^{th} guess for the root of the function $f(x) = 0$, x_{i+1} is an improved estimate of the root, and α_d is a damping factor. For $\alpha_d = 1$, this equation results in the Newton-Raphson method.

Applying this method to the general case of the system of non-linear equations in Eq. (3.60) gives:

$$\mathbf{u}_{i+1}^{t+\Delta t} = \mathbf{u}_i^{t+\Delta t} - \alpha_d \left[\frac{\partial \mathbf{G}(\mathbf{u}_i^{t+\Delta t})}{\partial \mathbf{u}} \right]^{-1} \mathbf{G}(\mathbf{u}_i^{t+\Delta t}) \quad (3.62)$$

where $\mathbf{u}_i^{t+\Delta t}$ is the current estimate of the nodal displacement vector for the i^{th} iteration at time $t + \Delta t$ and $\mathbf{u}_{i+1}^{t+\Delta t}$ is an improved estimate of the nodal displacement relative to $\mathbf{u}_i^{t+\Delta t}$. The partial derivative of the right hand side of this equation is known as the Jacobian matrix; it can also be referred to as the global stiffness matrix and in doing so Eq. (3.62) can be written as:

$$\mathbf{K}(\mathbf{u}_i^{t+\Delta t}) \delta \mathbf{u}_{i+1} = -\alpha_d \mathbf{G}(\mathbf{u}_i^{t+\Delta t}) \quad (3.63)$$

This equation must be solved for each iteration during the implicit process for the change in incremental displacement $\delta \mathbf{u}_{i+1}$. Further detail on the damped version of Newton's method can be found in COMSOL documentation.

COMSOL also utilises an automatic linearity algorithm by which it can detect problem linearity/non-linearity, and automatically applies linear or non-linear versions of the solver as appropriate. In this thesis, finite element structural problems are addressed in Chapter 6 to estimate the effective modulus of the

degraded scaffold under uniaxial compression strain. For these structural problems infinitesimal deformation kinematics are assumed and non-linearity due to large deformation kinematics are neglected, hence the structural problems are linear. Further details on the automatic linearity algorithm can be found in the COMSOL documentation.

3.3.2 Semi-analytical and Numerical Solutions for Polymer Degradation Problems (Molecular Weight Model)

In this thesis, semi-analytical and numerical solutions are generated for polymer degradation problems described by the reaction-diffusion based molecular weight model in section 3.2.3. A semi-analytical solution of the governing equations (Eqs. (3.40) - (3.42)) is obtained in an idealised one-dimensional form for the case of a PLGA film using the Galerkin method in MATLAB. This method will be described below in section 3.3.2.1. Also a numerical solution of these governing equations for the general three-dimensional case is obtained using the finite element method by implementation into COMSOL Multiphysics (v4.3b, COMSOL Inc., MA, USA), as will be described below in section 3.3.2.2. The finite element equations are solved at each time step in each finite element resulting in the determination of the concentrations of the monomers and ester bonds in the polymer over time. The finite element method is applied to both one-dimensional (PLGA film) and three-dimensional (PLGA scaffold) cases which are described in Chapter 6.

3.3.2.1 Semi-analytical Solution (the Galerkin Method)

The semi-analytical solution of Eqs. (3.40) - (3.42) in one-dimension is obtained using the Galerkin method through the use of the following trial functions for the primary dependent variables:

$$\hat{C}_m = \frac{1}{2} Y_1(\hat{t})(1 - \hat{x}^2) \tag{3.64}$$

$$\hat{C}_e = Y_2(\hat{t})\hat{x} + Y_3(\hat{t})$$

where \hat{C}_m and \hat{C}_e are the non-dimensional forms of the ester bond concentration and the monomer concentration, respectively (described in Eqs. (3.40) and (3.41)), which are normalised by their initial values, \hat{x} is the normalised distance through the film thickness, and Y_1 , Y_2 , and Y_3 are functions of normalised time \hat{t} , to be determined (Wang et al., 2008).

The one-dimensional problem geometry is shown in Figure 3.4. Contact on the outside of the film with the aqueous medium is represented by assuming the concentration of monomers at the boundary of the film is zero ($\hat{C}_m = 0$ at $\hat{x} = 1$), which means that all the monomers which reached the surface are immediately convected away from the surface by the environmental flow. The flux of monomers at all other boundaries, including the interface between the film and the substrate, is set to zero.

By substituting Eq. (3.64) into Eqs. (3.40) and (3.41), a set of ordinary differential equations are generated of the variables Y_1 , Y_2 , and Y_3 and the MATLAB (R2014a, Mathworks Inc., MA, USA) solver ODE45 is used to numerically integrate these equations with the initial conditions of $Y_1(0) = Y_2(0) = 0$ and $Y_3(0) = 1$. These initial conditions are applied to give the time evolution of the trial functions, consistent with the boundary conditions described above. Then, \bar{C}_e is determined by averaging the non-dimensional form of the ester bond concentration \hat{C}_e over the normalised thickness of the film \hat{x} according to Eq. (3.64). The MATLAB code is used to implement the solution is provided in Appendix A. The semi-analytical solution of the reaction-diffusion based molecular weight model described here is used for a one-dimensional form for the case of a PLGA film in Chapter 6.

3.3.2.2 Numerical Solution (the Finite Element Method)

Numerical solutions to the reaction-diffusion partial differential equations (PDEs) given in section 3.2.3, for the general three-dimensional case, are obtained using the finite element method. The numerical solutions of Eqs. (3.40) - (3.42) are

obtained using the *classical PDEs* module in COMSOL Multiphysics (v4.3b, COMSOL Inc., MA, USA). The general form of the classical PDEs in COMSOL is as follows:

$$k_c \frac{\partial^2 u}{\partial t^2} + d_c \frac{\partial u}{\partial t} - \nabla \cdot (D \nabla u + f_c u - f_s) + c_c \cdot \nabla u + a_c u = s_c \quad (3.65)$$

where u is the dependent variable, e.g. C_e or C_m . In this general equation, k_c is the mass coefficient, d_c is a damping coefficient, D is the diffusion coefficient, f_c is the conservative flux convection coefficient, f_s is the conservative flux source term, c_c is the convective coefficient, a_c is the absorption coefficient, and s_c is the source term.

In the case of C_m and C_e (Eqs. (3.40) and (3.41)), $d_c = 1$ and $k_c = f_c = f_s = c_c = a_c = 0$, and s_c is defined as the reaction terms. The effective diffusion coefficient D_{eff} based on Eq. (3.42) can be used for D in the equation for C_m .

There are two implicit time-dependent algorithms which can be used in COMSOL to solve time-dependent problems such as the reaction-diffusion equations (Eqs. (3.40) and (3.41)): backward differentiation formulas (BDF) and Generalised- α . These algorithms use the Newton-Raphson method (that was described previously in section 3.3.1.3 for structural problems) to find the solutions at several previous time steps (up to five) to numerically approximate the time derivatives of the fields and to predict the solution at the next time step. The COMSOL solver automatically chooses appropriate numerical time steps. These can be set to be as long as possible within a certain relative or absolute tolerance for the accuracy of the integration, which is estimated during runtime. In this thesis, the numerical solution of the reaction-diffusion equations was obtained at each time step in each element using the BDF implicit time-dependent method, with the maximum order of 2. Further details on this method can be found in the COMSOL documentation. The numerical solutions of the reaction-diffusion based molecular weight model described here are used in Chapter 6 for a general three-dimensional case.

3.3.3 The Mechanical Properties Model

In this thesis, the elasticity of a molecular network theory described in section 3.2.2.3 (Eq. (3.39)) is used to predict the elastic modulus of PLGA material during degradation. This theory was modified by Wang et al. (2010) by assuming that scissions of very long chains (which are constrained by surrounding chains) do not significantly affect the entropy change and, hence, the number of chains per unit volume in a polymer network N . Also, it was assumed that a chain with molecular weight smaller than a critical molecular weight is not included in counting the number of chains and consequently does not contribute to the polymer stiffness. Thus, N only decreases from its initial value; consequently the Young's modulus does not increase during degradation.

Polymer chains are affected by two degradation processes, similar to those described in Eqs. (3.40) and (3.41): polymer chain end scission (where scission occurs at the final bond at chain ends resulting in the production of a monomer) and random chain scission (where scission occurs randomly at any bond in a chain resulting in production of two chains with random lengths). In this thesis, to implement this theory for predicting the degradation behaviour of PLGA material, an initial distribution of chains is assumed (Figure 3.5 (A)) and, after each scission, the lengths of each newly produced chain are stored (Figure 3.5 (B)). The ratio of random scissions to end scissions $R_{scissions}$ determines how often each type of scission occurs.

Each original chain and the resulting shorter chains are stored in a row as one group, which is indicated by a yellow box in Figure 3.5 (B) and they are counted as one chain (with respect to Eq. (3.39)). Once the number average molecular weight (M_n) falls below a critical molecular weight M_n^{crit} , the group of chains does not contribute to the stiffness and is no longer counted. For each group of chains, M_n is calculated as the total weight of all chains divided by the number of chains:

$$M_n = \frac{N_{total}M_0}{n_{total}} \quad (3.66)$$

where N_{total} is the sum of polymer units in a group, M_0 is the average molar mass of poly(lactide) and poly(glycolide) (65 g mol^{-1}), and n_{total} is the total number of chains in the group.

In this thesis, the random occurrence of the scissions and the subsequent evolution of the molecular weight distribution, i.e. the lengths of the chains, are predicted using MATLAB (R2014a, Mathworks Inc., MA, USA). The mechanical properties model predicts a non-linear decrease in Young's modulus as M_n decreases. The MATLAB code used to implement the model is provided in Appendix B.

An initial distribution of the polymer molecular weight is required by the model and for the implementation in this thesis; this distribution is obtained from experimental GPC data for the PLGA material (which is presented in Chapter 5). For this, the total number of polymer chains N_{chains} is required to be chosen and the length of these chains are determined such that the molecular weight of the chains in the simulation matched the experimental GPC data.

The main model parameters, including the critical molecular weight M_n^{crit} , the ratio of random scissions to end scissions $R_{scissions}$, and the total number of polymer chains N_{chains} are required to be initially determined. This model is used in Chapter 6 to predict the relationship between the Young's modulus and the molecular weight distribution for PLGA material.

3.3.4 Coupling Molecular Weight and Mechanical Properties Models

In this thesis, the reaction-diffusion based molecular weight model (described in section 3.2.3) and the molecular network based mechanical properties model (defined in section 3.3.3) are coupled in order to simulate the mechanical behaviour of PLGA structures during degradation. To allow for the more general case of three-dimensional structures to be considered, the finite element implementation of the

molecular weight model (described in section 3.3.2.2) is used. Figure 3.6 presents a flowchart that gives an overview of each model and the coupling scheme which is used to generate the combined computational modelling framework.

With reference to Figure 3.6, the change in the molecular weight distribution as polymer chains undergo scissions is captured by COMSOL for the particular structure of interest. As the degradation proceeds, the molecular weight distribution at each solution point (node in the finite element mesh) is determined. This distribution is represented in COMSOL via the variables C_e and C_m , i.e. the concentrations of esters bonds and monomers, respectively.

At each time step, the mechanical properties model is then used to calculate the current modulus within each finite element (at each integration point). As described in Eq. (3.43) changes in C_e are assumed to capture changes in M_n . Thus, changes in C_e (as predicted by the molecular weight model) are related (via the mechanical properties model) to changes in the Young's modulus E of the material throughout the finite element mesh. Finally, the distribution of E can be used as the input to a further finite element structural simulations (using COMSOL, as described in section 3.3.1.3) to predict the mechanical performance of a PLGA structure during degradation.

In this thesis, the coupled modelling framework is calibrated using the experimental results for the degradation of PLGA film (determined from the experimental data of Chapter 5) (refer to Figure 3.6). The framework is then applied in Chapter 6 to predict the degradation and mechanical properties of PLGA films of different thicknesses and of a range of PLGA scaffolds.

3.4 Conclusion

This chapter gives an overview of the theoretical and numerical methods used in this thesis. The reaction-diffusion based molecular weight model and the molecular network based mechanical properties model are coupled in order to simulate the

mechanical behaviour of PLGA structures during degradation. The semi-analytical solution of the reaction-diffusion based molecular weight model is obtained in an idealised one-dimensional form for the case of a PLGA film. Also a numerical solution of this model for the general three-dimensional case is obtained using the finite element method. The coupled modelling framework is calibrated using the experimental results for the degradation of PLGA film (determined from the experimental data of Chapter 5). The coupled framework is then applied in Chapter 6 to predict the degradation and mechanical properties of PLGA films of different thicknesses and PLGA scaffolds. The finite element structural problems are addressed in Chapter 6 to estimate the effective modulus of the degraded scaffold under uniaxial compression strain assuming infinitesimal deformation kinematics.

3.5 Figures

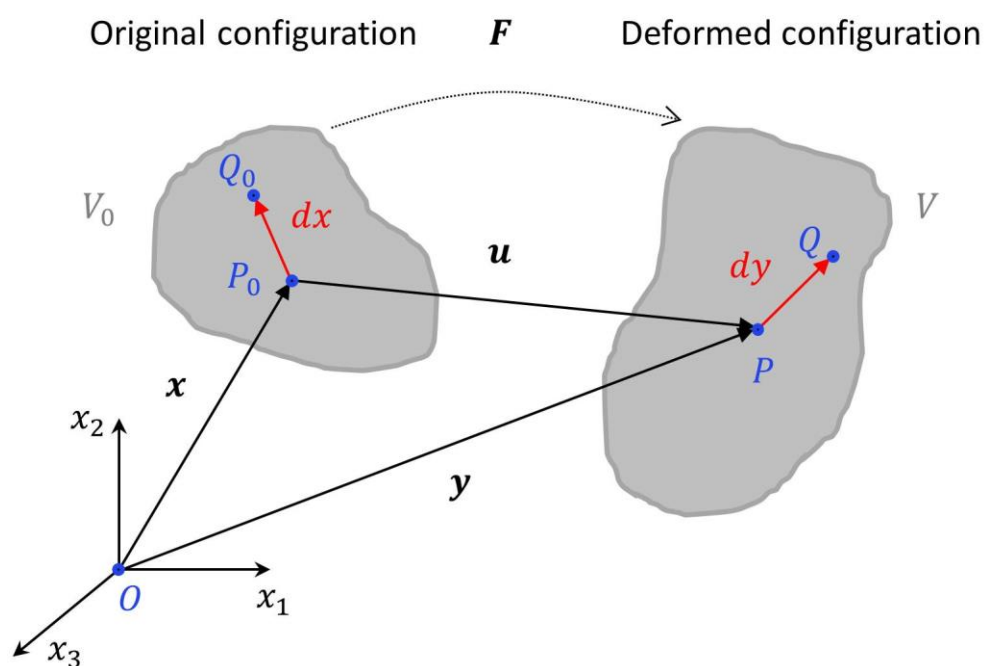


Figure 3.1: A schematic of a body with volume V_0 in the original configuration that is mapped to the volume V in the deformed configuration.

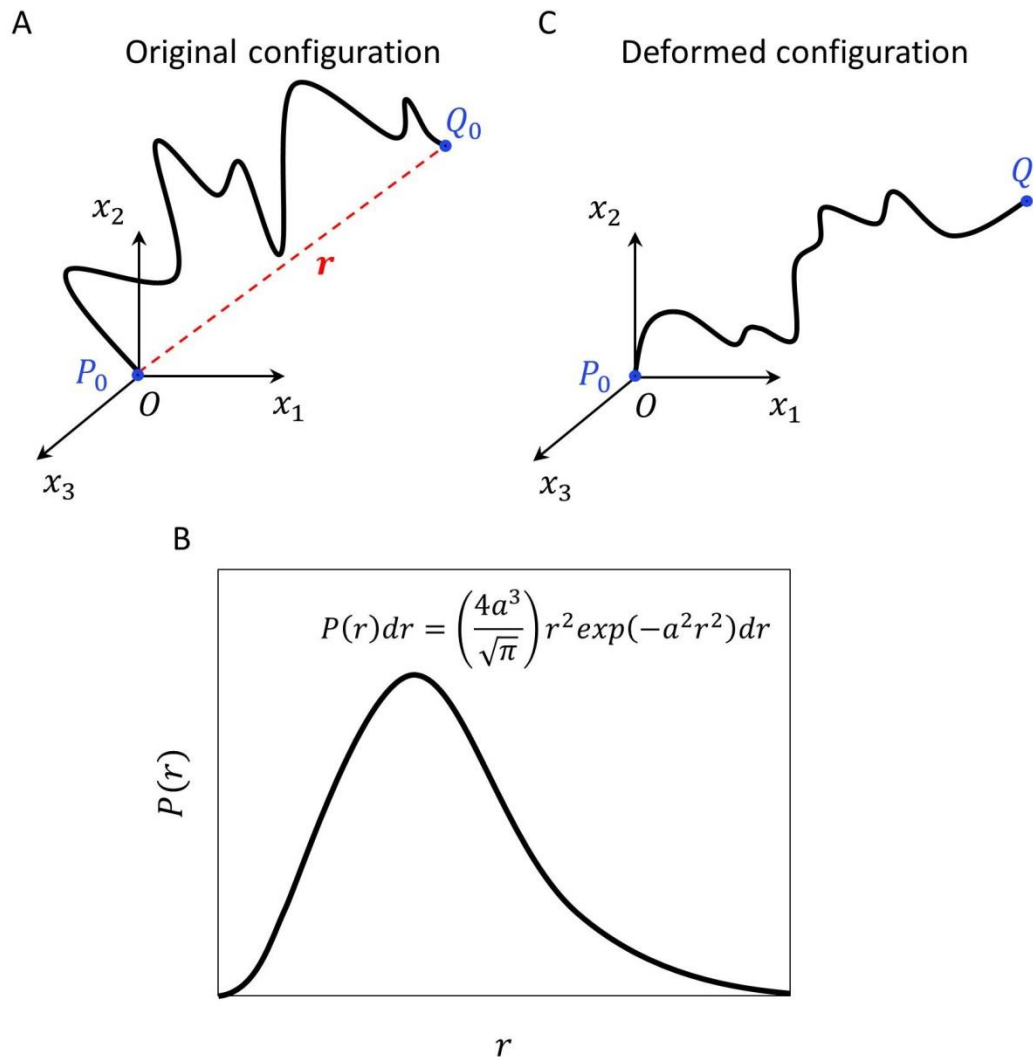


Figure 3.2: (A) A single freely jointed polymer chain with a chain end $Q_0(x_1, x_2, x_3)$ in the original configuration and with the end-to-end length r . (B) A Gaussian error function which shows the probability distribution of the end-to-end length $P(r)$. (C) The end of chain $Q_0(x_1, x_2, x_3)$ in the original configuration is displaced to $Q(x'_1, x'_2, x'_3)$ in the deformed configuration.

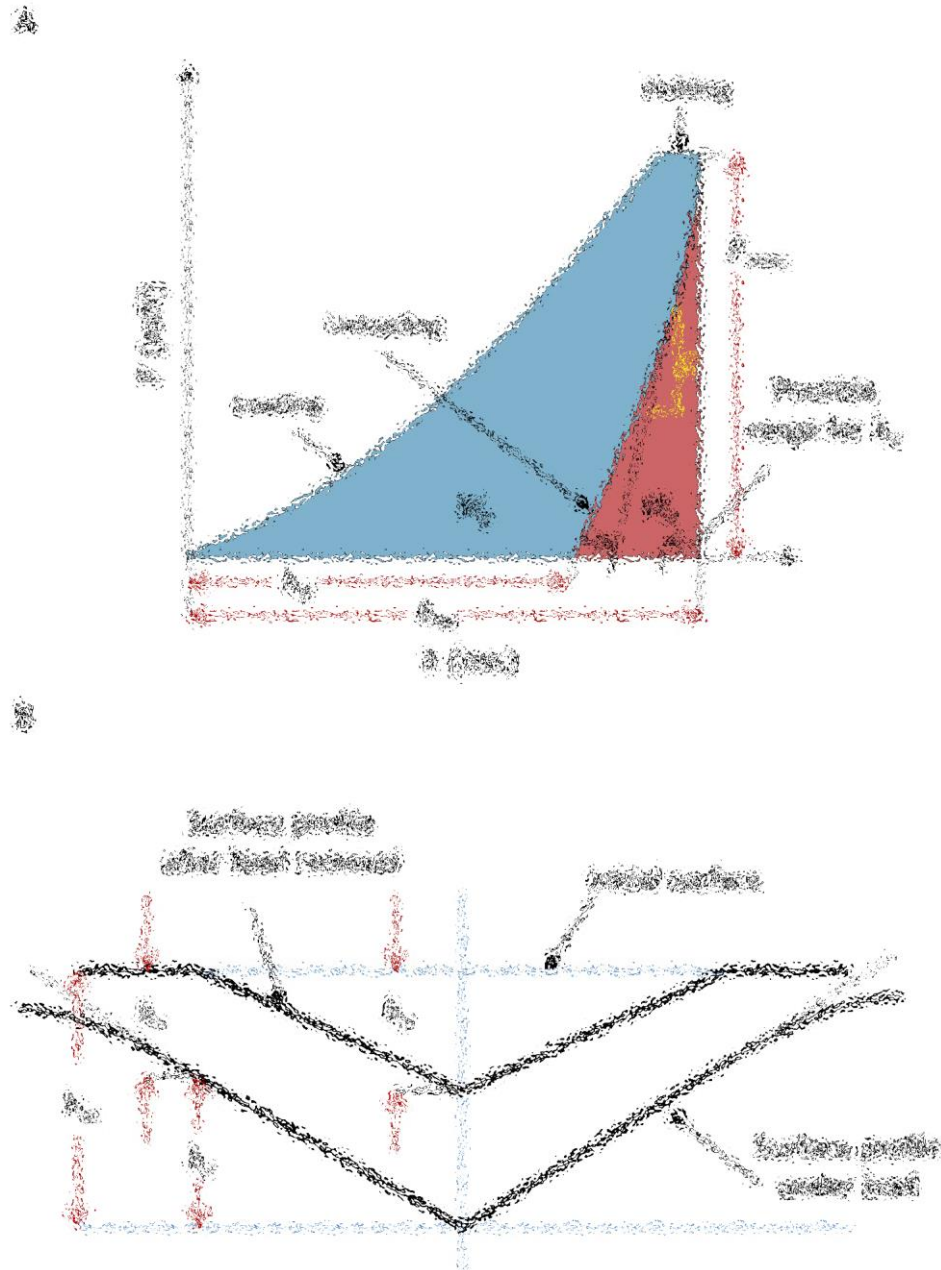


Figure 3.3: (A) A typical load-displacement ($F-h$) curve for an indentation experiment indicating the parameters used in the indentation analysis based on the Oliver and Pharr method. (B) A schematic representation of a section through an indentation. F_{max} =maximum load, S =contact stiffness, h_m =maximum indentation depth, h_p =permanent indentation depth, h_c =contact depth of the indenter with the sample at the maximum load. **Figure blurred due to copyright restrictions.**

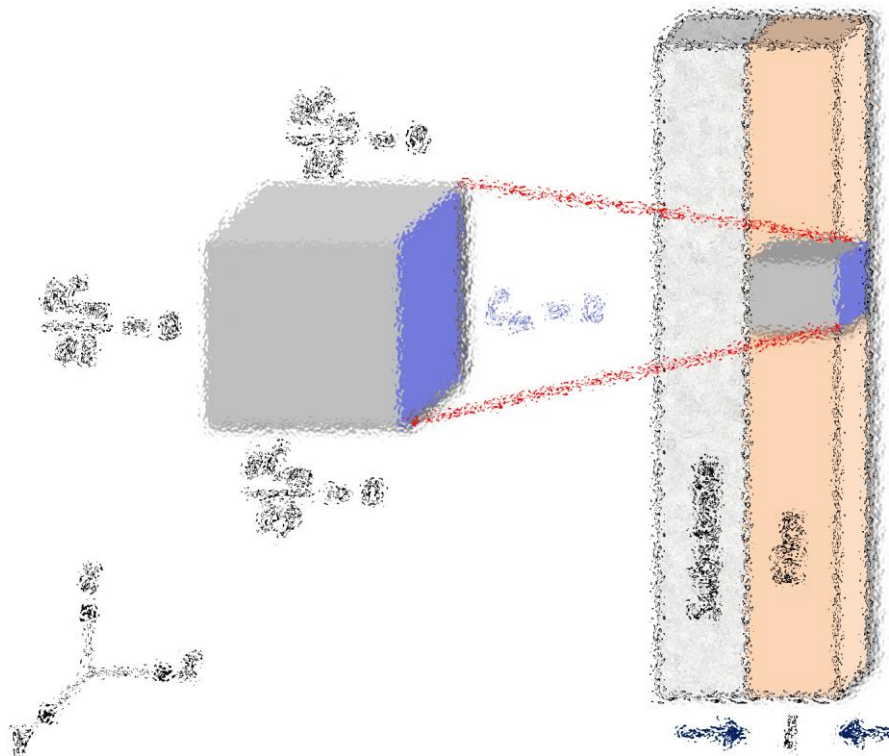
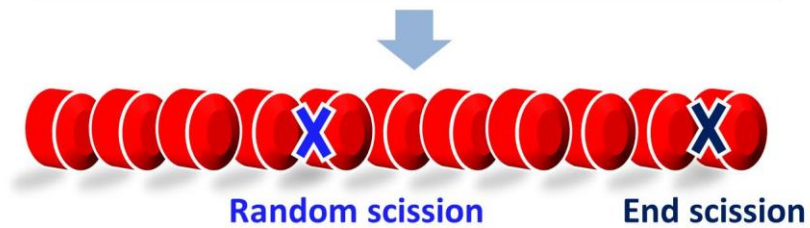


Figure 3.4: The boundary conditions used for the reaction-diffusion based molecular weight model. The thickness of the film is l . **Figure blurred due to copyright restrictions.**

A

Initial chain length

6205	0	0	0	0	0	0
6022	0	0	0	0	0	0
5845	0	0	0	0	0	0
5674	0	0	0	0	0	0
→ 5508	0	0	0	0	0	0
5348	0	0	0	0	0	0
5192	0	0	0	0	0	0
5040	0	0	0	0	0	0



B

Chain length after random/end scissions

6199	1	1	1	1	1	1
5894	123	1	1	1	1	1
3899	1941	1	1	1	1	1
5668	1	1	1	1	1	1
→ 545	1	1	1	4375	1	584
2843	2500	1	1	1	1	1
5190	1	1	0	0	0	0
5035	1	1	1	1	1	1

Figure 3.5: A schematic of (A) the initial chain length and (B) the produced chains stored after random and end scissions. The newly produced chains are stored in each row. The red box shows an example of the original chain length and the yellow box shows the resulting shorter chains after chain scissions.

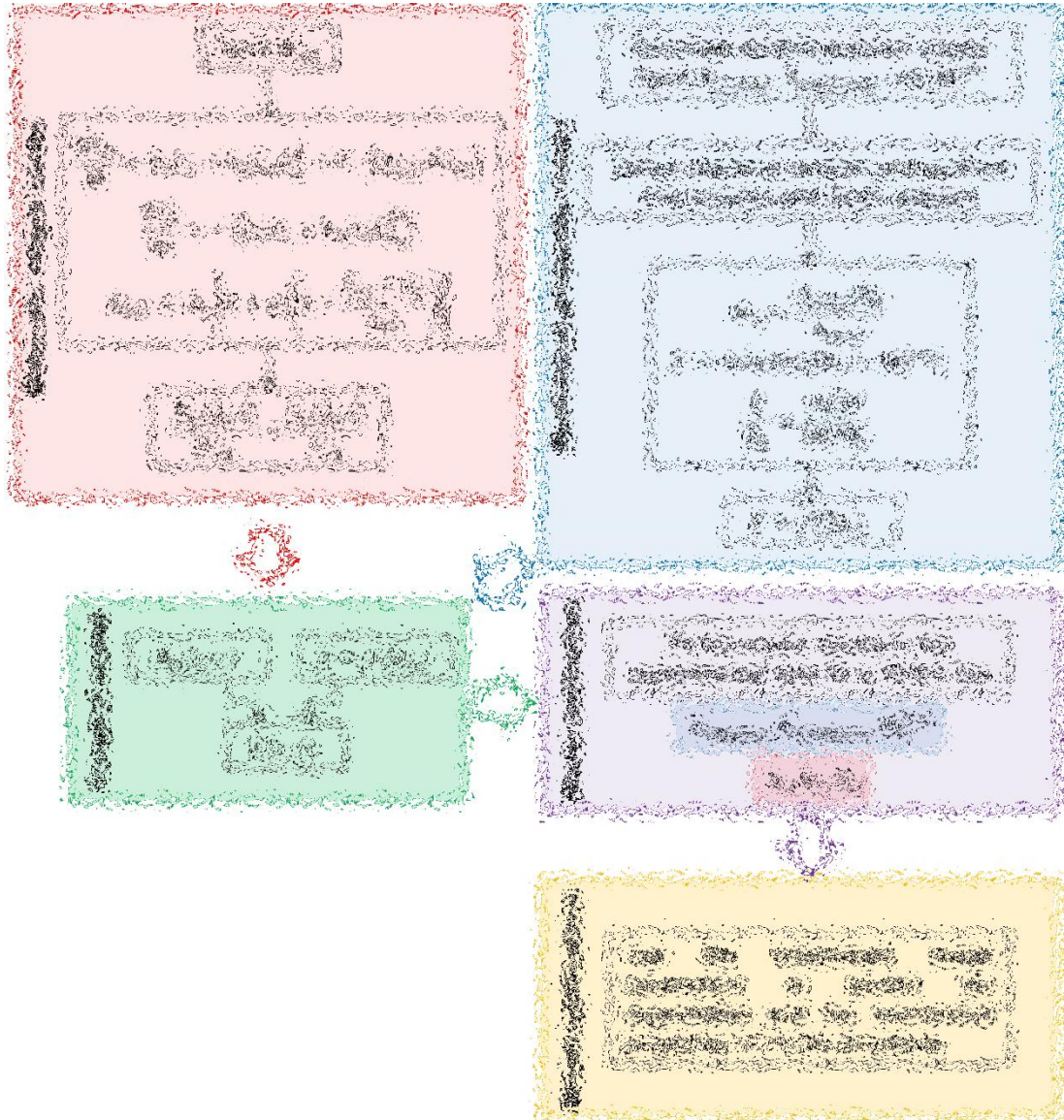


Figure 3.6: Flowchart of the coupled computational modelling framework used for the prediction of degradation behaviour and mechanical properties of PLGA structures. The coupled modelling framework is calibrated using the experimental results for the degradation of PLGA film. **Figure blurred due to copyright restrictions.**

4 Experimental Methods

4.1 Introduction

This chapter describes the sample preparations and the experimental methods used in this thesis. The materials and sample preparations are presented in section 4.2. The *in-vitro* degradation of PLGA materials is described in section 4.3, followed by the experimental methods, including optical microscopy and scanning electron microscopy (described in section 4.4), gel permeation chromatography (described in section 4.5), X-ray diffraction (described in section 4.6), and atomic force microscopy (described in section 4.7), to characterise the materials during degradation. The calibration processes and the testing protocol for performing the nanoindentation technique on PLGA material are described in section 4.8.

4.2 Materials and Sample Preparations

DL-lactide-glycolide copolymer with a molar ratio of 50:50 and an inherent viscosity midpoint of 1 dl g⁻¹ (PURASORB PDLG 5010) was supplied by Purac Biomaterials (Gorinchem, Netherlands). Chloroform (CHCl₃) and Dimethylformamide (DMF) were purchased from Sigma Aldrich (Missouri, USA). Phosphate-buffered saline solution (PBS) was prepared by dissolving one tablet supplied by Sigma Aldrich in 200 ml of deionised water.

In this thesis, PLGA samples were prepared by two different methods: solvent casting and compression moulding. A compression-moulded plate was supplied by Proxy Biomedical Ltd (Co. Galway, Ireland). The plate was cut into 20 x 20 mm² test pieces with thickness of 1.082 ± 0.006 mm. The density of the compression-

moulded material was $1.20 \pm 0.02 \text{ g cm}^{-3}$. The compression-moulded samples are referred to as CM1000, hereafter.

To prepare the samples by solvent casting, the polymer was first dissolved in chloroform. The mass concentration of the solution ρ_s was determined in order to obtain the desired thickness of the film l as follows:

$$\rho_s = \frac{A_s \rho_p l}{V_s} \quad (4.1)$$

where A_s is the surface area of the Petri dish, ρ_p is the density of the polymer, and V_s is the volume of the polymer solution which is added to each Petri dish. The density of PLGA 50:50 was assumed to be 1.34 g cm^{-3} (Arnold et al., 2007).

The solution of PLGA in chloroform was prepared at two different concentrations (ρ_s): 0.2 g ml^{-1} and 0.1 g ml^{-1} . Using a pipette, 2 ml of the polymer solution (V_s) was then cast onto a glass Petri dish (diameter 40 mm). To prevent the formation of air bubbles, the Petri dishes were covered by glass lids. The samples were then put into a desiccator for 48 h at room temperature and then dried in a vacuum for a week. The thickness and weight of the samples were measured by a digital micrometer and a digital balance, respectively. The thickness of the solvent-cast films prepared by the polymer solutions of 0.2 g ml^{-1} and 0.1 g ml^{-1} was $0.250 \pm 0.040 \text{ mm}$ and $0.120 \pm 0.002 \text{ mm}$, respectively. The density of the solvent-cast material was $1.06 \pm 0.06 \text{ g cm}^{-3}$. The films are referred to as SC250 and SC120, hereafter. The properties of the PLGA samples used in this thesis are shown in Table 4.1. An example of an undegraded solvent-cast PLGA film and a compression-moulded PLGA plate in the as-received condition are shown in Figure 4.1.

4.3 *In-vitro* Degradation

The degradation study was performed according to the ASTM F1635-11 standard (2011). The samples were weighed to measure the initial mass of the films m_{ini} . To

simulate *in-vitro* degradation conditions, the samples were placed in PBS with a pH of 7.4. The mass ratio of the PBS solution for each specimen was 100:1. Individual sterilized containers were used for each sample with sealed lids to prevent evaporation of the PBS solution. The containers were placed in an oven at 37°C during degradation.

The pH of the solution was periodically monitored by an Orion Star™ A111 pH meter (Thermo Fisher Scientific, Massachusetts, USA) through the course of the study. The pH meter was calibrated with three pH buffers: 4.0, 7.0 and 10.0.

The samples were removed from the PBS at each time point and weighed immediately to obtain the wet mass m_w . Then, they were gently washed with deionised water and blotted dry prior to further study. The dry mass m_d was measured after the specimens had been vacuum dried to a constant weight. The mass remaining and water content of the specimens were calculated as follows:

$$\text{Mass remaining (\%)} = 100 - \frac{m_{ini} - m_d}{m_d} \times 100 \quad (4.2)$$

$$\text{Water content (\%)} = \frac{m_w - m_d}{m_d} \times 100$$

4.4 Surface Morphology

The surface of the samples was imaged using a BX51M optical microscope (Olympus, Tokyo, Japan) immediately after removing them from the PBS solution. The samples were subjected to gold coating for 2 min at a current of 25 mA and examined using a Hitachi S-4700 scanning electron microscope (SEM) (Japan) at an accelerating voltage of 15 kV.

4.5 Molecular Weight Determination

The average molecular weight of the materials was determined using a gel permeation chromatography (GPC) system consisting of a Viscotek DM 400 data

manager, a Viscotek VE 3580 refractive-index detector, and two Viscotek Viscogel GMH_{HR}-M columns. The samples were removed from the PBS solution and dissolved in DMF (5 mg ml⁻¹). Then, 100 µl of the solution was injected into the GPC using an auto-sampler. Measurements were carried out at 60°C and at a flow rate of 1.0 ml min⁻¹ using HPLC-grade DMF containing 0.01 M LiBr as the eluent. The columns were calibrated using twelve polystyrene standards with molecular weights ranging from 376 to 2,570,000 g mol⁻¹; therefore, the weight average molecular weight (M_w) and the number average molecular weight (M_n) of the samples were measured with respect to polystyrene. The polydispersity index (PDI) was determined as the ratio of the weight average molecular weight to the number average molecular weight (M_w/M_n).

4.6 Crystallinity

The crystallinity of the PLGA materials was determined by X-ray diffraction (XRD) technique using an Intel Equinox 3000 diffractometer (Stratham, USA). Diffraction patterns were recorded between the angular ranges of 5° to 35° (2θ) using Cu K α radiation of wavelength 1.54 Å (30 kV, 20 mA).

4.7 Surface Roughness and Pile-up

The surface roughness of PLGA films was measured using a Dimension 3100 atomic force microscope (AFM) (Digital Instruments Veeco Metrology, Santa Barbara, CA) in non-contact mode at 1 Hz scan rate. The surface images of the impression left by the indentation were obtained using AFM and the cross-section profiles of the indents were analysed to investigate the formation of pile-up.

4.8 Mechanical Properties

The mechanical properties of PLGA materials were evaluated by the nanoindentation technique using a Nano Hardness Tester (CSM instruments SA, Switzerland) with a load and depth resolution of 0.04 µN and 0.04 nm, respectively. A general view of the nanoindentation instrument used in this thesis is shown in

Figure 4.2. The indentation tests were carried out using a Berkovich indenter tip. Before proceeding with an indentation test, the optical microscope and the area function were calibrated as will be described in detail below. Then, the indentation tests were performed on the PLGA materials to evaluate their mechanical properties.

4.8.1 Indenter-Microscope Distance Calibration

The indenter-microscope calibration was performed to measure the distance between the focal point of the visual optics field and the centre of the indenter in the X and Y axes in the plane. An accurate measure of this offset is essential to ensure that the indentation will be performed at the locations preselected using the visual optics. This positioning calibration is essential especially for heterogeneous materials, such as the degraded samples, where the indentation has to be performed in specific areas. A separate microscope with 5x and 120x magnification lenses and a digital camera attachment were used to photograph the specimen and to select the area to be indented.

4.8.2 Area Function Calibration

The area function $A(h_c)$ was defined as a function of the contact depth h_c using a fitting method involving six terms, according to Eq. (3.47). The area function was calibrated from nanoindentation of fused silica. The fused silica sample was cleaned with isopropanol (99.9%) and a soft tissue paper before testing. A matrix of 10 x 11 indents at different loads was performed for the calibration.

After tip calibration, an indentation test was performed on fused silica to verify the accuracy of the indentation measurement. The maximum load of 80 mN with a holding time of 10 s between loading and unloading was used (Figure 4.3 (A)). The loading and unloading rates were set at 160 mN min⁻¹. The contact point was precisely determined for the load-displacement curve as the first point at which the load starts to increase, which appears as a sharp rise in the load data (Figure 4.3 (B)), as described in section 2.3.4.3. The maximum indentation depths h_m and the

elastic modulus E_s were measured based on the Oliver and Pharr method described in Chapter 3. The Poisson's ratio of 0.17 was assumed for fused silica. The elastic modulus and the maximum indentation depth were 67.2 ± 0.8 GPa and 748.7 ± 6.6 nm, respectively. These values are close to the values reported by the manufacturer guidelines ($E_s = 70$ -75 GPa and $h_m = 780$ -900 nm) which confirmed the reliability of the measurements.

4.8.3 Indentation of PLGA Material

4.8.3.1 Sample Preparation and Testing Conditions

No polishing was employed in order to avoid possible changes in the properties of the material. The PLGA samples were indented on a glass coverslip (D263, Borosilicate glass) by mounting them on clear double-sided tape. All indentation tests were carried out at room temperature.

The mechanical testing of undegraded control samples was carried out in the dry condition. Degraded samples were removed from the PBS and blotted dry prior to mechanical testing at each time point. The mechanical properties of the degraded samples were evaluated in the wet condition in order to assess the *in-vivo* mechanical behaviour of these materials; although, the presence of water in the samples made the indentation testing more difficult to perform due to difficulties in surface detection procedure.

4.8.3.2 Testing Protocol

The desired indentation area was chosen using the optical microscope. By controlling the position of the table (Figure 4.2), the sample was placed under the tip for making a measurement. Before each multi-sample run, the surface to tip distance was set by adjusting the depth offset in a fine range (± 10 μm). After the initial range adjustment, the surface detection parameters, i.e. the approaching speed and delta contact slope were determined. Based on the manufacturer guidelines, the approaching speed and the delta slope are recommended to be

2000 nm min⁻¹ and 80% and 4000 nm min⁻¹ and 25% for stiff and compliant materials, respectively. In this thesis, for the undegraded PLGA materials and the degraded PLGA materials at the early stage of degradation, the approaching speed and the delta contact slope were set at 2000 nm min⁻¹ and 80%, respectively. For the degraded samples at the later stages of degradation, these values were set at 4000 nm min⁻¹ and 25% to make the surface detection procedure easier.

A linear load-controlled loading and unloading mode was used for all indentations. The indentation measurements were found to be more accurate when load-controlled loading was used compared with displacement-controlled loading. The contact load was first increased to a preset maximum load at a constant rate, kept at this load for 60 s holding time, and finally decreased to zero at the same rate as for the loading. For a shorter holding time, a nose, which described in Chapter 2, occurred in the load-displacement response upon unloading. Therefore, in all indentation tests, the holding time was fixed at 60 s to avoid the nose effect. Different maximum indentation loads and the loading and unloading rates were used, as will be described in next chapters.

A matrix of 5 x 5 indents was used (Figure 4.4 (A)) to perform a single batch of identical indentations with a distance between two indents set to be larger than 30 times the maximum indentation depth h_m in order to avoid overlaps in the elastic deformation of adjacent indents (Figure 4.4 (B)). The Poisson's ratio of 0.3 was assumed for the PLGA material as a typical value for polymers (Brandrup et al., 2003). The mechanical properties of PLGA material, specifically the elastic modulus and hardness, were determined according to the Oliver and Pharr method described in Chapter 3.

4.9 Conclusion

The samples used in this thesis, are prepared by the solvent casting and compression moulding methods. The experimental methods described in this chapter are used in the experimental studies presented in Chapters 5, 7, and 8.

4.10 Figures

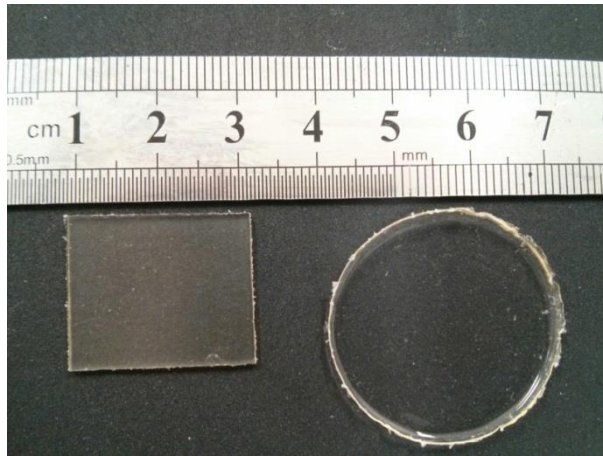


Figure 4.1: Example of undegraded PLGA samples prepared by compression moulding (left) and solvent casting (right).

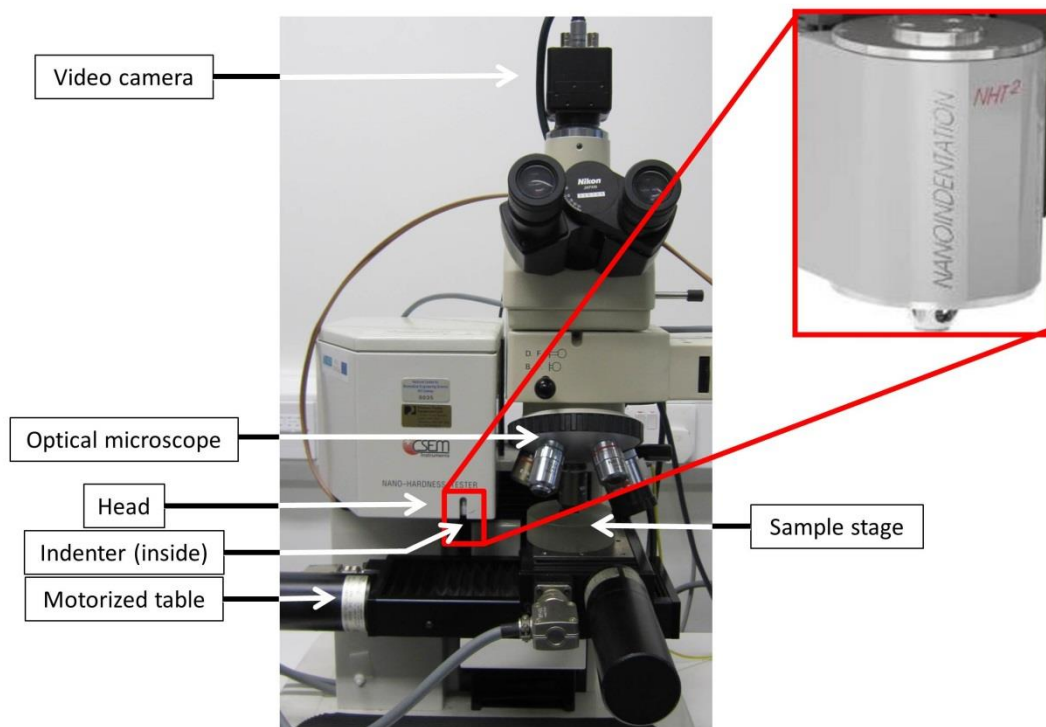


Figure 4.2: Nano hardness tester (CSM instruments SA, Switzerland) overview used in this thesis.

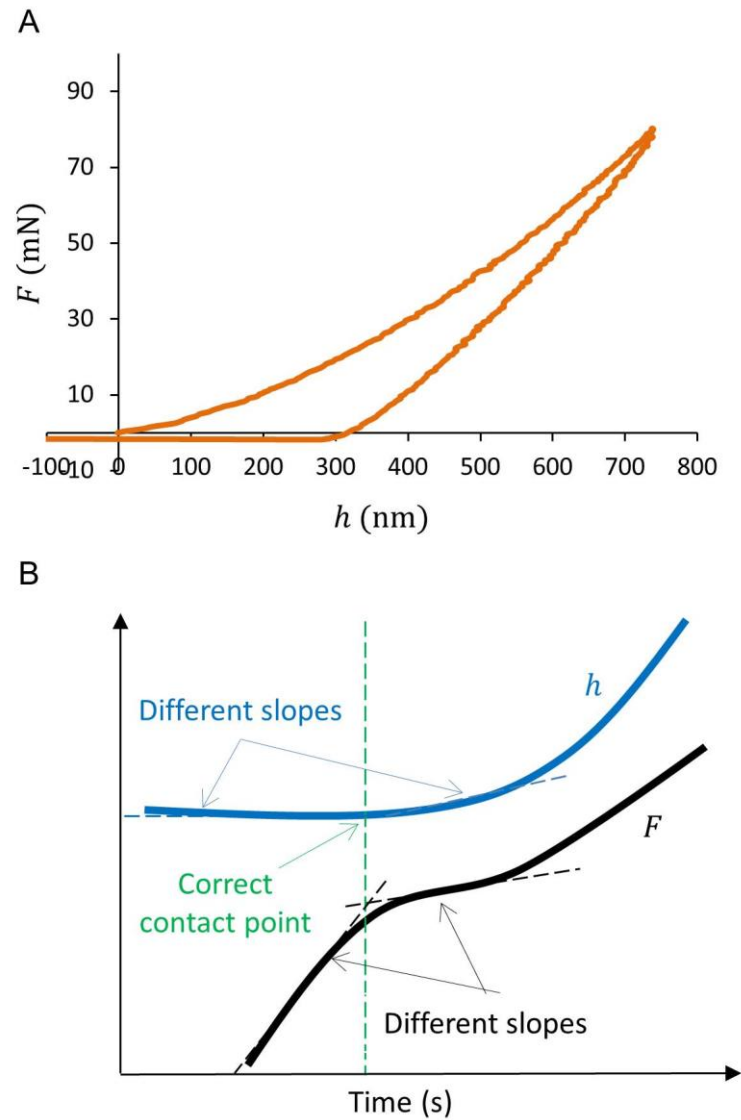


Figure 4.3: (A) An example of the load-displacement curve (F - h) obtained from nanoindentation on fused silica. The maximum load of 80 mN is applied with a holding time of 10 s between loading and unloading. The loading and unloading rates are 160 mN min^{-1} . (B) A schematic of determining a correct contact point (indicated in green) as the first point at which the applied load (F) starts to increase (indicated in black).

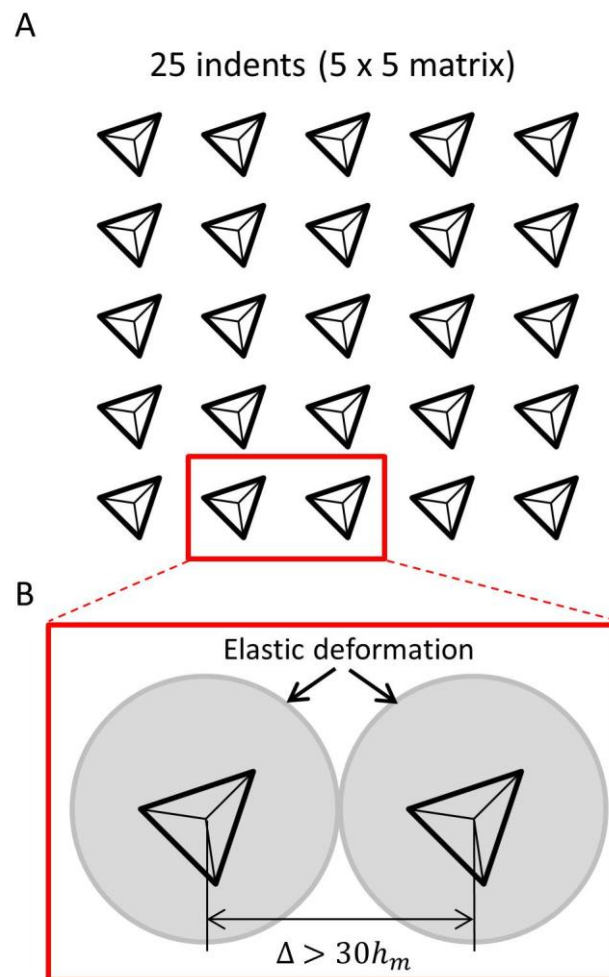


Figure 4.4: (A) A schematic of a matrix of 5 x 5 indents which is used to perform a single batch of identical indentations, and (B) an illustration of the distance between two indents to avoid an overlap in the elastic deformation of adjacent indents. This distance should be larger than 30 times the maximum indentation depth h_m .

4.11 Table

Table 4.1: The properties of the compression-moulded and solvent-cast PLGA materials used in this thesis.

Sample code	Method	Thickness (mm)	Weight (g)	ρ_s (g ml⁻¹)
SC120	Solvent casting	0.120 ± 0.002	0.16 ± 0.01	0.1
SC250	Solvent casting	0.250 ± 0.040	0.3 ± 0.05	0.2
CM1000	Compression moulding	1.082 ± 0.006	0.52 ± 0.01	none

5 Nanomechanical Properties of Solvent-cast PLGA Films During Degradation

5.1 Overview

The aim of this chapter is to evaluate the mechanical behaviour of solvent-cast PLGA film (SC250) during degradation. Hydrolysis of the films is studied under simulated physiological degradation condition (pH 7.4, 37°C). The mass loss and water uptake, surface morphology, molecular weight, and crystallinity of the films are characterised during degradation. The mechanical properties of the films are evaluated using the nanoindentation technique for different indentation loads.

The results of this chapter show that there is a significant delay between the decrease in the mechanical properties of the film and the decrease in the molecular weight. The mechanical properties of the film decrease when the number average molecular weight of the polymer chains reaches a critical molecular weight of 1500 g mol⁻¹. A sudden decline in the Young's modulus and hardness indicates that significant degradation occurs. These results provide an insight into the relationship between the changes in the mechanical properties and the degradation behaviour of PLGA material¹.

5.2 Introduction

Depending on the application, a medical implant can be subjected to a range of loads and stress conditions, which may cause mechanical failure of the material. In order for an implant to function, it must have sufficient mechanical stability.

¹ The following has been published as: Shirazi RN, Aldabbagh F, Erxleben A, Rochev Y, McHugh P. Nanomechanical properties of poly(lactic-co-glycolic acid) film during degradation. *Acta Biomaterialia* 2014; 10: 4695-4703.

Mechanical performance of biodegradable coatings in stent applications, for instance, is of significant importance when one considers coating deformation on stent expansion and mechanical loading on contact with the arterial tissue. Therefore, it is necessary to know the mechanical properties of PLGA films for understanding the performance of biodegradable coatings during degradation. Additionally, consideration of PLGA in this context presents a *model system* allowing for the study of film degradation and the effect on mechanical properties in a relatively rapid testing time frame.

Significant degradation studies have been focused on the mechanical performance of PLGA scaffolds (Agrawal et al., 2000; Cao et al., 2006; Lu et al., 2000; Wu and Ding, 2004; Wu et al., 2006b; Yang et al., 2010) and PLGA blended with some other materials (Yang et al., 2008; Zhou et al., 2012) for load bearing applications; however, the number of reported studies on the mechanical behaviour of PLGA films is limited.

In general, a wide range of mechanical testing methods are used to measure the mechanical properties of biodegradable polymers (Daniels et al., 1990; Hayman et al., 2014; Li et al., 2010b; Steele et al., 2011; Törmälä et al., 1987). As discussed before, in particular, heterogeneity due to degradation may cause inaccuracy in mechanical test, e.g. localisation of strain in a tensile test. Additionally, the low stiffness and strength of some biodegradable polymers due to degradation can lead to inaccurate test results, e.g. in a flexural test the self-weight of the specimen may be significant or in a tensile test failure may occur during gripping.

As an alternative, nanoindentation provides a powerful technique that can be used to measure the mechanical properties of biodegradable polymers (Maxwell and Tomlins, 2011; Wright-Charlesworth et al., 2005). Maxwell and Tomlins (2011) studied the changes in the mechanical properties of an injected moulded PLGA 85:15 cylindrical rod through the specimen thickness during degradation. The mechanical properties of the injected moulded PLA and self-reinforced composite

PLA plate were investigated by Wright-Charlesworth et al. (2005) using the nanoindentation technique. These studies have mainly focused on local variations in the mechanical properties during degradation; however, the degradation mechanism has not been described in detail.

Even though the nanoindentation technique has been successfully applied to estimate the elastic and elastic-plastic properties of materials, adapting this measurement technique to polymeric films remains challenging. As discussed previously in Chapter 2, time-dependent behaviour of the polymers causes a displacement at a constant maximum load and, therefore, a negative contact stiffness which causes inaccurate mechanical property measurements (Feng and Ngan, 2002; Tang et al., 2011; Yang et al., 2004; Zhou and Komvopoulos, 2006). Also, for many soft materials, adhesion between the indenter and the sample has a significant effect on the modulus determined by nanoindentation (Gupta et al., 2007; Liao et al., 2010). Adhesion is observed during indenter approach (pull-on adhesion) and indenter retraction (pull-off adhesion) resulting in a negative force in a load-displacement curve. Another issue, in case of thin film, is the effect of substrate on the measurement of the mechanical properties of the film. This is particularly important when there is a difference between the modulus of the film and the substrate, as in the case of relatively soft polymer on hard substrate. In order to avoid the effect of substrate, the indentation depth should be chosen -as a rule of thumb- to be less than 10% of the film thickness (Geng et al., 2005).

Taking all of the above into consideration, the first specific objective of this chapter is to study the *in-vitro* degradation mechanism of PLGA film. The second objective is to determine the relationship between the changes in the molecular weight and the relevant elastic modulus of PLGA material during degradation.

5.3 Material and Methods

In this chapter, SC250 material was used which was prepared by solvent casting as described in Chapter 4. Overall, 70 samples were generated: 30 samples were used

for calculating mass loss and water content; 30 samples were used for microscopy, XRD, and GPC; and 10 samples for measuring mechanical properties.

To simulate *in-vitro* degradation conditions, the materials were placed in PBS with pH 7.4, at 37°C as described in Chapter 4. The materials were removed from the PBS at each degradation time point. Three samples were used for each degradation time point to calculate the mass remaining and water content (according to Eq. (4.2)) and to determine the molecular weight. The degradation was assessed using a range of techniques described in Chapter 4 to characterise the surface morphology, molecular weight, crystallinity, and mechanical properties.

The mechanical properties of the material were measured by the nanoindentation technique using a linear load-controlled mode. Three maximum indentation loads were used: 5 mN, 7 mN, and 10 mN. The loading and unloading rates were set at 14 mN min⁻¹. The holding time was set at 60 s between loading and unloading. Figure 5.1 shows the typical trapezoidal loading function and the load-displacement response for undegraded PLGA material.

As described previously in Chapter 4, a matrix of 5 x 5 indents was used to perform a single batch of identical indentations with spacing of 50 µm to avoid overlapping the elastic field of each indent (refer to Figure 4.4). The indentation tests were performed on a reasonably homogeneous surface region to avoid the complicating influence of surface roughness in case of degraded material. Then, the average of 20 indents was used to determine the Young's modulus and hardness of the samples based on the Oliver and Pharr method (1992) described in Chapter 3.

All statistical analysis was performed by Microsoft Excel and OriginPro 8 software using one-way ANOVA with a post hoc Tukey test. A *p*-value of 0.05 was considered to be significantly different. Data were expressed as means ± standard deviation.

5.4 Results

5.4.1 Mass Loss and Water Content

Figure 5.2 shows the mass remaining and water content of the film during degradation. Diffusion of water into the film resulted in an increase in the water content from the initial days of degradation. Although water uptake was quite slow in the first 9 days, it increased significantly to $8.0 \pm 2.2\%$ after 15 days. The results showed a statistical difference between the water content at day 9 and day 15 ($p < 0.05$). At day 19, the water content was more than $12.0 \pm 0.1\%$. There was no statistical difference between the mass remaining over the first 11 days ($p > 0.05$). After 19 days of degradation, the film had lost 15% of its initial mass. During degradation, no statistical difference in pH was observed ($p > 0.05$) and the measured pH values remained within the range of 7.40 ± 0.03 (data not shown).

5.4.2 Surface Morphology

Micrographs of the surface of PLGA films at different degradation times are shown in Figure 5.3. The surfaces of the films were quite smooth before the films were placed into the medium. The root mean squared value of the surface roughness (R_{RMS}) of the undegraded PLGA films was 0.405 nm for a $2 \times 2 \mu\text{m}^2$ scan area (data not shown). Due to diffusion of water into the films, the appearance of the films changed gradually from being initially transparent to becoming opaque. After 3 days of degradation, small holes had appeared on the surface of the films. With time, the number of these holes increased and, after 11 days, the surface of the film had become quite rough. The sample surface had swollen after 15 days of degradation, resulting in a number of bumps emerging on the surface of the film. These bumps were also observed after 19 days.

In order to avoid the complicating influence of these bumps in the indentation measurements (presented below in section 5.4.5) and to achieve reproducible and reliable results, a reasonably homogeneous surface region on which to perform the indentation tests was selected for each sample. Figure 5.4 shows the relative size of

the indentation matrix and a single indentation with respect to the surface geometry of the degraded film (after 19 days) to clarify how the relatively smooth region of surface was selected.

Figure 5.5 shows the SEM micrographs of the degraded PLGA films after 3 and 19 days. It is important to note that the inside structure of the PLGA film was still intact after 3 days; however, it had become porous after 19 days of degradation.

5.4.3 Molecular Weight

Figure 5.6 (A) presents the molecular weight distributions (MWDs) for the solvent-cast PLGA film at different degradation times. The MWDs, which were normalised to peak height, were unimodal for all the films (although broader at longer times) and shifted to lower molecular weights as the degradation time increased. The lack of bimodality of peaks is indicative of the degradation near to the chain ends and the release of small molecular weight fragments rather than the cleavage of larger fragments. To clarify the difference in shape, the MWDs at day 11 and day 19 are shown in blue and red, respectively. The grey square shows the area with a number average molecular weight of more than $11,000 \text{ g mol}^{-1}$. Figure 5.6 (B) shows the total number of polymer chains with a number average molecular weight of more than $11,000 \text{ g mol}^{-1}$ which was calculated for each degradation time point by integrating the distribution curve in Figure 5.6 (A) in the grey area. The percentage of polymer chains with the number average molecular weight more than $11,000 \text{ g mol}^{-1}$ decreased from 92% at day 9 to 65% at day 11. After 19 days, only 10% of the molecular weight of all the polymer chains was greater than $11,000 \text{ g mol}^{-1}$.

The changes in the number average molecular weight and polydispersity index (PDI) (M_w/M_n) of the solvent-cast PLGA film during degradation are shown in Figure 5.7. The number average molecular weight of the films decreased almost linearly from $82,000 \text{ g mol}^{-1}$ to $11,000 \text{ g mol}^{-1}$ over the first 11 days and, after 19 days, it had decreased to less than $2,000 \text{ g mol}^{-1}$. The PDI of the undegraded material was 2.1. There was no statistical change in the PDI of the film over the first 9 days of

degradation ($p > 0.05$). After 11 days the PDI increased and reached 4.7 at day 19. As shown in Figure 5.6, the molecular weight distribution was relatively narrow until day 9. The increase in PDI was indicated by a broader molecular weight distribution after 11 days, which was expected due to a statistically greater difference between the polymer chains of lower molecular weight.

5.4.4 Crystallinity

Figure 5.8 shows the XRD patterns of the undegraded solvent-cast PLGA film and the film degraded for 19 days. This typical broad halo pattern with few maxima confirms that all films remained amorphous and no crystallinity was observed during degradation.

5.4.5 Mechanical Properties

Figure 5.9 shows the Young's modulus and hardness of the solvent-cast PLGA film during degradation for different maximum indentation loads. These results were obtained for the films in the wet condition. The Young's modulus and hardness of the films in the dry condition were larger than those in wet condition. These results are shown in Appendix C for comparison purposes.

As shown in Figure 5.9 (A), measurements of modulus using nanoindentation tended to increase with decreasing load. The differences between the elastic modulus for different loads appeared for both undegraded and degraded films. For undegraded film, maximum loads of 5 mN, 7 mN, and 10 mN resulted in 1017.8 ± 13.5 nm, 1256.6 ± 38.2 nm, and 1655.0 ± 22.7 nm indentation depths, respectively. These indentation depths implied indenter penetrations of less than 1% of the film thickness, indicating reliable elastic property measurements.

The Young's modulus value from a conventional tensile test for undegraded film (3.5 ± 0.2 GPa) was found to agree with the value obtained from nanoindentation for 7 mN indentation load (3.8 ± 0.1 GPa); consequently, attention was focused in particular on the values of Young's modulus for 7 mN indentation load during degradation. In the initial days of degradation, the change in the Young's modulus

was negligible until day 15 ($p > 0.05$). The Young's modulus decreased to 3.1 ± 0.4 GPa after 17 days, followed by a significant drop at day 19 to 0.30 ± 0.05 GPa. A significant statistical difference existed between the Young's modulus of the film at day 17 and day 19 ($p < 0.05$). The different maximum loads resulted in essentially the same trend during the degradation.

The hardness of the undegraded solvent-cast PLGA film was 157.9 ± 14.3 MPa for the maximum indentation load of 7 mN (Figure 5.9 (B)). The values of hardness were almost similar for different indentation loads and no statistical difference was observed ($p > 0.05$). This trend also existed for degraded films until day 5. After 5 days, the surface hardness showed different values for different indentation loads at each time point. Another important observation was the reduction in surface hardness after the films were put into the medium. This trend was also observed until day 9. After 9 days, significant fluctuation in hardness values appeared. The value of hardness decreased significantly and reached less than 15.1 ± 4.1 MPa after 19 days.

5.5 Discussion

This study presents, for the first time, a thorough investigation of the mechanical properties of the solvent-cast PLGA film using nanoindentation. The PLGA film was subjected to degradation in phosphate-buffered saline solution at 37°C. During degradation, the surface microstructure of the film gradually changed. Initially, the PLGA film had a transparent appearance and a smooth surface, whereas, with time, some small holes were observed on the film surface and the film became whitish and quite rough. The change in the surface microstructure of the film suggests a heterogeneous surface degradation.

The bulk degradation of PLGA film has been reported by a number of authors (Lu et al., 1999; Pamula and Menaszek, 2008; Vey et al., 2012; Vey et al., 2008). These studies concluded that the degradation is faster in the centre of the film than at the surface due to the increased concentration of acidic degradation products inside.

The change in the pH of the aqueous medium provides information on the release of acidic products from the bulk of the film into the environment. A rapid increase in the acidity of the medium solution can suggest that degradation is faster in the bulk rather than at the surface (Vey et al., 2008). In the present case, a very small change in pH was observed during the degradation study. This small change could well have been due to the high solution-to-specimen mass ratio of 100:1 which was used in order to ensure stable aging conditions (ASTM:F1635-11, 2011). At a lower ratio a larger change in pH may have been observed (Vey et al., 2008). Therefore, in the present case, the absence of observable change in pH does not support any conclusion regarding the bulk degradation. However, SEM microscopy of the PLGA film clearly showed the development of significant porosity throughout the film thickness after 19 days, which shows that the degradation is faster in the centre than at the surface. This is clearly indicative of heterogeneous bulk degradation of the film.

Diffusion of water caused a scission of polymer chains near to the chain ends and, as a result, the molecular weight reduced during the initial days of degradation; however, there was no noticeable change in PDI until day 9. The almost linear decrease in the number average molecular weight over the first 11 days indicates an insignificant reshuffling of the chain length distribution during degradation, as occurs under appropriate conditions in typical step-growth condensation polymerizations (Flory, 1942). Even though the molecular weight dropped at a significant rate initially, up to day 11 the mass loss was negligible, meaning that the degradation products were essentially trapped inside the film. The small change in the mass of the film in the initial days of degradation also suggests that the surface degradation occurred more slowly than the bulk. At day 11, the number average molecular weight of the polymer chains was $11,000 \text{ g mol}^{-1}$; beyond this, both the mass loss and the PDI increased, indicating that a significant number of molecules had been produced that were small enough to diffuse out of the film matrix into the medium. Similar results were found by Vey et al. (2008) for PLGA 50:50 film cast

onto a glass Petri dish with a smaller diameter (13 mm) but similar thickness (0.25 mm) to that in the present study. As expected the degradation rate was similar in the two studies due to the same thickness of the films.

After 11 days, the reduction in molecular weight of the film slowed down significantly; however, the modulus was still relatively constant by day 17. After 17 days, the elasticity of the film decreased and, at day 19, the modulus suddenly dropped to about 13% of the initial value for undegraded film, indicating that considerable degradation had occurred. Beyond that, it was too difficult to measure the mechanical properties of the film due to the degradation. At this stage, the number average molecular weight of the polymer chains reached 1500 g mol^{-1} and the polymer mass had reduced to 15%.

This study has highlighted that the Young's modulus reduction for PLGA material lagged significantly behind the reduction in the average molecular weight. This result is in agreement with the previous experimental observations for other biodegradable polymers. It has been shown that the mechanical strength decreases after the molecular weight reduces (Saha and Tsuji, 2006; Tsuji, 2000, 2002; Tsuji and Ikada, 2000; Tsuji et al., 2000; Weir et al., 2004a; Weir et al., 2004c; Wu and Ding, 2004). However, the result presented in this study are in marked contrast to those reported by Maxwell and Tomlins (2011) for an injection moulded PLGA 85:15 cylindrical rod with 8 mm diameter. They showed that the Young's modulus of the PLGA rod decreased during the initial days of degradation and the lagging behaviour was not observed in their study. This difference may relate to the different sample sizes or sample preparation methods. Several studies have investigated the effect of sample size and shape on the degradation behaviour of PLGA (Grizzi et al., 1995; Lu et al., 1999; Pamula and Menaszek, 2008; Witt and Kissel, 2001). Witt and Kissel (2001) investigated the degradation of PLGA film, tablet, rod, and microsphere. They reported different degradation rates for different sample shapes. In another study, Lu et al. (1999) demonstrated a significant effect of PLGA film thickness on mass loss and molecular weight;

increasing the film thickness from 10 to 100 μm accelerated the mass loss and decrease in the molecular weight.

The question arises here as to why the modulus of the film did not decline when the molecular weight reached $11,000 \text{ g mol}^{-1}$. In other words, why did the sudden drop in the Young's modulus occur after 19 days, whereas it was expected to have dropped after 11 days, when very short polymer chains were formed in significant numbers (refer to Figure 5.6 (B))? The observed effect may be due to the remaining polymer chains inside the film matrix being long enough to support the mechanical stability of the film beyond 11 days. The low value of Young's modulus at day 19 is consistent with the low percentage (10%) of polymer chains remaining with a molecular weight of more than $11,000 \text{ g mol}^{-1}$; however, the number of polymer chains above the molecular weight of $11,000 \text{ g mol}^{-1}$ at day 11 was approximately 65%.

For amorphous polymers, Wang et al. (2010) proposed an entropy spring model, which was introduced in Chapter 3, to explain the lagging behaviour and the relationship between the Young's modulus and the average molecular weight. They proposed that the long polymer chains are constrained by their surrounding chains; hence, the entropy elasticity of an amorphous polymer is not affected by isolated chain scissions of very long chains until a certain number of polymer chains are removed from the polymer. This phenomenon can account for the lagging behaviour in the present study, as all the initially amorphous films remained amorphous during the degradation.

In the present study, it was found that the measured Young's modulus value was different for three different indentation loads. The value of modulus tended to increase with decreasing applied load (Figure 5.9 (A)). In other words, as load increased, so did the indentation depth, resulting in lower modulus. As indicated in Chapter 2 (section 2.3.4.6), several studies of nanoindentation of polymer surfaces have indicated the depth dependence of the indentation modulus. A variety of

explanations for this phenomenon have been reported. A possible explanation is the adhesion between the tip and the sample which can lead to a significant variation of elastic modulus at different maximum loads (Dokukin and Sokolov, 2012; Gupta et al., 2007; Liao et al., 2010; Xu et al., 2011). In investigations where the adhesion is significant, the indenter tip is typically spherical. In the present study, however, a Berkovich tip was used and the load-displacement curve did not show the initial negative pull-on adhesion force that is typical of the effect. Also, any curves showing a negative pull-off adhesion force were removed from the measurements. Therefore, in this study, the effect of adhesion on the modulus measurements is negligible and adhesion is not the reason for the present observations.

Another possible explanation is based on the formation of a specific interfacial region between the indenter and the polymer surface during indentation which causes a reduction of molecular mobility at the surface resulting in a stiffer surface than the bulk (Tweedie et al., 2007; Xu et al., 2011). Additionally, a previous study has reported that a surface skin effect, due to the exposure of polymer surface to light and air before experiments, was initially considered as an explanation of the depth dependence of the indentation modulus (Briscoe et al., 1998). The surface dynamics of polymers tends toward lower energy. It has been shown that molecules closer to the polymer-air interface relax more quickly than molecules farther from the interface (Schwab et al., 2000; Wallace et al., 2001), which has a tendency to lower the glass transition temperature (T_g) at the surface relative to the bulk. This phenomenon, even if it were to exist in PLGA material, would be likely to have only a small influence on the mechanical properties as measured in the present case, whereas the indentation tests were performed at room temperature (21°C), i.e., well below the T_g of the PLGA film (38°C).

A potentially more likely explanation is based on the time-dependent behaviour of the polymers. Due to the time-dependent material properties, the unloading curve and, therefore, the contact stiffness depend on the unloading rate (Jakes et al.,

2012; Yang et al., 2004). As described in Chapter 3, the contact stiffness is determined by fitting the power law equation to the unloading curve and evaluating the derivative of this equation at the maximum load. For polymers with significant time-dependent properties, the transition between plastic to elastic deformation from very high to very low indentation loads affects the unloading curve (Oyen, 2007; Yang et al., 2004) resulting in a variable power law exponent and consequently modulus values that are high relative to the bulk measurements (Charitidis, 2010).

In the present study, the changes in the plastic deformation of the PLGA film were determined by measuring the apparent hardness. Consistency of hardness measurement for undegraded film over the three different loads indicates that the calculated hardness is not affected by the mechanical properties of the substrate. This is consistent with the indenter penetration having been much less than 10% of the coating thickness. As a result of the load consistency, the hardness measured in this condition can be considered to be not due to an elastic but to a fully developed plastic zone (Fischer-Cripps, 2006).

The observed reduction in the surface hardness of the film and the increase in water uptake in the initial days of degradation suggest that water acts as a plasticiser which results in reducing the yield strength of the film, i.e. the point at which plastic deformation begins to happen. In contrast, the results for Young's modulus do not appear to show a similar influence of the medium. Using microscopy, Vey et al. (2008) proposed that the degradation of PLGA film resulted in the formation of soft layer at the surface due to water penetration. The present results with regard to hardness changes would appear to support this, at least in terms of material changes close to the surface where the polymer has been plasticised; however, this effect was not observed in relation to changes in the elastic behaviour of the film; hence, the present observation is inconsistent with those published by Vey et al. in terms of defining the soft layer as applying to

plasticity only. However it is not clear how thick such a plasticising layer is; it could be a bulk plasticising effect or just a thin layer.

After 5 days, due to the diffusion of water into the film some small holes appeared on the surface layer, resulting in an increasingly rough surface. The inconsistency of the measured hardness after 5 days for three indentation loads may be ascribed to the surface roughness of the film or to the variation of the material properties through the depth due to the degradation (Wrucke et al., 2013). The optical microscopy results at day 11 showed a quite rough surface, which supports the fluctuation observed in the hardness. The large standard deviation obtained for the measured surface hardness also confirms that there is a significant variation in surface roughness. Due to the significant degradation of the film, the surface hardness dramatically decreased after 19 days and reduced to 16% of the initial value for undegraded film.

5.6 Conclusion

The *in-vitro* degradation behaviour and the changes in the mechanical properties of solvent-cast PLGA film were evaluated. The molecular weight of the film decreases from the initial days of degradation as a result of hydrolytic cleavage of the polymer chains due to the diffusion of water molecules. The morphology of the film surface changes during degradation and some small bumps appear on the surface, resulting in an increase in surface roughness and therefore the surface hardness of the film. After 11 days, due to the decrease in the polymer mass, a large amount of low molecular weight fragments diffuse out of the polymer matrix. At this stage, the rate of molecular weight reduction is very slow.

After 19 days, the number average molecular weight of the polymer chains reaches a critical molecular weight of 1500 g mol^{-1} and a significant reduction in the total number of polymer chains occurs which causes a sudden drop in elastic modulus and hardness, and consequently significant bulk degradation occurs.

The results of this chapter are used later in Chapter 6 for calibrating the computational modelling framework which predicts the degradation rate and the changes in the elastic modulus of PLGA material.

5.7 Figures

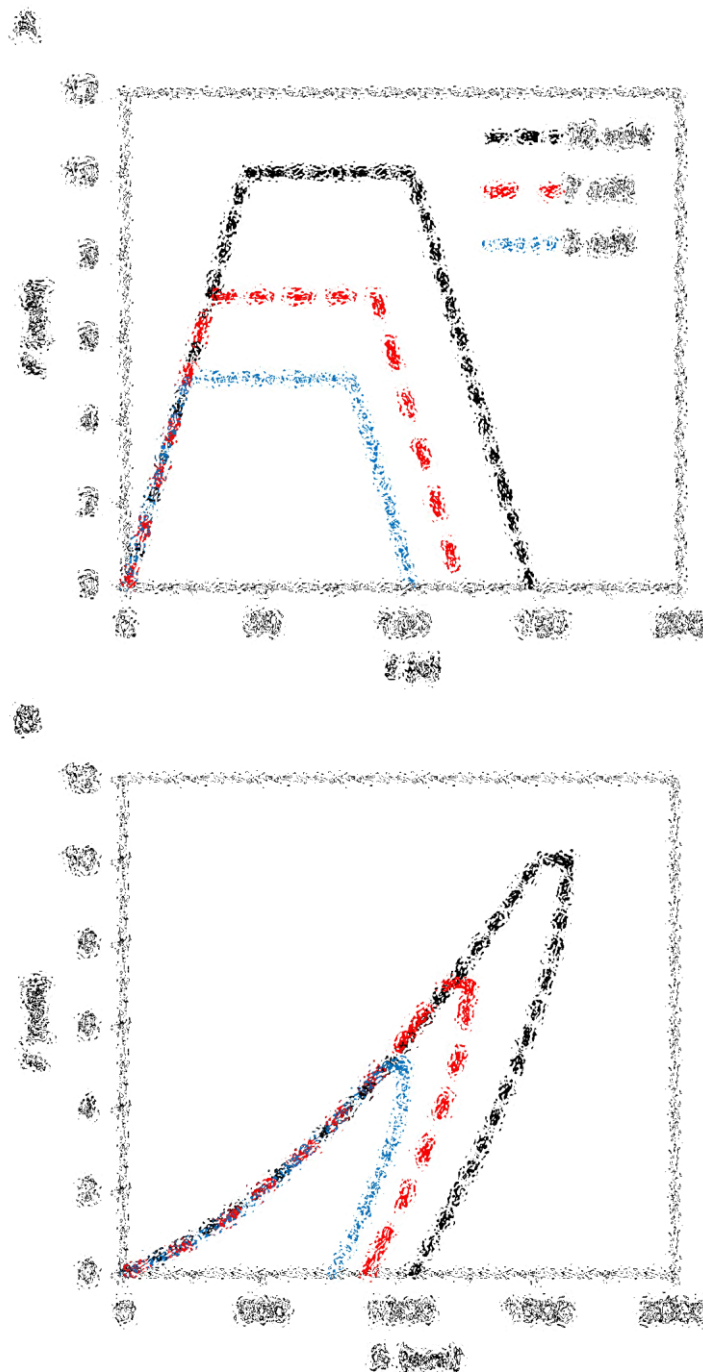


Figure 5.1: (A) Typical load-time ($F-t$) and (B) corresponding load-displacement responses ($F-h$) for a range of maximum load F_{max} values for the undegraded solvent-cast PLGA film. The unloading (loading) rate is 14 mN min^{-1} and the holding time is 60 s. **Figure blurred due to copyright restrictions.**

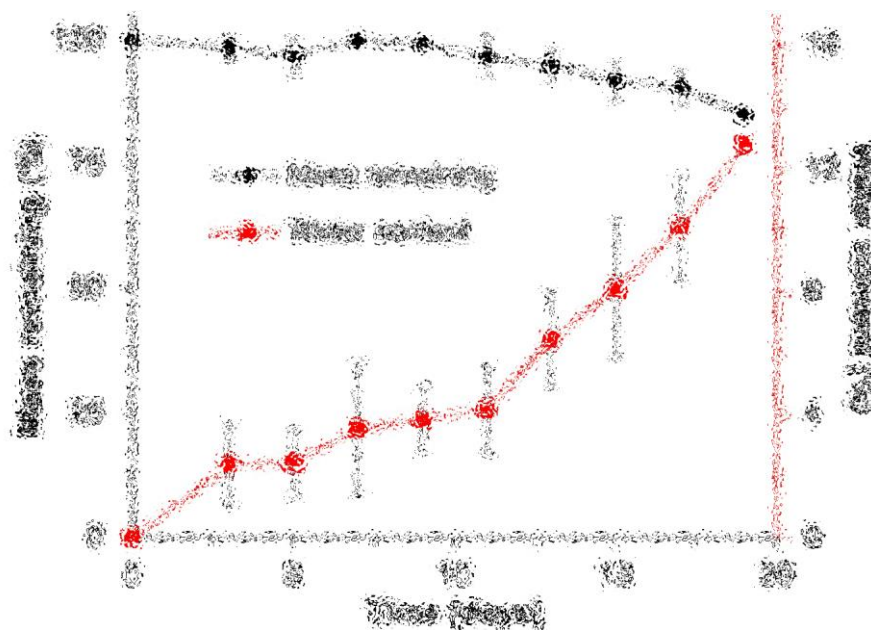


Figure 5.2: Changes in the mass remaining and water content of the solvent-cast PLGA film during degradation (mean \pm SD; n = 3). **Figure blurred due to copyright restrictions.**

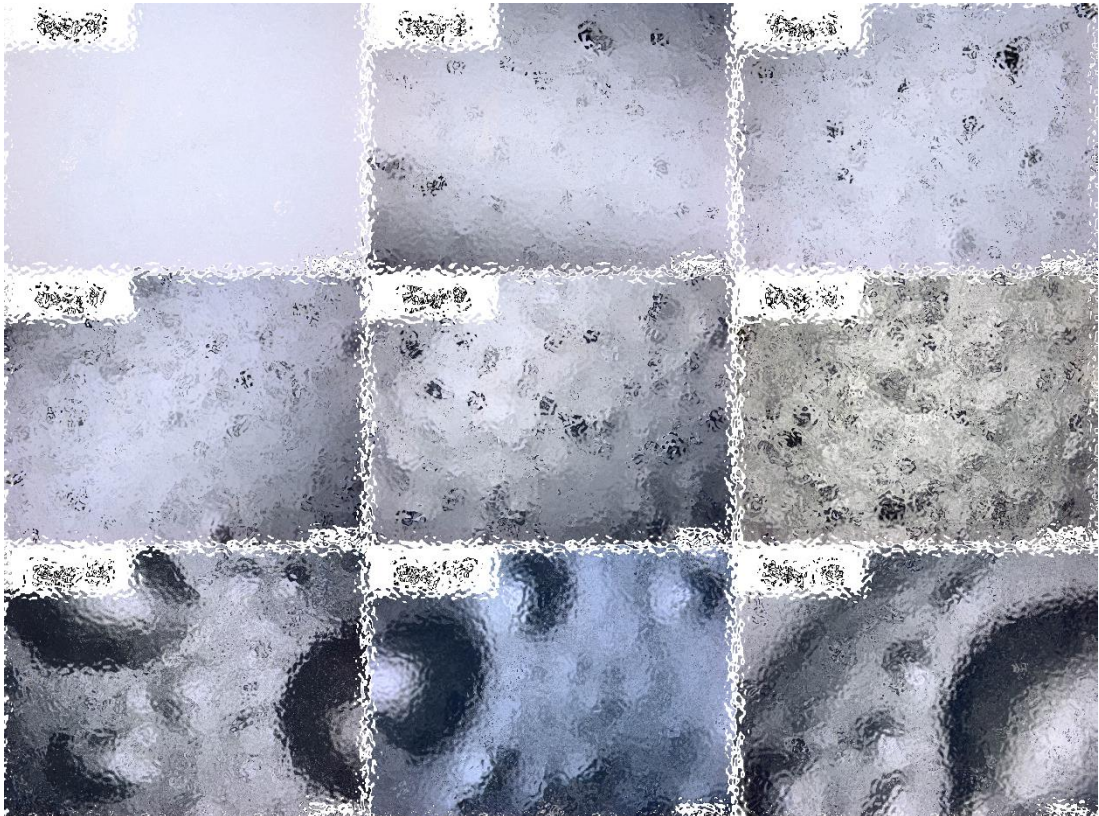


Figure 5.3: Micrographs of the surfaces of the solvent-cast PLGA film at different degradation times. The scale bars represent 500 μm . **Figure blurred due to copyright restrictions.**

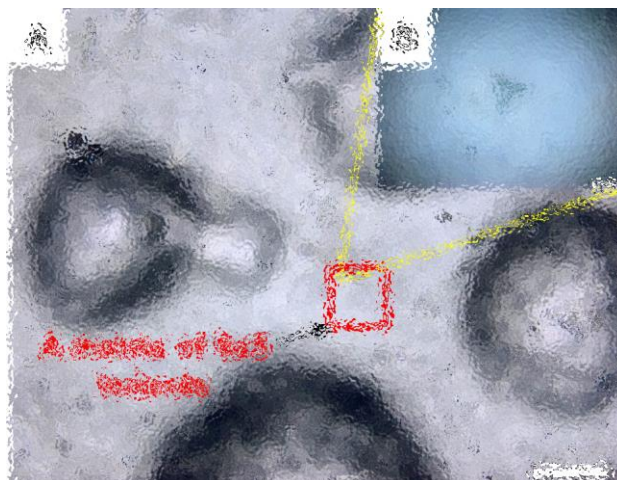


Figure 5.4: (A) Micrograph for a typical size-scale and location for a matrix of 5 x 5 indents on the PLGA film degraded after 19 days. The red box highlights the size of the indentation matrix. The scale bar represents 500 μm . (B) The zoomed-in area within the indentation matrix for a single indent. The scale bar represents 20 μm . **Figure blurred due to copyright restrictions.**

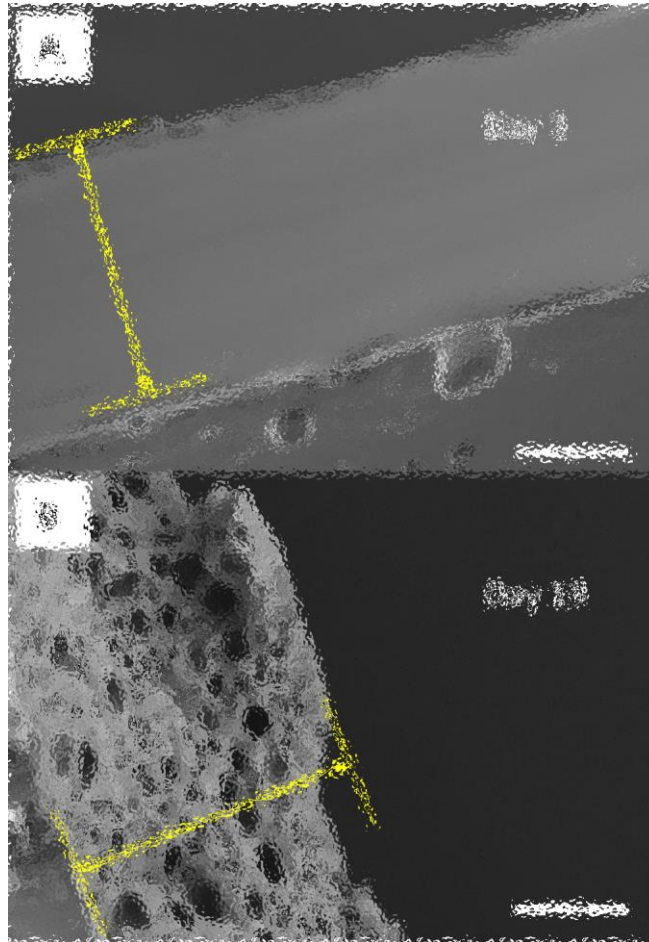


Figure 5.5: SEM images of the solvent-cast PLGA film degraded after (A) 3 days and, (B) 19 days. The yellow arrows show the cross section of the films. The scale bars represent 50 μm . **Figure blurred due to copyright restrictions.**

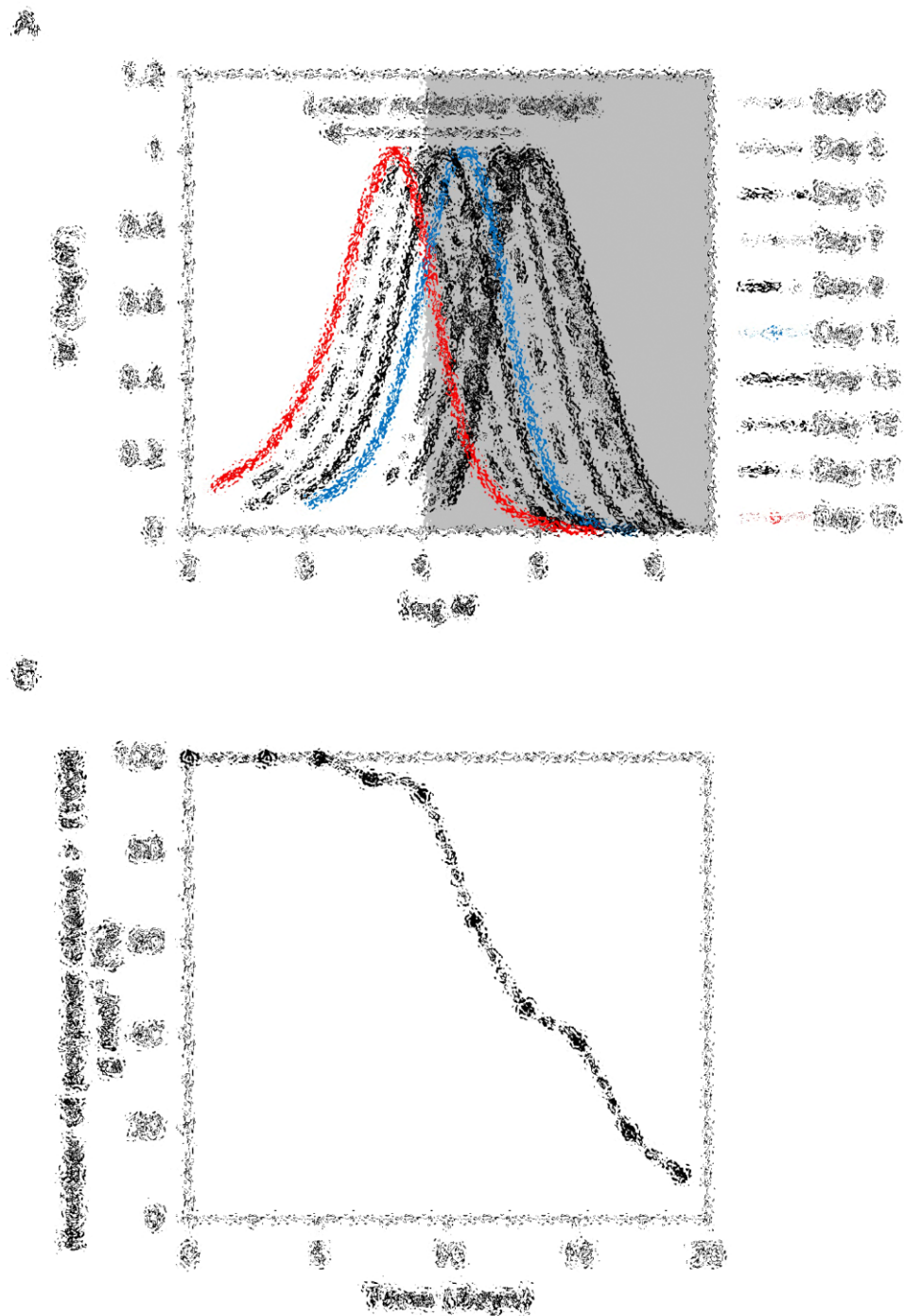


Figure 5.6: (A) GPC molecular weight distributions (MWDs) of solvent-cast PLGA film at different degradation times. The MWDs shift to the left as the degradation time increase. Each curve is the average of three samples. (B) The percentage of polymer chains with a number average molecular weight of more than 11,000 g mol⁻¹ at different degradation times. **Figure blurred due to copyright restrictions.**

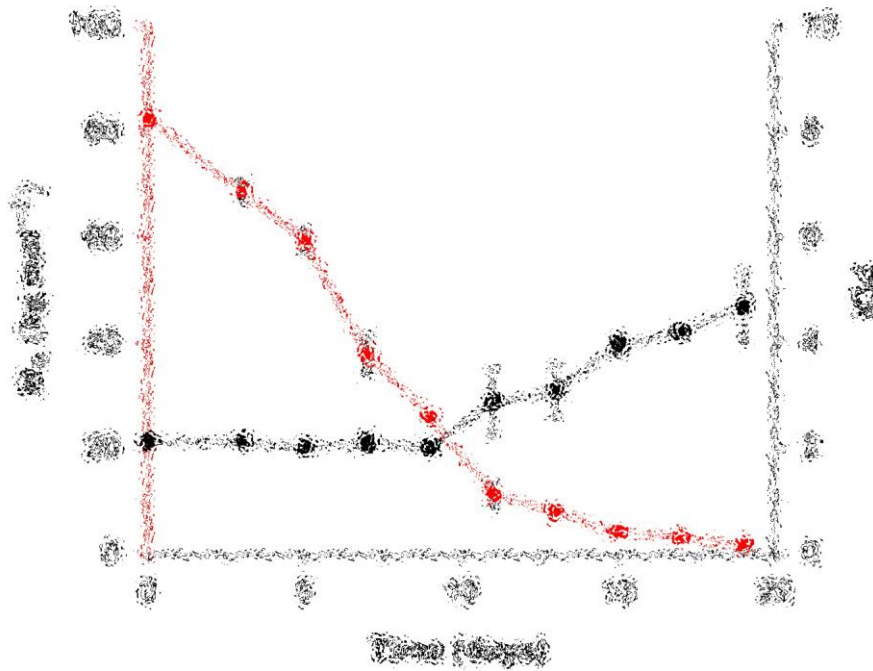


Figure 5.7: Changes in the number average molecular weight (M_n) and polydispersity index (PDI) of the solvent-cast PLGA film during degradation (mean \pm SD; n = 3). **Figure blurred due to copyright restrictions.**

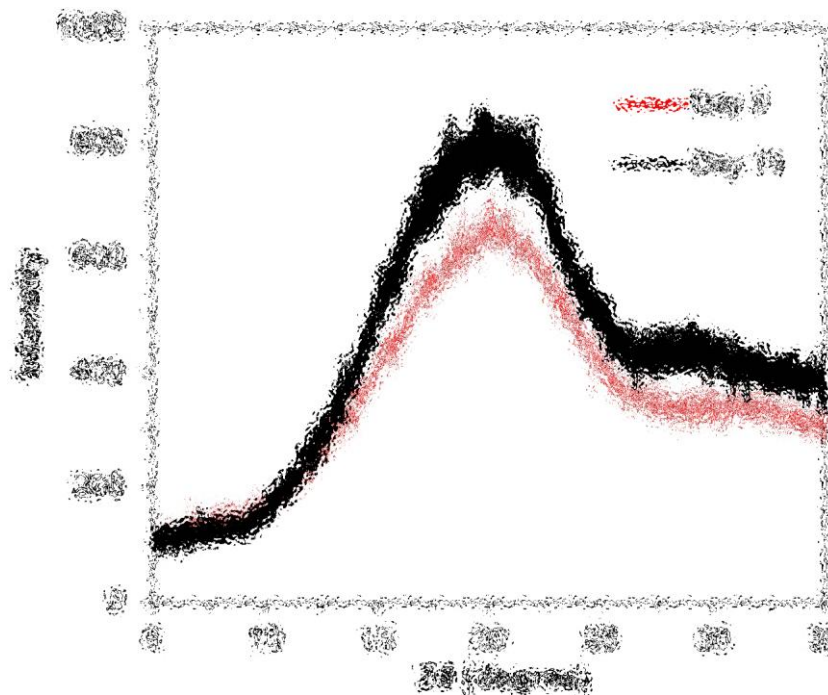


Figure 5.8: X-ray diffraction patterns for the undegraded solvent-cast PLGA film and the PLGA film degraded after 19 days. **Figure blurred due to copyright restrictions.**

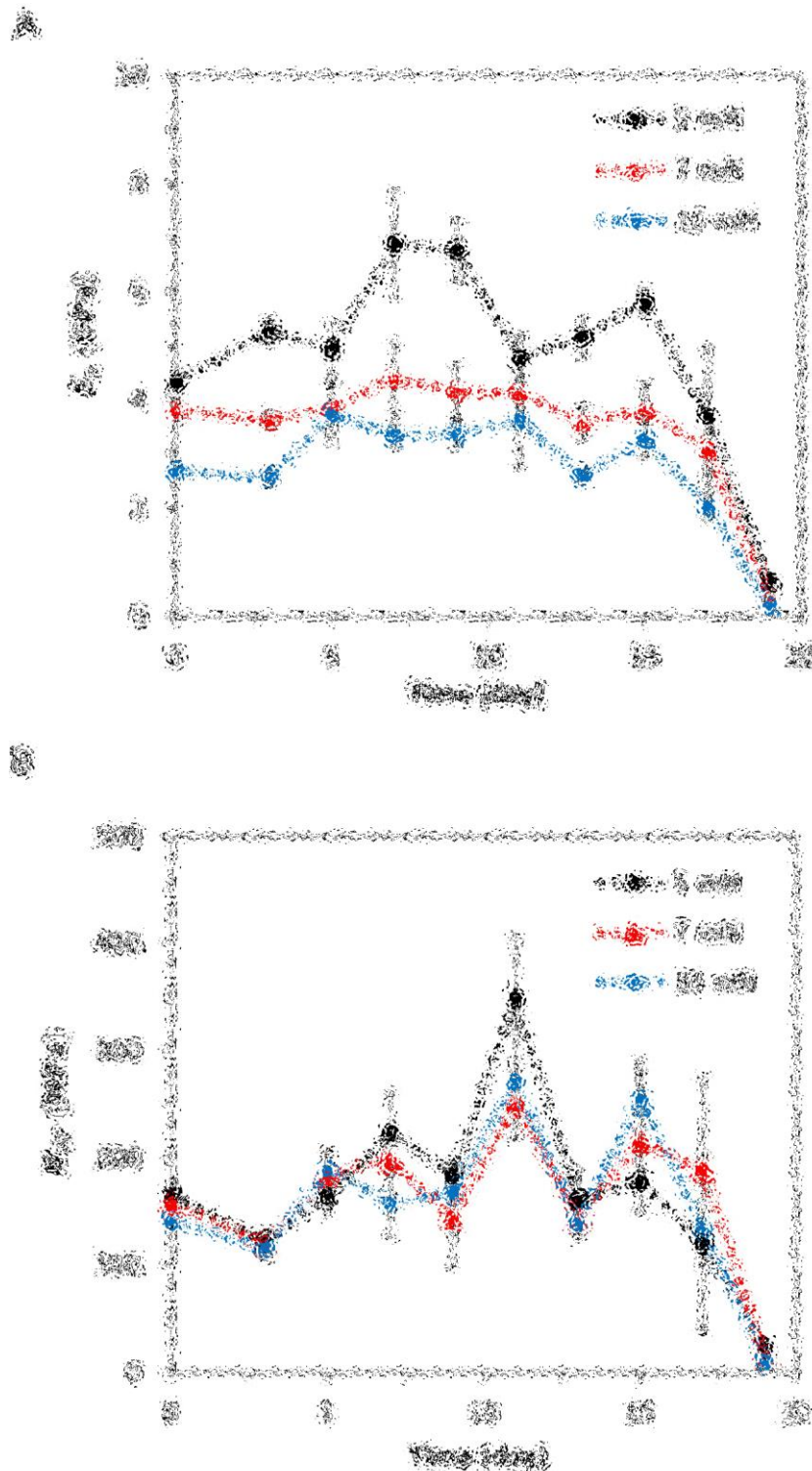


Figure 5.9: Changes in the (A) Young's modulus (E_s) and, (B) hardness (H_{IT}) of the solvent-cast PLGA film during degradation for the maximum load F_{max} of 5 mN, 7 mN, and 10 mN (mean \pm SD; $n = 20$). **Figure blurred due to copyright restrictions.**

6 Modelling the Degradation and Elastic Properties of PLGA Films and Regular Open-cell Tissue Engineering Scaffolds

6.1 Overview

This chapter presents a computational investigation of the molecular weight degradation and the mechanical performance of PLGA films and tissue engineering scaffolds. The coupled computational modelling framework, described in section 3.3.4 is used here to predict the degradation behaviour using the reaction-diffusion model based molecular weight, described in section 3.2.3, and the mechanical performance using the molecular network based mechanical properties model, described in section 3.3.3. The finite element prediction of the degradation behaviour is compared to a semi-analytical solution generated in MATLAB for a one-dimensional problem. The model parameters are determined based on the experimental data for the *in-vitro* degradation of the PLGA film presented in Chapter 5. The reduction in the molecular weight of the PLGA material during degradation is used to calibrate the molecular weight model. The experimentally observed critical molecular weight presented in Chapter 5 is used to calibrate the mechanical properties model. Microstructural models of three different scaffold architectures are used to investigate the degradation and mechanical behaviour of each scaffold.

The methods presented here show that changes in the molecular weight of PLGA material can be captured using both semi-analytical and numerical solutions; however, the semi-analytical solution does not determine differences in degradation rates for films of thickness 25 μm or above. The results show that

although the architecture of the scaffold does not have a significant influence on the degradation rate, it determines the initial stiffness of the scaffold. It is revealed that the size of the scaffold strut controls the degradation rate and the mechanical collapse. A critical length scale due to competition between diffusion of degradation products and autocatalytic degradation is determined to be in the range 2-100 μm . Below this range, slower homogenous degradation occurs; however, for larger samples monomers are trapped inside the sample and faster autocatalytic degradation occurs¹.

6.2 Introduction

It is well known that scaffolding plays a critical role in tissue engineering. Biodegradable polymers have been used widely to provide a three-dimensional structure that facilitates tissue regeneration (Harada et al., 2014; Ren et al., 2005; Uematsu et al., 2005). As mentioned before, the degradation process of biodegradable polyesters such as PLGA is based on a hydrolytic reaction. Diffusion of water causes hydrolysis of the ester bonds in the polymer chains, leading to the generation of water soluble oligomers. Consequently, the molecular weight of the polymer decreases. The degradation products diffuse into the surrounding medium, which results in a mass loss for the polymer (Pamula and Menaszek, 2008; Vey et al., 2012).

Diffusion of the degradation products may occur more slowly in a large-sized sample due to the greater diffusion length (Dunne et al., 2000; Grayson et al., 2005; Grizzi et al., 1995; Lu et al., 1999; Witt and Kissel, 2001). This leads to accumulation of degradation products inside the polymer matrix, which are able to catalyze hydrolysis of the other ester bonds and consequently accelerates the degradation process. Due to the autocatalytic effect, the large PLGA samples undergo

¹ A part of the following has been published as: Shirazi RN, Ronan W, Rochev Y, McHugh P. Modelling the degradation and elastic properties of poly(lactic-co-glycolic acid) films and regular open-cell tissue engineering scaffolds. *Journal of the Mechanical Behavior of Biomedical Materials* 2016; 54:48-59.

heterogeneous degradation with a degradation rate which is greater at the centre than at the surface.

It has been reported that fast degradation negatively affects cell viability and cell migration into the scaffold due to the acidic effect of the degradation products (Sung et al., 2004). Also, fast degradation may cause failure of the scaffold to occur before the tissue formation. Therefore, an appropriate degradation rate is required to be consistent with the rate of tissue formation and the replacement of the scaffold with the desired tissue type. A successful scaffold must provide sufficient mechanical stability during degradation. Despite the fact that the degradation of PLGA polymers results in a quick decrease in the polymer molecular weight, the Young's modulus does not decrease until the molecular weight of the polymer chains reaches a critical molecular weight as shown in Chapter 5. During this period, the scaffold retains its mechanical function, supporting the tissue during regeneration. Therefore, it is necessary to determine the mechanical properties and the degradation rate of the degradable scaffolds.

Towards this, computational modelling offers an efficient framework to understand the behaviour of biodegradable implants. Many models have been proposed to describe the degradation of biodegradable polymers (Sackett and Narasimhan, 2011) including PLGA (Ford Versypt et al., 2013). As introduced in Chapter 2, reaction-diffusion models have been applied to a range of aliphatic polyesters. Among these models, the ones which account for the autocatalytic effect are the most comprehensive, as autocatalysis plays a strong role in the degradation mechanism (Chen et al., 2011; Ford Versypt et al., 2013; Wang et al., 2008).

A number of models have been presented to predict the mechanical properties of biodegradable polymers (Hayman et al., 2014; Soares et al., 2010; Vieira et al., 2014; Vieira et al., 2011; Wang et al., 2010). A model was developed by Vieira et al. (2014) based on the relationship between fracture strength and molecular weight for thermoplastic polymers to predict the mechanical properties of PLA-PCL fibres

during degradation. Since this model is based on an empirical equation, the model parameters must be determined experimentally for each material and during degradation. Also, in this model, the hydrolytic degradation rate is assumed constant, which is a significant simplification for highly heterogeneous degradation as autocatalysis has a significant effect on degradation. The model of Soares et al. (2010) relates the degradation rate to mechanical deformation in order to determine the mechanical properties of PLLA fibres loaded under uniaxial extension. The degradation behaviour is determined from a thermodynamic analysis of the degradation process and as degradation proceeds the material loses its ability to store energy.

As introduced previously in Chapter 3, Wang et al. (2010) proposed a model for amorphous biodegradable polymers, based on the relationship between the Young's modulus and the number of polymer chains. This model is physically motivated by the hydrolytic random scission of the polymer chains. The model assumes that the number of polymer chains with a molecular weight above a critical molecular weight determines the Young's modulus as chain scissions occur. This model successfully predicted the experimentally observed degradation of PLLA films.

In this chapter, the developed coupled computational framework described in Chapter 3, which includes the molecular weight model and the mechanical properties model, is used to predict the degradation and the changes in the mechanical properties of biodegradable polymers and, in particular, PLGA. The first objective of this study is to calibrate the models based on the experimental data for the *in-vitro* degradation of the PLGA film presented in Chapter 5. The second objective is to use the modelling framework to predict the molecular weight and the reduction in the Young's modulus of PLGA films with different thicknesses and also of a range of PLGA tissue engineering scaffolds. The effects of strut size and architecture of the scaffolds on the degradation rate and mechanical performance are investigated.

6.3 Methods

6.3.1 Model Implementation

The changes in the molecular weight distribution during degradation were predicted using the phenomenological degradation model of Wang et al. (2008) described in section 3.2.3. The monomer concentration C_m and the ester bond concentration C_e were obtained for the semi-analytical and numerical solutions. The degradation of the polymer was then determined by the number average molecular weight of the polymer as described previously.

The relationship between the Young's modulus and the molecular weight distribution was determined using the mechanical properties model described in section 3.3.3. In this model, an initial distribution of the polymer molecular weight was obtained from the experimental GPC curve for the PLGA film presented in Chapter 5. The total number of polymer chains N_{chains} was chosen and then the lengths of these chains were determined such that the molecular weight of the chains in the simulation matched the experimental GPC data. The sensitivity of the model to the initial conditions, including the critical molecular weight M_n^{crit} , the ratio of random scissions to end scissions $R_{scissions}$, and the total number of polymer chains N_{chains} was assessed.

The coupled computational framework described in section 3.3.4 was used in a one-dimensional model for PLGA films and in a three-dimensional model for PLGA scaffolds using the molecular weight and the mechanical properties models. Figure 6.1 shows a flowchart of the coupled computational modelling framework used for the prediction of both degradation behaviour and mechanical performance of PLGA structures, and applied in this study to the degradation of PLGA films with different thicknesses and of PLGA tissue engineering scaffolds.

6.3.2 PLGA Film

The degradation of PLGA films was represented with a one-dimensional model as the diffusion of degradation products occurs only in the direction normal to the free surface. As described previously in Chapter 3, contact on the outside of the film with the aqueous medium was represented by assuming the concentration of monomers at the boundary of the film is zero (Figure 6.2 (A)), which means that all the monomers which reached the surface are immediately convected away from the surface by the environmental flow. The flux of monomers at all other boundaries, including the interface between the film and the substrate, was set to zero. A simple mesh of hexahedral elements was used through the film thickness, and thinner boundary layer elements were used at the surface where higher gradients in the solution variables occur (Figure 6.2 (B)).

6.3.3 PLGA Scaffold

In the second part of the study, microstructural models of three different scaffold architectures were used, based on those used in the literature (Bucklen et al., 2008; Luxner et al., 2005; Wettergreen et al., 2005). Unit cells for different architectures were generated for each scaffold, as shown in Figure 6.3. The porosity of each scaffold was kept at 63.5% by keeping the ratio of strut dimensions to unit cell size constant as the strut size was varied. Due to the symmetry of the scaffold geometry, only one-eighth of the unit cell was needed to generate the representative volume element (RVE) in each case, as shown in green in Figure 6.3. Table 6.1 shows the dimensions for the three scaffolds with the same strut thickness. Similar to the film simulations, C_m was set to zero on the free surface in contact with the aqueous medium (which are highlighted in red in Figure 6.3). The interior of the scaffolds were meshed with tetrahedral elements and thinner boundary layer elements were used at the surfaces where higher gradients in the solution variables occur.

In order to estimate the effective modulus of the degraded scaffold, uniaxial compression of the RVE was simulated. Periodic and symmetry boundary conditions were applied such that the faces on the boundaries of the RVE remained planar and parallel. A uniaxial compressive strain was applied in the Z direction and the RVE was free to expand or contract in the X and Y directions. As the applied strain was small (<1%), buckling of the structure was not considered and geometric non-linearity from large displacement were neglected. The material was assumed to be isotropic with a Poisson's ratio of 0.3. The effective modulus $E_{effective}$ was then calculated as follows:

$$E_{effective} = \frac{\Sigma_0}{\varepsilon_A}; \quad \Sigma_0 = \frac{F_R}{A_0} \quad (6.1)$$

where Σ_0 is the nominal stress on the loaded face of the RVE, ε_A is the applied nominal strain, A_0 is the initial total cross sectional area of the loaded face, and F_R is the resultant reaction force on the loaded face. In order to compare the degradation in stiffness of different scaffolds, the results were normalised by the initial Young's modulus of the solid cube E_0 :

$$E^* = \frac{E_{effective}}{E_0} \quad (6.2)$$

Finally, in order to compare the predictions of the molecular weight model for different scaffold geometries and films, a volume-averaged molecular weight was defined as:

$$\bar{M}_n = \frac{1}{V} \int_V M_n dV \quad (6.3)$$

6.4 Results

6.4.1 Model Calibration

The parameters of the molecular weight model (k_1 , k_2 , and D_0) and the mechanical properties model (N_{chains} , $R_{scissions}$, and M_n^{crit}) were calibrated to fit the experimental data obtained for the molecular weight and the Young's modulus for a PLGA film (SC250) degraded in the PBS, pH 7.4 at 37°C, as described in Chapter 5. Figure 6.4 (A-C) compares the \bar{M}_n experimental data with different combinations of parameters for the molecular weight model. The ratio of k_1 to k_2 was set at 1, 5, and 50. An initial number average molecular weight (M_{n0}) of 82,000 g mol⁻¹ was assumed and the initial concentration of ester bonds (C_{e0}) was set at 17,300 mol m⁻³. The next step of the calibration is to determine the correct value of M_n^{crit} so that the mechanical properties model correctly predicts the experimentally observed relationship between normalised E and M_n , as shown in Figure 6.5. The best model fit to the experimental data was achieved using $N_{chains} = 3000$ polymer chains and $M_n^{crit} = 1500$ g mol⁻¹. For less than 3000 polymer chains (300, 500, or 1000), the molecular weight of the chains in the simulation did not match the experimental GPC data. For more than 3000 polymer chains (10,000 or 20,000), similar results to the 3000 polymer chains were achieved (data not shown). Different values of random to end scission ratios (3:1, 1:1, 1:12 or 1:50) did not show any significant effect on the results (data not shown).

Finally, Figure 6.4 (D-F) shows the prediction for E as a function of time using the coupled molecular weight and mechanical properties model. Comparing the curves for \bar{M}_n versus time and the curves for E versus time (Figure 6.4), the best fit was achieved by setting $\beta=0.5$, $k_1=0.002$ day⁻¹, $k_2=0.002$ (m³ mol⁻¹)^{0.5} day⁻¹, and $D_0=10^{-12}$ m² day⁻¹. The computational model correctly predicted the experimentally observed decrease in \bar{M}_n and E .

6.4.2 Comparison of the Semi-analytical and Numerical Solutions of the Molecular Weight Model for PLGA films

The semi-analytical (Galerkin method) and numerical (the finite element method) solutions of the volume-averaged of the non-dimensional form of the ester bond concentration \bar{C}_e (refer to section 3.3.2.1) during degradation were obtained for PLGA films with different thicknesses, ranged between 2.5 μm to 2500 μm . Figure 6.6 shows the changes in the volume-averaged concentration of ester bonds during degradation for the semi-analytical solution and the finite element method using the same set of parameters as the best fit presented above in section 6.4.1 for the molecular weight model. The results show an almost perfect match for the 2.5 μm film (blue line); however, for the 25 μm film (green line), the semi-analytical solution showed less of an agreement to the finite element prediction. The difference between the semi-analytical solution and the finite element method was more significant for the 2500 μm film (red line), indicating that semi-analytical solution cannot accurately describe the degradation of PLGA films in this size range. Figure 6.7 shows that the semi-analytical solution cannot capture the gradient changes at the surface of the films.

6.4.3 Effect of Thickness on the Young's Modulus of PLGA Films

The coupled modelling framework was used to investigate the effect of film thickness on degradation behaviour. Figure 6.8 (A) shows the predicted changes in \bar{M}_n with time for PLGA films with thickness ranging from 0.25 to 2500 μm over 40 days, as predicted by the molecular weight model. For films thicker than 2.5 μm , \bar{M}_n was predicted to decrease rapidly over the first 10 days, after which the rate of degradation slowed significantly. After 20 days, the thicker films had almost completely degraded. In contrast, the 2.5 μm film had only degraded by 50% and the 0.25 μm film was still 95% of the initial value. The rate of change of \bar{M}_n for the thinnest film was consistent with purely homogenous degradation (i.e. $d\bar{M}_n/dt = -k_1\bar{M}_n(t = 0)$).

The coupled model was then used to predict the changes in E of the film as a function of time, as shown in Figure 6.8 (B). The Young's modulus was predicted to remain at the initial value until day 13, after which the thicker films underwent a rapid decrease in stiffness. For films larger than 2.5 μm , a significant reduction in Young's modulus did not begin until after ~ 13 days; however, for films smaller than 2.5 μm the Young's modulus did not reduce even after 40 days. For films thicker than 50 μm , the stiffness after 25 days was less than 10% of the initial value and the fastest decrease was predicted for the thickest 2500 μm film, which had lost all structural stiffness after 25 days.

As shown above in Figure 6.5, there is a highly non-linear relationship between modulus and molecular weight. Therefore it is possible to have a significant decrease in \bar{M}_n , e.g by 50% for the 2.5 μm film, without a significant decrease in E . Once the molecular weight drops below the critical level shown in Figure 6.5 ($M_n/M_{n0} < 0.2$), the polymer chains have undergone a significant amount of scissions such that the decrease in polymer chain entanglement causes a drop in stiffness, as shown in Eq. (3.39). Thus, the 2.5 μm film has sufficiently long chains to retain close to its initial stiffness, while the larger films have a lower molecular weight and the shorter chains give the polymer a lower stiffness.

6.4.4 Degradation Behaviour and Effective Elastic Modulus for PLGA Scaffolds

Next, degradation of PLGA scaffolds was predicted using the same model parameters as calibrated above for films. The predicted distribution of M_n for the scaffolds with 0.05 mm thick struts after 25 days of degradation is shown in Figure 6.9. The contour plots show that the molecular weight degradation was faster in the centre of the scaffold unit cells, as these are the areas in the scaffold that are furthest from a free surface. This demonstrated the heterogeneous bulk degradation of the scaffolds with 0.05 mm struts.

Figure 6.10 (A) shows that the volume averaged molecular weight \bar{M}_n was the same for the three different scaffold geometries with strut size of 0.05 mm. The decrease in \bar{M}_n began immediately at day 0 and continued approximately linearly until day 10, when the rate of degradation slowed significantly. After 30 days of degradation, \bar{M}_n was approximately zero. The decrease in \bar{M}_n was not affected by the scaffold architecture; however these scaffolds had a strut thickness of 0.05mm (the effect of strut thickness is discussed below). In contrast to the decrease in molecular weight, which began at day 0, the effective modulus of each of the scaffolds did not decrease until ~ 13 days, as shown in Figure 6.10 (B). Although the initial stiffness of each scaffold was strongly affected by the architecture; scaffold A was initially twice as stiff as the other two scaffolds.

Finally, the effect of strut thickness was investigated for each PLGA scaffold. Figure 6.11 shows \bar{M}_n and E^* for each scaffold with strut sizes ranging from 0.002 to 1 mm (note that the porosity of all scaffolds was kept fixed at 63.5% by varying the size of the unit cell). For each scaffold geometry, increasing the thickness from the 0.05 mm scaffolds shown in Figure 6.9 and Figure 6.10 did not alter either the volume averaged molecular weight (Figure 6.11 (A-C)), or the effective modulus (Figure 6.11 (D-F)). In contrast, decreasing the thickness significantly changed the behaviour. For the thinnest strut size, the degradation was slowed such that there was no change in E^* after 40 days. For intermediate strut thickness, the rate of decrease in \bar{M}_n and E^* was slower than for the thick 0.05 mm struts.

In order to illustrate how the degradation mechanism is affected by the strut thickness, the variation of M_n through the thickness of a strut for scaffold B is shown in Figure 6.12. The data is shown as a function of the dimensionless coordinate R/R_0 (where R_0 is the radius of the strut; R/R_0 is 0 at the centre of the strut and 1 at the free surface). For the scaffolds with thick struts (> 0.05 mm), M_n is significantly lower in interior of the strut and there is a very steep gradient in M_n near the surface, clearly showing the heterogeneous nature of the degradation. In

contrast, for the thinnest strut, M_n only varies by ~15% between the surface and the interior of the scaffold, showing that the degradation is homogenous.

6.5 Discussion

The present study provides a computational investigation of the molecular weight degradation and the mechanical performance of PLGA films and tissue engineering scaffolds. A coupled computational modelling framework described in Chapter 3 is used in this chapter to capture changes in molecular weight distribution during degradation and to determine the relationship between the molecular weight distribution and the mechanical properties of PLGA. The model framework was calibrated based on experimental data for the *in-vitro* degradation of a PLGA film described in Chapter 5. The calibrated model was then used to predict the molecular weight and the reduction in the Young's modulus of PLGA films with different thicknesses and also of a range of PLGA scaffolds.

This study has demonstrated the importance of the autocatalytic hydrolysis on the degradation rate of PLGA films. The calibration results have shown that the autocatalytic reaction constant (k_2) has a significant effect on M_n and the degradation rate is much faster for the higher values of k_2 ; in contrast, the effect of the non-catalytic reaction constant (k_1) is small. This suggests that, in the present study, the autocatalytic hydrolysis is the dominant degradation mechanism in PLGA.

The results of the semi-analytical solution and the finite element method showed that the weighted error residual method used to generate the semi-analytical solution in MATLAB cannot accurately describe the degradation of polymer films of thickness 25 μm or above. This may be due to the trial functions suggested for the semi-analytical solution (refer to Eq. (3.64)) used in the weighted residual error method. These functions are quite restrictive in the spatial variation that they allow, relative to that afforded by the finite element model with a relatively high number of nodes (> 100) in the thickness direction.

As the modulus is non-linearly dependent on the molecular weight, the degradation rate thus has a non-linear effect on the stiffness. The length of the polymer chains decreases as the PLGA degrades via end scissions and random scissions. Following from Eq. (3.39), once the polymer chains are shortened sufficiently during degradation, there is a sudden change in Young's modulus. This causes the collapse in stiffness seen for the film and scaffold compression.

In the present study, the Young's modulus was predicted to decrease faster for thicker PLGA films. Computed predictions correlate strongly with published experimentally observed trends of degradation for the PLGA devices with different sizes. Some authors have studied the degradation rates for PLGA devices 200 μm to as small as 0.53 μm in size (Dunne et al., 2000; Grayson et al., 2005; Grizzi et al., 1995; Lu et al., 1999; Witt and Kissel, 2001). In these studies, it has been observed frequently that the degradation time is significantly shorter in the thicker samples due to the autocatalytic effect of the degradation products. In the latter part of the present study, the combined model is used to investigate the degradation of different scaffold geometries. For larger strut sizes, autocatalytic heterogeneous degradation occurs and the scaffolds are shown to mechanically collapse after 13 days. In contrast, simulations predict that the degradation rate of the scaffold is much slower when the strut size of the scaffold is smaller than 0.05 mm.

These results are consistent with the experimental results obtained by Wu et al. (2005) for *in-vitro* degradation of PLGA porous scaffolds. Saito et al. (2013; 2012) has studied the effect of the strut size on *in-vivo* degradation of PLA and PLGA three-dimensional porous scaffolds and demonstrated that scaffolds with larger struts (~ 0.9 mm) degrade more rapidly than scaffolds with smaller struts (~ 0.4 mm). The present study elucidates the relationship between the strut size, scaffold architecture, and the stiffness of the scaffold during degradation. This study highlights that the architecture of the scaffold does not have a significant influence on the degradation rate; however, the initial stiffness of the scaffold is strongly influenced by the architecture. It is demonstrated that the effective modulus of the

scaffold is substantially dependent on the volume fraction. The simulations predict that different scaffold architectures with the same strut size collapse at approximately the same time.

In the very small scaffolds and films simulated in the present study, the degradation is shown to be homogenous with little variation in M_n through the thickness of the strut. In the smaller samples, the oligomers, which are created as degradation products, can quickly escape from the surface into the aqueous medium. Consequently, the possibility of autocatalysis is very limited for thinner samples, and therefore the Young's modulus for thinner samples decreases slower. In contrast, for larger struts and films, the degradation is shown to be autocatalytic with a steep gradient in M_n between the core and the surface of the sample.

In order to compare the different scaffold geometries and films, a characteristic diffusion length l_{char} is given by the volume V divided by the free surface area A_{free} , i.e. the surface in contact with the aqueous medium:

$$l_{char} = \frac{V}{A_{free}} \quad (6.4)$$

Figure 6.13 (A) shows the relative change in effective modulus after 25 days for different sizes of each scaffold, where the size of the scaffold is represented by l_{char} (instead of strut thickness). By using this diffusion length scale to describe the size of each scaffold and film, a single trend is elucidated which does not depend on sample shape. For $l_{char} < 2 \mu\text{m}$, the degradation is homogenous and there is no change in the Young's modulus. For $l_{char} > 100 \mu\text{m}$, the scaffold has completely degraded and the behaviour is similar for larger samples. Recall that in Figure 6.11 there is no change in the degradation behaviour for the larger scaffolds and also that Figure 6.12 shows the degradation of large scaffolds is heterogeneous with a steep gradient in M_n . For intermediate values of l_{char} , there is a smooth transition between these two plateaus.

The sample size at which this transition between homogenous and heterogeneous behaviour occurs is related to the competition between diffusion of monomers and autocatalysis due to high concentrations of monomers in the interior of the sample. The diffusion length scale l_{diff} associated with this competition is determined from the material parameters (the latter part of Eq. (3.40)):

$$l_{diff} = \sqrt{\frac{D_0}{k_2 \sqrt{C_{e0}}}} \quad (6.5)$$

The calibration in the present study suggests that, $l_{diff} \approx 2 \mu\text{m}$. Therefore, when $l_{char} < l_{diff}$, the concentration of monomers remains low due to rapid diffusion, and thus the degradation is homogenous, i.e. the term associated with k_1 dominates Eq. (3.40). For larger scaffolds, the critical diffusion length l_{diff} is much smaller than the characteristic length; thus the monomers remain trapped in the scaffold and autocatalysis (i.e. the part of Eq. (3.40) associated with k_2) is the dominant mechanism. Furthermore, the competition between diffusion and autocatalysis can be summarised using the following non-dimensional form of diffusion coefficient:

$$\widehat{D} = \frac{D_0}{k_2 l_{diff}^2 \sqrt{C_{e0}}} \quad (6.6)$$

As shown superimposed on Figure 6.13 (A), when $\widehat{D} > 1$ the degradation is homogenous and when $\widehat{D} \ll 1$, the degradation is heterogeneous. In the case of the homogenous degradation, it should also be noted that the time constant associated with the non-catalytic degradation is on the order of 500 days.

In Figure 6.13 (B), the homogenous, heterogeneous, and transition regimes predicted in the present study are compared to experimental observations of homogenous and heterogeneous diffusion in different sized samples (Chen et al., 1997; Grizzi et al., 1995; Lu et al., 1999; Park, 1995; Spenlehauer et al., 1989; Vey et

al., 2008). Grizzi et al. (1995) has proposed a range of 200-300 μm as a critical thickness above which the PDLLA polymers (plate, film, microsphere) undergo heterogeneous degradation. The heterogeneous degradation of PLGA film with thickness of 250 μm was shown in Chapter 5. Also, the heterogeneous degradation of PLGA films with thicknesses of 300 μm and 5-100 μm has been shown by Vey et al. (2008) and Lu et al. (1999), respectively. Spenlehauer et al. (1989) has showed that PLGA microspheres less than 200 μm in diameter undergo a homogeneous degradation. However, Park (1995) has shown the heterogeneous degradation of PLGA microspheres with diameters less than 10 μm . The heterogeneous degradation of PLGA microspheres has been also demonstrated in a study by Chen et al. (1997) for PLGA microspheres with diameters of 50-70 μm . While the predictions in the present study are in broad agreement with observations, the disparities in experimentally observed critical length for transition between heterogeneous and homogenous degradation highlight the need for further experimental investigation of both the mechanical and molecular behaviour of PLGA during degradation.

The PLGA scaffolds in the present study are shown to have a rapid change in stiffness. While it is not clear what the optimal rate of mechanical degradation should be, Heljak et al. (2012) have explored the performance of multiple material scaffolds to provide a tuneable degradation response. Fast degradation may affect negatively on cell viability and cell migration into the scaffold due to the acidic degradation products as a result of autocatalysis (Sung et al., 2004). Scaffold manufacturing methods have also been shown to have an effect on degradation; a PDLLA electrospun fibrous mat degrades slower than the PDLLA film prepared by solvent casting and the electrospun mat shows a surface erosion pattern rather than a typical bulk degradation (Cui et al., 2008). As the present study has shown the importance of the free surface area, the slower degradation of the electrospun mat may be due to faster diffusion of the autocatalytic degradation products.

6.6 Conclusion

This study used a numerical model that couples changes in molecular weight caused by degradation to the mechanical properties of PLGA. The predictions presented here show that heterogeneous degradation occurs in PLGA when the length scale of the PLGA sample results in a diffusion limited regime where autocatalysis is the dominant degradation mechanism. The results of the computational simulations indicated a critical length scale in the range 2-100 μm below which homogenous degradation occurs. Consequently, scaffolds with thicker struts demonstrate a higher degradation rate due to stronger autocatalysis and they collapse more rapidly. The presented results show that the architecture of the scaffold does not strongly influence the degradation rate but that it determines the initial stiffness of the scaffold.

The computational framework considered in this chapter is used later in Chapter 8 of this thesis to validate the critical length scale provided here and also to refine the model parameters for PLGA materials prepared by different processing methods and with different thicknesses.

6.7 Figures

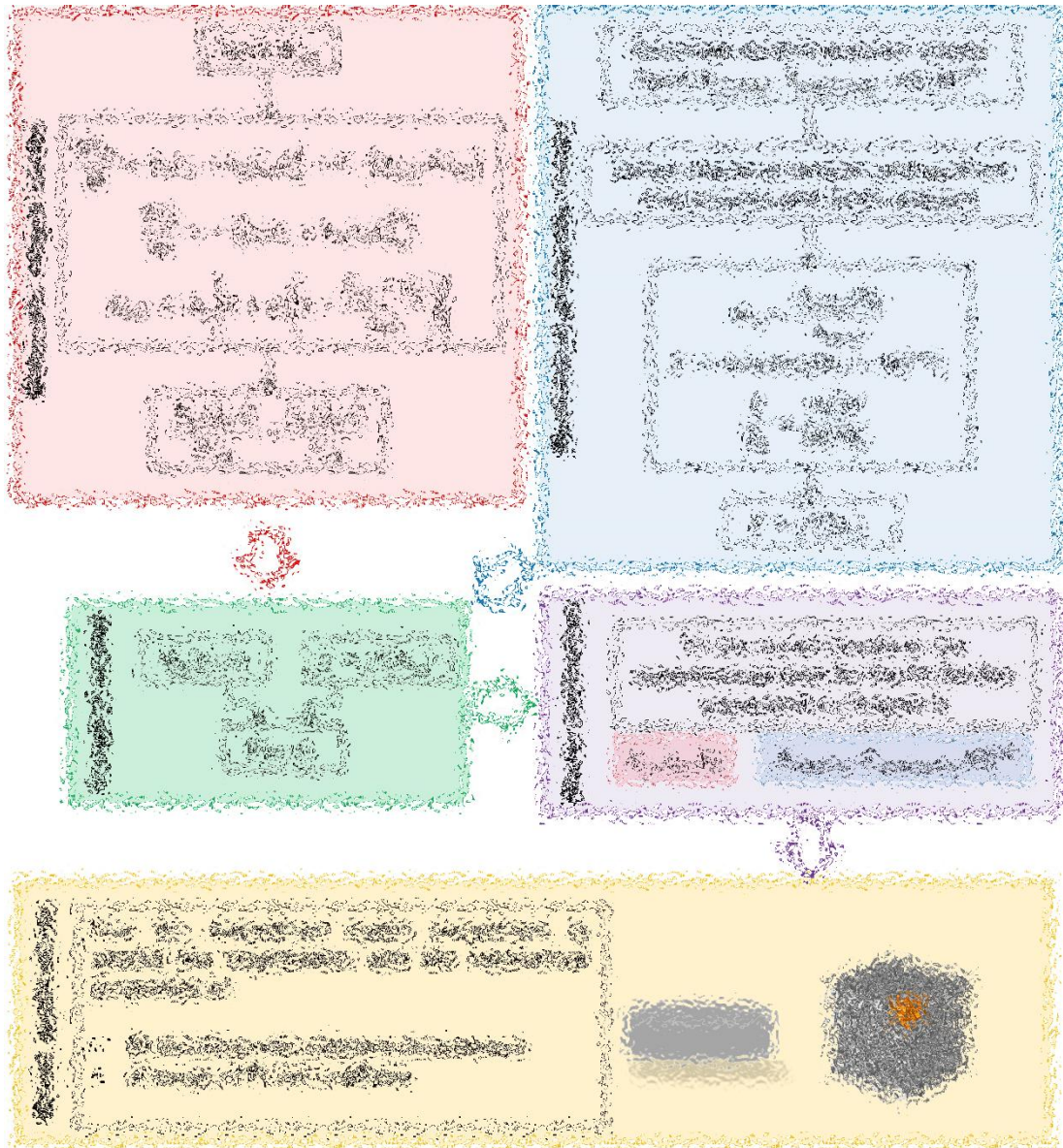


Figure 6.1: An illustration of the coupled computational modelling framework used for the prediction of degradation behaviour and mechanical properties of PLGA structures, and applied in this chapter to study the degradation of PLGA films with different thicknesses and of a range of PLGA tissue engineering scaffolds. **Figure blurred due to copyright restrictions.**

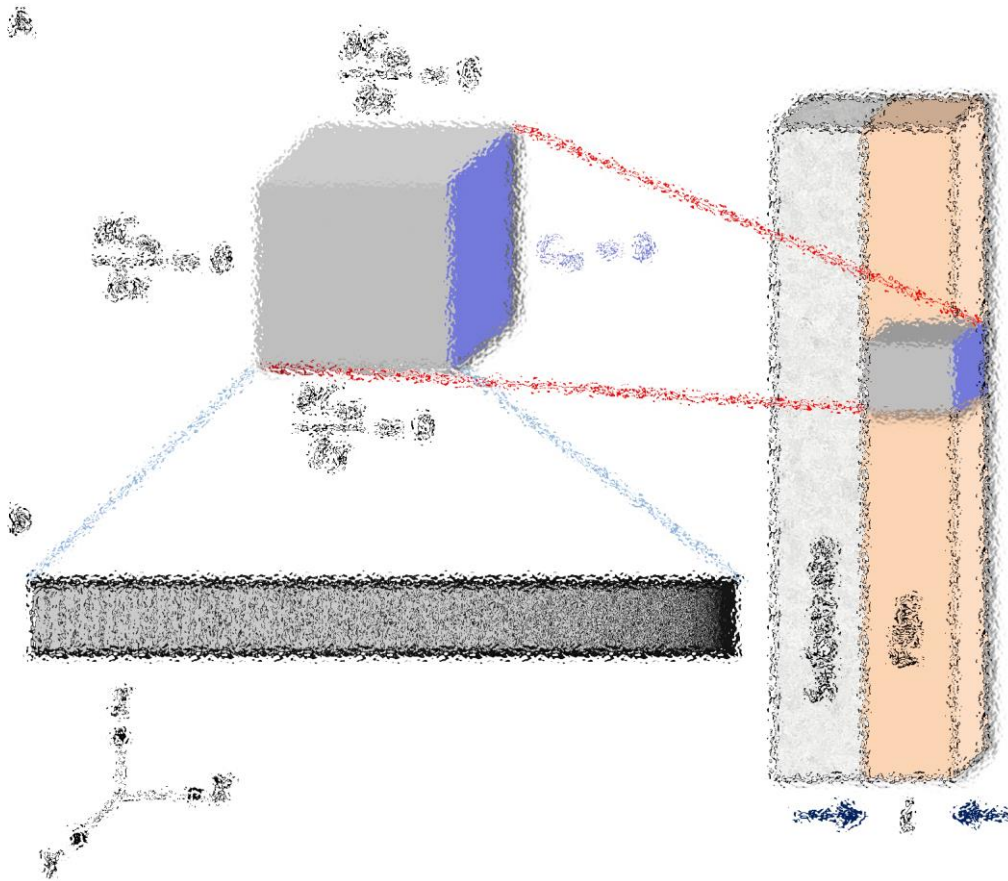


Figure 6.2: (A) The monomer boundary conditions and (B) the mesh element used through the film thickness l in the reaction-diffusion based molecular weight model. **Figure blurred due to copyright restrictions.**

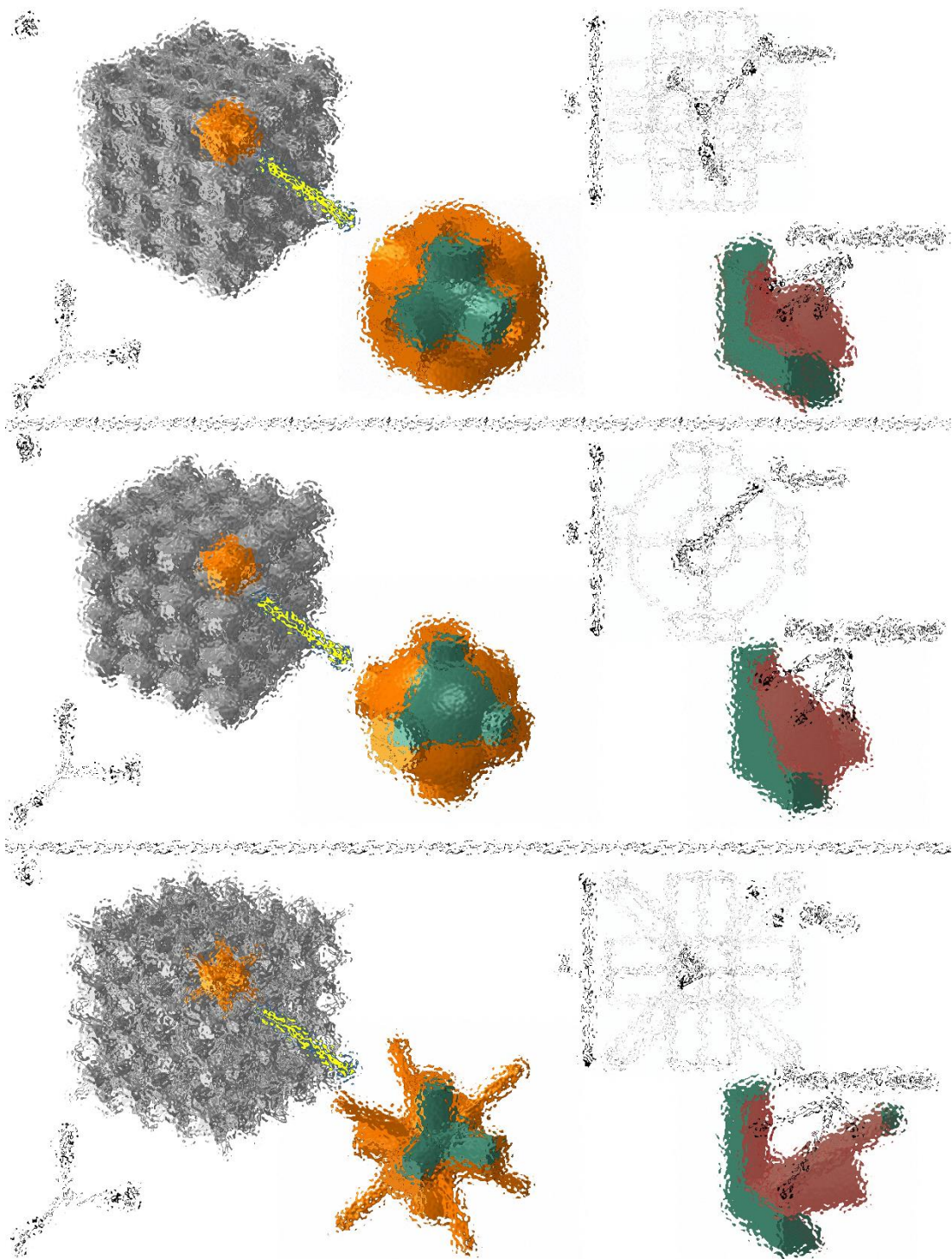


Figure 6.3: Representative volume element (in green), unit cell (in orange), and geometry of (A) Scaffold A, (B) Scaffold B, and (C) Scaffold C. The red colour shows the free surfaces in contact with the aqueous medium. **Figure blurred due to copyright restrictions.**

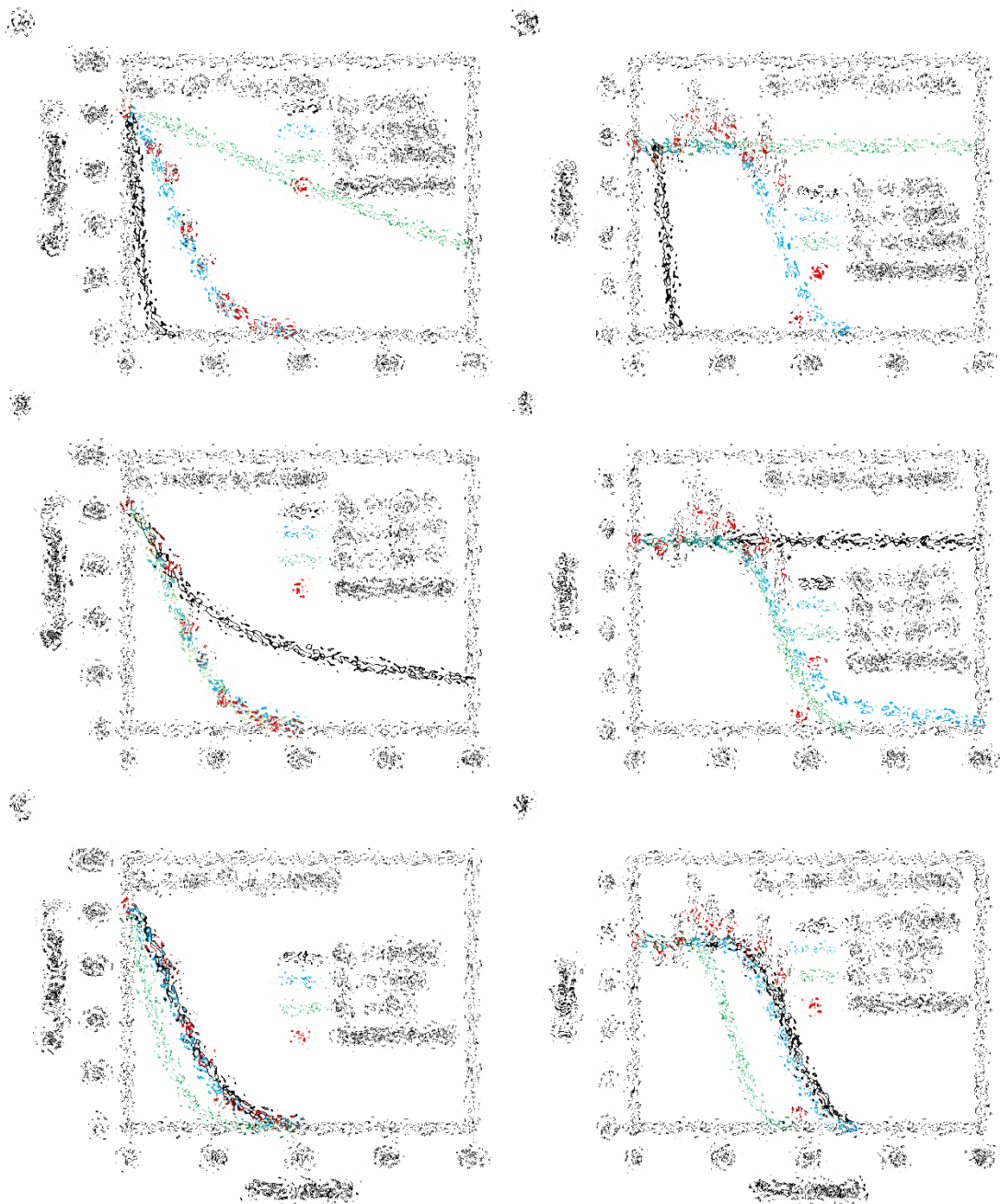


Figure 6.4: Model fittings of volume-averaged molecular weight (\bar{M}_n) (A-C) and Young's modulus (E) (D-F) to the PLGA film experimental data obtained in Chapter 5 for different values of k_2 (A, D), D_0 (B, E), and k_1 (C, F). The best fit to both experimental data for \bar{M}_n and E was achieved by setting $\beta=0.5$, $k_1=0.002 \text{ day}^{-1}$, $k_2=0.002 (\text{m}^3 \text{ mol}^{-1})^{0.5} \text{ day}^{-1}$, and $D_0=10^{-12} \text{ m}^2 \text{ day}^{-1}$. **Figure blurred due to copyright restrictions.**

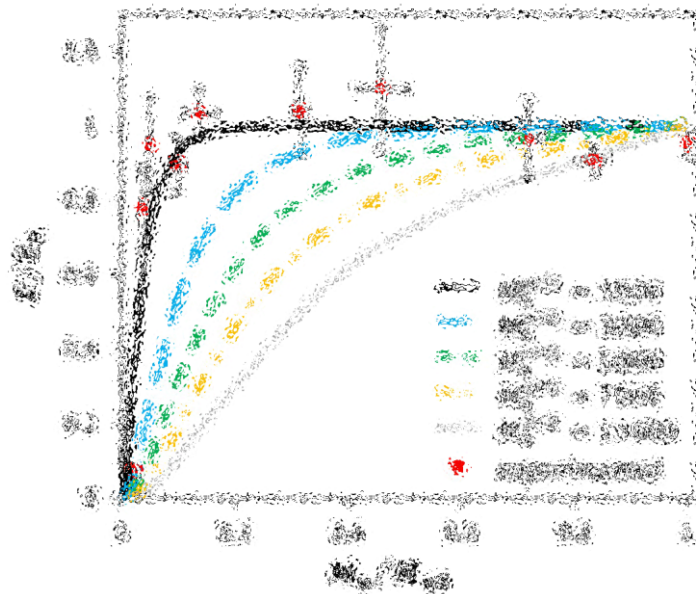


Figure 6.5: Normalised Young's modulus (E/E_0) versus normalised number average molecular weight (M_n/M_{n0}) for different values of the critical molecular weight (M_n^{crit}) in comparison with the experimental data (red discrete dots) obtained in Chapter 5 for a degraded PLGA film. **Figure blurred due to copyright restrictions.**

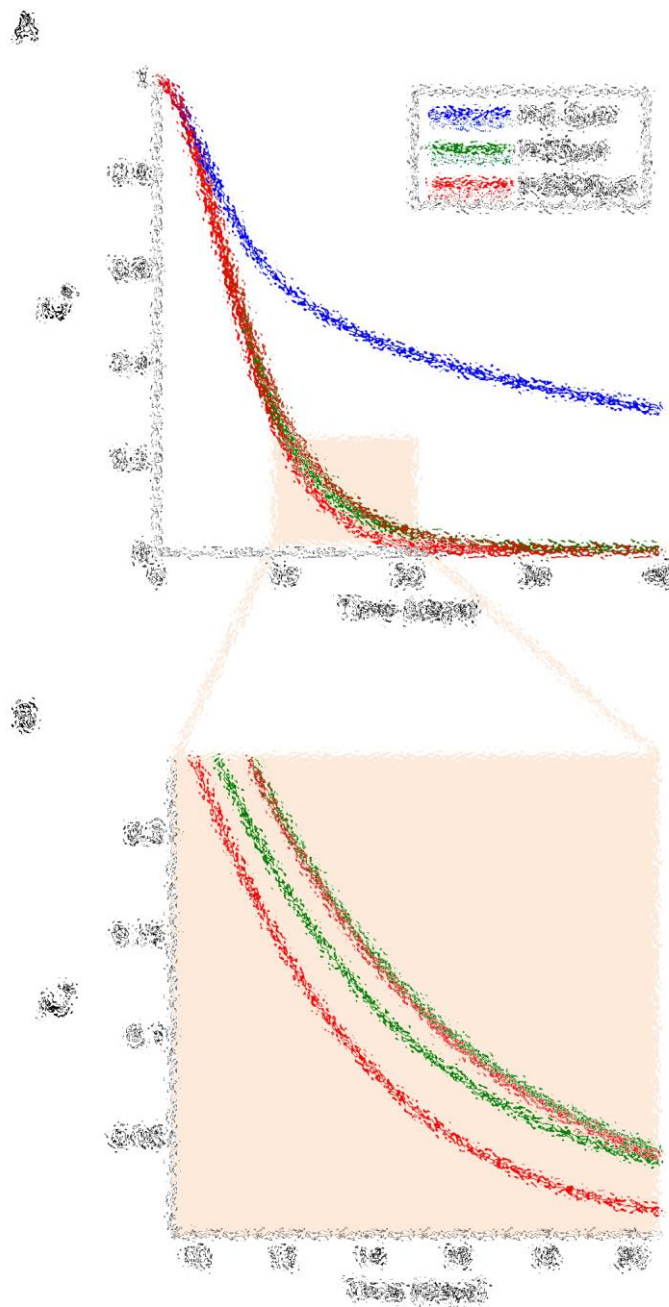


Figure 6.6: (A) Comparison of the volume-averaged of the non-dimensional form of the ester bond concentration \bar{C}_e changes in PLGA films of different thicknesses using semi-analytical (dashed lines) and numerical (solid lines) solutions. (B) Zoomed-in area of the comparison between these two methods. **Figure blurred due to copyright restrictions.**

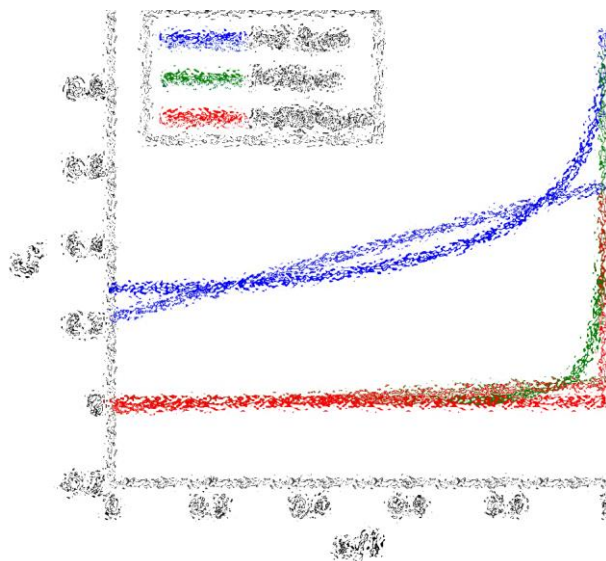


Figure 6.7: Gradient of the concentration of ester bonds C_e at the surface of PLGA films of different thicknesses after 25 days of degradation for semi-analytical (dashed lines) and numerical (solid lines) solutions. x is the distance through the film thickness l . **Figure blurred due to copyright restrictions.**

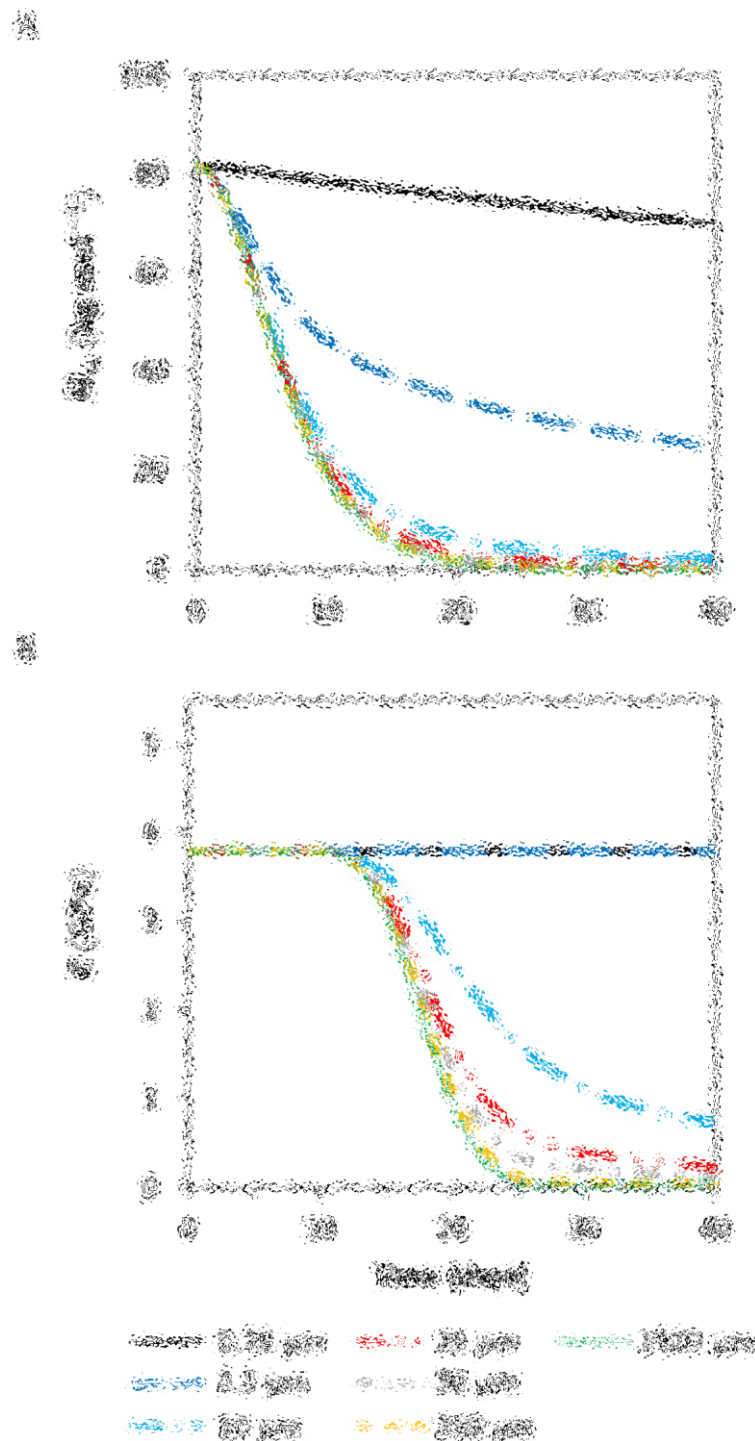


Figure 6.8: (A) Volume-averaged molecular weight (\bar{M}_n) and (B) Young's modulus (E) for PLGA films of different thicknesses during degradation. The effect of thickness on the Young's modulus of PLGA films with thicknesses of smaller than 2.5 μm is significant. **Figure blurred due to copyright restrictions.**

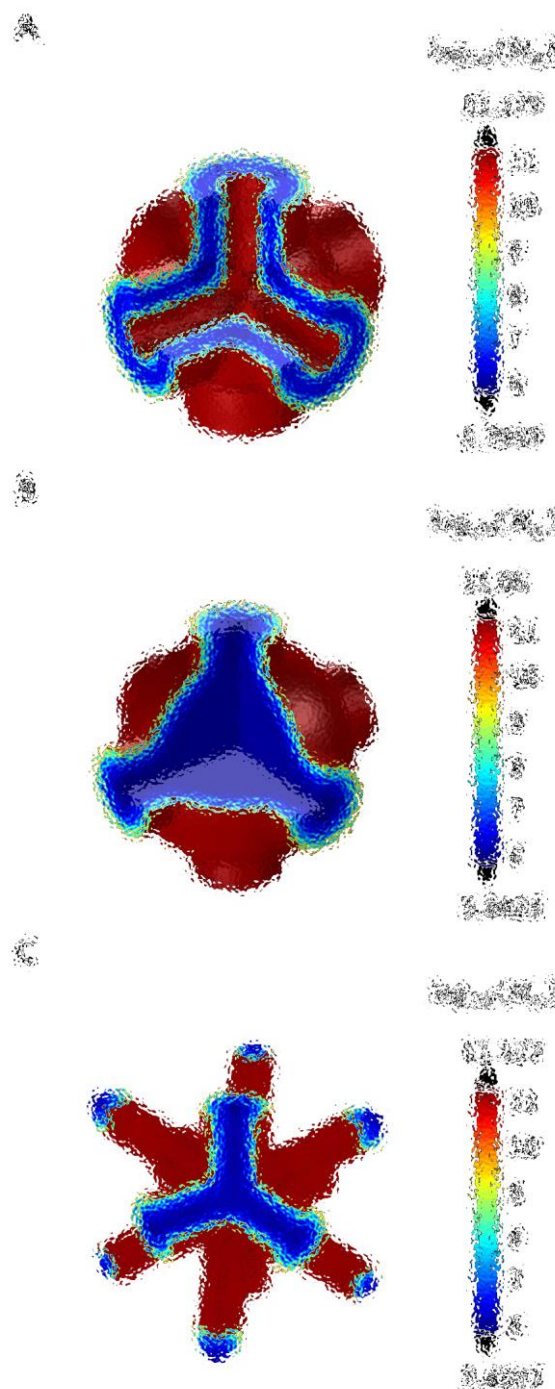


Figure 6.9: Distribution of molecular weight (M_n) for (A) Scaffold A, (B) Scaffold B, and (C) Scaffold C with 0.05 mm strut thickness after 25 days of degradation shown on a log scale. **Figure blurred due to copyright restrictions.**

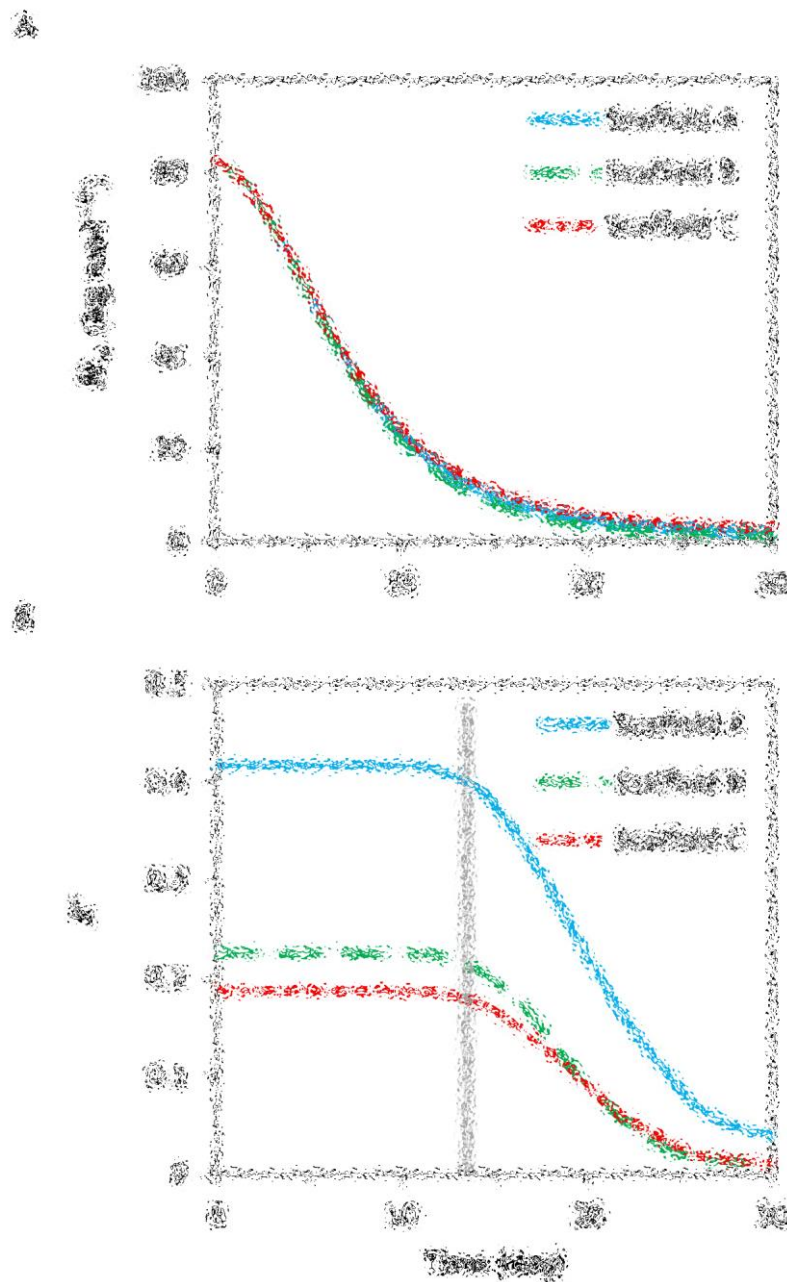


Figure 6.10: Comparison of (A) Volume-averaged molecular weight (\bar{M}_n) and (B) normalised effective modulus ($E^* = E_{effective}/E_0$) of a different PLGA scaffolds with a strut sizes of 0.05 mm. The grey dashed line indicates that the scaffolds collapse at approximately the same time (~13 days). **Figure blurred due to copyright restrictions.**

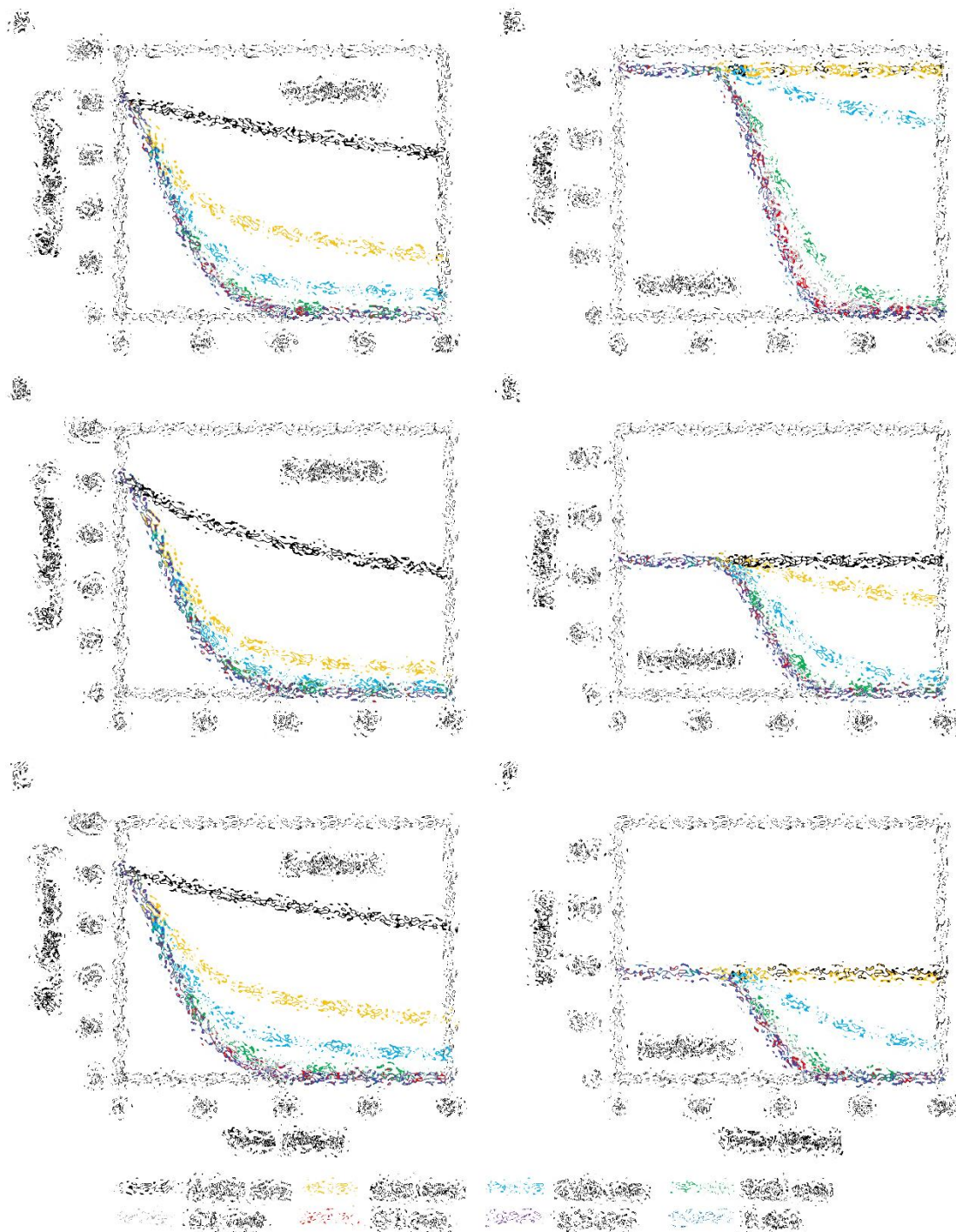


Figure 6.11: Volume-averaged molecular weight (\bar{M}_n) (A-C) and normalised effective modulus ($E^* = E_{effective}/E_0$) (D-F) of PLGA scaffolds with different architectures and strut sizes. The decrease in effective modulus was significantly different for the struts thinner than 0.02mm. **Figure blurred due to copyright restrictions.**

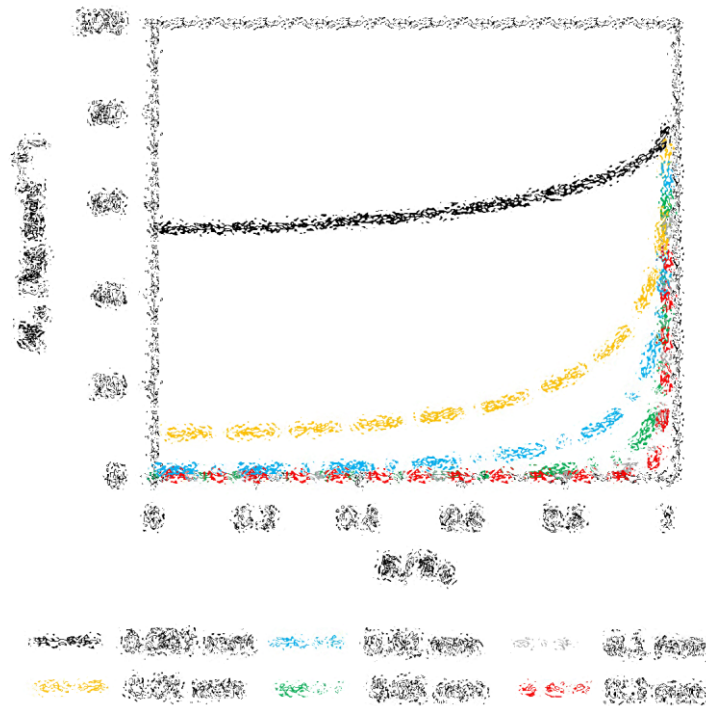


Figure 6.12: Variation of molecular weight (M_n) for scaffold B with different strut sizes through the thickness of the strut. R_0 is the radius of the strut; R/R_0 is 0 at the centre of the strut and 1 at the free surface. **Figure blurred due to copyright restrictions.**

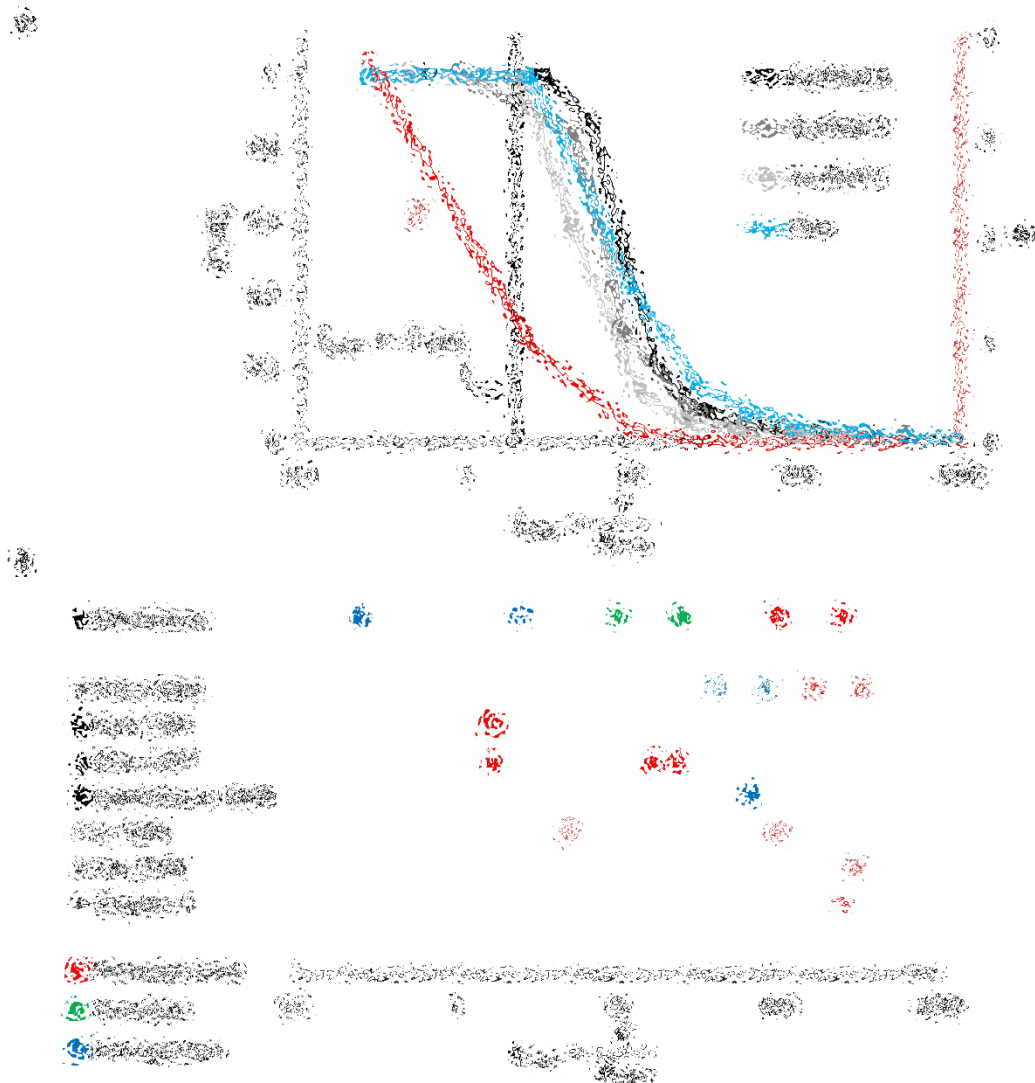


Figure 6.13: (A) the relative change in effective modulus (E^*/E_0^*) after 25 days for different sizes of each scaffold and the dimensionless diffusion coefficient (\hat{D}) versus the characteristic length ($l_{char} = V/A_{free}$) for different scaffold architectures and films with different thicknesses. (B) Comparison of homogenous, heterogeneous, and transition regimes between the simulations performed in the current study and the experimental observations in the literature and Chapter 5. **Figure blurred due to copyright restrictions.**

6.8 Table

Table 6.1: Dimensions for the three scaffolds with the strut thickness of 0.02 mm.

Scaffold	Thickness (mm)	L (μm)	R_o (μm)	R_i (μm)	R_{cyl} (μm)	R_{sphere} (μm)
A	0.02	60	15	5	n/a	22.72
B	0.02	60	10	n/a	n/a	25.38
C	0.02	60	10	n/a	6.38	n/a

7 Nanoindentation of Undegraded Solvent-cast and Compression-moulded PLGA

7.1 Overview

Given to the depth dependence of the elastic modulus and hardness of the degraded solvent-cast PLGA material (SC250) presented in Chapter 5, in the present chapter, nano- and micro-mechanical properties of undegraded solvent-cast (SC120) and compression-moulded (CM1000) PLGA materials are investigated. Nanoindentation experiments are performed at different indentation depths and used to investigate the elastic modulus, hardness, contact stiffness, plasticity index, and indentation pile-up behaviour of the material for a range of loading and unloading rates.

The results show that the solvent-cast material is more elastically compliant and plastically softer than the compression-moulded material, and it also displays lower work hardening characteristics. Loading rate dependence is found to be relatively insignificant. The measured elastic modulus and hardness are strongly depth dependent for both forms of the material, for indentations less than 3000 nm. The results presented in this chapter allow recommendations to be made on the choice of test protocol parameters for reliable nanoindentation testing of this material¹.

7.2 Introduction

The application of nanoindentation has increased over recent years; however, applying this measurement technique to polymers, particularly soft polymers,

¹ The following has been published as: Shirazi RN, Rochev Y, McHugh P. Nanoindentation of solvent-cast and compression-moulded poly(lactic-co-glycolic acid) to determine elastic modulus and hardness. *Polymer Testing* 2016; 50:111-118.

remains challenging for a variety of reasons, as described in Chapter 2, including material rate dependence (Briscoe et al., 1998; Tang and Ngan, 2003a; Zhou and Komvopoulos, 2006), adhesion (Dokukin and Sokolov, 2012; Gupta et al., 2007; Liao et al., 2010), and size effects (Alisafaei et al., 2014; Alisafaei et al., 2013; Briscoe et al., 1998; Charitidis, 2010; Chong and Lam, 1999; Flores and Calleja, 1998; Han, 2010; Lam and Chong, 2000; Tranchida et al., 2007; Tweedie et al., 2007; Voyiadjis et al., 2014; Zhang et al., 2004).

As discussed previously, one aspect of material rate dependence is viscoelasticity. In nanoindentation, viscoelasticity causes the indenter to continue penetrating the material during the initial part of unloading, which results in a forward-going *nose* in the unloading curve. This phenomenon occurs when the creep rate of the material, i.e. the rate of increase in the indentation depth, is initially higher than the imposed unloading rate. In this case, the slope of the initial part of the unloading curve is changed which causes a negative contact stiffness and therefore inaccurate mechanical property measurements (Briscoe et al., 1998; Feng and Ngan, 2002; Tang and Ngan, 2003a). One way to eliminate this nose is to use a holding time between loading and unloading at the maximum load in order to allow the material to relax and therefore the creep rate to dissipate prior to unloading. The appropriate holding time should be selected based on the creep and the unloading rates used in the experiment for each material. The holding time should be long enough such that the rate of increase in the indentation depth, i.e. the creep rate, is less than 1% per minute (Chudoba and Richter, 2001). Additionally, due to the time-dependent material properties, the unloading curve and, therefore, the contact stiffness depend on the unloading rate. A sufficiently fast unloading rate is desirable to limit the relaxation phenomenon for viscoelastic materials (Fischer-Cripps, 2006; Jakes et al., 2012; Ngan and Tang, 2002).

As discussed in Chapters 2 and 5, an important issue in nanoindentation of polymers is that the elastic modulus and hardness may increase with decreasing the indentation depth. This phenomenon has been reported by many authors (Alisafaei

and Han, 2015; Alisafaei et al., 2014; Alisafaei et al., 2013; Briscoe et al., 1998; Charitidis, 2010; Chong and Lam, 1999; Dokukin and Sokolov, 2012; Flores and Calleja, 1998; Gupta et al., 2007; Han, 2010; Lam and Chong, 2000; Liao et al., 2010; Tranchida et al., 2007; Tweedie et al., 2007; Voyiadjis et al., 2014; Zhang et al., 2004; Zhou and Komvopoulos, 2006). The factors which have been proposed to explain this phenomenon include: formation of a specific interfacial region between the indenter and the polymer surface during indentation (Tweedie et al., 2007), lower entanglement interactions at the surface due to the surface dynamics of polymers (Zhou and Komvopoulos, 2006), surface roughness (Zhang et al., 2004), changes in the material properties through thickness (Briscoe et al., 1998; Charitidis, 2010), tip imperfection (Flores and Calleja, 1998), adhesion (Dokukin and Sokolov, 2012; Gupta et al., 2007; Liao et al., 2010), and higher order displacement gradients (Alisafaei et al., 2014; Han, 2010; Lam and Chong, 2000; Voyiadjis et al., 2014).

For most polymeric and soft materials, adhesion between the indenter and the polymer surface occurs as the indenter approaches the surface (pull-on adhesion), causing a region of negative load in the load-displacement curve. This complicates the determination of the contact point (the point where the indenter first comes into contact with the sample surface) and, therefore, results in overestimation of the elastic modulus (Deuschle et al., 2007; Kaufman and Klapperich, 2009).

For most materials with low work hardening, the determination of the elastic modulus is affected by pile-up, where the sides of the residual impression are curved upward. When pile-up is large, the true contact area is larger than the nominal contact area which is based on the cross-sectional area of the indenter tip; consequently, the elastic modulus and hardness are overestimated (Bolshakov and Pharr, 1998; Oliver and Pharr, 2004). The results of finite element analysis by Bolshakov and Pharr (1998) have shown that pile-up is significant when the ratio of the residual depth to the maximum depth is larger than 0.7 and the degree of the work hardening is small.

A number of the factors mentioned above were discussed previously in Chapter 5 as possible explanations for the depth dependence of elastic modulus for solvent-cast PLGA material. Chapter 5 was mainly focused on the changes in the mechanical properties of PLGA during degradation and the load dependence was examined only to a limited extent. Given the results presented in Chapter 5, the present study is focused on the nanoindentation of undegraded PLGA material in order to investigate the depth dependence of modulus and hardness and also the material rate dependence for a wide range of applied loads and loading rates. Also, the mechanical properties of PLGA material prepared by two different processing methods (compression moulding and solvent casting) are explored.

The first objective of this study is to characterise the material response under variation in applied load and loading rate. The second objective is to compare the effects of two different material processing methods on the material response. The final objective is to make practical recommendations on appropriate test parameters for successful nanoindentation testing of this material.

7.3 Materials and Methods

In this chapter, a 0.12 mm film (SC120) and a 1 mm plate (CM1000) were used which were prepared by solvent casting and compression moulding, respectively, as described in Chapter 4. The mechanical properties of the materials were evaluated by the nanoindentation technique using a linear load-controlled mode. Different loading and unloading rates and maximum indentation loads were used for the compression-moulded and solvent-cast PLGA materials (Table 7.1). The holding time was set at 60 s between loading and unloading. Figure 7.1 shows the typical trapezoidal loading function and the corresponding load-displacement response for the compression-moulded and solvent-cast PLGA materials for different loads, illustrating success in the indentation procedure for these materials.

A matrix of 5 x 5 indents was used to perform a single batch of identical indentations with spacing of 300 μm between indents to avoid overlapping the

elastic field of each indent (refer to Figure 4.4). The elastic modulus, hardness, contact stiffness, power law exponent, the ratio of the permanent indentation depth to the maximum indentation depth, and the plasticity index of each material were calculated for different unloading (loading) rates based on the Oliver and Pharr method (1992) described in Chapter 3. Data were expressed as means \pm standard deviation.

The surface images of the impression left by the indentation were obtained using AFM measurements as described in Chapter 4. The cross-section profiles of the indents were analysed to investigate the formation of pile-up.

7.4 Results

7.4.1 Elastic Modulus and Hardness

Figure 7.2 (A) shows that the elastic modulus E_s of the compression-moulded PLGA material was larger than that of the solvent-cast material for all indentation depths. The largest value for the compression-moulded material was 8.4 ± 0.5 GPa for the applied load of 5 mN; however, for the same load, the modulus for the solvent-cast material was 5.9 ± 0.9 GPa.

The results show that the elastic modulus of the PLGA material decreased when the indentation depth (or the maximum applied load) increased (Figure 7.2 (A)). This phenomenon was observed for the samples prepared by both solvent casting and compression moulding. The depth dependence of the elastic modulus was more significant for the solvent-cast material, e.g. the elastic modulus of the solvent-cast material decreased to 30% of the initial modulus for the applied load of 20 mN. However, for the same load, the elastic modulus of the compression-moulded material decreased to only 60% of the initial modulus.

Figure 7.2 (B) shows that the values of hardness H_{IT} for the compression-moulded material were larger than those for the solvent-cast material. However, the depth dependence of the hardness was not as significant as that of the elastic modulus.

Figure 7.2 shows the results for the unloading (loading) rate of 40 mN min^{-1} . The results of the elastic modulus and hardness for other rates are shown in Appendix D.

7.4.2 Influence of Unloading Rate

Figure 7.3 shows the elastic modulus and hardness for the PLGA material for all unloading (loading) rates. The results show that the unloading rate did not significantly influence the depth dependence of the elastic modulus (Figure 7.3 (A)). A small deviation was observed for indentation depths larger than 3000 nm for the compression-moulded material; however, this difference was not pronounced. The unloading rate did not significantly influence the hardness measurements (Figure 7.3 (B)).

Figure 7.3 (C) shows the contact stiffness S for the PLGA material for all unloading (loading) rates. The contact stiffness for the compression-moulded material increased almost linearly with the increase in indentation depth up to 3000 nm. For indentations larger than 3000 nm, the contact stiffness slightly departed from the linear profile; however, this deviation was not pronounced. For the solvent-cast material, the change in the contact stiffness was not significant for indentations smaller than 3000 nm.

Figure 7.3 (D) shows the values of the power law exponent m obtained from the unloading curve for all unloading (loading) rates. Values of less than 2 were determined; the values for the compression-moulded material were between 1.2 and 1.6 which is a typical range reported for a Berkovich indenter (Oliver and Pharr, 1992; Oliver and Pharr, 2004).

7.4.3 Influence of Pile-Up due to Plastic Deformation

Figure 7.4 shows the plasticity index η and the ratio of the permanent indentation depth to the maximum indentation depth (h_p/h_m) for the PLGA materials for the unloading (loading) rate of 40 mN min^{-1} . Values for the plasticity index were larger

than 0.8 at low indentation depths for both solvent-cast and compression-moulded materials (Figure 7.4 (A)). The values decreased considerably with the increase in indentation depth. For the maximum indentation depths, larger than 8000 nm, the plasticity index of the compression-moulded material approached 0.6.

For indentation depths smaller than 3000 nm, the values of h_p/h_m were well above 0.7 for the compression-moulded material; however, these values decreased with increasing indentation depth and were smaller than 0.7 for the maximum indentation depths, larger than 8000 nm (Figure 7.4 (B)). This trend was similar to that of η in Figure 7.4 (A). Note that, for a fully elastic deformation, $h_p/h_m = 0$ and, when the deformation is substantially plastic, $h_p/h_m = 1$. For the solvent-cast material, the values of h_p/h_m dropped sharply to less than 0.7 for indentation depth of 3000 nm. The slope of the decrease in the values of h_p/h_m with the indentation depth for the solvent-cast material was sharper than that for the compression-moulded material. The results for other unloading rates were similar (not shown).

Figure 7.5 shows AFM images and indentation depth profiles taken after indentation for different loads (loading and unloading rates of 20 mN min⁻¹) on the solvent-cast PLGA material. The vertical distance was normalised by the permanent indentation depth for each load in order to compare the amount of pile-up. The results show a large amount of pile-up for all loads. These results are supported by the large amount of plastic deformation observed in Figure 7.4 (A) for indentation depths smaller than 3000 nm. Due to sample surface quality, reliable AFM indentation profile measurements were not achieved for the compression-moulded material.

7.5 Discussion

In this study, the nano- and micro-mechanical properties of the solvent-cast and the compression-moulded PLGA materials were determined with the nanoindentation technique. The study has demonstrated the importance of the processing method

on the mechanical properties of the PLGA material. The results for the elastic modulus and contact stiffness show that the solvent-cast material is more elastically compliant than the compression-moulded material. While the difference in density between the two materials may contribute to the difference in the elastic properties of the two materials, the difference in modulus is significantly greater than the difference in density. The reader is reminded here that the density of the compression-moulded and solvent-cast materials are $1.20 \pm 0.02 \text{ g cm}^{-3}$ and $1.06 \pm 0.06 \text{ g cm}^{-3}$, respectively.

It is more likely that the difference in elasticity is related to the presence of residual solvent in the solvent-cast material which tends to increase the mobility of the polymer chains as a plasticiser, resulting in less stiffness. These results are consistent with the results obtained by Rhim et al. (2006) for PLA. They showed that more than 10% of the solvent was retained in the solvent-cast film leading to a smaller modulus than that of the PLA films prepared by compression moulding. The higher value of hardness for the compression-moulded PLGA material may be due to the heat treatment during the compression moulding process which may increase the degree of crystallinity. Fouad et al. (2005) showed that the time and temperature of the heat treatment increase the degree of crystallinity and strongly affect the mechanical properties of ultra-high molecular weight polyethylene.

Depth dependence of the elastic modulus and hardness for the PLGA material prepared by both solvent casting and compression moulding methods was observed. Adhesion between the indenter and the polymer surface has been suggested as a cause for such a phenomenon (Dokukin and Sokolov, 2012; Gupta et al., 2007; Liao et al., 2010). In the present study, the negative pull-on adhesion force which is typical of this effect was not observed in the load-displacement curves. Therefore, it is unlikely that this is the cause of the depth dependence here.

The material inhomogeneity has been suggested as a possible reason for the depth dependence of mechanical properties (Briscoe et al., 1998; Charitidis, 2010), viz. the

existence of a *skin* where the material glass transition temperature is lowered. However, as discussed in Chapter 5, this is unlikely to be of major significance here since testing was performed well below the PLGA transition temperature. Also, there is a small variation in the density of the samples for each material and no evidence that the density changes across the thickness of the samples; this suggests that changes in density do not cause the observed depth dependence.

The results revealed that material loading rate dependence, and hence the influence of viscoelasticity, was not significant for the range of loading rates considered here, particularly for indentation depths less than 3000 nm (Figure 7.3 (A, C)). These results are consistent with the observations of Zhou and Komvopoulos (2006) for PMMA thin films, who showed that the effect of loading rate on the contact stiffness was more significant for larger indentation depths. These results contradict the discussion of Chapter 5 which suggested loading rate as an explanation for the observed modulus and hardness dependence. Corrections to the contact stiffness measurements, introduced in Chapter 2, have been proposed in order to reduce the effect of the time-dependent behaviour (Feng and Ngan, 2002; Tang and Ngan, 2003b); however, such discussion is beyond the scope of this study.

The present study showed that the power law exponent for the PLGA material is less than 2 for the range of indentation depths considered. This result is supported by the theoretical estimation of the power law exponent, which is equal to 2 for a perfect Berkovich indenter (Oliver and Pharr, 2004); however, empirical estimations have been shown to be in the range $1.2 \leq m \leq 1.6$ for a Berkovich indenter for a wide variety of metals and ceramics (Oliver and Pharr, 1992; Oliver and Pharr, 2004). In the present study, the values of the power law exponent for the compression-moulded material were all in this range, and the values for the solvent-cast material were all less than 2, irrespective of the indentation depth. This then strongly suggests that the increase in modulus at small indentation depths is not related to a change in power law exponent for the material of interest here.

This is in contrast to previous studies where this link has been demonstrated for polymers (Charitidis, 2010; Tranchida et al., 2007). Tranchida et al. (2007) reported that the power law exponent for isotactic polypropylene is larger than 2, even at very high indentation rates where the effect of viscoelasticity is expected to be small. Charitidis (2010) reported that the power law exponent varies between 0.6 and 1.35 when the indentation depth increases from 250 nm to 4000 nm for PDMS.

This study has demonstrated that significant plastic deformation occurs for indentation depths smaller than 3000 nm, as indicated by the increase in the plasticity index. Such a phenomenon has also been observed for other polymers, including PMMA and poly(vinylidene fluoride) (Tang et al., 2011), and also PDMS (Alisafaei et al., 2013). The result presented here is consistent with the substantial pile-up at lower indentation depths due to the upward flow of the material that was observed for the solvent-cast material (Figure 7.5). The presence of pile-up has been known to cause inaccuracy in the calculation of contact area for the determination of the elastic modulus and hardness through the Oliver and Pharr method (Bolshakov and Pharr, 1998; Oliver and Pharr, 2004). The effect of pile-up is explored here, with a view to improving the accuracy of the elastic modulus and hardness calculation and potentially giving insight into the depth dependence.

Cheng and Cheng (1998) proposed a method that does not require measuring the contact area for determining the modulus and hardness, thereby overcoming the difficulty caused by pile-up. They proposed a linear relationship between the plasticity index (η) and the ratio of the hardness to the reduced modulus (H_{IT}/E_r), regardless of the work hardening behaviour. This relationship was given for a Berkovich indenter (70.3° cone) when $h_p/h_m > 0.4$ (Cheng et al., 2002) as follows:

$$\eta = 1 - \gamma \frac{H_{IT}}{E_r} \quad (7.1)$$

where $\gamma = 5.74$ is obtained empirically.

To accompany this, the following equation is generated by combining Eqs. (3.48) and (3.50) and eliminating the area function (Joslin and Oliver, 1990):

$$\frac{4\kappa^2 F_{max}}{\pi S^2} = \frac{H_{IT}}{E_r^2} \quad (7.2)$$

The values of η , F_{max} , and S can be measured from the load-displacement curves and substituted into Eqs. (7.1) and (7.2). Subsequently, the values of H_{IT} and E_r can be calculated by solving these two independent equations. The elastic modulus is then obtained according to Eq. (3.49). This method is referred to the Cheng method herein.

Applying the above method to the PLGA data, results in new values of elastic modulus and hardness that are shown in Figure 7.6 (A, B). The Cheng method values are smaller than the Oliver and Pharr method values, indicating that the Oliver and Pharr method overestimates the elastic modulus and hardness, due to pile-up. The difference is substantially greater for the solvent-cast material in comparison to the compression-moulded material, indicating that pile-up is much less of an issue for the latter material. Using the results of the Cheng method and Eq. (3.48), the corrected contact area is calculated. Figure 7.6 (C) shows that the contact area obtained from the Oliver and Pharr method is smaller than that calculated by the Cheng method. Consistent with the elastic modulus and hardness results, the difference between the contact areas is more significant for the solvent-cast material at small indentation depths. For the compression-moulded material, a difference in the contact areas is observed for indentation depths larger than 8000 nm, and hence pile-up effects are relevant. After correcting for pile-up, the mechanical properties still exhibit the depth dependence. Therefore, while pile-up affected the material properties, this is not the reason for depth dependence in the present case.

As the material properties are significantly different when calculated using the Cheng method, it is important to check the actual applicability of the method (Eq. (7.1)) to PLGA in the present context. Several authors have previously explored the relationship between η and H_{IT}/E_r (Cheng et al., 2002; Choi et al., 2004; Ma et al., 2004; Malzbender and de With, 2002). The linear relationship proposed by Cheng and Cheng (1998) provides a good fit to materials with low H_{IT}/E_r , but a significant deviation can occur when H_{IT}/E_r is larger than 0.1 (Chen and Bull, 2009). Figure 7.6 (D) shows that for the PLGA data for all unloading (loading) rates, the linear relationship between η and H_{IT}/E_r captures the experimental data very well. The slight deviation when $H_{IT}/E_r > 0.05$ (or $\eta < 0.7$) is associated with larger indentation depths, but not with the small indentations where the depth dependence of the modulus is observed.

Notwithstanding the depth dependence, the results of this study show that the processing method has had a significant impact on the mechanical behaviour of the PLGA material. As discussed above, the solvent-cast material is more elastically compliant and exhibits lower hardness than the compression moulded material. It also exhibits significantly greater indentation pile-up effects, that are indicative of much lower work-hardening characteristics (Farrissey and McHugh, 2005); a large amount of pile-up may occur for a material with no work hardening and a large ratio of Young's modulus to yield strength (E/σ_y) (Bolshakov and Pharr, 1998; Cheng and Cheng, 2004), as discussed in Chapter 2. For the PLGA material considered in this study, E/σ_y is estimated to be between 76 and 85 (using data reported by the material supplier), which is close to the values reported for amorphous polymers (Brown, 1971). As noted above, such difference in the observed pile-up may be due to the compression moulding heat treatment and the associated possibility of crystallinity generation.

Finally, given all of the above considerations, the depth dependence in the present case is most likely explained, at least in part, by the influence of higher order displacement gradients. Indentation size effects in polymers, including the depth

dependence of the hardness and elastic modulus, have been shown to be attributed to higher order displacement gradients such as strain gradient plasticity (Chong and Lam, 1999; Voyiadjis et al., 2014) and rotational gradients due to the finite bending stiffness of polymer chains and their interactions (Nikolov et al., 2007). Alisafaei et al. (2014) showed that the depth dependence of the elastic modulus of epoxy could be attributed to the strain gradient due to a sharp Berkovich indenter; however using a spherical indenter, the elastic modulus remained constant with indentation depth as the strain gradient is independent of indentation depth for a spherical indenter.

7.6 Conclusion

The results of the present study showed that the solvent-cast material is more elastically compliant and plastically softer than the compression-moulded material, and it also displays lower work hardening characteristics. The measured elastic modulus and hardness are strongly depth dependent for both forms of the material, particularly for indentation depths lower than 3000 nm, which is most likely due to higher order displacement gradient effect. At larger depths, the measurement is slightly affected by the unloading rate; however, this effect is not pronounced. Despite the inherent difficulty in testing soft polymers, reliable and repeatable results should be achievable for the holding time and unloading (loading) rates given here. The Cheng method can be used to overcome difficulties in measurement of mechanical properties caused by indentation pile-up, and it is, therefore, arguably more accurate than the Oliver and Pharr method in the calculation of the elastic modulus and hardness.

The indentation test parameters presented in this chapter for the undegraded solvent-cast and compression-moulded PLGA materials are used later in Chapter 8 to investigate the changes in the mechanical properties of both forms of the material during degradation.

7.7 Figures

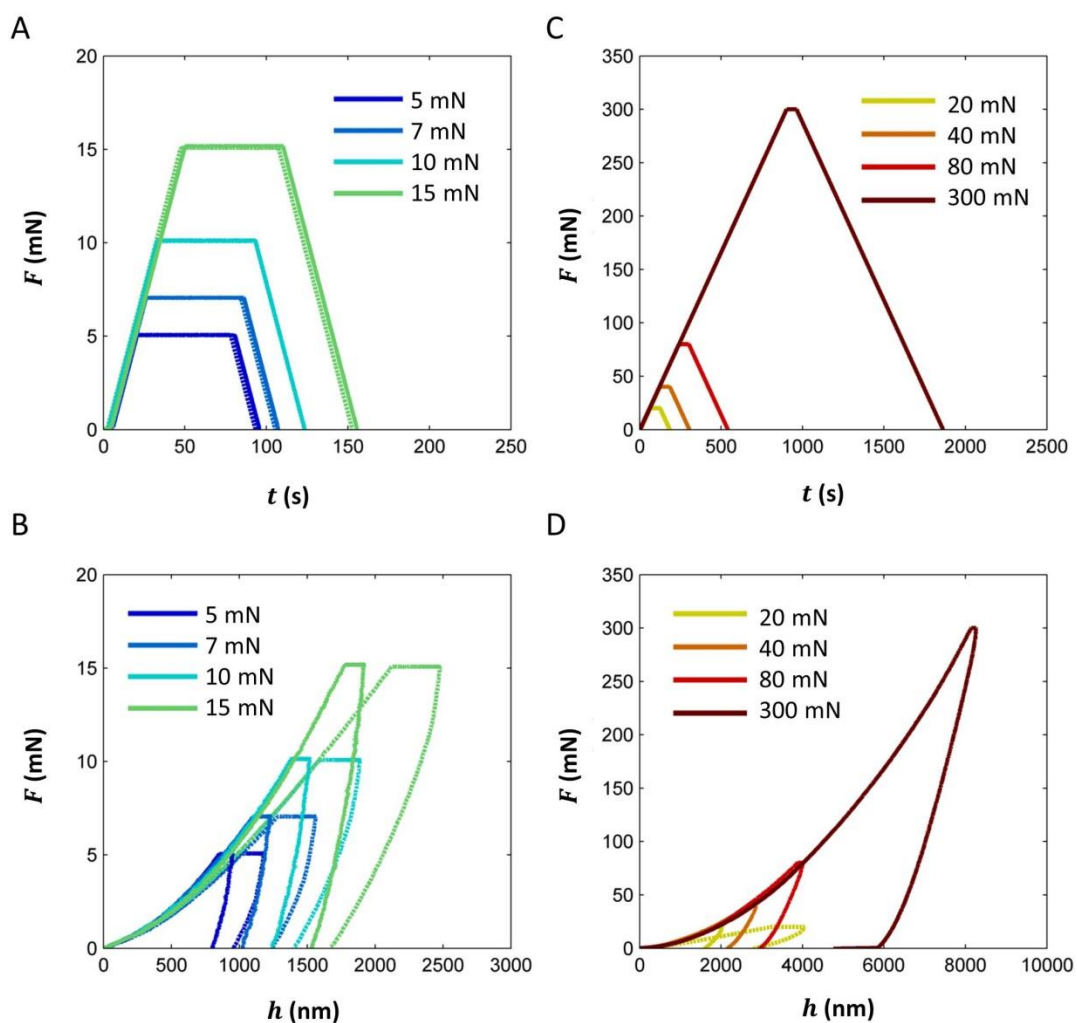


Figure 7.1: (A, C) Typical force-time ($F-t$) and (B, D) corresponding force-displacement ($F-h$) responses for the solvent-cast (solid lines) and compression-moulded (dashed lines) PLGA materials. The maximum applied load F_{max} is (A, B) 5 mN, 7 mN, 10 mN, 15 mN and (C, D) 20 mN, 40 mN, 80 mN, 300 mN. The loading and unloading rates are 20 mN min^{-1} and the holding time is 60 s.

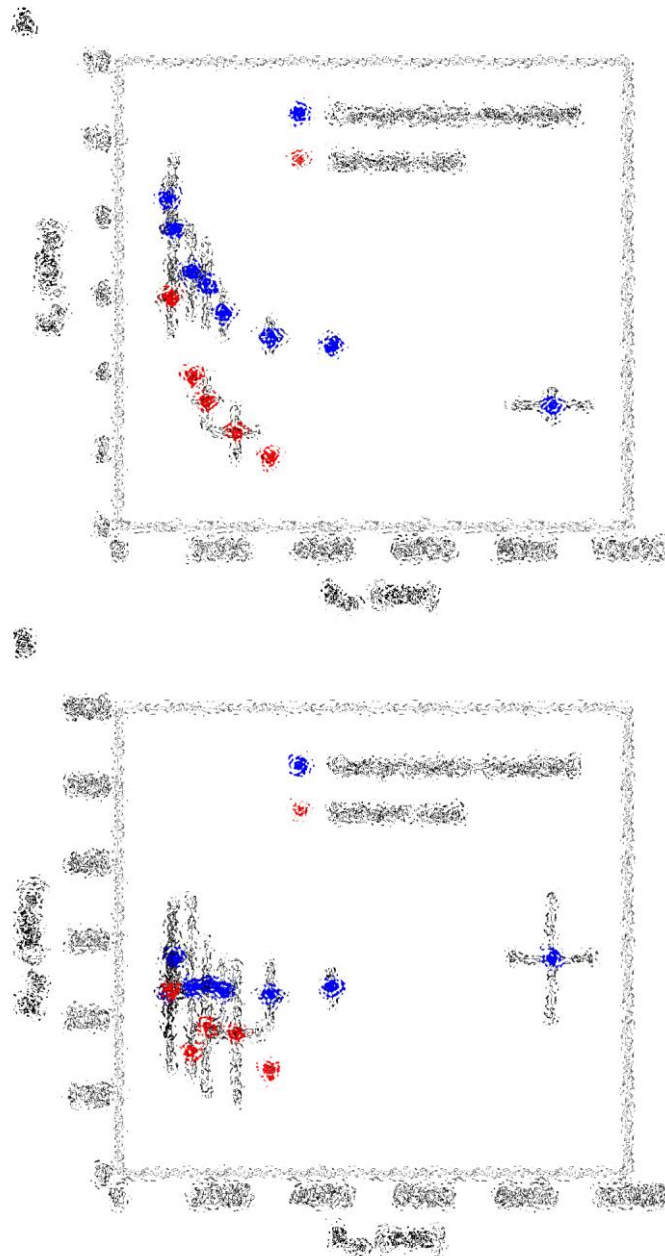


Figure 7.2: (A) Elastic modulus (E_s) and (B) hardness (H_{IT}) for the compression-moulded (solid circle) and solvent-cast (triangle) PLGA materials (mean \pm SD; $n = 20$), for the unloading (loading) rate of 40 mN min^{-1} . **Figure blurred due to copyright restrictions.**

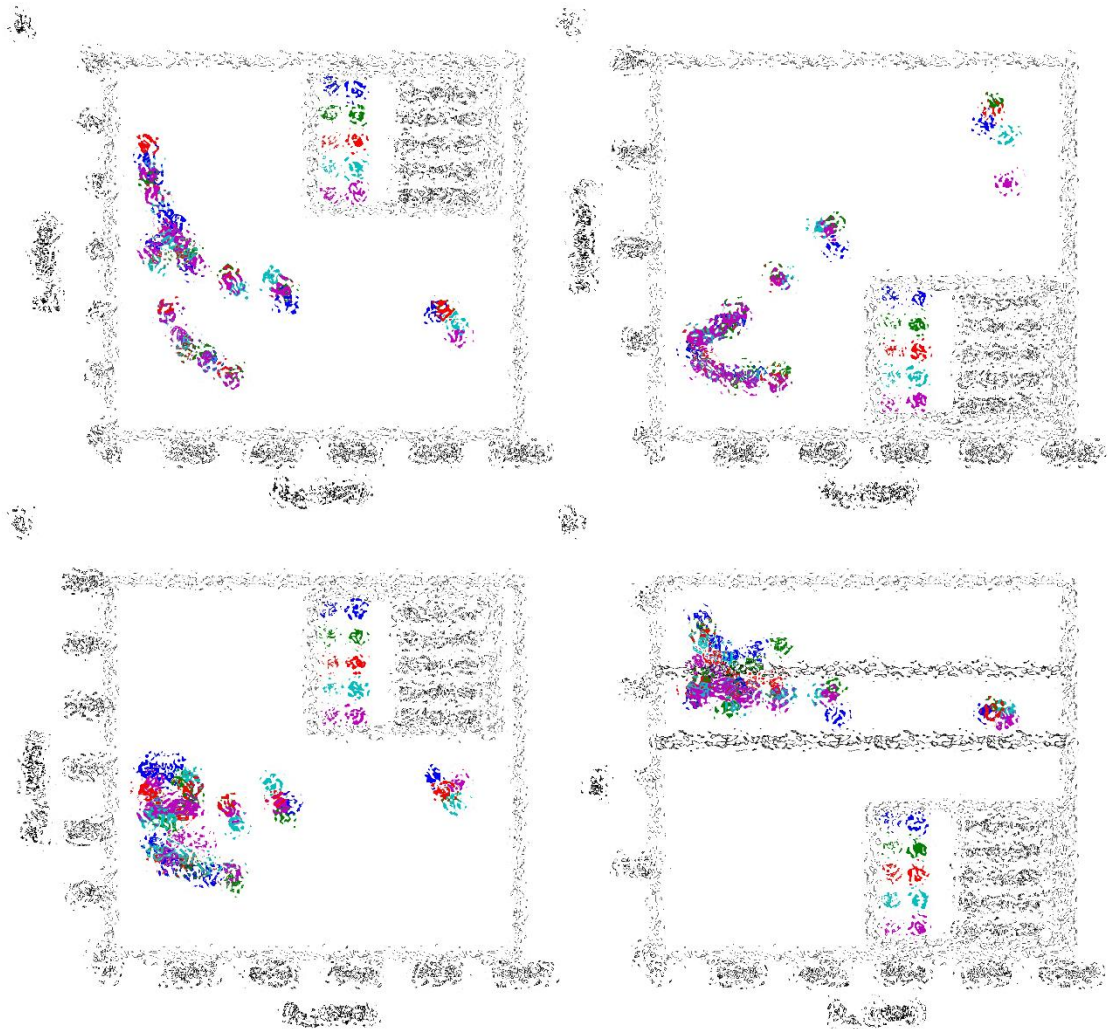


Figure 7.3: (A) Elastic modulus (E_s), (B) hardness (H_{IT}), (C) contact stiffness (S), and (D) power law exponent of the unloading curve (m) for the compression-moulded (solid circle) and the solvent-cast (triangle) PLGA materials (mean; $n = 20$, SD not included for clarity). The dashed lines in (D) indicate a typical range reported for a Berkovich indenter. **Figure blurred due to copyright restrictions.**

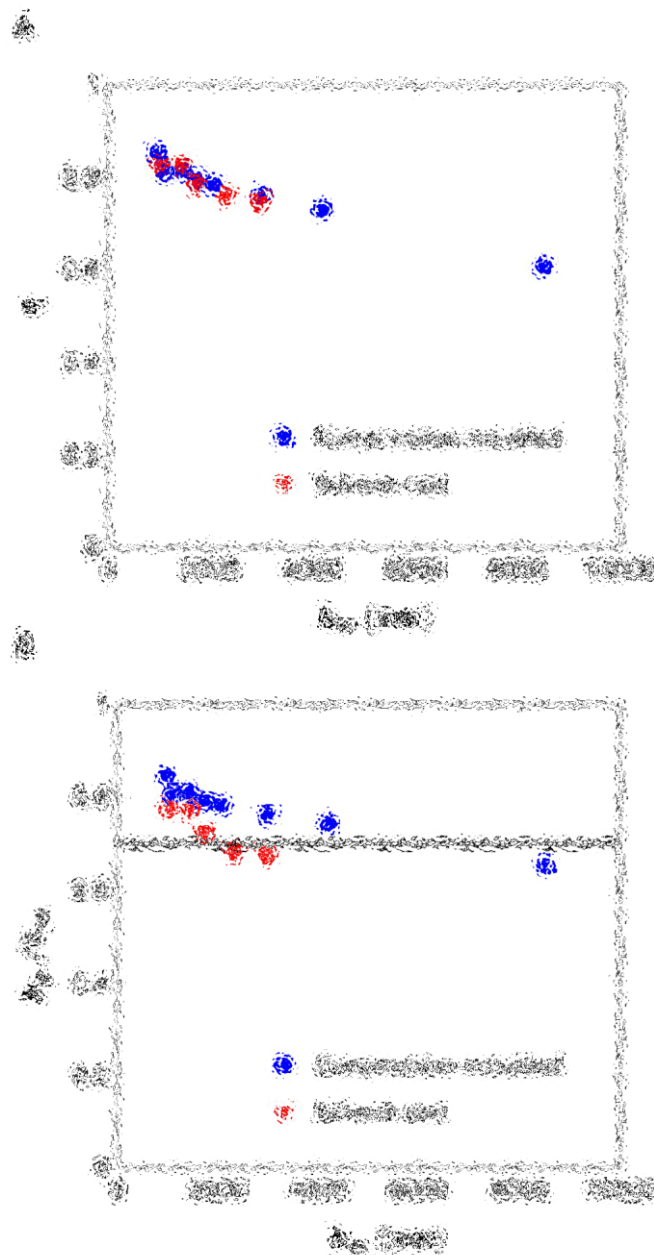


Figure 7.4: (A) Plasticity index (η) and (B) ratio of the permanent indentation depth (h_p) to the maximum indentation depth (h_m), for the unloading (loading) rate of 40 mN min^{-1} for the compression-moulded (solid circle) and solvent-cast (triangle) PLGA materials (mean; $n = 20$, SD not included for clarity). **Figure blurred due to copyright restrictions.**

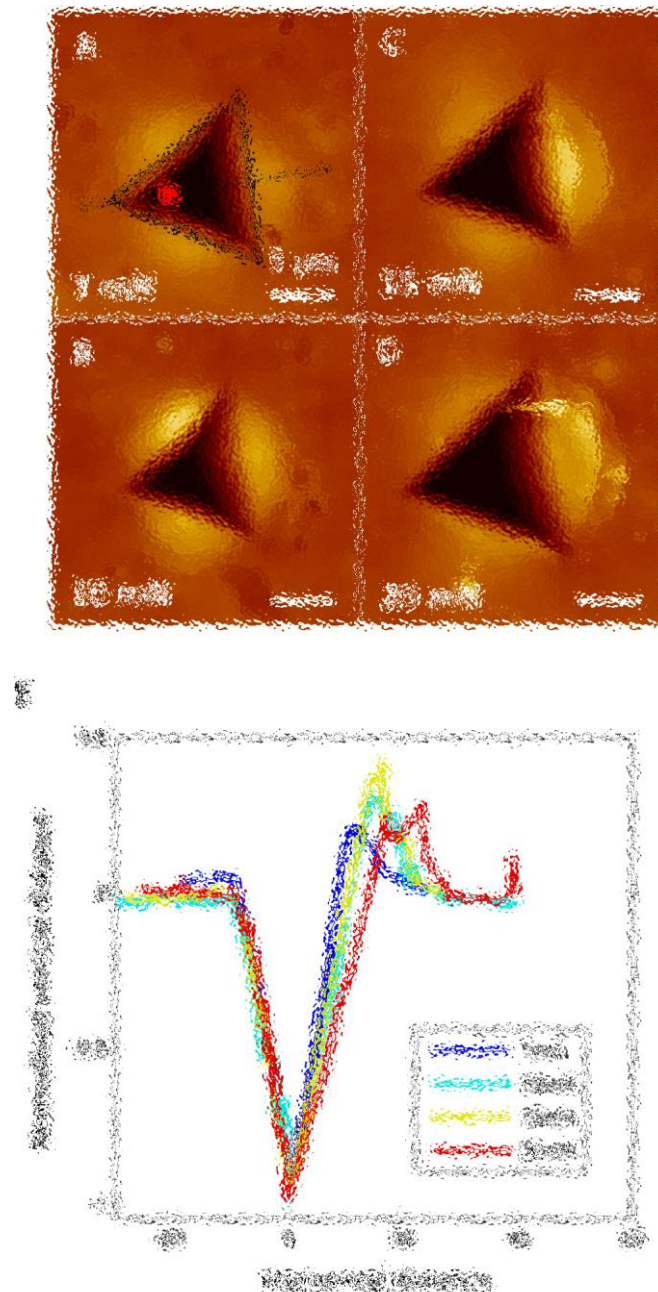


Figure 7.5: (A-D) AFM images of the solvent-cast PLGA material taken after indentation for different loads. (E) Cross sections show the indentation profile taken along a line through the deepest point (the dashed line in (A) with the red cross marking the deepest point). The scale bars indicate 5 μm . **Figure blurred due to copyright restrictions.**

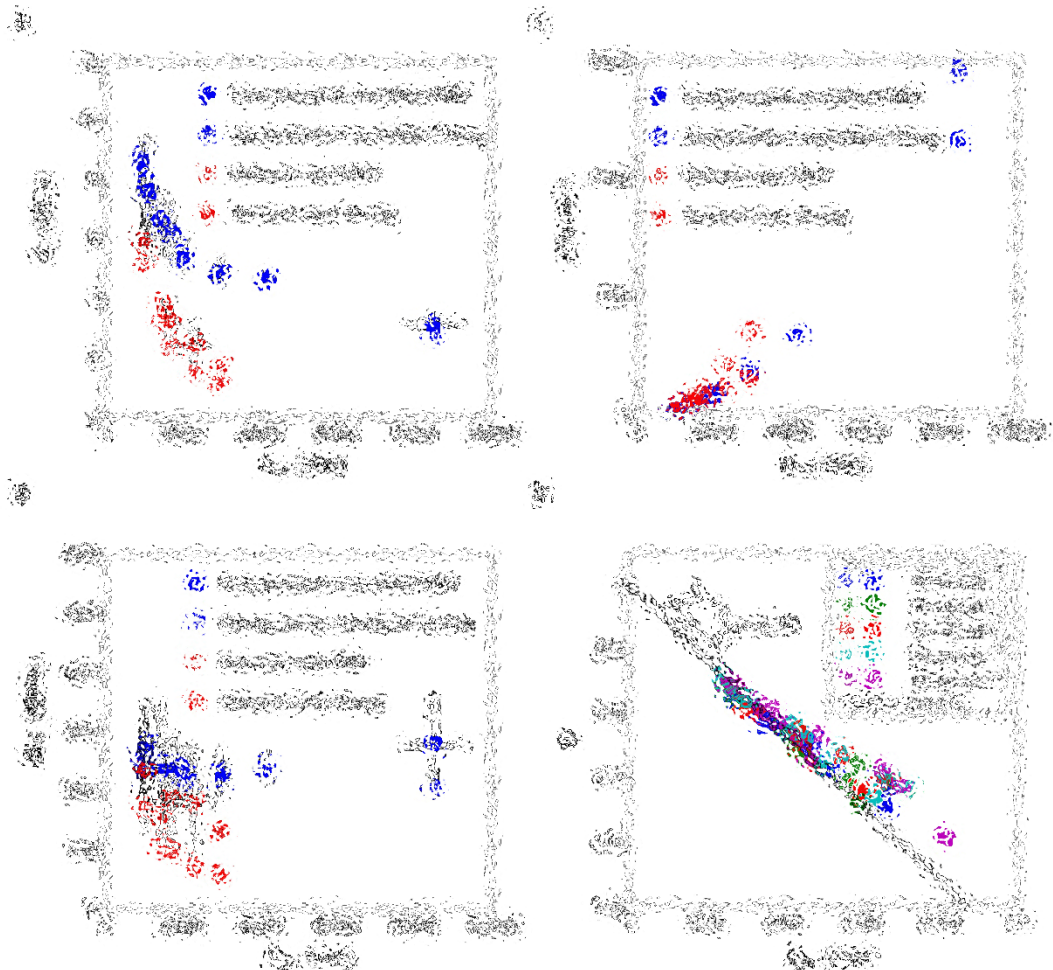


Figure 7.6: (A) Elastic modulus (E_s) (mean \pm SD; $n = 20$), (B) hardness (H_{IT}) (mean \pm SD; $n = 20$), and (C) contact area (A) (mean; $n = 20$) for the compression-moulded and the solvent-cast PLGA materials obtained by the Oliver and Pharr method (1992) and the method of Cheng and Cheng (1998). The unloading (loading) rate is 40 mN min^{-1} . (D) Relationship between the plasticity index (η) and the ratio of the hardness to the reduced modulus (E_r) for the compression-moulded (solid circle) and the solvent-cast (triangle) PLGA materials for different unloading rates (mean; $n = 20$, SD not included for clarity). The dashed line indicates Eq. (7.1). **Figure blurred due to copyright restrictions.**

7.8 Table

Table 7.1: The maximum loads, unloading (loading) rates, and the holding time used for the compression-moulded and the solvent-casted PLGA materials.

Method	Solvent casting	Compression moulding
Maximum load (mN)	5, 7,10, 15, 20	5, 7,10, 15, 20, 40, 80, 300
Unloading rates (mN min⁻¹)	10, 14, 20, 30, 40	10, 14, 20, 30, 40
Holding time (s)	60	60

8 Nanoindentation of Degraded Solvent-cast and Compression-moulded PLGA

8.1 Overview

In this chapter, the effects of material thickness and processing method on the degradation rate and the changes in the mechanical properties of PLGA material during simulated physiological degradation are investigated. Two types of PLGA materials are considered: 0.12 mm solvent-cast film (SC120) and 1 mm compression-moulded plate (CM1000). The experimental data presented in this chapter are compared to the experimental data for 0.25 mm solvent-cast film (SC250) presented in Chapter 5. These experimental observations are used to validate the computational model predictions on critical length scale in Chapter 6. The results presented here are used to refine the model parameters in order to predict more accurately the degradation behaviour and the mechanical performance of PLGA material during degradation.

The results show that the processing methods considered here do not have a significant effect on the degradation rate and the changes in mechanical properties during degradation; however, they influence the initial molecular weight and the stiffness of the PLGA material. The experimental observations in this chapter strongly support the computational modelling predictions that there is no significant difference between the degradation rate and the changes in the elastic modulus of PLGA films larger than 100 μm .

8.2 Introduction

Optimising the degradation rate of biodegradable polymers is one of the major challenges in designing degradable devices. As discussed previously in this thesis, length scales play an important role in the autocatalytic effect and in determining the degradation rate. As discussed in Chapter 6, in devices with a long diffusion length (l_{diff} refer to Eq. (6.5)), the acidic polymer fragments remain inside the polymer matrix which leads to acceleration of hydrolysis. The autocatalytic effect becomes more pronounced as the degradation proceeds. This causes heterogeneous degradation which is faster in the centre than at the surface, as shown in Chapter 5 for a 0.25 mm solvent-cast film. Fast degradation may cause negative effects such as local or systemic toxicity (Athanasidou et al., 1996) and a loss in cell viability (Sung et al., 2004) due to the acidic effect of degradation products. Therefore, it is important to determine a critical length scale above which the device undergoes heterogeneous degradation. Experimental studies have shown the effect of thickness on the degradation rate in various biodegradable polymers (Dunne et al., 2000; Grayson et al., 2005; Grizzi et al., 1995; Jonnalagadda and Robinson, 2004; Lu et al., 1999).

Despite extensive experimental studies on the degradation of biodegradable polymers, the critical thickness at which the effect of autocatalysis becomes pronounced is unclear; there is no consensus in the literature. Computational modelling has been used in an effort to provide insightful interpretation of experimental results (Chen et al., 2011; Ford Versypt et al., 2013; Sackett and Narasimhan, 2011; Wang et al., 2008) and can be very useful when attempting to quantify the thickness dependence, as discussed in Chapter 6.

One of the most important mechanisms to include when developing a model of polymer degradation behaviour is diffusion transport. As discussed in Chapter 6, it plays a critical role in determining the type of degradation that will occur, given that autocatalysis is the fundamental reason for the size dependence. Such reaction-

diffusion models have significant potential to assess and predict the rate of degradation and to aid the design of biodegradable devices. The change in the mechanical properties of biodegradable polymers during degradation is another critical design factor. Biodegradable devices are intended to degrade over time and, from a mechanical perspective, the design requirement for an implanted device is that it must have appropriate mechanical properties and an adequate degradation rate to maintain the mechanical integrity over the desired lifetime. Therefore, it is important that the influence of degradation on the mechanical properties of biodegradable materials is fully understood.

As shown in Chapter 5, PLGA material retains its mechanical integrity until the molecular weight of the polymer chains reaches a critical molecular weight. Based on this, a computational modelling framework, introduced in Chapter 3, was used in Chapter 6 to predict the degradation rate and the changes in the elastic modulus of PLGA structures during degradation. The results of the computational simulations indicated a critical length scale in the range 2-100 μm below which homogenous degradation occurs.

Further to the results presented in the previous chapters, the first objective of this study is to evaluate the effects of material thickness and the processing method on *in-vitro* degradation and the changes in the mechanical properties of PLGA material during simulated physiological degradation. The first objective is achieved in part by comparing experimental data generated here with experimental data presented in Chapter 5. Additionally, this comparison contributes to the validation of the computational model predictions on critical length scale presented in Chapter 6. This leads on to the second objective of this study which is to refine the model parameters determined in Chapter 6 based on the experimental observations for the degradation and the changes in the elastic modulus of the three PLGA materials with different thicknesses. This allows for more accurate predictions of the degradation rate and the mechanical performance of PLGA material during degradation.

8.3 Methods

8.3.1 Materials and Experimental Methods

In this chapter, a 0.12 mm film (SC120) and a 1 mm plate (CM1000) were used which were prepared by solvent casting and compression moulding, respectively, as described in Chapter 4. Overall, 42 solvent-cast samples and 36 compression-moulded samples were generated.

To simulate *in-vitro* degradation conditions, the specimens were placed in PBS with pH 7.4, at 37°C as described in Chapter 4. The 1 mm plate was immersed and exposed to the solution on both sides, whereas the film was cast onto dishes and exposed to media at one side only. The specimens were removed from the PBS at each degradation time point. Three samples were used for each degradation time point to calculate the mass remaining and water content (according to Eq. (4.2)) and to determine the molecular weight by gel permeation chromatography as described in Chapter 4. The results for the mass loss and water uptake and also the molecular weight of the solvent-cast 0.25 mm film (SC250) presented in Chapter 5 are included here for comparison purposes.

The mechanical properties of each material were measured using the nanoindentation technique. A linear force-controlled loading and unloading mode was used with a maximum load F_{max} of 7 mN and 40 mN (refer to Figure 7.1). These two values were used in order to investigate the depth dependence of the elastic modulus of the material of interest during degradation, for maximum indentation depths h_m lower and higher than 3000 nm, as discussed in Chapter 7. However, attention was primarily focused on the maximum load of 7 mN in order to compare the results with the mechanical properties of the 0.25 mm solvent-cast film (SC250) presented in Chapter 5.

The loading and unloading rates of 14 mN min⁻¹ were used with 60 s holding time between loading and unloading. A matrix of 5 x 5 indents was used to perform a

single batch of identical indentations with spacing of 100 μm to avoid overlapping the elastic field of each indent (refer to Figure 4.4). Then, the average of 20 indents was used to determine the Young's modulus and hardness of the samples based on the Oliver and Pharr method (1992) described in Chapter 3. Data were expressed as means \pm standard deviation.

8.3.2 Computational Modelling

The coupled computational modelling framework described in Chapter 3 was used in order to predict the degradation behaviour and the changes in the elastic modulus of the PLGA films and plate. A 0.12 mm thick film was modelled as a one-dimensional problem. As described in Chapter 6, contact on the outside of the film with the aqueous medium was represented by assuming the concentration of monomers at the boundary of the film is zero (refer to Figure 6.2 (A)), which means that all the monomers which reached the surface are immediately convected away from the surface by the environmental flow. The flux of monomers at all other boundaries, including the interface between the film and the substrate, was set to zero.

A 0.5 mm thick film was modelled as a one-dimensional problem representing the 1 mm plate, exposed on both sides. The plate is represented in terms of half its thickness in conjunction with symmetry boundary conditions as described above for the film (Figure 8.1 (A)). A simple mesh of hexahedral elements was used through the film and plate thickness, and thinner boundary layer elements were used at the surface where higher gradients in the solution variables occur (Figure 8.1 (B)). The same number of elements was used for the 0.12 mm film and 1 mm plate.

The changes in the molecular weight of the polymer during degradation were simulated using the molecular weight model in COMSOL, described in Chapter 3, via variables C_e and C_m , i.e. the concentrations of esters bonds and monomers, respectively. The numerical solution of the molecular weight model was obtained at each time step in each finite element using an implicit backward differentiated

formula (BDF) method, with the maximum order of 2. The changes in the Young's modulus during degradation were predicted using the relationship between the molecular weight and the Young's modulus obtained from the mechanical properties model described in Chapter 3.

8.4 Results

8.4.1 Mass Loss and Water Uptake

The water uptake and mass remaining of the 0.12 mm and 0.25 mm solvent-cast films and the 1 mm compression-moulded plate during degradation are shown in Figure 8.2. The results show that there was no significant difference between the amounts of water uptake for the films and the plate at the earlier stages of degradation (Figure 8.2 (A)). The amount of water uptake increased to $30.4 \pm 1.1\%$ for the 0.12 mm film after 21 days of degradation; however, the water uptake of the 0.25 mm film and 1 mm plate were $12.7 \pm 0.1\%$ and $8.7 \pm 0.2\%$, respectively, after 19 days.

The results show that the rate of decrease in the weight of the 0.12 mm film was more than that of the 0.25 mm film and 1 mm plate for the initial 7 days of degradation (Figure 8.2 (B)). However, following this the rate of weight decrease for the 0.25 mm film and 1 mm plate increased, and the materials had lost 15% and 13% of their initial masses, respectively, after 19 days. The 0.12 mm film had lost 14% of its initial mass after 21 days of degradation.

8.4.2 Molecular Weight

The changes in the molecular weight and polydispersity of the 0.12 mm and 0.25 mm solvent-cast films and the 1 mm compression-moulded plate are shown in Figure 8.3. The results show that the molecular weight of the undegraded compression-moulded material was smaller than that of the undegraded solvent-cast material (Figure 8.3 (A, B)). During degradation, the molecular weight decreased gradually; the rate of decrease in the number average molecular weight

M_n of the 0.12 mm film was faster than that of the other two materials. However, there was no significant difference between the rates of reduction for the weight average molecular weight M_w of the three materials.

The polydispersity of the undegraded materials was very similar (Figure 8.3 (C)). For the 0.12 mm film and the 1 mm plate, the polydispersity increased for the first 13 days of degradation and then it decreased; however, the polydispersity of the 0.25 mm film was constant until day 9 and then it increased reasonably linearly.

8.4.3 Mechanical Properties

Figure 8.4 shows the changes in the elastic modulus E_s and hardness H_{IT} of the 1 mm compression-moulded plate for the maximum indentation loads F_{max} of 7 mN and 40 mN. The results show that the elastic modulus of the undegraded materials decreased when the applied load (or the indentation depth) increased. The depth dependence of the hardness was not significant as that of the elastic modulus. The elastic modulus and hardness of the compression-moulded material were 7.5 ± 0.9 GPa and 227.29 ± 46.19 MPa, respectively for the indentation load of 7 mN. Apart from the increase in hardness after 9 days, the changes in the elastic modulus and hardness of the material were not significant over the first 17 days of degradation. After 19 days, the elastic modulus and hardness decreased significantly by more than 95% and 85% of their initial values, respectively.

The mechanical properties of the 0.12 mm solvent-cast film were measured for the indentation load of 7 mN, and these will be presented below. Due to sample degradation, reliable indentation measurements were not achieved for the solvent-cast material for the indentation load of 40 mN.

Figure 8.5 shows the changes in the Young's modulus and hardness of the 0.12 mm and 0.25 mm films and the 1 mm plate during degradation. These results for the 0.12 mm film and the 1 mm plate for the indentation load of 7 mN allow a comparison with the results presented in Chapter 5 for the 0.25 mm film. As discussed in Chapter 7, the elastic modulus and hardness of the undegraded

compression-moulded material were larger than those of the undegraded solvent-cast material. The hardness of the compression-moulded material increased after 9 days of degradation. The elastic modulus and hardness of the 0.25 mm film and the 1 mm plate decreased significantly after 19 days of degradation; however, a significant decrease in the elastic modulus and hardness of the 0.12 mm film occurred at day 21.

8.4.4 Model Calibration

The parameters of the molecular weight model (k_1 , k_2 , and D_0) and the mechanical properties model (N_{chains} , $R_{scissions}$, and M_n^{crit}) presented in Chapter 6 were updated in order to obtain a set of parameters which give a good fit to the experimental data for the molecular weight and the changes in the elastic modulus of the 0.12 mm and 0.25 mm films and the 1 mm plate during degradation.

An initial number average molecular weight (M_{n0}) of 79,000 g mol⁻¹, 82,000 g mol⁻¹, and 68,000 g mol⁻¹ were assumed for the 0.12 mm and 0.25 mm films, and the 1 mm plate, respectively. These values were obtained from the experimental GPC results presented in section 8.4.2. As described in Chapter 6, the initial concentration of ester bonds (C_{e0}) was set at 17,300 mol m⁻³ (Wang et al., 2008). A wider range of parameters (k_1 , k_2 , and D_0) relative to that used in Chapter 6 was applied here in order to obtain a set of parameters which give a good fit to the experimental data for the three materials. The values of k_1 and k_2 were set in a range between 0.0006 and 0.2. The values of D_0 were set in a range between 10⁻¹² and 10⁻⁹.

The mechanical properties model was used to predict the experimentally observed relationship between normalised E and M_n . As discussed in Chapter 6, the best model fit to all experimental data was achieved using $N_{chains}=3000$ polymer chains and $M_n^{crit}=1500$ g mol⁻¹. For less than 3000 polymer chains (300, 500, or 1000), the molecular weight of the chains in the simulation did not match the experimental GPC data. For more than 3000 polymer chains (10,000 or 20,000), similar results to

the 3000 polymer chains were achieved. Different values of random to end scission ratios (3:1, 1:1, 1:12 or 1:50) did not show any significant effect on the results.

Figure 8.6 shows the best fit for the normalised M_n and E to the experimental data presented above for the 0.12 mm and 0.25 mm films, and the 1 mm plate. The goodness of the fitting was established by the R^2 values. A computer code was developed in MATLAB (R2014a, Mathworks Inc., MA, USA) to calculate the R^2 values based on the linear least squares regression method. The R^2 values were calculated for each set of parameters (k_1 , k_2 , and D_0) and for each of the three materials with different thicknesses. Then, the maximum value of R^2 was given for the normalised M_n and E versus time. Comparing the maximum values of R^2 for the normalised M_n versus time and those for the normalised E versus time, the best fit was achieved by setting $\beta = 0.5$, $k_1 = 0.02 \text{ day}^{-1}$, $k_2 = 0.001 (\text{m}^3 \text{ mol}^{-1})^{0.5} \text{ day}^{-1}$, and $D_0 = 10^{-12} \text{ m}^2 \text{ day}^{-1}$ for all materials. The R^2 values for the best fit are included in the figure.

8.5 Discussion

In this study, the degradation rate and the changes in the mechanical properties of the solvent-cast and compression-moulded PLGA materials with different thicknesses were considered. The material parameters for the computational model predictions described in Chapter 3, corresponding to the 0.25 mm solvent-cast film, were refined to give the best fit to the experimentally observed changes in the molecular weight and the elastic modulus of the 0.12 mm solvent-cast film and 1 mm compression-moulded plate.

The results of this study showed the depth dependence of the elastic modulus of the compression-moulded PLGA materials during degradation. The depth dependence of the hardness was not significant as that of the elastic modulus. Similar results were observed previously in Chapter 5, for degraded solvent-cast PLGA film and also in Chapter 7, for undegraded solvent-cast PLGA film and compression-moulded PLGA plate. A number of possible explanations for the depth

dependent of the elastic modulus and hardness of PLGA material were discussed previously in Chapters 5 and 7.

The present study has demonstrated that there is no significant difference in the degradation rate of PLGA material thicker than 0.12 mm, as indicated by the decrease in the weight average molecular weight. However, the decrease in the number average molecular weight of 0.12 mm film was faster than that of 0.25 mm film and 1 mm plate. The difference between the decrease in the weight average molecular weight and the number average molecular weight is due to the fact that the number average molecular weight is strongly influenced by the relatively small number of molecules of low molecular weight. The molecules of small molecular weight can be produced as a result of end scissions, where scissions occur at the final bond at chain ends resulting in the production of monomers.

A faster decrease in the weight of 0.12 mm film at the earlier stages of degradation indicates that a significant number of polymer chains which were produced as a result of end scission were small enough to diffuse from the polymer matrix to the surrounding medium. An initial delay in the reduction of the number average molecular weight and the mass loss of 0.25 mm film and 1 mm plate may be related to the small polymer chains, which are produced as a result of end scission, being unable to diffuse to the medium due to the larger diffusion length. If this were the case then this would result in the accumulation of the carboxylic acid chain ends of water-soluble oligomers and monomers inside the polymer matrix which would accelerate the hydrolytic degradation and therefore the mass loss at the later stage of degradation. This is consistent with the observations here after 7 days of degradation; however, this effect is not pronounced.

The experimentally observed results for the degradation rate of PLGA materials presented in this chapter are in agreement with the computational modelling predictions presented in Chapter 6. The computational predictions suggested a critical length scale in a range 2-100 μm , above which the PLGA material undergoes

heterogeneous degradation. Although the experimental results presented here did not consider the degradation rate of PLGA thinner than 120 μm , the agreement here suggests that the model has captured the correct behaviour.

As discussed in Chapter 5, despite the fact that the degradation of PLGA material results in a quick decrease in the material molecular weight, the elastic modulus of PLGA material does not decrease until the number average molecular weight of the polymer chains reaches a critical molecular weight, i.e. 1500 g mol^{-1} .

The results of the present study showed that there was no significant difference in the decrease in the elastic modulus of the 0.12 mm and 0.25 mm films and the 1 mm plate. On this basis, the experimental observation further supports the computational predictions discussed in Chapter 6 (refer to Figure 6.8) which showed no significant difference between the changes in the elastic modulus of PLGA films larger than 100 μm . The set of model parameters which have been proposed in the present study results in a critical length scale equals to 3 μm below which degradation is homogenous. This result is very similar to the critical length presented in Chapter 6. The set of model parameters proposed here can be used to characterise the PLGA material irrespective of thickness.

The present study has demonstrated that the specific processing method considered here affects the initial molecular weight of PLGA material and it determines the initial stiffness of the material. The smaller molecular weight of the undegraded compression-moulded material may be related to the heat treatment during the compression moulding process which may cause the degradation of polymer. This result is consistent with the observations of Gogolewski and Mainil-Varlet (1997) for PDLLA orthopaedic pins. They showed that the molecular weight of the heat-treated pins decreased due to the heat treatment over 50 hours at 135°C under moisture-free argon. As discussed in Chapter 7, the heat treatment during the compression moulding process may cause an increase in the degree of crystallinity of the polymer (Fouad et al., 2005), which results in an increase in the

hardness of the compression-moulded material relative to that of the solvent-cast material. The lower stiffness of the solvent-cast material relative to the compression-moulded material may be due to the residual solvent in the solvent-cast material which causes an increase in the mobility of the polymer chains (Rhim et al., 2006).

The present study has demonstrated that the material processing methods considered here do not have a significant influence on the degradation rate and the changes in the mechanical properties of PLGA during degradation. This can be concluded despite the observed increase in the hardness of the compression-moulded material after 9 days of degradation, which is more likely due to the influence of the surface roughness, indicated by the large scatter in the hardness measurements.

A number of studies have shown the effect of materials processing method on the degradation rate of PDLLA material (Cui et al., 2008; Miller et al., 2001); although the material considered in these studies are different to that in the present study. Cui et al. (2008) showed that a PDLLA electrospun fibrous mat degrades more slowly than a PDLLA film prepared by solvent casting, due to the enrichment of hydrophobic methyl group on the surface of the electrospun mat. They proposed that the high voltage of electrospinning process may cause the enrichment of the chemical groups, which results in slower water diffusion rate from the medium in the fibre matrix. This result is in contrast to the observation of the present study, which may be due to the different processing methods to those applied here.

Miller et al. (2001) showed that 10 μm by 3 μm grooves on the surface of PDLLA films degrade faster for compression moulded films compared with solvent cast; however, they attribute this to elevated temperatures during the compression moulding process. Furthermore, Miller et al. visually inspect their samples for signs of degradation using scanning electron microscopy, rather than measuring the molecular weight.

In Chapter 5, the experimental results showed that the amorphous solvent-cast PLGA material remains amorphous during degradation. In the case of the compression-moulded material, any crystallinity present may have an effect on the degradation behaviour; however, as there were no significant differences in the degradation behaviour and the material properties, either the degree of crystallinity must be small or the effect of crystallinity on PLGA degradation is small. In the case of PLA, a crystallinity of 30% did not affect the initial degradation behaviour, but did alter the water uptake and swelling during the later stages of degradation (Pantani and Sorrentino, 2013). However, the effect of crystallinity on PLGA degradation is complicated by the fact that the crystallinity can increase the degradation rate (Chye Joachim Loo et al., 2005).

8.6 Conclusion

This study investigated the experimental and computational analysis of the degradation behaviour and the changes in the mechanical properties of PLGA material with different thicknesses which were prepared by solvent casting and compression moulding. The experimental results presented here show that the specific material processing methods considered here do not have a significant effect on the degradation rate and the changes in the mechanical properties during degradation; however, it influences the initial molecular weight and it determines the stiffness of the material. It was shown that the initial molecular weight of the compression-moulded material is smaller than that of the solvent-cast material. The experimental observations in this chapter strongly support the computational modelling prediction that show no significant difference between the degradation rate and the changes in the elastic modulus of PLGA film larger than 100 μm .

8.7 Figures

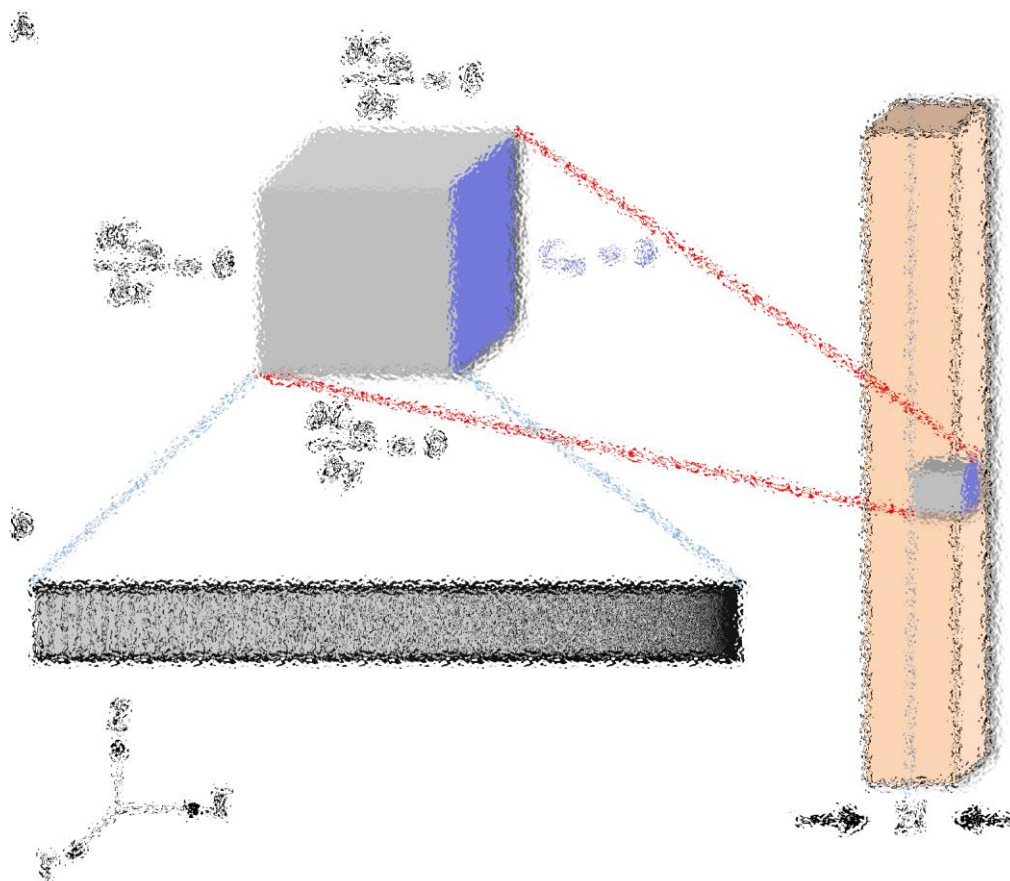


Figure 8.1: (A) The monomer boundary conditions and (B) the mesh element used through the plate thickness $2l$ in the molecular weight model. The thickness of a film l is equal to half the thickness of the plate. **Figure blurred due to copyright restrictions.**

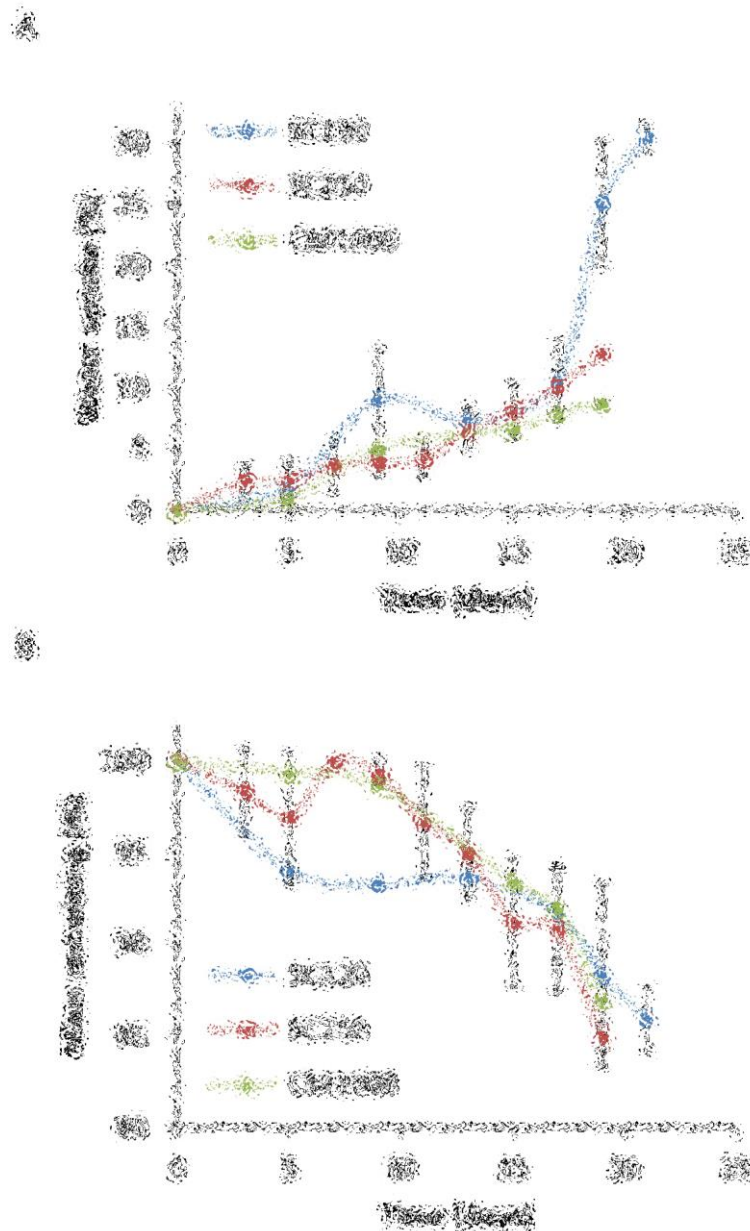


Figure 8.2: Changes in the (A) water uptake and (B) mass remaining of the 0.12 mm and 0.25 mm solvent-cast PLGA films (SC120 and SC250) and the 1 mm compression-moulded PLGA plate (CM1000) during degradation (mean \pm SD; n = 3). **Figure blurred due to copyright restrictions.**

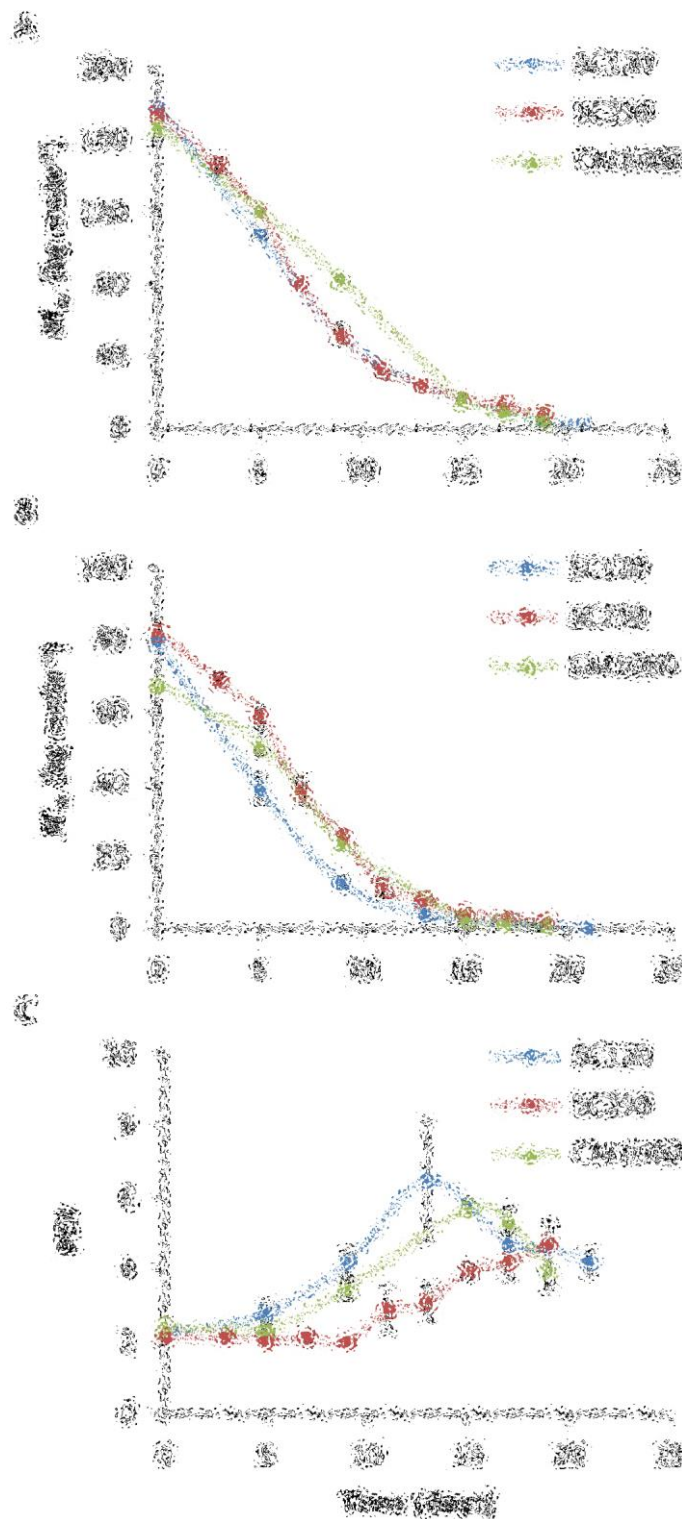


Figure 8.3: Changes in the (A) weight average molecular weight (M_w), (B) number average molecular weight (M_n), and (C) polydispersity index (PDI) of the 0.12 mm and 0.25 mm solvent-cast PLGA films (SC120 and SC250) and the 1 mm compression-moulded PLGA plate (CM1000) during degradation (mean \pm SD; $n = 3$). **Figure blurred due to copyright restrictions.**

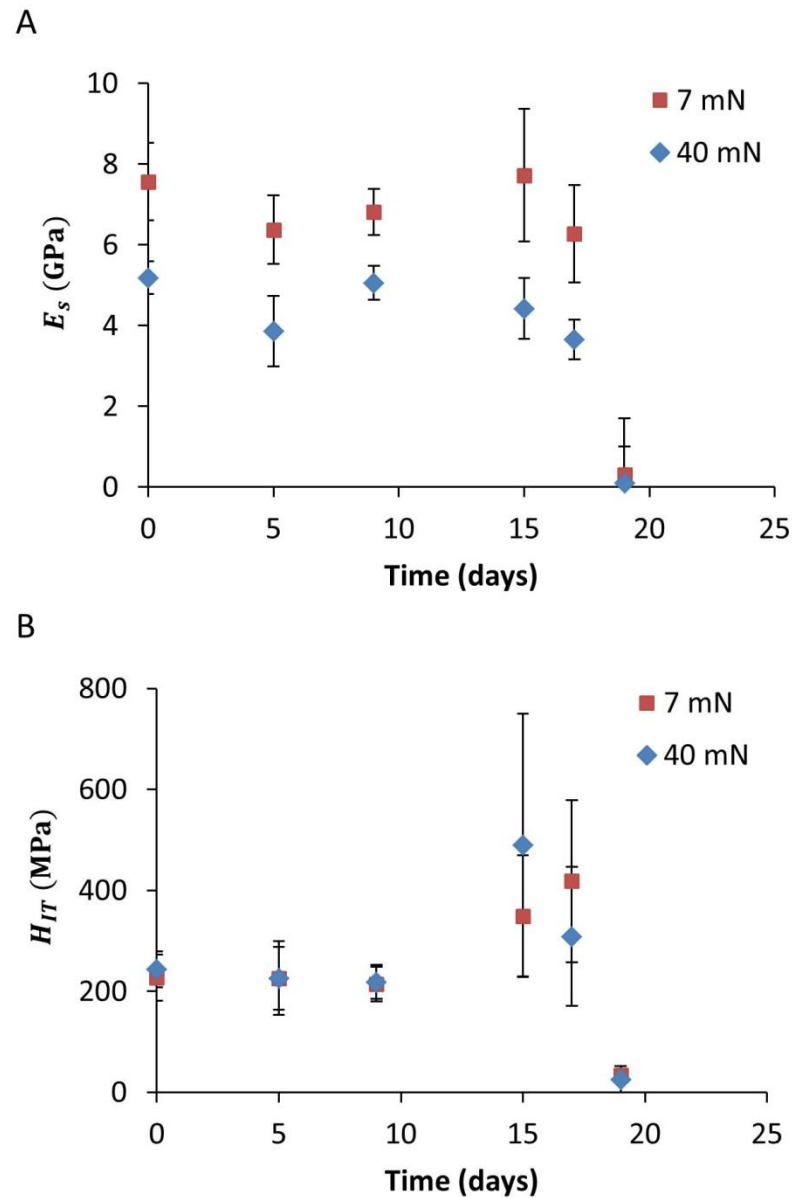


Figure 8.4: Changes in the (A) Young's modulus (E_s) and (B) hardness (H_{IT}) of the 1 mm compression-moulded PLGA plate (CM1000) during degradation for the maximum loads F_{max} of 7 mN and 40 mN (mean \pm SD; $n = 20$).

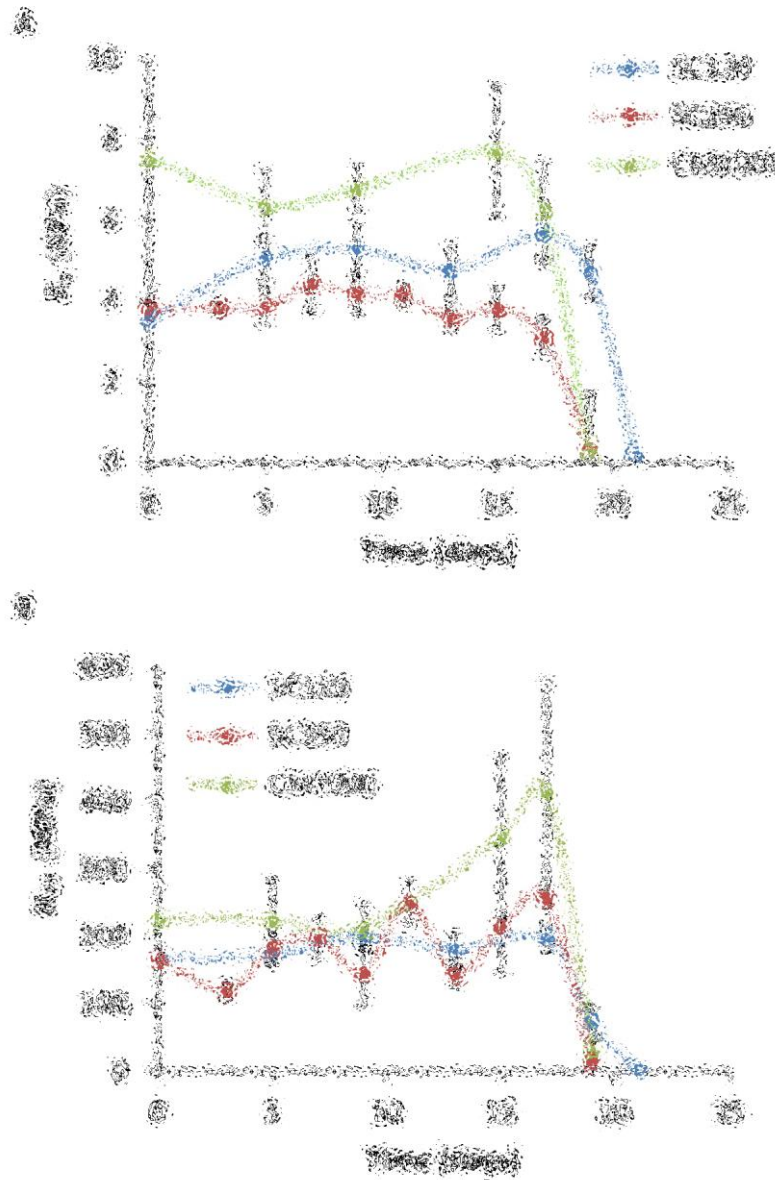


Figure 8.5: Changes in the (A) Young's modulus (E_s) and (B) hardness (H_{IT}) of the 0.12 mm and 0.25 mm solvent-cast PLGA films (SC120 and SC250) and the 1 mm compression-moulded PLGA plate (CM1000) during degradation (mean \pm SD; $n = 20$). The maximum load F_{max} of 7 mN is used. **Figure blurred due to copyright restrictions.**

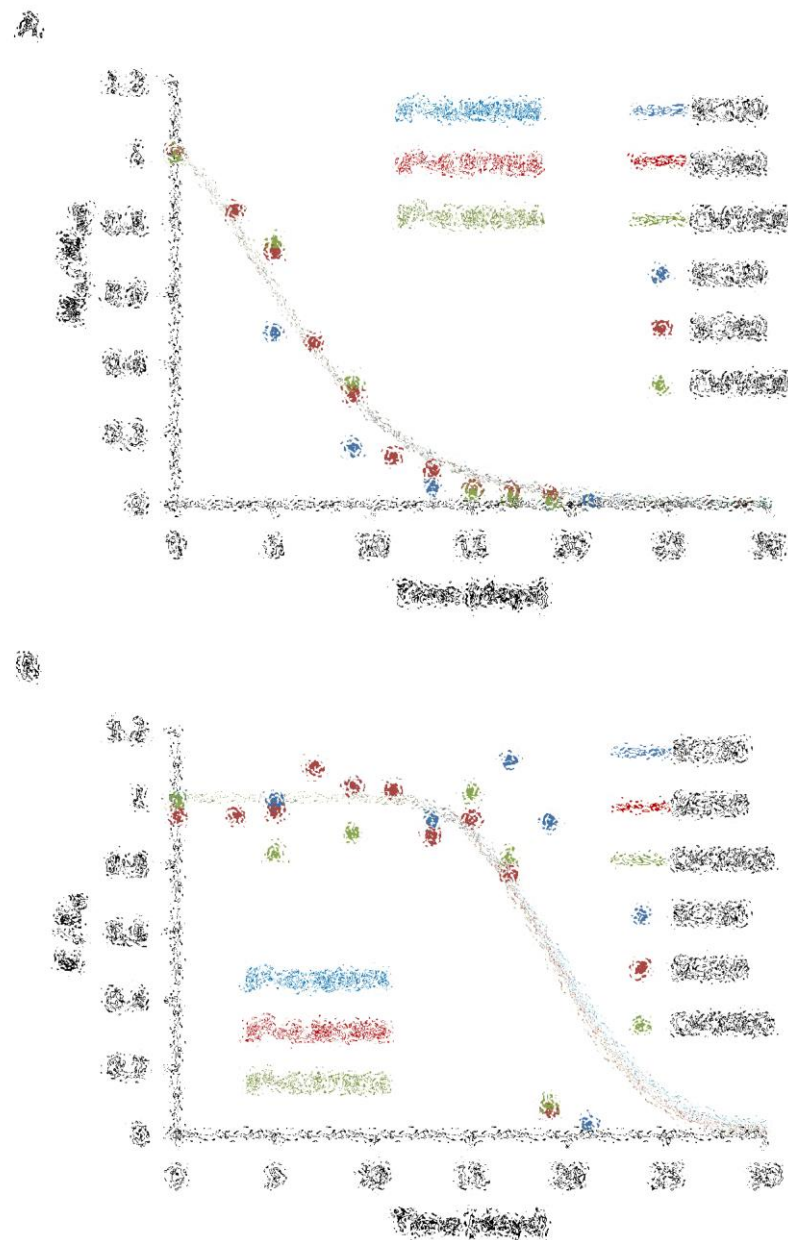


Figure 8.6: Model fittings of normalised (A) number average molecular weight (M_n/M_{n0}) and (B) Young's modulus (E/E_0) to the 0.12 mm and 0.25 mm solvent-cast PLGA films (SC120 and SC250) and the 1 mm compression-moulded PLGA plate (CM1000). The solid lines and the discrete dots show the model predictions and the experimental data, respectively. The R^2 values show the best fits which were achieved by setting $\beta = 0.5$, $k_1 = 0.02 \text{ day}^{-1}$, $k_2 = 0.001 \text{ (m}^3 \text{ mol}^{-1})^{0.5} \text{ day}^{-1}$, and $D_0 = 10^{-12} \text{ m}^2 \text{ day}^{-1}$. The different R^2 values are related to SC120, SC250, and CM1000 which are indicated by blue, red, and green. **Figure blurred due to copyright restrictions.**

9 Discussion and Conclusions

9.1 Introduction

This chapter summarises and discusses the outcomes of the work in this thesis. A brief overview of the novelty of the work performed is given in section 9.2. A summary and discussion of the outcomes of each of the result chapters is given in section 9.3. Overall conclusions are given in section 9.4. Finally, proposals for future investigations involving the approach used in this thesis are presented in section 9.5.

9.2 Overview and Novelty

In this thesis, for the first time, the mechanical property degradation of solvent-cast and compression-moulded PLGA materials with different thicknesses was evaluated using the nanoindentation technique. A computational modelling framework was developed that coupled reaction-diffusion kinetics and a molecular network based mechanical model in order to predict the degradation behaviour and the changes in the mechanical properties of biodegradable polymers during degradation. The main novelties of the work presented in this thesis are summarised as follows:

- Establishing the relationship between the changes in the molecular weight and the mechanical properties of PLGA material during degradation.
- Developing a coupled computational framework to predict the degradation behaviour and the mechanical performance of PLGA films of different thicknesses and of a range of regular open-cell tissue engineering PLGA scaffolds.

- Characterising the elasticity and plasticity properties of PLGA material using the nanoindentation technique and making practical recommendations on appropriate test parameters for successful nanoindentation testing of this material.
- Considering the effects of two different material processing methods on the undegraded material response of PLGA, and also on the degradation behaviour and the changes in the mechanical properties of PLGA during degradation.
- Considering the effect of material thickness on the degradation rate and the mechanical performance of PLGA films in order to establish a critical length scale above which the material undergoes heterogeneous degradation.

9.3 Summary and Discussion

A summary of the key findings of each of the result chapters presented in this thesis is given and discussed below.

The changes in the mechanical properties of solvent-cast PLGA 50:50 films under simulated physiological degradation condition (pH 7.4, 37°C) were evaluated in **Chapter 5**. It was shown that the molecular weight of the film decreases from the initial days of degradation as a result of the scission of the polymer chains due to the diffusion of water molecules which cause the hydrolytic cleavage of the ester bonds. The morphology of the film surface changes during degradation resulting in an increase in surface roughness and hardness of the film. Due to the decrease in the polymer mass, a large amount of low molecular weight fragments diffuse out of the polymer specimen. At this stage, the rate of molecular weight reduction is very slow. Similar results were found by Vey et al. (2008) for PLGA 50:50 solvent-cast film with a smaller diameter but similar thickness to that in the present study. Despite the fact that the degradation of PLGA material results in a quick decrease in the polymer molecular weight, the mechanical properties do not decrease until the molecular weight of the polymer chains reaches a critical molecular weight. A

significant reduction in the total number of polymer chains causes a sudden drop in the mechanical properties and consequently significant degradation occurs. The experimentally observed results revealed the critical molecular weight of 1500 g mol^{-1} for PLGA 50:50 in which the mechanical properties of the material significantly decrease. This critical molecular weight may be different for PLGA material with various lactic and glycolic acid ratios (Maxwell and Tomlins, 2011) or for other biodegradable polymers (Tsuji, 2002). Similar to other reported observations (Lu et al., 1999; Pamula and Menaszek, 2008; Vey et al., 2012; Vey et al., 2008), heterogeneous bulk degradation was found for PLGA film with a thickness similar to that considered in this chapter. It has been shown that the degradation of larger specimens is faster due to the effect of autocatalysis (Chen et al., 1997; Dunne et al., 2000; Grayson et al., 2005; Grizzi et al., 1995; Lu et al., 1999; Park, 1995; Witt and Kissel, 2001). Fast degradation may cause negative effects such as local or systemic toxicity (Athanasidou et al., 1996) and a loss of cell viability (Sung et al., 2004) due to the acidic effect of degradation products. Therefore, it is important to determine a critical length scale above which the device undergoes heterogeneous degradation.

To achieve this aim, a phenomenological model based on reaction-diffusion kinetics was used in **Chapter 6** in order to capture the changes in the molecular weight of PLGA material during degradation. The predictions of this model were obtained using semi-analytical and finite element methods for a one-dimensional problem which was presented in Chapter 3. It was found that the changes in the molecular weight of the PLGA film during degradation can be evaluated using both semi-analytical and finite element solutions; however, the semi-analytical solution does not capture the differences in degradation rates for films larger than $25 \mu\text{m}$. This may be due to the trial functions used in the Galerkin method, used to generate the semi-analytical solution, that are quite restrictive in the spatial variation that they allow, relative to that afforded by the finite element model with a relatively high number of nodes in the thickness direction. A molecular network based model,

described in Chapter 3, was used to relate the molecular weight to the elastic modulus of the PLGA material in order to predict the mechanical properties of PLGA during degradation. In this model, the critical molecular weight is the most important parameter which is required for the model to generate physically accurate predictions.

A coupled computational modelling framework, which was described in Chapter 3, was used to predict the degradation behaviour and the changes in the elastic modulus of PLGA films with different thicknesses and of a range of regular open-cell tissue engineering scaffolds. The models were validated by establishing their accurate simulation of the experimentally observed degradation behaviour and the changes in the elastic modulus of PLGA film during degradation presented in Chapter 5. The computed predictions revealed that the elastic modulus decreases faster for thicker PLGA films. The degradation and mechanical performance of PLGA films predicted in this chapter are in strong agreement with published experimentally observed trends of degradation for the PLGA devices with different sizes (Dunne et al., 2000; Grayson et al., 2005; Grizzi et al., 1995; Lu et al., 1999; Witt and Kissel, 2001).

Attention was then focused on PLGA scaffold structures. Microstructural models of three different scaffold architectures were used to investigate the degradation and mechanical behaviour of each scaffold. Simulations predicted that the degradation rate of the scaffold is much slower when the strut size of the scaffold is smaller. These results are in agreement with the experimental observations of Wu et al. (2005) and Saito et al. (2013; 2012) for *in-vitro* and *in-vivo* degradation of three-dimensional porous PLGA scaffolds. It was found that the architecture of the scaffold does not strongly influence the degradation rate but that it determines the initial stiffness of the scaffold. It was revealed that the size of the scaffold strut controls the degradation rate and the mechanical collapse. The homogenous, heterogeneous, and transition regimes predicted in the this chapter were compared to experimental observations of homogenous and heterogeneous

diffusion in different sized samples (Chen et al., 1997; Grizzi et al., 1995; Lu et al., 1999; Park, 1995; Spenlehauer et al., 1989; Vey et al., 2008). The results demonstrated that heterogeneous degradation occurs in PLGA when the length scale of the PLGA sample results in a diffusion limited regime where autocatalysis is the dominant degradation mechanism. A critical length scale due to competition between diffusion of degradation products and autocatalytic degradation was determined to be in the range 2-100 μm . Below this range, slower homogenous degradation occurs; however, for larger samples monomers are trapped inside the sample and faster autocatalytic degradation occurs.

Previous studies have shown a wide use of solvent casting methods for preparation of biodegradable films (Houchin and Topp, 2009; Huang et al., 2007; Lichun et al., 1998; Lu et al., 1999; Lu et al., 2001; Pamula and Menaszek, 2008; Pan et al., 2007; Schliecker et al., 2003; Steele et al., 2011; Vey et al., 2008; Witt and Kissel, 2001; Xi et al., 2010). This method usually requires a quite long time to fully remove solvents from the polymer during the drying steps (Manson and Dixon, 2012). Also, the residual solvent in the polymer may be harmful to cells or nearby tissues. Alternatively, the compression moulding method is useful because of its simplicity and capability for producing materials without using organic solvents (Grizzi et al., 1995; Witt et al., 2000); however, the heat treatment process may cause the degradation of polymer (Gogolewski and Mainil-Varlet, 1997).

Given this, the effect of two different processing methods on the mechanical properties of PLGA material, pre-degradation, was investigated in **Chapter 7**. Due to the complexities of performing nanoindentation on polymers generally, including material rate dependence (Briscoe et al., 1998; Tang and Ngan, 2003a; Zhou and Komvopoulos, 2006), adhesion (Dokukin and Sokolov, 2012; Gupta et al., 2007; Liao et al., 2010), and size effects (Alisafaei et al., 2014; Alisafaei et al., 2013; Briscoe et al., 1998; Charitidis, 2010; Chong and Lam, 1999; Flores and Calleja, 1998; Han, 2010; Lam and Chong, 2000; Tranchida et al., 2007; Tweedie et al., 2007; Voyiadjis et al., 2014; Zhang et al., 2004), the nano- and micro-mechanical properties of

solvent-cast and compression-moulded PLGA materials were investigated in order to make practical recommendations on appropriate test parameters for nanoindentation testing of this material. The elastic modulus and hardness of these materials were evaluated for a wide range of applied loads and loading rates.

It was revealed that the solvent-cast material is more elastically compliant than the compression-moulded material, which may be due to the presence of residual solvent in the solvent-cast material which tends to increase the mobility of the polymer chains as a plasticiser, resulting in less stiffness. These results are consistent with the results obtained by Rhim et al. (2006) which showed that more than 10% of the solvent was retained in the solvent-cast PLA film, leading to a smaller modulus than that of the PLA films prepared by compression moulding. Also, it was found that the compression-moulded material is plastically harder than the solvent-cast material, which may be due to the heat treatment during the compression moulding process which may increase the degree of crystallinity (Fouad et al., 2005; Pillin et al., 2008).

The results of this chapter also highlighted the depth dependence of the mechanical properties of PLGA materials. The depth dependence of the elastic modulus has been experimentally observed in various polymers such as epoxy (Alisafaei et al., 2014; Chong and Lam, 1999; Lam and Chong, 2000), PCL (Briscoe et al., 1998; Chong and Lam, 1999; Fang and Chang, 2004), PMMA (Briscoe et al., 1998), PDMS (Alisafaei et al., 2013; Charitidis, 2010; Wrucke et al., 2013), silicon rubber (Chandrashekar et al., 2015), nylon (Shen et al., 2005), and PS (Briscoe et al., 1998). The length scale at which indentation size effects occur in polymers can vary widely in different polymers. The results of this chapter revealed that the depth dependence of the elastic modulus and hardness of PLGA material was observed in particular for indentations lower than 3000 nm, which is most likely due to higher order displacement gradient effects (Alisafaei et al., 2014; Voyiadjis et al., 2014).

Additionally, the formation of pile-up due to the large amount of plastic deformation revealed that the solvent-cast material displays lower work hardening characteristics. The indentation data was analysed with a method proposed by Cheng and Cheng (1998) to correct for pile-up in the calculations. The results showed that the Cheng method can be used to overcome difficulties in measurement of mechanical properties caused by indentation pile-up, and it is therefore arguably more accurate than the Oliver and Pharr method (1992) in the calculation of the elastic modulus and hardness. Despite the inherent difficulty in testing soft polymers, the results of this chapter showed that reliable measurements for PLGA material is achieved using the holding time of 60 s, and loading rate dependence is found to be relatively insignificant.

Despite the significant effect of processing method on the initial stiffness of PLGA materials which was shown in Chapter 7, the experimentally observed results presented in **Chapter 8** highlight that the specific material processing methods considered in this chapter do not have a significant influence on the degradation rate and the changes in the mechanical properties of PLGA material during degradation. These results are in contrast to the results shown for PDLLA material (Cui et al., 2008; Miller et al., 2001). In Chapter 5, the experimental results showed that the amorphous solvent-cast PLGA material remains amorphous during degradation. In the case of the compression-moulded material, any crystallinity present may have an effect on the degradation behaviour; however, as there were no significant differences in the degradation behaviour and the material properties, either the degree of crystallinity must be small or the effect of crystallinity on PLGA degradation is small. In the case of PLA, a crystallinity of 30% did not affect the initial degradation behaviour, but did alter the water uptake and swelling during the later stages of degradation (Pantani and Sorrentino, 2013). However, the effect of crystallinity on PLGA degradation is complicated by the fact that the crystallinity can increase during degradation (Chye Joachim Loo et al., 2005). This chapter did demonstrate that the processing method affects the initial molecular weight of

PLGA. The smaller molecular weight of the undegraded compression-moulded material may be related to the heat treatment during the compression moulding process (Gogolewski and Mainil-Varlet, 1997).

It was revealed that there was no significant difference in the degradation rate of PLGA material with a range of thicknesses considered in this chapter. The experimental observations in this chapter strongly support the computational modelling predictions presented in Chapter 6. The computational predictions suggested a critical length scale in a range 2-100 μm , above which the PLGA material undergoes heterogeneous degradation. Although the experimental results presented here did not consider the degradation rate of PLGA thinner than 120 μm , the agreement here suggests that the model has captured the correct behaviour.

9.4 Conclusions

The combined experimental-computational approach presented in this thesis has led to an improved understanding of the influence of the processing method and the size scale on the degradation behaviour and the mechanical performance during degradation of an implanted PLGA device. The work presented here has also provided practical recommendations on appropriate test parameters for successful nanoindentation testing of this material. The following specific conclusions can be drawn:

- The experimentally observed results indicated that the solvent-cast material is more elastically compliant and plastically softer than the compression-moulded material and it also shows lower work hardening characteristics.
- The measured elastic modulus and hardness are strongly depth dependent for both forms of the solvent-cast and compression-moulded materials when indentation depths are lower than a certain threshold. Results suggested a threshold of 3000 nm for the specific materials studied in this thesis. At larger depths, the measurement is somewhat affected by the loading rate; however, this effect is not pronounced.

- The PLGA mechanical properties during degradation do not decrease until the number average molecular weight of the polymer chains reaches a critical molecular weight. For the specific materials considered here, the critical molecular weight was observed to be 1500 g mol^{-1} .
- The experimental observations in this thesis demonstrate that there is no significant difference in the degradation rate and the changes in the mechanical properties of PLGA thicker than $120 \mu\text{m}$, based on the materials considered here.
- The results indicated that the specific material processing methods considered in this thesis do not have a significant effect on the degradation rate and the changes in the mechanical properties of PLGA material.
- The simulations provided in this thesis elucidate a critical length scale due to competition between diffusion of degradation products and autocatalytic degradation which is determined to be in the range $2\text{-}100 \mu\text{m}$. Below this range, slower homogenous degradation occurs; however, for larger samples faster autocatalytic degradation occurs.
- The computational predictions presented in this thesis suggest that the architecture of a PLGA scaffold does not have a significant influence on the degradation rate, but it determines the initial stiffness of the scaffold. The size of the scaffold strut controls the degradation rate and the mechanical collapse.

In conclusion, the experimental results and the computational methods presented in this thesis provide a very useful and novel insight into the mechanical performance of PLGA during degradation. Based on this, this thesis presents a very powerful framework for the rational analysis and designing of future biodegradable medical implants and devices.

9.5 Future Research

The degradation of biodegradable polymers is most commonly assessed by immersion in simulated physiological conditions (pH 7.4, 37°C). This results in exposure of material to the surrounding aqueous medium which provides a reasonable environment to consider the material degradation under static condition; however, for the case of polymeric coatings in vascular applications, the degradation kinetics of material is likely to be affected where the device is immersed in blood flow *in-vivo*. Also, for the case of tissue engineering scaffolds which are subjected to loading condition *in-vivo*, cycling loading may lead an excessive degradation which may result in premature decrease in the mechanical integrity of the scaffold; as a result, the efficacy of the scaffold cell structure and the tissue growth may be affected. This suggests investigating the *in-vitro* evaluation of the degradation behaviour of these materials under a constant fluid flow environment and a dynamic loading condition.

The computation modelling framework presented in Chapters 3 and 6 was shown to accurately predict the degradation behaviour and also the mechanical performance of PLGA films larger than 120 μm when compared to experimentally observed changes in the molecular weight and elastic modulus. As this methodology generates a relationship between the molecular weight and the elastic modulus of the PLGA material, there are numerous possibilities of the application of this method. The methodology presented here can be used to predict the changes in the elastic modulus of various types of materials with different thicknesses as it is capable of accounting for the autocatalytic effect of carboxylic acid products. This is the case for other biodegradable polyesters, in particular PLGA materials with different PGA/PLA ratios. Once calibrated against experimental testing of one thickness, this method would enable the prediction of the degradation behaviour and the mechanical performance of different sized devices composed of a range of materials.

The results of Chapter 6 indicate that the developed computational framework has the ability to predict the degradation behaviour and the mechanical performance of tissue engineering scaffolds. The computational predictions indicate that strut size can control the degradation rate and therefore the mechanical performance of the scaffold during degradation. This modelling framework could be used to design an optimal composite scaffold (multiple materials with different degradation rates) with different architectures and pore sizes. The incorporation of different materials and different architectures can potentially improve the design of tissue engineering scaffold by controlling the rate of degradation and the therefore their mechanical performance during degradation.

The results of Chapter 7 indicate that the elastic modulus and hardness are strongly depth dependent for indentation less than 3000 nm. The elastic modulus of solvent-cast and compression-moulded PLGA materials decreases with the increase in the indentation depth. Also, the results are significantly affected by pile-up which causes overestimation of the elastic modulus. This suggests investigating alternative methods such as conventional tensile testing for evaluation of the elastic modulus of these materials for comparison purposes, at least for the case of undegraded material.

Appendices

A. The Galerkin Method

```

clear all
clc
close all

set(0,'defaultLineMarkerSize',20)
set(0,'defaultLineLinewidth',2)
set(0,'defaultfigurecolor',[1 1 1])

alpha=4.5;
n=0.5;

options=odeset();
timespan=0:0.2:40;yinitial=[0,0,1];
day_to_plot=25;

% COMSOL-experimental's parameters
Ce0=17300;%[mol/m3]
Do=1e-12;%[m2/day]
k2 = 0.002;%[(m3/mol)^0.5/day]
k1= 0.002;%[1/day]
L = 250/1e6;% thickness of film[m]
D0hat = Do/(k2*Ce0^n*L^2);
k1hat = k1/(k2*Ce0^n);

%COMSOL data for different film thicknesses
[~,~,raw] = xlsread('COMSOL_experimental.xlsx','COMSOL_EXP','A5:J205');
COMSOLexperimental = reshape([raw(:, #503)],size(raw));
COMSOL_Time=COMSOLexperimental(:,1);
COMSOL_ce=COMSOLexperimental(:,2:10);
[~,~,COMSOL_film_names] = xlsread('COMSOL_experimental.xlsx','COMSOL_EXP','B4:J4');
good_films=[1,2,4,7,9];

%find thickness to match
listL=[];
for string=[COMSOL_film_names[good_films]]
    listL(end+1)=str2double(string[1, #503](1:end-2));

```

```

end

%magic to keep colors the same
figg=get(gcf); axx=get(figg.CurrentAxes); colrs=axx.ColorOrder;

legendnames=[];
k=0;
for L=listL/1e6;          k=k+1 ;%COMSOL thickness

    % non dim params
    D0hat = Do/(k2*Ce0^n*L^2);
    K1hat = k1/(k2*Ce0^n);
    thattspan=timespan*(k2*Ce0^n);

%solve ode
[thatt,y_solv]=ode45(@Galerkin5,thattspan,yinitial,options,K1hat,D0hat,alpha);
t=thatt/(k2*Ce0^n);

xhat=linspace(0,1,100);

cehat=zeros(length(xhat),length(thatt) );

% use shape functions to get variables accross domain
for i=1:1:length(xhat)
    for j=1:1:length(thatt)
        cehat(i,j)=y_solv(j,2)*xhat(i)+y_solv(j,3);
    end
end

% get volume averaged
cehat_avg=sum(cehat,1)./length(xhat);

%plot ce-time
figure(99)
plot(t,cehat_avg,'-','Color', colrs(k,:)); hold all;
legendnames[end+1]=sprintf('l=%g\mum',L*1e6);

%plot ce-through thickness
figure(98)
plot(xhat,cehat(:,t==day_to_plot)' , 'Color', colrs(k,:) ); hold all;

end

figure(98)
legend(legendnames[:, #503])
xlabel('xhat =x/L')
ylabel('ce')

all_font_resize(8)
resize_fig(8.8,7.8)

```

```

figure(99)
legend(COMSOL_film_names[good_films],legendnames[:, #503])
legend(COMSOL_film_names[good_films],legendnames[:, #503])
xlabel('Time (days)')
ylabel('Average Normalised \itM_n')

all_font_resize(8)
resize_fig(8.8,7.8)

```

```

function dydt=Galerkin5(time,y,k1hat,D0hat,alpha)

D1=(1/2)^0.5;
A1=15/16;
A2=5/2;
A3=3/4;
A4=45*pi/64;
A5=1/2;
A6=15/8;
B1=(3*pi/4)-2;
B2=4-(3*pi/2);
C1=(3*pi/8)-(4/3);
C2=2-pi;

dydt=zeros(3,1);

dydt(1,1)=A1*k1hat*y(2)+A2*k1hat*y(3)+A3*D1*y(1)^0.5*y(2)+A4*D1*y(1)^0.5*y(3)-
A2*D0hat*(1+alpha)*y(1)+A5*alpha*D0hat*y(1)^2+A6*D0hat*alpha*y(1)*y(2)+A2*alpha*D0hat
*y(1)*y(3);

dydt(2,1)=-k1hat*y(2)-B1*D1*y(1)^0.5*y(2)-B2*D1*y(1)^0.5*y(3);

dydt(3,1)=-k1hat*y(3)+C1*D1*y(1)^0.5*y(2)+C2*D1*y(1)^0.5*y(3);

end

```

[Published with MATLAB® R2014a](#)

B. The Mechanical Properties Model

```

clear all
close all

t1=cputime;
global OriginalTotalChains numberofmonomers nrr nee OriginalEsters
global NumberofRandomScission NumberofEndScission numberofcuttablechains chainlist
global numbertoclean times_cleaned Nsubchains sizz CurrentChains longestchain

%determine the polymer chains ditribution
MolarMass=65; %wieght of one unit for PLGA

%call the chain distribution function
[OriginalChain]=chain_distribution(x,r);

%total number of polymer chains at the beginning
OriginalTotalChains=length(OriginalChain);
TotalBonds=sum((OriginalChain-1));
OriginalEsters=sum(OriginalChain);
Nsubchains=ones(OriginalTotalChains,1);

%number of random and end scission per step
%set what % of bonds to break
NtotalScission=TotalBonds/100*100;
% set the number of data points
NumberOfScissionSteps=500;
%set the ratio of random to end
nrandom          = 1;
nend              = 12;

%arrays
ChainArray          =
zeros(OriginalTotalChains,max(OriginalChain));
molecularweight     =
zeros(OriginalTotalChains,max(OriginalChain));
chainlist           = zeros(length(ChainArray(:)/2),1);
countnumchains     = zeros(1,NumberOfScissionSteps+1);
normalisedmodulus  = zeros(1,NumberOfScissionSteps+1);
NumberAverageMolecularWeight = zeros(1,NumberOfScissionSteps+1);
sizz                = size(ChainArray);
longestchain       = max(OriginalChain);

%initial arrays
ChainArray(:,1)=OriginalChain.';
chainlist(1:OriginalTotalChains,1)=find(ChainArray>1);
countnumchains(1)=OriginalTotalChains;

%The chain length smaller than the Mw threshold

```

```

MwThreshold=3000; %numberaverage molecular weight

countnumchains(i)=sum(molecularweight(:,i)>=MwThreshold);
normalisedmodulus(i)=countnumchains(i)/OriginalTotalChains;

%calculate initial molecular weight and initial normalised molecular weight
molecularweight(:,1)=OriginalChain'*MolarMass; %molecular weight for all chains

%initial values
StepsDone=0;
numberofmonomers=0;
nrr=0;
nee=0;
numbertoclean=0;
times_cleaned=0;
numberofcuttablechains=OriginalTotalChains;
CurrentChains=0;

%do random or end scission until all chains are cut
for i=2:NumberOfScissionSteps+1 % i=1 is for the original chains

    [ChainArray]=Steps(ChainArray,NumberOfScissionsPerStep);

    %count the chains greater than the molecular weight threshold
    for j=1:OriginalTotalChains
        molecularweight(j,i)= OriginalChain(j)/Nsubchains(j)*MolarMass;
    end

    %calculate molecular weight of all chains
    NumberAverageMolecularWeight(i)=OriginalEsters/sum(Nsubchains)*MolarMass;

    StepsDone=StepsDone+1;
end
normalisedmodulus=normalisedmodulus/Eorig;

function [ChainArray]=OneEndScission(ChainArray)

global numberofmonomers OriginalTotalChains chainlist
global numbertoclean Nsubchains sizz CurrentChains

    %select a chain to cut
    chaintocut=findchaintocut();
    row=mod(chaintocut,OriginalTotalChains);
    if row==0
        row=OriginalTotalChains;
    end
    Nsubchains(row)=Nsubchains(row)+1;
    if ChainArray(chaintocut)==1
        numberofmonomers=numberofmonomers+1;
    end
end

```

```
function[ChainArray]=OneRandomScission(ChainArray)

global OriginalTotalChains numberofmonomers chainlist numberofcutablechains
global numbertoclean Nsubchains sizz CurrentChains

    %select a chain to cut
    chaintocut=findchaintocut();
    row=mod(chaintocut,OriginalTotalChains);
    if row==0
        row=OriginalTotalChains;
    end

    %number of bonds of the selected chain to cut
    BondsofChainNumberToCut=ChainArray(chaintocut)-1
    if ChainArray(newchain)==1
        numberofmonomers=numberofmonomers+1;
    else
        chainlist(numberofcutablechains+1)=newchain;
        numberofcutablechains=numberofcutablechains+1;
    end
    ChainArray(chaintocut)=BondToCut;
    cut=1; %cut=true

end
```

[Published with MATLAB® R2014a](#)

C. Elastic Modulus and Hardness of the Undegraded and Degraded Solvent-Cast PLGA Material in the Dry and Wet Conditions

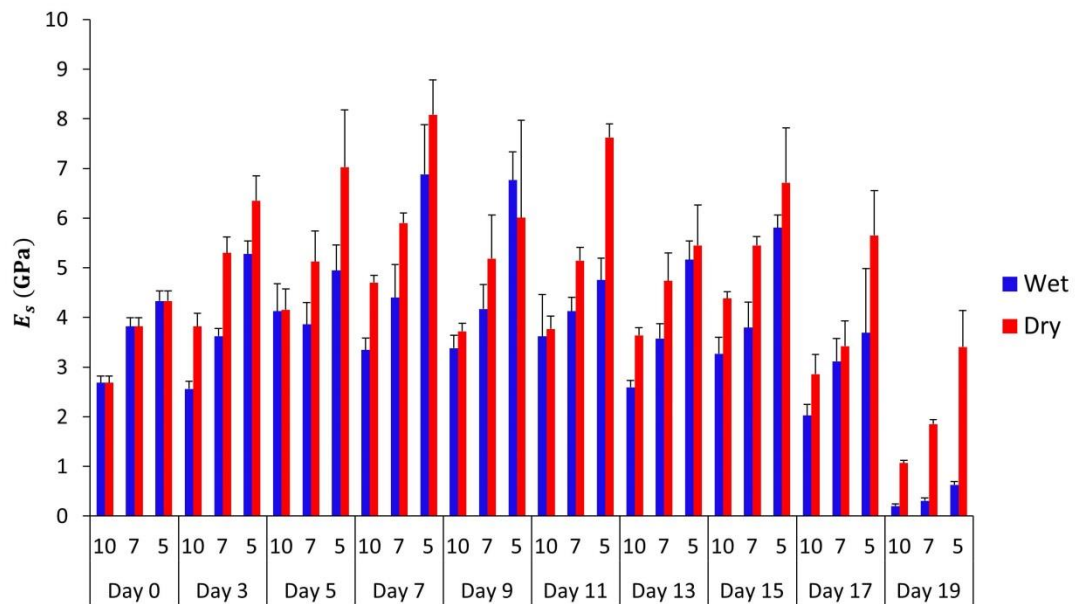


Figure C.1: Comparison of the elastic modulus (E_s) of the undegraded and degraded solvent-cast PLGA films in the dry and wet conditions

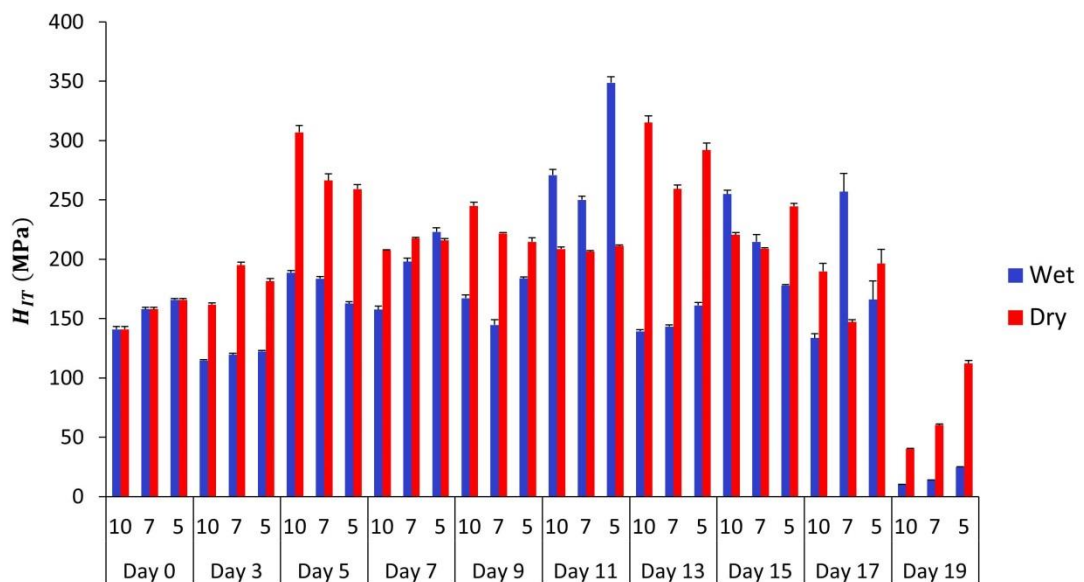


Figure C.2: Comparison of the hardness (H_{IT}) of the undegraded and degraded solvent-cast PLGA films in the dry and wet conditions

D. Elastic Modulus and Hardness of the Undegraded Solvent-Cast and Compression-Moulded PLGA Materials

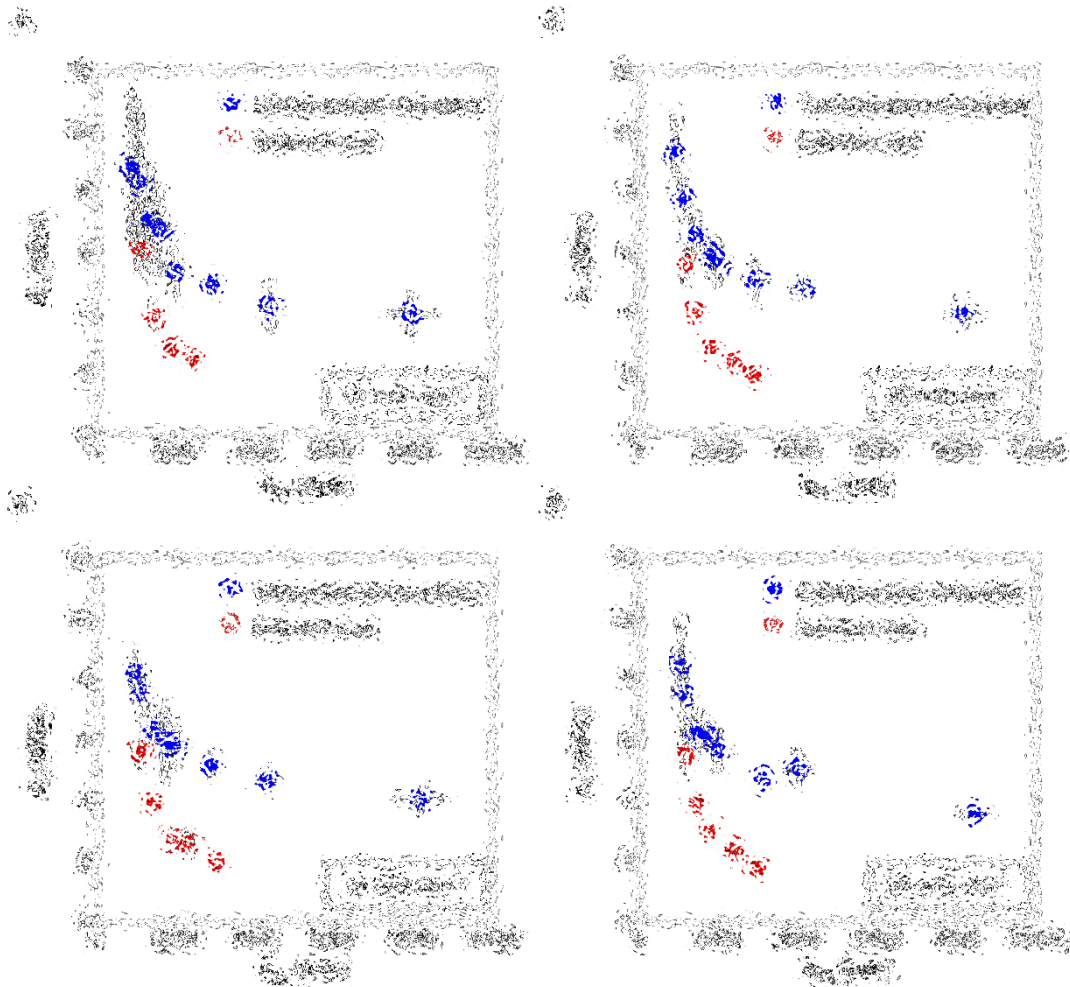


Figure D.1: Elastic modulus (E_s) for the undegraded compression-moulded (solid circle) and solvent-cast (triangle) PLGA materials (mean \pm SD; $n = 20$), for the unloading (loading) rate of (A) 10 mN min^{-1} (B) 14 mN min^{-1} (C) 20 mN min^{-1} (D) 30 mN min^{-1} . **Figure blurred due to copyright restrictions.**

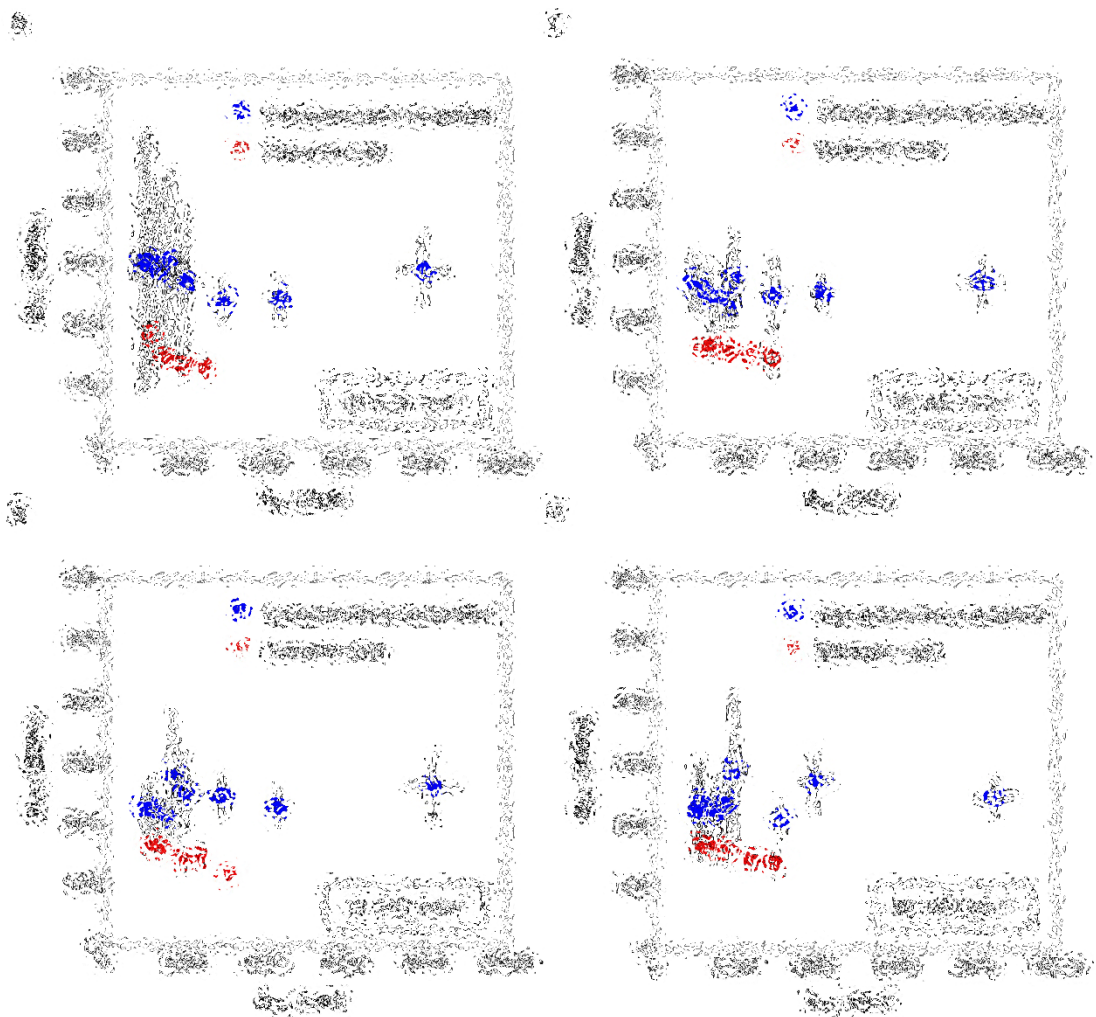


Figure D.2: Hardness (H_{IT}) for the undegraded compression-moulded (solid circle) and solvent-cast (triangle) PLGA materials (mean \pm SD; $n = 20$), for the unloading (loading) rate of (A) 10 mN min^{-1} (B) 14 mN min^{-1} (C) 20 mN min^{-1} (D) 30 mN min^{-1} . **Figure blurred due to copyright restrictions.**

References

Agrawal, C.M., McKinney, J.S., Lanctot, D., Athanasiou, K.A., 2000. Effects of fluid flow on the in vitro degradation kinetics of biodegradable scaffolds for tissue engineering. *Biomaterials* 21, 2443-2452.

Alisafaei, F., Han, C.-S., 2015. Indentation Depth Dependent Mechanical Behavior in Polymers. *Advances in Condensed Matter Physics* 2015, 20.

Alisafaei, F., Han, C.-S., Lakhera, N., 2014. Characterization of indentation size effects in epoxy. *Polymer Testing* 40, 70-78.

Alisafaei, F., Han, C.-S., Sanei, S.H.R., 2013. On the time and indentation depth dependence of hardness, dissipation and stiffness in polydimethylsiloxane. *Polymer Testing* 32, 1220-1228.

Anderson, J.M., Shive, M.S., 2012. Biodegradation and biocompatibility of PLA and PLGA microspheres. *Advanced Drug Delivery Reviews* 64, Supplement, 72-82.

Andreas, K., Zehbe, R., Kazubek, M., Grzeschik, K., Sternberg, N., Bäuml, H., Schubert, H., Sittlinger, M., Ringe, J., 2011. Biodegradable insulin-loaded PLGA microspheres fabricated by three different emulsification techniques: Investigation for cartilage tissue engineering. *Acta Biomaterialia* 7, 1485-1495.

Antheunis, H., Van Der Meer, J.C., De Geus, M., Heise, A., Koning, C.E., 2010. Autocatalytic equation describing the change in molecular weight during hydrolytic degradation of aliphatic polyesters. *Biomacromolecules* 11, 1118-1124.

Antheunis, H., Van Meer, J.C.D., De Geus, M., Kingma, W., Koning, C.E., 2009. Improved mathematical model for the hydrolytic degradation of aliphatic polyesters. *Macromolecules* 42, 2462-2471.

Arnold, M.M., Gorman, E.M., Schieber, L.J., Munson, E.J., Berklund, C., 2007. NanoCipro encapsulation in monodisperse large porous PLGA microparticles. *Journal of Controlled Release* 121, 100-109.

ASTM:F1635-11, 2011. in vitro Degradation Testing of Hydrolytically Degradable Polymer Resins and Fabricated Forms for Surgical Implants. DOI:10.1520/F1635-11, www.astm.org.

Atala, A., Mooney, D.J., 2013. *Synthetic Biodegradable Polymer Scaffolds*. Birkhäuser Boston.

- Athanasίου, K., Natoli, R., 2008. Introduction to Continuum Biomechanics. Morgan & Claypool Publishers.
- Athanasίου, K.A., Niederauer, G.G., Agrawal, C.M., 1996. Sterilization, toxicity, biocompatibility and clinical applications of polylactic acid/ polyglycolic acid copolymers. *Biomaterials* 17, 93-102.
- Bashur, C.A., Dahlgren, L.A., Goldstein, A.S., 2006. Effect of fiber diameter and orientation on fibroblast morphology and proliferation on electrospun poly(d,l-lactic-co-glycolic acid) meshes. *Biomaterials* 27, 5681-5688.
- Bolshakov, A., Pharr, G.M., 1998. Influences of pileup on the measurement of mechanical properties by load and depth sensing indentation techniques. *Journal of Materials Research* 13, 1049-1058.
- Brandrup, J., Immergut, E.H., Grulke, E.A., 2003. *Polymer Handbook*, 2 Volumes Set. Wiley.
- Briscoe, B.J., Fiori, L., Pelillo, E., 1998. Nano-indentation of polymeric surfaces. *Journal of Physics D: Applied Physics* 31, 2395.
- Brown, N., 1971. The relationship between yield point and modulus for glassy polymers. *Materials Science and Engineering* 8, 69-73.
- Brożyna, B., Szymańska, H., Ptaszyński, K., Woszczyński, M., Lechowska-Piskorowska, J., Gajewska, M., Rostkowska, J., Chełmiński, K., Bulski, W., Krajewski, R., 2015. Tissue response after implantation of pure titanium and bioresorbable screws in scapula with postoperative irradiation: an experimental study on rats. *Oral Surgery, Oral Medicine, Oral Pathology and Oral Radiology* 120, 443-452.
- Bucklen, B.S., Wettergreen, W.A., Yuksel, E., Liebschner, M.A.K., 2008. Bone-derived CAD library for assembly of scaffolds in computer-aided tissue engineering. *Virtual and Physical Prototyping* 3, 13-23.
- Bull, S.J., 2005. Nanoindentation of coatings. *Journal of Physics D: Applied Physics* 38, R393.
- Cao, Y., Mitchell, G., Messina, A., Price, L., Thompson, E., Penington, A., Morrison, W., O'Connor, A., Stevens, G., Cooper-White, J., 2006. The influence of architecture on degradation and tissue ingrowth into three-dimensional poly(lactic-co-glycolic acid) scaffolds in vitro and in vivo. *Biomaterials* 27, 2854-2864.
- Cao, Y., Yang, D., Soboyejoy, W., 2005. Nanoindentation Method for Determining the Initial Contact and Adhesion Characteristics of Soft Polydimethylsiloxane. *Journal of Materials Research* 20, 2004-2011.
- Carrillo, F., Gupta, S., Balooch, M., Marshall, S.J., Marshall, G.W., Pruitt, L., Puttlitz, C.M., 2005. Nanoindentation of polydimethylsiloxane elastomers: Effect of

crosslinking, work of adhesion, and fluid environment on elastic modulus. *Journal of Materials Research* 20, 2820-2830.

Chandrashekar, G., Alisafaei, F., Han, C.-S., 2015. Length scale dependent deformation in natural rubber. *Journal of Applied Polymer Science* 132, n/a-n/a.

Charitidis, C.A., 2010. Nanoscale Deformation and Nanomechanical Properties of Polydimethylsiloxane (PDMS). *Industrial & Engineering Chemistry Research* 50, 565-570.

Chen, J., Bull, S.J., 2009. Relation between the ratio of elastic work to the total work of indentation and the ratio of hardness to Young's modulus for a perfect conical tip. *Journal of Materials Research* 24, 590-598.

Chen, L., Apte, R.N., Cohen, S., 1997. Characterization of PLGA microspheres for the controlled delivery of IL-1 α for tumor immunotherapy. *Journal of Controlled Release* 43, 261-272.

Chen, Y., Zhou, S., Li, Q., 2011. Mathematical modeling of degradation for bulk-erosive polymers: Applications in tissue engineering scaffolds and drug delivery systems. *Acta Biomaterialia* 7, 1140-1149.

Cheng, Y.-T., Cheng, C.-M., 1998. Relationships between hardness, elastic modulus, and the work of indentation. *Applied Physics Letters* 73, 614-616.

Cheng, Y.-T., Cheng, C.-M., 2004. Scaling, dimensional analysis, and indentation measurements. *Materials Science and Engineering: R: Reports* 44, 91-149.

Cheng, Y.-T., Li, Z., Cheng, C.-M., 2002. Scaling relationships for indentation measurements. *Philosophical Magazine A* 82, 1821-1829.

Choi, Y., Lee, H.-S., Kwon, D., 2004. Analysis of sharp-tip-indentation load–depth curve for contact area determination taking into account pile-up and sink-in effects. *Journal of Materials Research* 19, 3307-3315.

Chong, A.C.M., Lam, D.C.C., 1999. Strain gradient plasticity effect in indentation hardness of polymers. *Journal of Materials Research* 14, 4103-4110.

Chudoba, T., Richter, F., 2001. Investigation of creep behaviour under load during indentation experiments and its influence on hardness and modulus results. *Surface and Coatings Technology* 148, 191-198.

Chye Joachim Loo, S., Ooi, C.P., Hong Elyna Wee, S., Chiang Freddy Boey, Y., 2005. Effect of isothermal annealing on the hydrolytic degradation rate of poly(lactide-co-glycolide) (PLGA). *Biomaterials* 26, 2827-2833.

Clark, A., Milbrandt, T.A., Hilt, J.Z., Puleo, D.A., 2014. Tailoring properties of microsphere-based poly(lactic-co-glycolic acid) scaffolds. *Journal of Biomedical Materials Research - Part A* 102, 348-357.

- Cui, W., Li, X., Zhou, S., Weng, J., 2008. Degradation patterns and surface wettability of electrospun fibrous mats. *Polymer Degradation and Stability* 93, 731-738.
- Cui, Y., Liu, Y., Cui, Y., Jing, X., Zhang, P., Chen, X., 2009. The nanocomposite scaffold of poly(lactide-co-glycolide) and hydroxyapatite surface-grafted with l-lactic acid oligomer for bone repair. *Acta Biomaterialia* 5, 2680-2692.
- Daniels, A.U., Chang, M.K.O., Andriano, K.P., Heller, J., 1990. Mechanical properties of biodegradable polymers and composites proposed for internal fixation of bone. *Journal of Applied Biomaterials* 1, 57-78.
- Dechy-Cabaret, O., Martin-Vaca, B., Bourissou, D., 2004. Controlled ring-opening polymerization of lactide and glycolide. *Chemical Reviews* 104, 6147-6176.
- Derjaguin, B.V., Muller, V.M., Toporov, Y.P., 1975. Effect of contact deformations on the adhesion of particles. *Journal of Colloid and Interface Science* 53, 314-326.
- Deuschle, J., Enders, S., Arzt, E., 2007. Surface detection in nanoindentation of soft polymers. *Journal of Materials Research* 22, 3107-3119.
- Doerner, M.F., Nix, W.D., 1986. A method for interpreting the data from depth-sensing indentation instruments. *Journal of Materials Research* 1, 601-609.
- Dokukin, M.E., Sokolov, I., 2012. On the measurements of rigidity modulus of soft materials in nanoindentation experiments at small depth. *Macromolecules* 45, 4277-4288.
- Dreher, M.L., Nagaraja, S., Li, J., 2015. Creep loading during degradation attenuates mechanical property loss in PLGA. *Journal of Biomedical Materials Research - Part B Applied Biomaterials* 103, 700-708.
- Dunne, M., Corrigan, O.I., Ramtoola, Z., 2000. Influence of particle size and dissolution conditions on the degradation properties of polylactide-co-glycolide particles. *Biomaterials* 21, 1659-1668.
- Ebenstein, D.M., Wahl, K.J., 2006. A comparison of JKR-based methods to analyze quasi-static and dynamic indentation force curves. *Journal of Colloid and Interface Science* 298, 652-662.
- Elmustafa, A.A., Stone, D.S., 2003. Nanoindentation and the indentation size effect: Kinetics of deformation and strain gradient plasticity. *Journal of the Mechanics and Physics of Solids* 51, 357-381.
- Engineer, C., Parikh, J., Raval, A., 2011. Effect of copolymer ratio on hydrolytic degradation of poly(lactide-co-glycolide) from drug eluting coronary stents. *Chemical Engineering Research and Design* 89, 328-334.
- Fang, T.-H., Chang, W.-J., 2004. Nanoindentation characteristics on polycarbonate polymer film. *Microelectronics Journal* 35, 595-599.

- Farrissey, L.M., McHugh, P.E., 2005. Determination of elastic and plastic material properties using indentation: Development of method and application to a thin surface coating. *Materials Science and Engineering: A* 399, 254-266.
- Feng, G., Ngan, A.H.W., 2002. Effects of creep and thermal drift on modulus measurement using depth-sensing indentation. *Journal of Materials Research* 17, 660-668.
- Fischer-Cripps, A.C., 2006. Critical review of analysis and interpretation of nanoindentation test data. *Surface and Coatings Technology* 200, 4153-4165.
- Fischer-Cripps, A.C., 2013. *Nanoindentation*. Springer New York.
- Flores, A., Calleja, F.J.B., 1998. Mechanical properties of poly(ethylene terephthalate) at the near surface from depth-sensing experiments. *Philosophical Magazine A* 78, 1283-1297.
- Flory, P.J., 1942. Random reorganization of molecular weight distribution in linear condensation polymers. *Journal of the American Chemical Society* 64, 2205-2212.
- Ford Versypt, A.N., Pack, D.W., Braatz, R.D., 2013. Mathematical modeling of drug delivery from autocatalytically degradable PLGA microspheres — A review. *Journal of Controlled Release* 165, 29-37.
- Fouad, H., Mourad, A.H.I., Barton, D.C., 2005. Effect of pre-heat treatment on the static and dynamic thermo-mechanical properties of ultra-high molecular weight polyethylene. *Polymer Testing* 24, 549-556.
- Fredenberg, S., Wahlgren, M., Reslow, M., Axelsson, A., 2011. The mechanisms of drug release in poly(lactic-co-glycolic acid)-based drug delivery systems—A review. *International Journal of Pharmaceutics* 415, 34-52.
- Ge, Z., Wang, L., Heng, B.C., Tian, X.F., Lu, K., Fan, V.T.W., Yeo, J.F., Cao, T., Tan, E., 2009. Proliferation and differentiation of human osteoblasts within 3D printed poly-lactic-co-glycolic acid scaffolds. *Journal of Biomaterials Applications* 23, 533-547.
- Geng, K., Yang, F., Druffel, T., Grulke, E.A., 2005. Nanoindentation behavior of ultrathin polymeric films. *Polymer* 46, 11768-11772.
- Ginjunpalli, K., Averineni, R.K., K, M.B., N, U., 2014. Preparation and characterization of biodegradable scaffolds of poly(lactide-co-glycolide) 50:50 and hydroxyapatite for dental applications. *Composite Interfaces* 21, 31-44.
- Gogolewski, S., Mainil-Varlet, P., 1997. Effect of thermal treatment on sterility, molecular and mechanical properties of various polylactides: 2. Poly(l/d-lactide) and poly(l/dl-lactide). *Biomaterials* 18, 251-255.

- Grayson, A.C.R., Cima, M.J., Langer, R., 2005. Size and temperature effects on poly(lactic-co-glycolic acid) degradation and microreservoir device performance. *Biomaterials* 26, 2137-2145.
- Griffiths, M.C., Strauch, J., Monteiro, M.J., Gilbert, R.G., 1998. Measurement of Diffusion Coefficients of Oligomeric Penetrants in Rubbery Polymer Matrixes. *Macromolecules* 31, 7835-7844.
- Grizzi, I., Garreau, H., Li, S., Vert, M., 1995. Hydrolytic degradation of devices based on poly(dl-lactic acid) size-dependence. *Biomaterials* 16, 305-311.
- Grunlan, J.C., Xia, X., Rowenhorst, D., Gerberich, W.W., 2001. Preparation and evaluation of tungsten tips relative to diamond for nanoindentation of soft materials. *Review of Scientific Instruments* 72, 2804-2810.
- Gulati, K., Ramakrishnan, S., Aw, M.S., Atkins, G.J., Findlay, D.M., Losic, D., 2012. Biocompatible polymer coating of titania nanotube arrays for improved drug elution and osteoblast adhesion. *Acta Biomaterialia* 8, 449-456.
- Gupta, S., Carrillo, F., Li, C., Pruitt, L., Puttlitz, C., 2007. Adhesive forces significantly affect elastic modulus determination of soft polymeric materials in nanoindentation. *Materials Letters* 61, 448-451.
- Han, C.-S., 2010. Influence of the molecular structure on indentation size effect in polymers. *Materials Science and Engineering: A* 527, 619-624.
- Han, X., Pan, J., 2009. A model for simultaneous crystallisation and biodegradation of biodegradable polymers. *Biomaterials* 30, 423-430.
- Harada, N., Watanabe, Y., Sato, K., Abe, S., Yamanaka, K., Sakai, Y., Kaneko, T., Matsushita, T., 2014. Bone regeneration in a massive rat femur defect through endochondral ossification achieved with chondrogenically differentiated MSCs in a degradable scaffold. *Biomaterials* 35, 7800-7810.
- Hay, J.L., Olive, W.C., Bolshakov, A., Pharr, G.M., 1998. Using the Ratio of Loading Slope and Elastic Stiffness to Predict Pile-Up and Constraint Factor During Indentation. *MRS Online Proceedings Library* 522, null-null.
- Hayman, D., Bergerson, C., Miller, S., Moreno, M., Moore, J.E., 2014. The Effect of Static and Dynamic Loading on Degradation of PLLA Stent Fibers. *Journal of Biomechanical Engineering* 136, 081006-081006.
- Heljak, M.K., Świążkowski, W., Lam, C.X.F., Hutmacher, D.W., Kurzydłowski, K.J., 2012. Evolutionary design of bone scaffolds with reference to material selection. *International Journal for Numerical Methods in Biomedical Engineering* 28, 789-800.

- Hertz, H., 1881. On the contact of elastic solids. *Journal für die reine und angewandte Mathematik* 92, 156-171.
- Houchin, M.L., Topp, E.M., 2009. Physical properties of PLGA films during polymer degradation. *Journal of Applied Polymer Science* 114, 2848-2854.
- Huang, Y.-Y., Qi, M., Liu, H.-Z., Zhao, H., Yang, D.-Z., 2007. Degradation of porous poly(D,L-lactic-co-glycolic acid) films based on water diffusion. *Journal of Biomedical Materials Research Part A* 80A, 909-915.
- Jackson, J.K., Smith, J., Letchford, K., Babiuk, K.A., Machan, L., Signore, P., Hunter, W.L., Wang, K., Burt, H.M., 2004. Characterization of perivascular poly(lactic-co-glycolic acid) films containing paclitaxel. *International Journal of Pharmaceutics* 283, 97-109.
- Jakes, J.E., Lakes, R.S., Stone, D.S., 2012. Broadband nanoindentation of glassy polymers: Part I. Viscoelasticity. *Journal of Materials Research* 27, 463-474.
- Jee, A.-Y., Lee, M., 2010. Comparative analysis on the nanoindentation of polymers using atomic force microscopy. *Polymer Testing* 29, 95-99.
- Jeong, Y.-I., Na, H.-S., Seo, D.-H., Kim, D.-G., Lee, H.-C., Jang, M.-K., Na, S.-K., Roh, S.-H., Kim, S.-I., Nah, J.-W., 2008. Ciprofloxacin-encapsulated poly(DL-lactide-co-glycolide) nanoparticles and its antibacterial activity. *International Journal of Pharmaceutics* 352, 317-323.
- Jie, L., Zhiye, Q., Shenqi, W., Lei, Z., Shengmin, Z., 2010. A modified double-emulsion method for the preparation of daunorubicin-loaded polymeric nanoparticle with enhanced in vitro anti-tumor activity. *Biomedical Materials* 5, 065002.
- Johnson, K.L., Kendall, K., Roberts, A.D., 1971. 301.
- Jonnalagadda, S., Robinson, D.H., 2004. Effect of thickness and PEG addition on the hydrolytic degradation of PLLA. *Journal of Biomaterials Science -- Polymer Edition* 15, 1317-1326.
- Joshi, A., Himmelstein, K.J., 1991. Dynamics of controlled release from bioerodible matrices. *Journal of Controlled Release* 15, 95-104.
- Joslin, D.L., Oliver, W.C., 1990. New method for analyzing data from continuous depth-sensing microindentation tests. *Journal of Materials Research* 5, 123-126.
- Jung, M.R., Shim, I.K., Chung, H.J., Lee, H.R., Park, Y.J., Lee, M.C., Yang, Y.I., Do, S.H., Lee, S.J., 2012. Local BMP-7 release from a PLGA scaffolding-matrix for the repair of osteochondral defects in rabbits. *Journal of Controlled Release* 162, 485-491.
- Karlsson, O.J., Stubbs, J.M., Karlsson, L.E., Sundberg, D.C., 2001. Estimating diffusion coefficients for small molecules in polymers and polymer solutions. *Polymer* 42, 4915-4923.

- Karp, J.M., Shoichet, M.S., Davies, J.E., 2003. Bone formation on two-dimensional poly(DL-lactide-co-glycolide) (PLGA) films and three-dimensional PLGA tissue engineering scaffolds in vitro. *Journal of Biomedical Materials Research Part A* 64A, 388-396.
- Kaufman, J.D., Klapperich, C.M., 2009. Surface detection errors cause overestimation of the modulus in nanoindentation on soft materials. *Journal of the Mechanical Behavior of Biomedical Materials* 2, 312-317.
- Klose, D., Siepmann, F., Elkharraz, K., Krenzlin, S., Siepmann, J., 2006. How porosity and size affect the drug release mechanisms from PLGA-based microparticles. *International Journal of Pharmaceutics* 314, 198-206.
- Klose, D., Siepmann, F., Elkharraz, K., Siepmann, J., 2008. PLGA-based drug delivery systems: Importance of the type of drug and device geometry. *International Journal of Pharmaceutics* 354, 95-103.
- Kranz, H., Ubrich, N., Maincent, P., Bodmeier, R., 2000. Physicomechanical properties of biodegradable poly(D,L-lactide) and poly(D,L-lactide-co-glycolide) films in the dry and wet states. *Journal of Pharmaceutical Sciences* 89, 1558-1566.
- Lam, C.X.F., Mo, X.M., Teoh, S.H., Hutmacher, D.W., 2002. Scaffold development using 3D printing with a starch-based polymer. *Materials Science and Engineering: C* 20, 49-56.
- Lam, D.C.C., Chong, A.C.M., 2000. Effect of cross-link density on strain gradient plasticity in epoxy. *Materials Science and Engineering: A* 281, 156-161.
- Lee, J.J., Lee, S.-G., Park, J.C., Yang, Y.I., Kim, J.K., 2007. Investigation on biodegradable PLGA scaffold with various pore size structure for skin tissue engineering. *Current Applied Physics* 7, Supplement 1, e37-e40.
- Lee, M., Dunn, J.C.Y., Wu, B.M., 2005. Scaffold fabrication by indirect three-dimensional printing. *Biomaterials* 26, 4281-4289.
- Li, J.N., Cao, P., Zhang, X.N., Zhang, S.X., He, Y.H., 2010a. In vitro degradation and cell attachment of a PLGA coated biodegradable Mg-6Zn based alloy. *Journal of Materials Science* 45, 6038-6045.
- Li, P., Feng, X., Jia, X., Fan, Y., 2010b. Influences of tensile load on in vitro degradation of an electrospun poly(l-lactide-co-glycolide) scaffold. *Acta Biomaterialia* 6, 2991-2996.
- Li, X., Bhushan, B., 2000. Continuous stiffness measurement and creep behavior of composite magnetic tapes. *Thin Solid Films* 377-378, 401-406.

- Liao, Q., Huang, J., Zhu, T., Xiong, C., Fang, J., 2010. A hybrid model to determine mechanical properties of soft polymers by nanoindentation. *Mechanics of Materials* 42, 1043-1047.
- Lichun, L., Garcia, C.A., Mikos, A.G., 1998. Retinal pigment epithelium cell culture on thin biodegradable poly(DL-lactic-co-glycolic acid) films. *Journal of Biomaterials Science, Polymer Edition* 9, 1187-1205.
- Lin, A.S.P., Barrows, T.H., Cartmell, S.H., Guldborg, R.E., 2003. Microarchitectural and mechanical characterization of oriented porous polymer scaffolds. *Biomaterials* 24, 481-489.
- Lin, H.-R., Kuo, C.-J., Yang, C.Y., Shaw, S.-Y., Wu, Y.-J., 2002. Preparation of macroporous biodegradable PLGA scaffolds for cell attachment with the use of mixed salts as porogen additives. *Journal of Biomedical Materials Research* 63, 271-279.
- Lin, L.-Y., Kim, D.-E., 2012. Measurement of the elastic modulus of polymeric films using an AFM with a steel micro-spherical probe tip. *Polymer Testing* 31, 926-930.
- Lu, L., Garcia, C.A., Mikos, A.G., 1999. In vitro degradation of thin poly(DL-lactic-co-glycolic acid) films. *Journal of Biomedical Materials Research* 46, 236-244.
- Lu, L., Peter, S.J., D. Lyman, M., Lai, H.-L., Leite, S.M., Tamada, J.A., Uyama, S., Vacanti, J.P., Robert, L., Mikos, A.G., 2000. In vitro and in vivo degradation of porous poly(DL-lactic-co-glycolic acid) foams. *Biomaterials* 21, 1837-1845.
- Lu, L., Yaszemski, M.J., Mikos, A.G., 2001. Retinal pigment epithelium engineering using synthetic biodegradable polymers. *Biomaterials* 22, 3345-3355.
- Lucca, D.A., Herrmann, K., Klopstein, M.J., 2010. Nanoindentation: Measuring methods and applications. *CIRP Annals - Manufacturing Technology* 59, 803-819.
- Luxner, M., Stampfl, J., Pettermann, H., 2005. Finite element modeling concepts and linear analyses of 3D regular open cell structures. *Journal of Materials Science* 40, 5859-5866.
- Lyu, S., Sparer, R., Untereker, D., 2005. Analytical solutions to mathematical models of the surface and bulk erosion of solid polymers. *Journal of Polymer Science Part B: Polymer Physics* 43, 383-397.
- Lyu, S., Untereker, D., 2009. Degradability of polymers for implantable biomedical devices. *International Journal of Molecular Sciences* 10, 4033-4065.
- Ma, D., Ong, C.W., Wong, S.F., 2004. New relationship between Young's modulus and nonideally sharp indentation parameters. *Journal of Materials Research* 19, 2144-2151.

- Ma, X., Oyamada, S., Wu, T., Robich, M.P., Wu, H., Wang, X., Buchholz, B., McCarthy, S., Bianchi, C.F., Sellke, F.W., Laham, R., 2011. In vitro and in vivo degradation of poly(D, L -lactide-co-glycolide)/ amorphous calcium phosphate copolymer coated on metal stents. *Journal of Biomedical Materials Research - Part A* 96 A, 632-638.
- Malvern, L.E., 1969. *Introduction to the mechanics of a continuous medium*. Prentice-Hall.
- Malzbender, J., de With, G., 2002. Indentation load–displacement curve, plastic deformation, and energy. *Journal of Materials Research* 17, 502-511.
- Manavitehrani, I., Fathi, A., Badr, H., Daly, S., Shirazi, A.N., Dehghani, F., 2016. Biomedical Applications of Biodegradable Polyesters. *Polymers (20734360)* 8, 1-32.
- Manson, J., Dixon, D., 2012. The influence of solvent processing on polyester bioabsorbable polymers. *J Biomater Appl* 26, 623-634.
- Maxwell, A.S., Tomlins, P.E., 2011. New approaches to mapping through-thickness variations in the degradation in poly (lactide-co-glycolide). *Polymer Degradation and Stability* 96, 1015-1021.
- McElhaney, K.W., Vlassak, J.J., Nix, W.D., 1998. Determination of indenter tip geometry and indentation contact area for depth-sensing indentation experiments. *Journal of Materials Research* 13, 1300-1306.
- Mehrer, H., 2007. *Diffusion in Solids: Fundamentals, Methods, Materials, Diffusion-Controlled Processes*. Springer.
- Middleton, J.C., Tipton, A.J., 2000. Synthetic biodegradable polymers as orthopedic devices. *Biomaterials* 21, 2335-2346.
- Miller, C., Shanks, H., Witt, A., Rutkowski, G., Mallapragada, S., 2001. Oriented Schwann cell growth on micropatterned biodegradable polymer substrates. *Biomaterials* 22, 1263-1269.
- Moeller, G., 2009. AFM nanoindentation of viscoelastic materials with large end-radius probes. *Journal of Polymer Science Part B: Polymer Physics* 47, 1573-1587.
- Naughton, G., Bartel, R., Mansbridge, J., 1997. Synthetic Biodegradable Polymer Scaffolds, in: Atala, A., Mooney, D. (Eds.), *Synthetic Biodegradable Polymer Scaffolds*. Birkhäuser Boston, pp. 121-147.
- Ngan, A.H.W., Tang, B., 2002. Viscoelastic effects during unloading in depth-sensing indentation. *Journal of Materials Research* 17, 2604-2610.
- Ngan, A.H.W., Wang, H.T., Tang, B., Sze, K.Y., 2005. Correcting power-law viscoelastic effects in elastic modulus measurement using depth-sensing indentation. *International Journal of Solids and Structures* 42, 1831-1846.

- Nikolov, S., Han, C.S., Raabe, D., 2007. On the origin of size effects in small-strain elasticity of solid polymers. *International Journal of Solids and Structures* 44, 1582-1592.
- Oh, S., Kang, S., Lee, J., 2006. Degradation behavior of hydrophilized PLGA scaffolds prepared by melt-molding particulate-leaching method: Comparison with control hydrophobic one. *Journal of Materials Science: Materials in Medicine* 17, 131-137.
- Oliver, W.C., Pharr, G.M., 1992. Improved technique for determining hardness and elastic modulus using load and displacement sensing indentation experiments. *Journal of Materials Research* 7, 1564-1580.
- Oliver, W.C., Pharr, G.M., 2004. Measurement of hardness and elastic modulus by instrumented indentation: Advances in understanding and refinements to methodology. *Journal of Materials Research* 19, 3-20.
- Oyen, M.L., 2007. Sensitivity of polymer nanoindentation creep measurements to experimental variables. *Acta Materialia* 55, 3633-3639.
- Oyen, M.L., 2013. Nanoindentation of Biological and Biomimetic Materials. *Experimental Techniques* 37, 73-87.
- Pamula, E., Menaszek, E., 2008. In vitro and in vivo degradation of poly(L-lactide-co-glycolide) films and scaffolds. *Journal of Materials Science: Materials in Medicine* 19, 2063-2070.
- Pan, C.J., Tang, J.J., Weng, Y.J., Wang, J., Huang, N., 2006. Preparation, characterization and anticoagulation of curcumin-eluting controlled biodegradable coating stents. *Journal of Controlled Release* 116, 42-49.
- Pan, C.J., Tang, J.J., Weng, Y.J., Wang, J., Huang, N., 2007. Preparation and characterization of rapamycin-loaded PLGA coating stent. *J Mater Sci Mater Med* 18, 2193-2198.
- Pan, Z., Ding, J., 2012. Poly(lactide-co-glycolide) porous scaffolds for tissue engineering and regenerative medicine.
- Pantani, R., Sorrentino, A., 2013. Influence of crystallinity on the biodegradation rate of injection-moulded poly(lactic acid) samples in controlled composting conditions. *Polymer Degradation and Stability* 98, 1089-1096.
- Park, T.G., 1995. Degradation of poly(lactic-co-glycolic acid) microspheres: effect of copolymer composition. *Biomaterials* 16, 1123-1130.
- Perron, J.K., Naguib, H.E., Daka, J., Chawla, A., Wilkins, R., 2009. A study on the effect of degradation media on the physical and mechanical properties of porous PLGA 85/15 scaffolds. *Journal of Biomedical Materials Research Part B: Applied Biomaterials* 91B, 876-886.

- Pillin, I., Montrelay, N., Bourmaud, A., Grohens, Y., 2008. Effect of thermo-mechanical cycles on the physico-chemical properties of poly(lactic acid). *Polymer Degradation and Stability* 93, 321-328.
- Prabhu, S., Hossainy, S., 2007. Modeling of degradation and drug release from a biodegradable stent coating. *Journal of Biomedical Materials Research Part A* 80A, 732-741.
- Ren, T., Ren, J., Jia, X., Pan, K., 2005. The bone formation in vitro and mandibular defect repair using PLGA porous scaffolds. *Journal of Biomedical Materials Research Part A* 74A, 562-569.
- Renouf-Glauser, A.C., Rose, J., Farrar, D.F., Cameron, R.E., 2005. The effect of crystallinity on the deformation mechanism and bulk mechanical properties of PLLA. *Biomaterials* 26, 5771-5782.
- Rettler, E., Hoepfner, S., Sigusch, B.W., Schubert, U.S., 2013. Mapping the mechanical properties of biomaterials on different length scales: Depth-sensing indentation and AFM based nanoindentation. *Journal of Materials Chemistry B* 1, 2789-2806.
- Rhim, J.-W., Mohanty, A.K., Singh, S.P., Ng, P.K.W., 2006. Effect of the processing methods on the performance of polylactide films: Thermocompression versus solvent casting. *Journal of Applied Polymer Science* 101, 3736-3742.
- Sackett, C.K., Narasimhan, B., 2011. Mathematical modeling of polymer erosion: Consequences for drug delivery. *International Journal of Pharmaceutics* 418, 104-114.
- Saha, S.K., Tsuji, H., 2006. Effects of rapid crystallization on hydrolytic degradation and mechanical properties of poly(l-lactide-co- ϵ -caprolactone). *Reactive and Functional Polymers* 66, 1362-1372.
- Saito, E., Liao, E.E., Hu, W.-W., Krebsbach, P.H., Hollister, S.J., 2013. Effects of designed PLLA and 50:50 PLGA scaffold architectures on bone formation in vivo. *Journal of Tissue Engineering and Regenerative Medicine* 7, 99-111.
- Saito, E., Liu, Y., Migneco, F., Hollister, S.J., 2012. Strut size and surface area effects on long-term in vivo degradation in computer designed poly(l-lactic acid) three-dimensional porous scaffolds. *Acta Biomaterialia* 8, 2568-2577.
- Schliecker, G., Schmidt, C., Fuchs, S., Wombacher, R., Kissel, T., 2003. Hydrolytic degradation of poly(lactide-co-glycolide) films: effect of oligomers on degradation rate and crystallinity. *International Journal of Pharmaceutics* 266, 39-49.
- Schmitt, E.A., Flanagan, D.R., Linhardt, R.J., 1994. Importance of distinct water environments in the hydrolysis of poly(DL-lactide-co-glycolide). *Macromolecules* 27, 743-748.

- Schwab, A.D., Agra, D.M.G., Kim, J.H., Kumar, S., Dhinojwala, A., 2000. Surface dynamics in rubbed polymer thin films probed with optical birefringence measurements. *Macromolecules* 33, 4903-4909.
- Shanshan, C., Lili, T., Yingxue, T., Bingchun, Z., Ke, Y., 2013. Study of drug-eluting coating on metal coronary stent. *Materials Science and Engineering: C* 33, 1476-1480.
- Shen, L., Liu, T., Lv, P., 2005. Polishing effect on nanoindentation behavior of nylon 66 and its nanocomposites. *Polymer Testing* 24, 746-749.
- Shi, X., Wang, Y., Ren, L., Lai, C., Gong, Y., Wang, D.-A., 2010. A novel hydrophilic poly(lactide-co-glycolide)/lecithin hybrid microspheres sintered scaffold for bone repair. *Journal of Biomedical Materials Research Part A* 92A, 963-972.
- Shum, A.W.T., Mak, A.F.T., 2003. Morphological and biomechanical characterization of poly(glycolic acid) scaffolds after in vitro degradation. *Polymer Degradation and Stability* 81, 141-149.
- Siparsky, G., Voorhees, K., Miao, F., 1998a. Hydrolysis of Polylactic Acid (PLA) and Polycaprolactone (PCL) in Aqueous Acetonitrile Solutions: Autocatalysis. *Journal of Environmental Polymer Degradation* 6, 31-41.
- Siparsky, G.L., Voorhees, K.J., Miao, F., 1998b. Hydrolysis of polylactic acid (PLA) and polycaprolactone (PCL) in aqueous acetonitrile solutions: Autocatalysis. *Journal of Environmental Polymer Degradation* 6, 31-41.
- Smutz, W.P., Daniels, A.U., Andriano, K.P., France, E.P., Heller, J., 1991. Mechanical test methodology for environmental exposure testing of biodegradable polymers. *Journal of Applied Biomaterials* 2, 13-22.
- Sneddon, I.N., 1965. The relation between load and penetration in the axisymmetric boussinesq problem for a punch of arbitrary profile. *International Journal of Engineering Science* 3, 47-57.
- Soares, J.S., Rajagopal, K.R., Moore Jr, J.E., 2010. Deformation-induced hydrolysis of a degradable polymeric cylindrical annulus. *Biomechanics and Modeling in Mechanobiology* 9, 177-186.
- Soares, J.S., Zunino, P., 2010. A mixture model for water uptake, degradation, erosion and drug release from polydisperse polymeric networks. *Biomaterials* 31, 3032-3042.
- Spenlehauer, G., Vert, M., Benoit, J.P., Boddaert, A., 1989. In vitro and In vivo degradation of poly(D,L lactide/glycolide) type microspheres made by solvent evaporation method. *Biomaterials* 10, 557-563.

Steele, T.W.J., Huang, C.L., Widjaja, E., Boey, F.Y.C., Loo, J.S.C., Venkatraman, S.S., 2011. The effect of polyethylene glycol structure on paclitaxel drug release and mechanical properties of PLGA thin films. *Acta Biomaterialia* 7, 1973-1983.

Sung, H.-J., Meredith, C., Johnson, C., Galis, Z.S., 2004. The effect of scaffold degradation rate on three-dimensional cell growth and angiogenesis. *Biomaterials* 25, 5735-5742.

Tabor, D., 1948. A Simple Theory of Static and Dynamic Hardness. *Proceedings of the Royal Society of London A: Mathematical, Physical and Engineering Sciences* 192, 247-274.

Tabor, D., 1977. Surface forces and surface interactions. *Journal of Colloid and Interface Science* 58, 2-13.

Takayama, T., Todo, M., Tsuji, H., 2011. Effect of annealing on the mechanical properties of PLA/PCL and PLA/PCL/LTI polymer blends. *Journal of the Mechanical Behavior of Biomedical Materials* 4, 255-260.

Tang, B., Ngan, A.H.W., 2003a. Accurate measurement of tip-sample contact size during nanoindentation of viscoelastic materials. *Journal of Materials Research* 18, 1141-1148.

Tang, B., Ngan, A.H.W., 2003b. Accurate measurement of tip - Sample contact size during nanoindentation of viscoelastic materials. *Journal of Materials Research* 18, 1141-1148.

Tang, X.G., Hou, M., Truss, R., Zou, J., Yang, W., Dong, Z.G., Huang, H., 2011. An unexpected plasticization phenomenon and a constant of the change rate of viscoelastic properties for polymers during nanoindentation test. *Journal of Applied Polymer Science* 122, 885-890.

Thombre, A.G., Himmelstein, K.J., 1984. Modelling of drug release kinetics from a laminated device having an erodible drug reservoir. *Biomaterials* 5, 250-254.

Törmälä, P., Vainionpää, S., Kilpikari, J., Rokkanen, P., 1987. The effects of fibre reinforcement and gold plating on the flexural and tensile strength of PGA/PLA copolymer materials in vitro. *Biomaterials* 8, 42-45.

Tranchida, D., Piccarolo, S., Loos, J., Alexeev, A., 2007. Mechanical characterization of polymers on a nanometer scale through nanoindentation. A study on pile-up and viscoelasticity. *Macromolecules* 40, 1259-1267.

Troyon, M., Abbès, F., Garcia Guzman, J.A., 2012. Is the exponent 3/2 justified in analysis of loading curve of pyramidal nanoindentations? *Scanning* 34, 410-417.

Tsuji, H., 2000. In vitro hydrolysis of blends from enantiomeric poly(lactide)s Part 1. Well-stereo-complexed blend and non-blended films. *Polymer* 41, 3621-3630.

- Tsuji, H., 2002. Autocatalytic hydrolysis of amorphous-made polylactides: effects of l-lactide content, tacticity, and enantiomeric polymer blending. *Polymer* 43, 1789-1796.
- Tsuji, H., Ikada, Y., 2000. Properties and morphology of poly(l-lactide) 4. Effects of structural parameters on long-term hydrolysis of poly(l-lactide) in phosphate-buffered solution. *Polymer Degradation and Stability* 67, 179-189.
- Tsuji, H., Mizuno, A., Ikada, Y., 2000. Properties and morphology of poly(L-lactide). III. Effects of initial crystallinity on long-term in vitro hydrolysis of high molecular weight poly(L-lactide) film in phosphate-buffered solution. *Journal of Applied Polymer Science* 77, 1452-1464.
- Tweedie, C.A., Constantinides, G., Lehman, K.E., Brill, D.J., Blackman, G.S., Van Vliet, K.J., 2007. Enhanced Stiffness of Amorphous Polymer Surfaces under Confinement of Localized Contact Loads. *Advanced Materials* 19, 2540-2546.
- Uematsu, K., Hattori, K., Ishimoto, Y., Yamauchi, J., Habata, T., Takakura, Y., Ohgushi, H., Fukuchi, T., Sato, M., 2005. Cartilage regeneration using mesenchymal stem cells and a three-dimensional poly-lactic-glycolic acid (PLGA) scaffold. *Biomaterials* 26, 4273-4279.
- Vey, E., Rodger, C., Meehan, L., Booth, J., Claybourn, M., Miller, A.F., Saiani, A., 2012. The impact of chemical composition on the degradation kinetics of poly(lactic-co-glycolic) acid copolymers cast films in phosphate buffer solution. *Polymer Degradation and Stability* 97, 358-365.
- Vey, E., Roger, C., Meehan, L., Booth, J., Claybourn, M., Miller, A.F., Saiani, A., 2008. Degradation mechanism of poly(lactic-co-glycolic) acid block copolymer cast films in phosphate buffer solution. *Polymer Degradation and Stability* 93, 1869-1876.
- Vieira, A.C., Guedes, R.M., Tita, V., 2014. Constitutive modeling of biodegradable polymers: Hydrolytic degradation and time-dependent behavior. *International Journal of Solids and Structures* 51, 1164-1174.
- Vieira, A.C., Vieira, J.C., Ferra, J.M., Magalhães, F.D., Guedes, R.M., Marques, A.T., 2011. Mechanical study of PLA–PCL fibers during in vitro degradation. *Journal of the Mechanical Behavior of Biomedical Materials* 4, 451-460.
- Voyiadjis, G.Z., Shojaei, A., Mozaffari, N., 2014. Strain gradient plasticity for amorphous and crystalline polymers with application to micro- and nano-scale deformation analysis. *Polymer* 55, 4182-4198.
- Vozzi, G., Flaim, C., Ahluwalia, A., Bhatia, S., 2003. Fabrication of PLGA scaffolds using soft lithography and microsyringe deposition. *Biomaterials* 24, 2533-2540.
- Wallace, W.E., Fischer, D.A., Efimenko, K., Wu, W.L., Genzer, J., 2001. Polymer chain relaxation: Surface outpaces bulk [3]. *Macromolecules* 34, 5081-5082.

- Wang, Y., Han, X., Pan, J., Sinka, C., 2010. An entropy spring model for the Young's modulus change of biodegradable polymers during biodegradation. *Journal of the Mechanical Behavior of Biomedical Materials* 3, 14-21.
- Wang, Y., Pan, J., Han, X., Sinka, C., Ding, L., 2008. A phenomenological model for the degradation of biodegradable polymers. *Biomaterials* 29, 3393-3401.
- Ward, I.M., Sweeney, J., 2012. *Mechanical Properties of Solid Polymers*. Wiley.
- Waris, E., Ashammakhi, N., Kaarela, O., Raatikainen, T., Vasenius, J., 2004. Use of bioabsorbable osteofixation devices in the hand. *Journal of Hand Surgery* 29, 590-598.
- Weir, N., Buchanan, F., Orr, J., Dickson, G., 2004a. Degradation of poly-L-lactide. Part 1: in vitro and in vivo physiological temperature degradation. *Proceedings of the Institution of Mechanical Engineers, Part H: Journal of Engineering in Medicine* 218, 307-319.
- Weir, N.A., Buchanan, F.J., Orr, J.F., Farrar, D.F., Boyd, A., 2004b. Processing, annealing and sterilisation of poly-l-lactide. *Biomaterials* 25, 3939-3949.
- Weir, N.A., Buchanan, F.J., Orr, J.F., Farrar, D.F., Dickson, G.R., 2004c. Degradation of poly-L-lactide. Part 2: Increased temperature accelerated degradation. *Proceedings of the Institution of Mechanical Engineers, Part H: Journal of Engineering in Medicine* 218, 321-330.
- Westedt, U., Wittmar, M., Hellwig, M., Hanefeld, P., Greiner, A., Schaper, A.K., Kissel, T., 2006. Paclitaxel releasing films consisting of poly(vinyl alcohol)-graft-poly(lactide-co-glycolide) and their potential as biodegradable stent coatings. *Journal of Controlled Release* 111, 235-246.
- Wettergreen, M.A., Bucklen, B.S., Starly, B., Yuksel, E., Sun, W., Liebschner, M.A.K., 2005. Creation of a unit block library of architectures for use in assembled scaffold engineering. *Computer-Aided Design* 37, 1141-1149.
- Witt, C., Kissel, T., 2001. Morphological characterization of microspheres, films and implants prepared from poly(lactide-co-glycolide) and ABA triblock copolymers: is the erosion controlled by degradation, swelling or diffusion? *European Journal of Pharmaceutics and Biopharmaceutics* 51, 171-181.
- Witt, C., Mäder, K., Kissel, T., 2000. The degradation, swelling and erosion properties of biodegradable implants prepared by extrusion or compression moulding of poly(lactide-co-glycolide) and ABA triblock copolymers. *Biomaterials* 21, 931-938.
- Wright-Charlesworth, D.D., Miller, D.M., Miskioglu, I., King, J.A., 2005. Nanoindentation of injection molded PLA and self-reinforced composite PLA after in

vitro conditioning for three months. *Journal of Biomedical Materials Research Part A* 74A, 388-396.

Wrucke, A.J., Han, C.-S., Majumdar, P., 2013. Indentation size effect of multiple orders of magnitude in polydimethylsiloxane. *Journal of Applied Polymer Science* 128, 258-264.

Wu, L., Ding, J., 2004. In vitro degradation of three-dimensional porous poly(D,L-lactide-co-glycolide) scaffolds for tissue engineering. *Biomaterials* 25, 5821-5830.

Wu, L., Ding, J., 2005. Effects of porosity and pore size on in vitro degradation of three-dimensional porous poly(D,L-lactide-co-glycolide) scaffolds for tissue engineering. *Journal of Biomedical Materials Research Part A* 75A, 767-777.

Wu, L., Jing, D., Ding, J., 2006a. A "room-temperature" injection molding/particulate leaching approach for fabrication of biodegradable three-dimensional porous scaffolds. *Biomaterials* 27, 185-191.

Wu, L., Zhang, J., Jing, D., Ding, J., 2006b. "Wet-state" mechanical properties of three-dimensional polyester porous scaffolds. *Journal of Biomedical Materials Research Part A* 76A, 264-271.

Xi, T., Gao, R., Xu, B., Chen, L., Luo, T., Liu, J., Wei, Y., Zhong, S., 2010. In vitro and in vivo changes to PLGA/sirolimus coating on drug eluting stents. *Biomaterials* 31, 5151-5158.

Xu, W., Chahine, N., Sulchek, T., 2011. Extreme hardening of PDMS thin films due to high compressive strain and confined thickness. *Langmuir* 27, 8470-8477.

Xu, X., Liu, T., Zhang, K., Liu, S., Shen, Z., Li, Y., Jing, X., 2008. Biodegradation of poly(L-lactide-co-glycolide) tube stents in bile. *Polymer Degradation and Stability* 93, 811-817.

Yang, S., Zhang, Y.W., Zeng, K., 2004. Analysis of nanoindentation creep for polymeric materials. *Journal of Applied Physics* 95, 3655-3666.

Yang, Y., Tang, G., Zhao, Y., Yuan, X., Fan, Y., 2010. Effect of Cyclic Loading on In Vitro Degradation of Poly(L-lactide-co-glycolide) Scaffolds. *Journal of Biomaterials Science, Polymer Edition* 21, 53-66.

Yang, Y., Zhao, Y., Tang, G., Li, H., Yuan, X., Fan, Y., 2008. In vitro degradation of porous poly(L-lactide-co-glycolide)/ β -tricalcium phosphate (PLGA/ β -TCP) scaffolds under dynamic and static conditions. *Polymer Degradation and Stability* 93, 1838-1845.

Yoon, J.J., Park, T.G., 2001. Degradation behaviors of biodegradable macroporous scaffolds prepared by gas foaming of effervescent salts. *Journal of Biomedical Materials Research* 55, 401-408.

Zeng, K., Chiu, C.h., 2001. An analysis of load–penetration curves from instrumented indentation. *Acta Materialia* 49, 3539-3551.

Zhang, T.-Y., Xu, W.-H., Zhao, M.-H., 2004. The role of plastic deformation of rough surfaces in the size-dependent hardness. *Acta Materialia* 52, 57-68.

Zhou, H., Lawrence, J.G., Bhaduri, S.B., 2012. Fabrication aspects of PLA-CaP/PLGA-CaP composites for orthopedic applications: A review. *Acta Biomaterialia* 8, 1999-2016.

Zhou, J., Komvopoulos, K., 2006. Surface and interface viscoelastic behaviors of thin polymer films investigated by nanoindentation. *Journal of Applied Physics* 100.

Zolnik, B.S., Burgess, D.J., 2007. Effect of acidic pH on PLGA microsphere degradation and release. *Journal of Controlled Release* 122, 338-344.